Shibaura Institute of Technology

Ph.D. Thesis

An analysis of drying characteristics of Polish lignite in superheated steam atmosphere

Marcin Zakrzewski

Supervisors:

Professor Shinji Kimijima   Professor Janusz S. Szmyd

Tokyo, 2018

Acknowledgments

I would like to convey my sincere gratefulness to Professor Shinji Kimijima for his invaluable support during the preparation of this thesis as well as for the benevolence, enthusiasm and welcoming atmosphere provided during my stay at his laboratory at Shibaura Institute of Technology.

It is my pleasure to express my appreciation towards Professor Janusz S. Szmyd for the research opportunities he offered me, for the inspiration to unceasingly enhance knowledge, for his invaluable academic guidance as well as for the time and attention he has been giving me throughout my doctoral studies at AGH University of Science and Technology.

I would like to acknowledge Professor Shozo Kaneko, who kindly accepted me in his research group at The University of Tokyo. His visionary ideas, splendiferous knowledge and willingness to share them with people deserve the highest recognition.

I do express my honest gratitude to Dr. Anna Ściążko and Dr. Yosuke Komatsu for the collaboration during the research that preceded the formulation of this dissertation. Their relentless efforts, good will, patience and professionalism cannot be overestimated in regard to raising the quality of this work.

I truly appreciate Dr. Tsuyoshi Kiriyama who introduced me to the superheated steam drying of lignite. The information gained from him had a great importance in conducting the research described in this work.

Contents

x

Nomenclature

Symbols

A – area [m^2]

b – half of layer's thickness [m]

c – specific heat [$J \, kg^{-1} \, K^{-1}$]

B – uniformity constant for coal particle distribution equation [-]

CDRP – constant drying rate period

$C\%$ – carbon content [mass%]

$\{CO_2\_kg\}$ – unit emission of carbon dioxide per mass unit [$kg \, kg^{-1}$]

$\{CO_2\_kWh\}$ – unit emission of carbon dioxide per electricity unit [$kg \, kWh^{-1}$]

d – diameter [m]

D – apparent diffusion coefficient of free water [$m^2 \, s^{-1}$]

DBC – dry base coal

DDRP – decreasing drying rate period

DR – drying rate [s^{-1}]

DT – number of simulation steps [-]

E_kg – electricity generation per fuel mass unit [$kWh \, kg^{-1}$]

F – analytical solution equation coefficient

h – heat transfer coefficient [$W \, m^{-2} \, K^{-1}$]

$H\%$ – hydrogen content [mass%]

HHV – higher heating value [J kg^{-1}]

ΔH – enthalpy change of bound water evaporation [J kg^{-1}]

I – number of iterations of the simulation

k – parameter of equilibrium moisture content function

L – latent heat of free water evaporation [J kg^{-1}]

LHV – lower heating value [J kg^{-1}]

m – mass [kg]

n – normal vector

N – number of layers within a spherical model

NMAE – normalized mean absolute error [-]

p – pressure [Pa]

$\dot{q}$ – heat flux [W m^{-2}]

$\dot{Q}$ – rate of heat flow [W]

ΔQ – heat input/consumption [J]

r – radius [m]

R – characteristic linear dimension [m]

RMSE – root-mean squared error of temperature [$^{\circ}$C]

t – time [s]

Δt – time step [s]

T – temperature [$^{\circ}$C]

ΔT – change/difference of temperature [$^{\circ}$C]

V – volume [m^{3}]

WP – water percentage [mass%]

WS – water share [mass%]

X – moisture content [-]

Greek letters

α – thermal diffusivity [m^2 s^{-1}]

β – root of the characteristic equation

ε – emissivity [-]

η – thermal efficiency [%]

ϑ – excess temperature [$^{\circ}$C]

λ – thermal conductivity [W m^{-1} K^{-1}]

ν – kinematic viscosity [m^2 s^{-1}]

ρ – density [kg m^{-3}]

σ – Stefan-Boltzmann constant [W m^{-2} K^{-4}]

υ – evaporation rate [kg m^{-2} s^{-1}]

φ – volumetric fraction [-]

Dimensionless numbers

Bi – Biot number [-]

Fo – Fourier number [-]

Gr – Grashof number [-]

Nu – Nusselt number [-]

Pr – Prandtl number [-]

Ra – Rayleigh number [-]

Subscripts

1 – referring to the first layer (surface)

a – superheated steam

b – bulk

ad – air-dried coal

apr – approximated

avg – average

c – dry coal

cent – center

cond – condensation

cons – consumption

conv – convective

CDRP – referring to constant drying rate period

dry – drying

e – characteristic (particle diameter)

exp – experimental

eq – equilibrium

evap – evaporated water

free – free water removal

in – entering the layer

int – interface

m – sequence of roots of the characteristic equation index

max – maximum

mid – midpoint

n – referring to n-th layer

out – leaving the layer

r – relative

rad – radiative

raw – as-received coal

s – water vapor

sim – simulated

surf – surface

sw – swelling water

trans – water transfer

V – volumetric

w – water

Superscripts

+ – superscript of dimensionless radius

0 – initial

i – referring to time instance i

Table captions

Figure captions

CHAPTER 1

Introduction

1.1 Role of lignite in global economy

The name "coal" describes the general category of solid-state fossil fuels of significant hydrocarbon content. Although there are many classifications, from an economical point of view, two major groups of this fuel are distinguished: hard coal and lignite, also known as brown coal. Besides arbitrary and vague threshold of lower heating value, which can vary from 16.5 MJ kg^{-1} [1] to 28.7 MJ kg^{-1} [2], the major difference is related to the specificity of production and utilization of those two categories of coal.

The deliberation on structural and technological properties of coal ranks is summarized by the Hilt's Law, which states *In a vertical sequence, at any one locality in a coalfield, the rank of the coal seams rises with increasing depth* [3,4]. Hard coal is commonly produced in deep mines, and comes in the form of compact pieces of rock, which are feasible to be transported at virtually any distance. Lignite, on the other hand, is mined in opencast excavation sites, what is connected with relatively shallow deposits of this fuel. However, due to low heating value per mass unit, attributed mostly to the high natural water content in lignite, the ratio of prospective energy output to cost of transportation is impaired. In addition, low rank coals, which brown coal is assigned to, often exhibit significant share of volatile matter. That feature enhances their

vulnerability to spontaneous combustion while being stored on a stockpiles [4].

For the reasons stated above, over 95% of lignite production in particular countries is consumed domestically [1], with a prevailing model of lignite-fueled power plant situated next to or surrounded by the deposits. That specificity brings about the economic contradistinction of hard coal as an international and lignite as a regional commodity, because the price of the former is much more prone on the global trends. For instance, production cut-backs in China, the largest producer, in 2016 caused the significant increase of the spot price of hard coal after a 5-year period of steady decline of average price level on export coals [1]. Lignite is not immune to the international events in the field of economy and politics, as for example cap and trade introduced by the European Union to reduce the carbon dioxide emissions, still the local circumstances play a greater role in shaping of its market position. Among these, one can list the ownership and geographical location of the lignite complex within a domestic power system, the current level of domestic reserves or the cost of mining [5]. The relatively low value of the latter in the case of lignite, makes it an important compound of energy mixes in countries that possess its deposits.

In 2015, lignite accounted for 1.7% of primary energy consumption worldwide (the corresponding value for hard coal was 27.5%) with a cumulated value of 9.9×10^{18} J [1]. In Tab. 1.1 and 1.2, the countries in possession of largest reserves and resources are listed, respectively. It should be recognized that the term "reserves" describes the total proven mass of feedstock economically feasible in terms of production and exploitation with reference to present market situation and state of technology. Meanwhile, the expression "resources" gives a hint about a material that is currently not justified to be exploited for any reason or a material unproven, but estimated geologically to exist. In general, reserves are analogical to "possibility", whereas resources to "potential".

Table 1.1 Countries possessing largest lignite reserves (as of 2015) [1]

rank	country	reserves [Gt]	share [%]
1	Russia*	90.7	28.6%
2	Australia	76.5	24.2%
3	Germany	36.2	11.4%
4	USA	30.2	9.5%
5	Turkey	11.0	3.5%
6	Indonesia	8.2	2.6%
7	China	7.7	2.4%
8	Serbia	7.1	2.2%
9	New Zealand	6.8	2.1%
10	Poland	5.5	1.7%
-	others	36.9	11.7%
-	total	316.8	100%

*including subbituminous coal reserves

Table 1.2 Countries possessing largest lignite resources (as of 2015) [1]

rank	country	resources [Gt]	share [%]
1	USA	1368.0	30.9%
2	Russia*	1288.9	29.1%
3	Australia	403.4	9.1%
4	China	324.9	7.3%
5	Poland	222.4	5.0%
6	Vietnam	199.9	4.5%
7	Pakistan	176.7	4.0%
8	Mongolia*	119.4	2.7%
9	Canada	118.3	2.7%
10	India	38.1	0.9%
-	others	162.3	3.7%
-	total	4422.2	100%

*including subbituminous coal resources

Judging from the information gathered in the tables 1.1 and 1.2, the ratio of reserves to resources varies considerably, what influences the current production

potential of the countries. The major lignite producers are pointed out in Tab. 1.3, and their share in global production is illustrated by Fig. 1.1.

Table 1.3 Leading lignite producers in 2015 [1]

rank	country	production [Mt]	share [%]
1	Germany	178.1	17.6%
2	China	140.0	13.8%
3	Russia*	73.2	7.2%
4	USA	64.7	6.4%
5	Poland	63.1	6.2%
6	Australia	63.0	6.2%
7	Indonesia	60.0	5.9%
8	Turkey	50.4	5.0%
9	Greece	46.0	4.5%
10	India	43.9	4.3%
-	others	228.8	22.5%
-	total	1011.2	100%

*including subbituminous coal resources
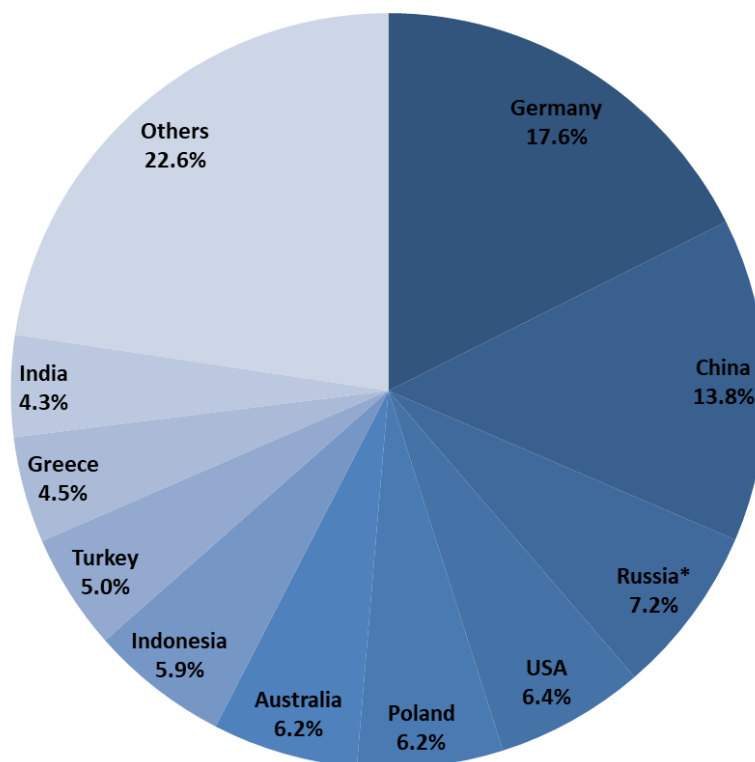
Figure 1.1 Global share of leading lignite producers in 2015

1.2 Lignite industry in Poland

The origin of brown coal exploitation in the area of present-day Poland dates back to the 18th century. There were several mines established since 1740 in Turoszow region and 1770 became the milestone for beginning of industrial scale exploitation [6]. In the entire 19th century the lignite-abundant territories of present-day central and western Poland were under control of Prussia (Germany). The Prussian government put efforts to take advantage of available resources, founding a number of lignite mines, listed in Tab. 1.4.

Table 1.4 Lignite mines founded on present territory of Poland in the 19th century [6]

name	former name (German)	location	established
Conrad	-	Witoszyn	1877
Cybinka	Bach	Cybinka	1864
Dzialoszyn	Edward	Dzialoszyn	mid 19th c.
Henryk	Lohser Werke	Kunice Zarskie	1889
Jadwiga	Gluckstern	Kunice Zarskie	1890
Luban	Gluckauf	Zareba Gorna	late 19th c.
Pustkowie	Max	Bodzew	1844
Sieniawa	Emiliensgluck	Sieniawa	1873
Slone	Grunterberger Gruben	Zielona Gora	1840
Smogory	Oskar	Smogory	1886
Teresa	-	Kunice Zarskie	1897
Turow	Hirschfelde	Bogatynia	1836
Wiktor	-	Buczyce	1898
Zapomniana	Joseph Hermann	Trojca	1875

No industrial exploitation of lignite was undertaken in the period between the First and Second World War, when the Polish state regained independence. In the first period after 1945, the Polish lignite industry based on the mines established by Germans

in the previous century. The major part of lignite production in the first decade after war was covered by Turow lignite mine (see Fig. 1.2), followed by several deep and opencast mines in Konin region. However, there was no power generation relying on lignite. Significant share of production was assigned to briquetting facilities or exported to German Democratic Republic, due to proximity of Turow mine to the western border.
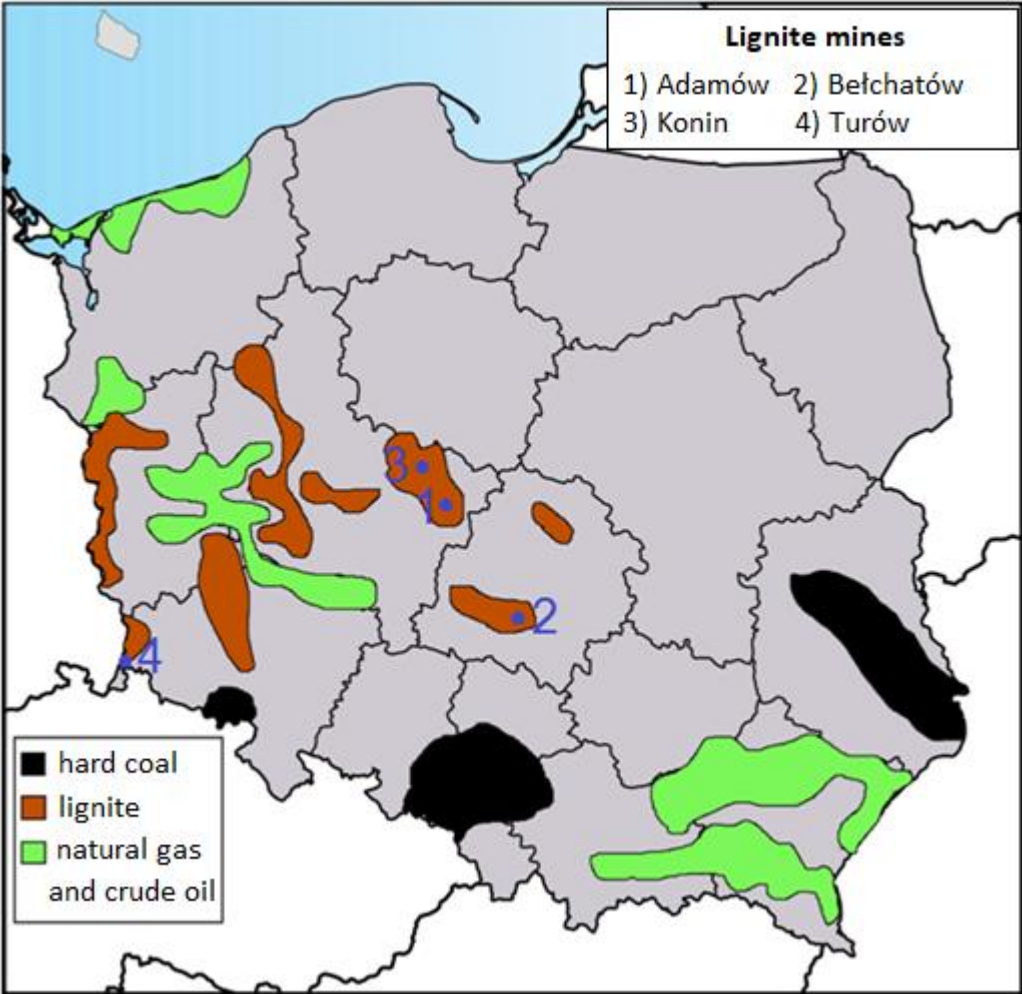
Figure 1.2 Deposits of fossil fuels in Poland (lignite mines marked)

The first power generation unit fuelled with brown coal was connected to the domestic grid in 1958, when Konin power plant (580 MW) started its operation. It was shortly followed by Turow (1400 MW) and Adamow (600 MW) plants, established in 1962 and 1964, respectively. The latter year was the first, when domestic consumption

of lignite exceeded exported tonnage [7]. In 1967, Patnow power plant (1200 MW) was synchronized, constituting the Patnow-Adamow-Konin complex of three lignite-fueled plants. The second part of this triad was decommissioned in January 2018.

A remarkable step in Polish lignite industry was taken in 1980, when first batches of lignite were sent from Belchatow mine to nearby power plant. This complex shortly achieved the leading position among lignite production sites due to strategic location for domestic power system (geographical center of Poland), as well as abundant deposits. In 1988, the annual target production capacity of Belchatow mine was reached (38,5 Mt) what contributed to setting the all-time record of domestic lignite industry at 73,5 Mt [8]. In 2011 a new unit of 858 MW was appended to Belchatow power plant, what totalled its installed capacity to over 5400 MW. Due to that fact it is the largest power plant in Poland, satisfying around 20% of domestic electricity demand, and the second largest coal power plant in the world (following Taichung in Taiwan). The selected annual statistics of lignite production and its impact on power generation during the post-war era in Poland are gathered in Tab. 1.5.

Table 1.5 Utilization of lignite in Poland on selected years between 1945 and 1990 [7]

year	export [Mt]	power plants [Mt]	other industries [Mt]	total production [Mt]	electricity generation [GWh]
1945	-	-	40	40	-
1957	4116	-	1838	5954	-
1958	5192	573	1774	7539	396
1963	5736	6916	2692	15344	4716
1964	5381	12098	2800	20279	8479
1976	3084	34803	1418	39305	27136
1977	3387	35842	1531	40760	27007
1978	3332	36373	1300	41005	27195
1988	-	70559	2928	73487	52585
1990	223	66416	945	67584	52182

After the fall of communism in Eastern Europe accompanied by economic transformation of 1989, lignite retained its important role in Polish energy mix. Still, due to overall changes in domestic industry, Poland was able to overfulfill the commitments of Kyoto Protocol, achieving 30% decrease of greenhouse gases emission on the period of 1990 – 2008, having been committed to one fifth of this value [9]. Over the last couple of years the share of lignite in Poland's electricity generation has been slightly declining, what also concerns hard coal. In 2016, out of total 164.6 TWh of consumed electricity, 51.2 TWh was covered by domestic generation in lignite power plants. The major cause for decline in coal role in the energy mix is the increasing share of renewable energy sources, what is forced by regulations of the European Union aiming at further reduction of carbon intensity. That trend does not concern another fossil fuel – natural gas. The reasons might be connected with commissioning of LNG terminal in Swinoujscie in 2015, what reduced the dependence on import from Russia, and the necessity of increasing the flexibility of the system that increases the share of unstable renewable energy sources.

Table 1.6 Electricity generation in Poland [10]

category	2014	2015	2016
total production	98.6%	100.2%	98.8%
professional power plants	88.4%	87.9%	85.5%
water	1.6%	1.4%	1.5%
conventional heat	86.8%	86.5%	84.0%
hard coal	50.6%	50.7%	49.4%
lignite	34.2%	33.2%	31.1%
gas	2.1%	2.6%	3.5%
wind power plants and other renewables	4.6%	6.3%	7.1%
industrial power plants	5.7%	6.0%	6.2%
transborder exchange	1.4%	-0.2%	1.2%
total consumption [% / GWh]	100.0%	100.0%	100.0%
	158733	161438	164625

The details of lignite production and its influence on power generation in Poland are given in Tab. 1.7. It includes the list of Polish lignite mines, matched with the power plants that are fueled with their output. Out of 60 million tons extracted in Poland in 2016, Belchatow mine accounts for roughly 2/3 of the total value. It is followed by Konin opencast mine which supplies fuel to three surrounding plants: Konin, Patnow I and Patnow II. Together with Adamow power plant, that ended operation in January 2018, they belong to Zespol Elektrowni Patnow-Adamow-Konin S.A (ZE PAK) company. Meanwhile, Belchatow and Turow are owned by the largest Polish power company, Polska Grupa Energetyczna S.A. (PGE) which besides production of electricity is active in the field of distribution and trade. Note that lignite-fueled power plants scored in 2016 the highest capacity utilization rate among various types of power generation industries of average 5400 hours per annum. Meanwhile, power plants fueled with hard coal attained the mean result of 4200 hours per annum and combined heat and power plants worked for average of 3900 hours during the entire 2016 [11].

Table 1.7 Polish lignite mines and power plants [11–14]

mines		power plants			
name	production in 2016 [Mt]	name	beginning of operation	installed capacity [MW]	owner
Belchatow	40.2	Belchatow	1981	5472	PGE
Turow	7.5	Turow	1962	1498	
Konin	9.0	Konin	1958	178	ZE PAK
		Patnow I	1967	1244	
		Patnow II	2008	474	
Adamow	3.5	Adamow	1964 (end in 2018)	600	
total	60.2	total		9466	

CHAPTER 2

Technology of coal drying

2.1 Moisture in lignite

2.1.1 Structural and thermodynamic classification

As indicated in the previous chapter, lignite has an important position in energy mixes of numerous countries. Still, due to elevated content of water (30-70% of a raw mass), its utilization is undermined in terms of economical calculation and environmental impact. To overcome this obstacle, drying of brown coal is frequently applied. The design or selection of the drying system appropriate for the particular material should rely on the knowledge about the nature of moisture stored within coal structure as well as its interactions with the solid matter of the fuel.

According to various research [15–17], several types of water may be distinguished in lignite, regarding to the circumstances of their structural occurrence, and therefore, manners of their removal. The desorption of each type depends on relative vapor pressure next to the surface of moisture layer. One of possible moisture classifications is presented in Tab. 2.1.

In general, bulk water represents (Fig. 2.1) the moisture that is deposited by forces of adhesion on the surface of the coal or in the space between its particles. Meanwhile, capillary water is stored within vessels of plant origin. With the exception for some small capillaries of slightly deviated thermodynamics [18], this type, together

with bulk water is subject to an uninhibited desorption at a certain constant value of latent heat of evaporation. For the purposes of this study, moisture satisfying this criterion is classified in general as free water.
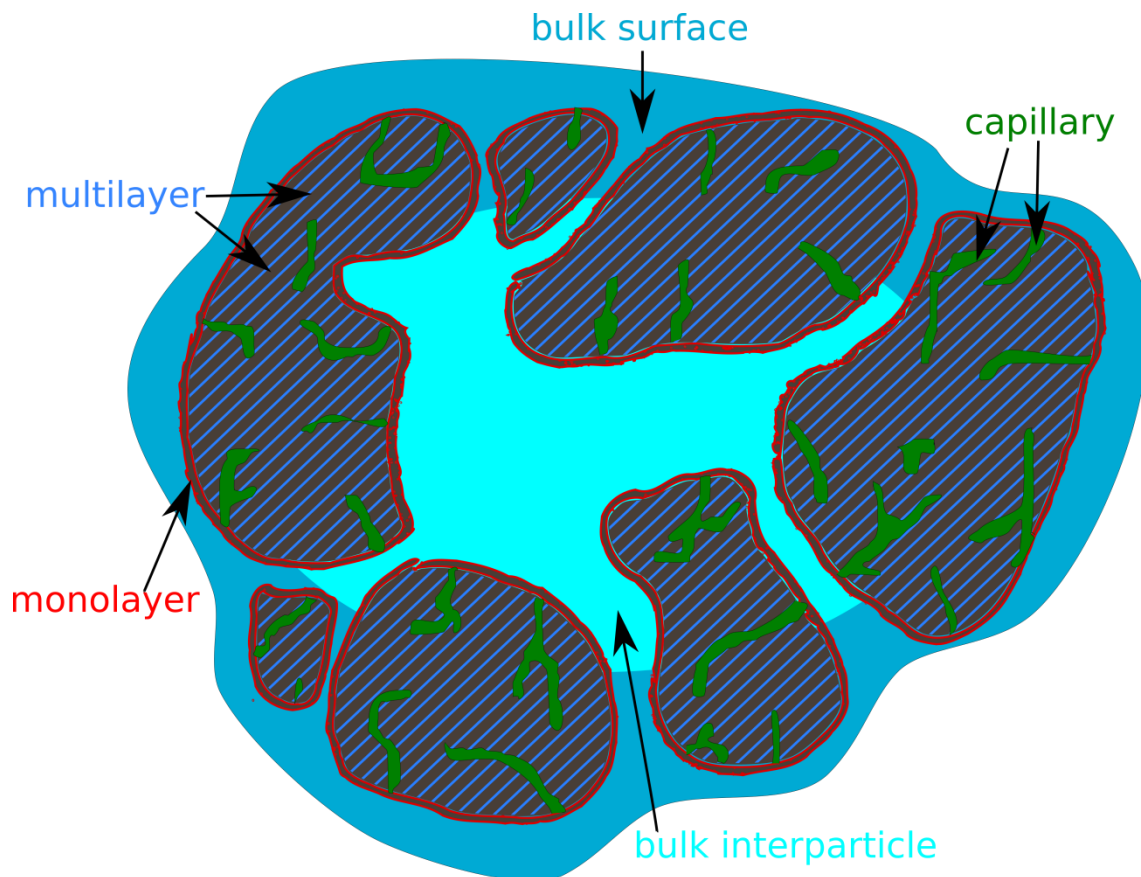
Figure 2.1 Types of water in lignite

On the other hand, there is a substantial amount of water that requires larger amount of heat to be removed from coal. To a certain degree that is attributed to oxygen functional groups in coal, occurring especially in the form of carboxylate salts, that tend to bind chemically with hydrogen in water, therefore influencing the high hydrophilicity of lignite [19]. That type of chemically adsorbed water, either form a series of layers within pores and crevices of the inherent structure or exists as a singular layer of molecules bound tightly on the surface of coal [20]. The moisture forming a chemically

stabilized layers is classified in this study as bound water, which contains also partially water stored in narrow capillaries. Some researchers also mentioned moisture held in a closed pores which can only be removed following the destruction of surrounding structures [21] or so-called non-freezing water which does not turn to solid phase during coal analysis by means of differential scanning calorimetry (DSC) [22] or nuclear magnetic resonance [23]. The simplified chart of water types from Tab. 2.1, relating to classification used in this study is shown in Fig. 2.2.

Table 2.1 Classification of water in brown coal [15]

water type	relative vapor pressure range p/p^0	approximate classification	share	description
bulk	0.96 to 1.0	free water	63.7%	regular liquid condensed on or between coal particles
capillary	0.5 to 0.96	free/bound water	27.5%	moisture condensed in capillaries
multilayer	0.1 to 0.5	bound water	4.8%	weakly hydrogen-bounded water on the monolayer surface
monolayer	below 0.1	bound water	4.0%	water on interior coal surface, constituted relying on strong hydrogen-oxygen bonds

2.1.2 Technological aspects

The high level of water content, ranging from 30 to 75% [24] deteriorate the usefulness of brown coal in power generation technologies. The desired level of moisture in lignite assigned for combustion in the pulverized coal boiler is around 12-15%, whereas gasification may require coal of water share around 5% [25].
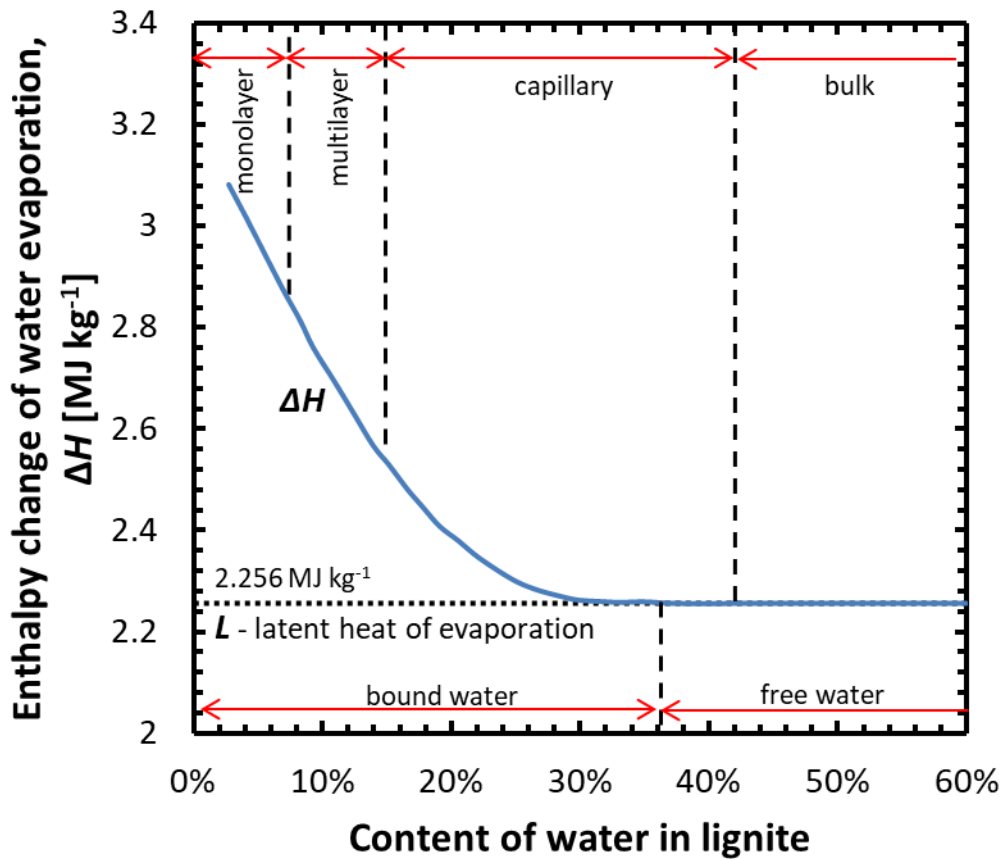
Figure 2.2 Evaporation heat demand in regard to water types (data from [15] included)

The negative influence of considerable moisture content is observable as soon as during the storage and transportation of mined fuel. In countries, where temperatures below 0 ^{o}C are reported, the problem of freezing arises. Not only does it hinder the fragmentation of coal into transportable batches, but due to volumetric expansion accompanying ice formation, the devices serving to bring coal from the excavation site to the power generation unit may be subject to damage [20].

Another issue related to that part of brown coal handling is relatively high vulnerability to spontaneous combustion at the stockpile. In general, this phenomenon is prompted when the rate of low temperature oxidation in air generates more heat than the coal bed is giving off to the ambience. According to the observations, the long period of dry weather followed by a shower rain fosters spontaneous ignition. This is because the

condensation and wetting processes release self-heat in coal, what leads to increase in its temperature and consequently to growth of oxidation rate [15].

The processes of fuel preparation are also undermined by water in coal, which decreases the friability of the rock. Thus, the efficiency of coal grinding prior to further utilization is reduced, making the preparation workload higher [18].

The major concern, however, related to significant water share in lignite is connected with calorific value. Both sensible and latent heat of water diminish the energy output from the fuel by 20-25% [26]. As a consequence, higher fuel input is required to generate a certain value of electricity, comparing to bituminous coal. As a consequence, more flue gas is produced, increasing the atmospheric concentration of carbon dioxide. According to some studies, reduction in water share from 60% to 40% may entail decline in CO_2 emission per generated electricity by 30% [27]. This matter is especially important for the national power systems, which recently are often obliged to keep up with the emission caps set for greenhouse gases by international organizations, such as the European Union or United Nations [28,29].

Another troublesome issue is related to the size of boiler. Due to high inert gas input, the temperature of lignite combustion is usually several hundred degrees lower than in the case of bituminous coal boiler of the same output. Although this technological feature affects beneficially the reduction of nitrogen oxide emissions, a larger surface wall of the boiler is required to efficiently collect the radiative heat of the hot gases produced in combustion. This requirement significantly elevates the initial cost of a boiler adapted to burn lignite, as the height of the construction may exceed the bituminous coal furnace by 40-50% [24]. In general, the enhancement in total thermal efficiency of the lignite-fueled power plant achievable by means of drying is estimated at 4 to 6% [30].

2.2 Available methods of coal drying

As it was justified in section 2.1.2, moisture in brown coal poses a vital threat for its applicability in the power generation industry. Among different methods of lignite upgrading, dewatering and drying are frequently used as primary fuel preparation or preliminary treatment before advanced coal utilization such as liquefaction, gasification, briquetting etc. In Fig. 2.3, the selected major methods of drying are presented within the classification of coal upgrading.
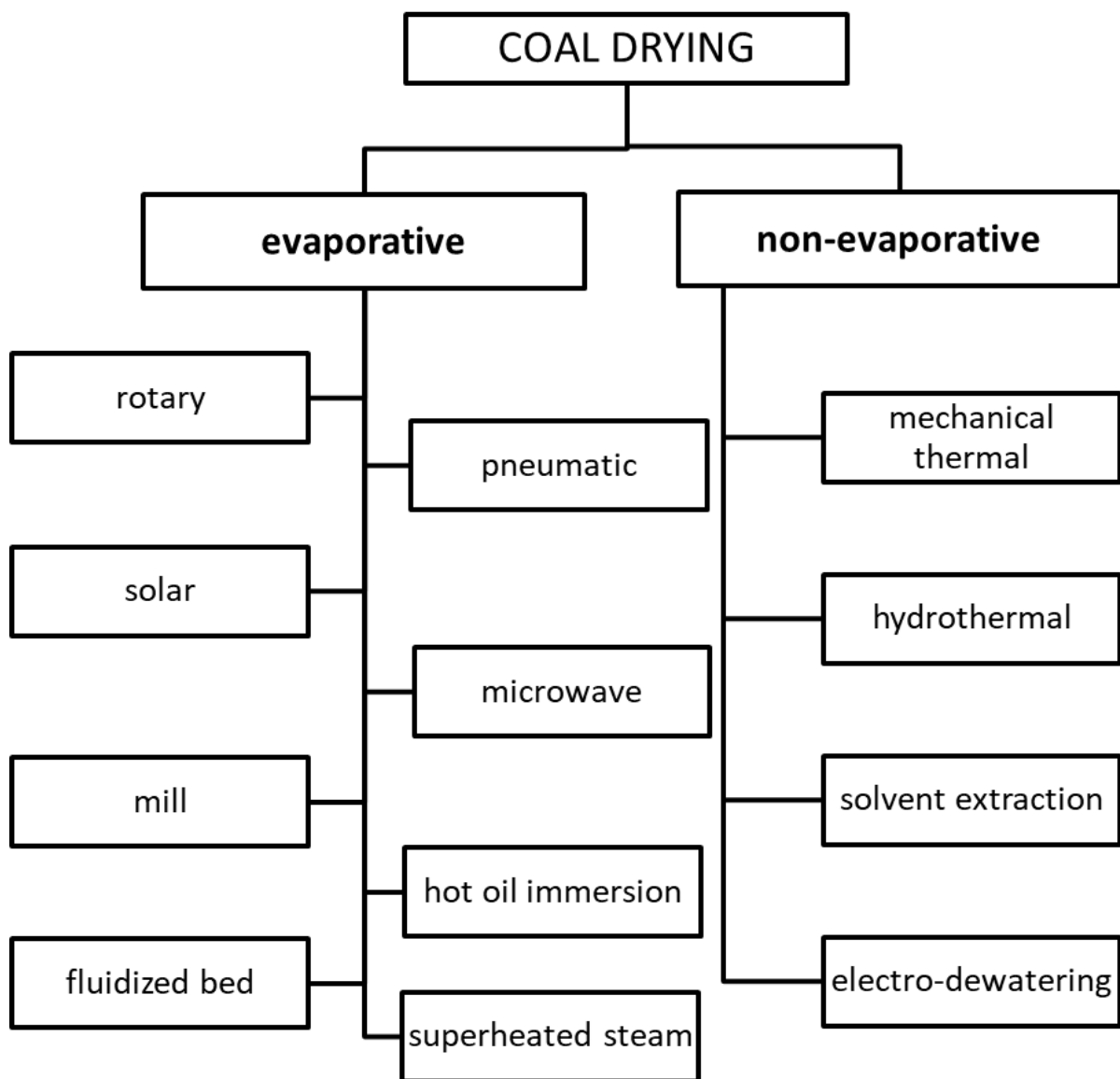
Figure 2.3 Proposed classification of coal drying techniques [18,20]

Note that particular techniques may be applied in a combined manner for the sake of the optimized effectiveness. The technology of dewatering is adjusted to the type of the input (slurry, lumps, fine coal) and the further step of utilization (combustion, gasification etc.).

2.2.1 Evaporative drying

Rotary drying is a developed technology and the most commonly used for low-rank coal upgrading. This method is used in rotary-tube and rotary-drum dryers. The latter utilizes a direct heat transfer, where a hot flue gas, at over 350 ^{o}C, flows through coal or an indirect heating scheme, in which a central chamber is surrounded by a concentric pipes of heat exchanger. Due to lack of interaction of gaseous medium and coal, various fluids, for instance hot steam, may be applied in this scheme. The typical consumption of heat for drying is around 3.7 MJ per kilogram of wet material [18]. Rotary-tube dryer uses steam of temperature below 200 ^{o}C. Due to improved exchange of heat, the heat transfer coefficient may be 2-3 times larger than in case of rotary-drum solution [20]. What is more, its heat consumption is around 3 MJ kg^{-1} [18]. Rotary drying system usually operate on coal particles of the size order of 10^{-1} - 10^{-2} m. In general, direct drying requires strict control and limitation on oxygen content within the drying medium to prevent the hazard of ignition [20].

The idea of pneumatic dryer relies on a vertical tube, where hot gas is driven at high velocity, connected to the wet material feeder. The particles of material hover on the flowing gas, up to the dry product collector. Speed of particles free falling cannot exceed the speed of gas, what limits the size of dried particles, and precludes operation on lump materials. Another drawback of this technology relates to the high dustiness of the stream, what requires installation of efficient filters at the output of the system [31]. On the other hand, the construction of the system is not sophisticated and relatively low

budget. Around 3.1 MJ of heat input is required for drying of 1 kg of the material [18].

The basic feature of solar dryers relates to the general characteristics of renewable energy sources, to which solar energy can be assigned: it is free, but moderately foreseeable. Solar drying is in fact the ancient method of dewatering, applied from conservation of food to manufacturing of construction materials. The solar dryers applied in non-industrial drying of food or timber commonly and purposefully take advantage of the stack effect, thanks to which hot air is driven from the bottom to the top of the device, enhancing the convective heat transfer [31]. As to brown coal drying, the efforts were made in Latrobe Valley, Australia, to produce an aqueous slurry of fine (10 μm) grinded lignite, which was subsequently driven into a pond to dry in the sun. Due to slow drying accompanied with shrinkage, the compact hard lumps of brown coal were produced in that process [15].

Short drying time and high heat transfer rate contributed to growth of interest in microwave drying. This technology differs from the majority of techniques by harnessing the radiation and marginal role of convective heat transfer. Due to permeability of microwaves, the energy is transferred at a high rate to the wet part of the material and couples within moisture. Therefore, a low thermal inertia accompanies the drying process, which intensity may be readily regulated or switched on/off [31,32]. In fact, the precise control is not only an advantage, but also a must in this technique of drying. The mass of vaporized water is directly proportional to the energy transferred by microwaves, thus the fixed drying power adjustment for objects of variable moisture content may result in under- or overdrying. The latter is more hazardous, as it can lead to carbonization or ignition, depending on the drying atmosphere [15]. The common construction of microwave dryers incorporates a microwave oven, through which a conveyor belt with wet material is passed [31]. According to the research on

microwave dewatering of coal, the increase of dried particle size enhanced the drying rate and contributed to reduction in the drying time, what is an inverse correlation, regarding those observed in traditional methods of convective drying [33].

When fragmentation of coal is required, what is often the case in electricity generation, mill drying is frequently applied to produce pulverized coal. In terms of dewatering, it utilizes the heat of friction combined with enthalpy of hot flue gas that is driven from the boiler. The mill dryers are relatively easy in construction and operation, often formed in cylindrical shape and grind coal using numerous metal balls (30-80 mm in diameter) or beaters (4-10 kg per each) [25]. Due to short residence time of coal in the dryer (order of seconds), the substantial moisture reduction is achieved when the particles are crushed to 1 mm or less [15]. The heat input of mill dryers operating on brown coal, ranges between 4 and 14 kWh per 1 Mg of fuel [25].

Hot oil drying is a technique, which bases on immersion of wet material in the oil bath of temperature higher than required for water evaporation. The occurrence of water boiling induces high turbulent flow along the material surface what contributes to the rapid removal of significant amount of both surface and inherent moisture. Due to alike mechanism of heat transfer, this technique is also known as "fry drying" [20]. Oil immersion drying was experimentally applied to Indonesian low-rank coals, resulting in reduction of water share from 32 to 2-3% and doubling of the initial heating value of 12.5 MJ kg^{-1} [34]. An interesting feature of oil drying is formation of the hydrophobic film within coal that reduces the readsorption of water during the storage. The absorption of oil in coal may increase its calorific value, however, it raises the costs of dryer operation, depleting the stock of drying medium [25].

Elevated heat transfer rate stemming from high contact area to mass ratio is one of the main advantages of fluidized bed drying. Fine (reason for large heat transfer area)

particles of coal float on the upstream which prevents them from falling down. The available drying mediums blowing through this dynamic suspension are hot air, gaseous combustion products or steam. Incline in the fluidization velocity was found to enhance the speed of drying of Australian brown coal mined in Loy Yang [35]. Various aspects of the fluidized bed technique have been investigated in experimental and analytical studies for coals from numerous geographical locations, including USA, China, Greece or Poland [36–39]. In case of the latter, a study has been prepared recently for fluidized spouted bed operating on Belchatow lignite and supplied with low temperature heat source (50-60 ^{o}C), which produced the output fuel of water share at 15-20% [40]. The heat demand for drying of 1 kg fuel is in range of 3.1-4.0 MJ for fluidized bed drying [41]. This method of drying has been frequently combined with superheated steam as a drying medium. The latter will be discussed in separate section.

2.2.2 Non-evaporative dewatering

The methods of non-evaporative drying commonly apply increased pressure level in order to prevent moisture from evaporation and save its heat of vaporization. The pioneer of non-evaporative fuel drying was Hans Fleissner who invented the method, utilizing both high pressure and vacuum [42]. At first, highly-pressurized steam interacts with a lump of brown coal. As its temperature rises, the water is being expelled from the inside, due to the pressure, in the liquid state. When the water leaves, the lignite shrinks. When the pressure is decreased, an additional amount of moisture is removed by flash evaporation, which lowers the temperature of the lump. The method has been utilized and modified in many applications worldwide [15]. Its energy consumption per mass unit fuel using superheated steam is estimated even below 1.75 MJ kg^{-1} [41].

Another process of dewatering without phase change is the mechanical thermal

expression (MTE) technique, invented to lift the efficiency of German brown coal plants [43]. The idea of this method extends the Fleissner process. Lignite is fitted in the form, heated to around 200 ^{o}C and compressed by the hydraulic press, what drives the moisture out of the material to be collected by the output tanks. Final part of the process involves cooling, accompanied with flash evaporation. The optimal results of dewatering were obtained for pressure of 6 MPa. Mechanical thermal expression became in the range of interest of Australian government, considered appropriate for coal pre-drying in IGCC (integrated gasification combined cycle) [24].

Hot water drying (HWD) is a process of non-evaporative dewatering, product of which is a quasi-liquid fuel. The moisture is expelled from the internal structure of brown coal by carbon dioxide produced in decomposition of functional groups at temperatures of 240 ^{o}C and higher. Oils and tars from the decarboxylation mix with aqueous solvent on the surface of coal and are claimed to form a coating that limits the moisture readsorption after drying finishes. The method is applied to produce low-rank coal-water fuels (LRCWF) [25].

The very high reduction of water share, exceeding 90% of the initial level, can be obtained by solvent extraction method. In this technique, coal is placed within the stream of the solvent, which under the influence of increased temperature binds with the reactive compound and leaves the original rock. Several solvents has been tried, such as tetrahydronaphthalene, methylnaphthalene, supercritical carbon dioxide and liquefied dimethylether (DME) [44–47].

Electro-dewatering of coal sludges [48,49] takes advantage of the electrical charging mechanism of cations. Under the influence of electrical currents, the ions interact with water by means of viscous forces and drag its molecules to the cathode, where it is drained out of the sludge. This approach leads to dewatering of 25 to 50%.

2.3 Superheated steam drying

Superheated steam drying (SSD) is classified as an evaporative thermal method of removing moisture from wet materials. The nature of vapor as a high temperature gas without free oxygen molecules and at the same time very easy to be produced (contrarily to e.g. nitrogen) brings about the supposition of the beneficial drying medium that reduce the spontaneous ignition hazard. However, probably due to the paradoxical idea of removing a form of water with another form of water, drying by means of steam was not under consideration until late 19th century.

In 1903, Hausbrand wrote a book, which German title might be translated as *The Drying with Air and Steam* [50]. Wenzel and White in 1950s compared drying of granular solid object with air and humidified air, coming to the conclusion that vapor in air not only does not affect the general characteristics of the drying process, but might be even beneficial, providing higher drying rate and thermal efficiency than in the case of pure air-blown conditions [51]. Studies of Yoshida and Hyodo supported this claim, proposing and validating the idea of the inversion point [52]. This term relates to the temperature above which, at the certain conditions (humidity, pressure, geometry), the drying rate for steam as a medium is higher than in the case of air. Kiiskinen and Edelmann [53] found that drying of paper with jet streams of superheated steam at 300 ^{o}C is performed at 26% higher rate than in the case of air at the same temperature, however power output of the fans was higher by 150% for superheated steam. Though in general the dewatering rate is higher for air in low temperatures and for steam in high temperatures, the inversion point can be lowered to benefit from steam drying without large energy expenditures [54].

A variety of drying gases can be applied in fluidized bed dryer, to mention but a few examples of hot air, flue gas after combustion and superheated steam [18,55]. The

utilization of the latter in a combination with fluidized bed dryer was proposed with regard to coal upgrading by Potter et al. [56,57]. They obtained encouraging coefficients of heat transfer ranging around 300 W m^{-2} K^{-1} [58]. Such high values of superheated steam fluidized bed drying (SSFBD) promote the decline in the size of the drying equipment. Association of SSD with fluidized bed has been investigated by studies focusing on increasing lignite applicability in electricity generation operating on pressurized steam of temperature range 180-260 ^{o}C [59,60]. This studies also took issues of shrinkage and equilibrium moisture content into account. According to some research, which tested a fluidized bed drying of pulverized coal, the capital cost was reduced by 20% and the total energy by 15% when air was replaced by superheated steam [54]. Another study by the same authors claimed that for decreasing the water share of activated carbon pellets from 50 to 2% in fluidized bed might bring 40% cost reduction of SSFBD in comparison to conventional air drying [54]. According to Woods et al. who discussed steam drying of 1-13 mm coal particles, the residence time of drying does not affect the volatilization, unlike hot air drying. They found out that for SSD the period of constant drying rate is 6-7 times longer and the heat transfer rate 1.7-2 times higher than for drying in air atmosphere. This manner of drying might be suitable to deliver high quality fine-graded fuel to emerging power generation technologies, such as IGCC. Although it operates currently on the pulverized bituminous coal [61], the raise in calorific value, combined with significant volatile matter content which facilitates gasification, might contribute to some breakthrough in development of this highly efficient system of electricity generation.

An issue of great importance in relation with advantage of SSD over hot air drying was raised by Fushimi et al. [62] who discussed the possibility of self-heat recuperation. They proposed to evaporate the moisture from the wet material, superheat

and compress it, before directing it to the heat exchanger which supports the operation of the dryer. By that means not only the latent heat loss, but also sensible heat loss might be reduced. The idea of latent heat recuperation was also utilized in the industry. German power company RWE introduced a WTA (*Wirbelschichttrocknung mit interner Abwärmenutzung*) technology that utilizes SSFBD to enhance the quality of brown coal prior to its combustion [63]. The scheme of installation is presented in Fig. 2.4. The moisture expelled from the dried lignite is slightly superheated and compressed before turning back to the heat exchanger in the fluidized bed dryer. After depressurization, along with the hot condensate it also passes through the preheater, which is applied to increase the initial temperature of lignite prior to drying. With utilization of this technology, the water share in lignite is reduced from 55-60% to around 12% [18].
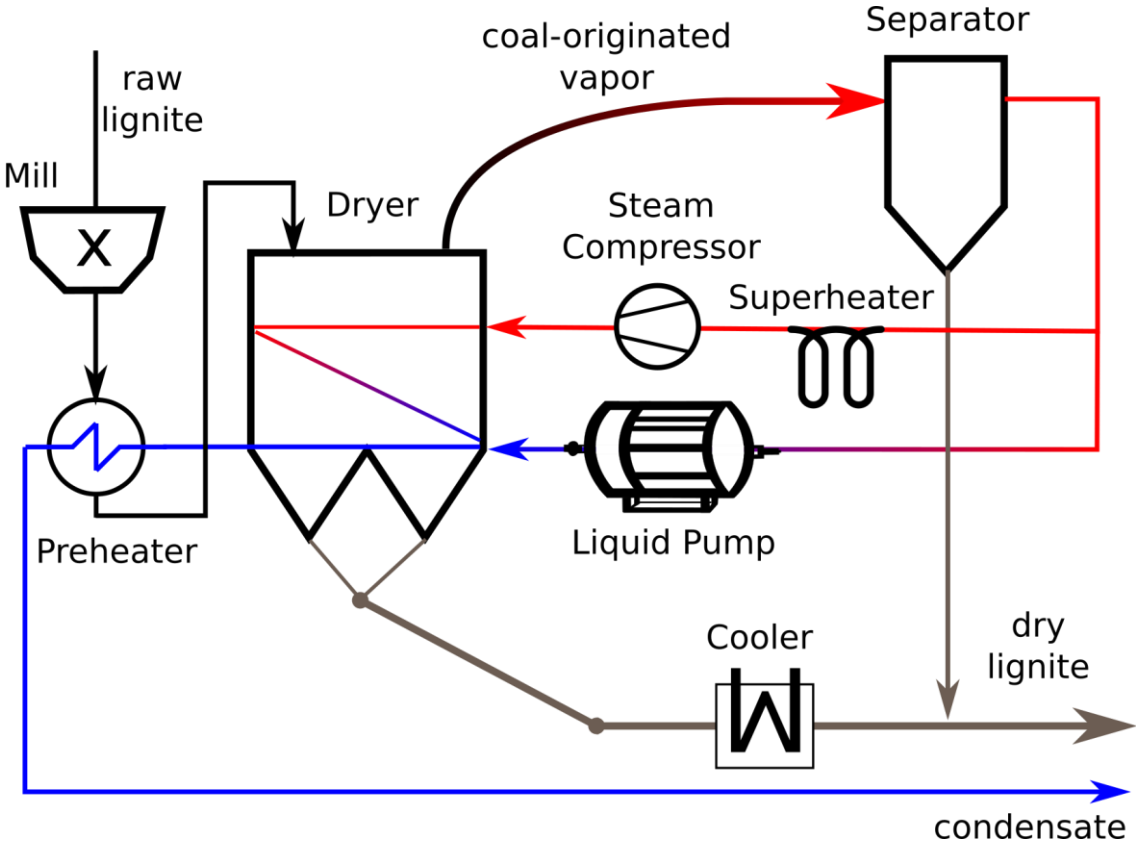
Figure 2.4 Scheme of WTA technology of superheated steam drying

In Fig. 2.5 the general idea of latent heat recuperation is presented regarding to scheme from Fig. 2.4. The major benefit of such a configuration is utilization of the latent heat of the phase change in order to limit the energy input to the dryer. Also, some savings are made on the preheater which utilizes the heat of a condensate to raise the temperature of the raw coal.
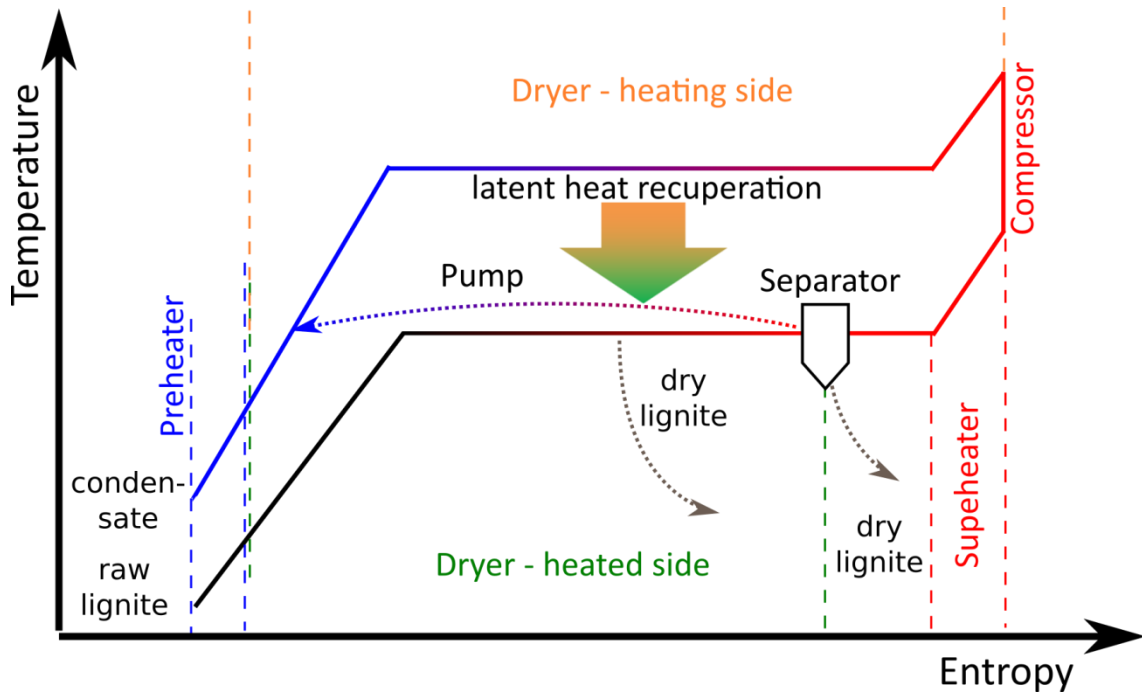
Figure 2.5 Simplified scheme of latent heat recovery

The reliable approach to the design and construction of a superheated steam drying (SSD) system coupled with a power generation unit, entails a thorough study on fuel taken into consideration. This kind of works often include numerical analysis as a cheap and precise manner of describing heat and mass transfer phenomena which occur in the drying process. The food industry has commonly adapted such a method of drying optimization. The model of fixed bed dryer of brewers' spent grain using superheated steam one of the examples [64]. Applying the finite difference method, changes in moisture content and temperature in the slice of pork were simulated for

25

SSD [65]. Power engineering also reached for the superheated steam drying models, what resulted in the numerical analysis of the combined heat and power plant fueled by corn ethanol [66] as well as the self-heat recuperative fluidized bed dryer of biomass, which consumed 95% less energy than conventional systems [67].

In Tab. 2.2, the benefits and drawbacks of superheated steam drying are listed. The characteristics refer especially to the system configured to recuperate heat of evaporation.

Table 2.2 Characteristic features of superheated steam drying [54]

advantages	disadvantages
• no hazard of oxidation or ignition	• high complexity of the system
• higher drying rate over the inversion point than for hot air drying	• necessity of leak control
• relatively low flow of the drying gas	• considerable cost of auxiliary devices
• possibility of latent heat recovery	

2.4 Modelling of coal drying

One of the first attempts to reflect the coal drying process by means of mathematical modelling was made by Chen et al. in 2000 [68]. They analyzed drying of surface water and porous material for spheres made of ceramic and coal. The applied drying media were air and superheated steam. Their model involved receding interface assumption. The simulated results were in fine agreement with empirical data in case of the drying of ceramic spheres in steam as well as the drying of single water droplets in steam and in air.

The study described above, found a follow-up in another investigation performed by the same research group [69]. The content revolved around modelling the work of fluidized bed dryer. In the first paper, a mathematical model was developed for the drying of a single porous particle in steam. In the second one, the single particle model has been integrated with a two-phase hydrodynamic model to simulate the continuous drying of coal in a bed fluidized with superheated steam. Besides aspects related to engineering approach, such as variation in the superficial gas flow, inversion temperature or residence time, the model incorporated phenomena of initial condensation during the heating period and growth in temperature accompanied by decline in moisture content with residence time in drying bed. The authors conclude that "the most significant operating variables are the steam-tube duty and the initial moisture content of the wet coal".

In 2001, Looi et al. published the work entitled "Drying kinetics of single porous particles in superheated steam under pressure" [70], where they discussed superheated steam drying kinetics of spherical single porous object on the case of lignite and ceramic. They used objects of diameters in the range 10-14 mm and exposed them to steam of 155-197 $^{\circ}$C, under pressure of 1.7-8.4 bar. The mathematical model was solved using the Crank-Nicholson method. The experimental results for ceramic spheres drying were successfully applied to verify the model. In the case of lignite, the model underestimated the drying rate – the authors supposed cracking to be the factor of heat transfer area enhancement. According to the study, the drying rate for porous structures is limited by the rate of external convective heat transfer. Simulation and experimental results, indicate that the evaporation of moisture occurs on a drying front which recedes towards the center of the particle. However, for lignite, a study did not find an optimal numerical solution.

Olufemi and Udefiagbon [71] modified the kinetic parameters of the drying process. They also included deliberation on particle shrinkage. The experimental results of Victorian (Australia) lignite drying applied to validate the numerical model were taken from the study of Looi et al. [70]. The study also adapted receding core model with evaporation of water at the boundary of wet and dry regimes. However, the mathematical model involved also the term for shrinking volume of the particle. Description of the process by partial differential equation was solved numerically with the finite element analysis, as the opposition to previously applied finite difference analysis. The latter one relied on rectangular, while the former approximated the solution using triangular mesh. The geometry can be simplified to circular cross-section of the sphere. Approaching the numerical problem with triangular mesh in this case provides greater accuracy of the results, due to better matching of nodal points, especially on the sample surface. Although authors claim to have received perfect consistency between simulated and experimental results, the distribution of empirical data points assumed in this work might be misleading. The density of experimental measurements along the time scale is significantly lower than in the source of those data [70], making the imaginable shape of experimental curve somewhat different from the original. However, it should be noted that the reason might be related to imperfect experimental attempts rather than numerical solution.

The finite difference method has been applied to model superheated steam drying of Polish lignite of the same origin, as in the present study, Belchatow mine [39]. The cylindrical pellets of 14 g and 55% of water share were dried in a superheated steam chamber. The mass transfer in the mathematical model was supposed to rely on the Darcy flow of liquid moisture caused by generated pressure gradient as well as diffusion of vapor and bound water triggered by moisture content gradient. The

28

simulated drying curve appeared less convex than the results obtained in the experimental part of the study.

Zhang and You [72] investigated drying of Chinese coarse lignite particles. They conducted empirical attempts using hot air at a velocity of 0.7 and 1.5 m s^{-1} and temperature of 100 and 140 $^{\circ}$C. Simultaneously they derived a mathematical model of drying, assuming multiphase flow of air and water in the porous structure of coal, combining convection of the free water and diffusion of the bound water. The model was successfully validated with regard to experimental results and used to discuss the influence of such conditions as particle diameter, gas temperature, relative humidity and drying medium velocity on the drying characteristics.

Recently, the numerical simulations have been designed and conducted by Kiriyama et al., in terms of single particle model as well as fluidized bed scenario [73–75]. The findings of the mentioned articles were utilized in selected parts of this work.

CHAPTER 3

Goal of the thesis

Lignite is the second most important source of primary energy for electricity generation in Poland, what was indicated in chapter 1. Despite the general tendency of reducing the share of fossil fuels in energy mixes of highly developed countries, the decline in coal use in Polish energy sector over the last years is very slow and no forecasts predict the acceleration of this gradual shift in the next decades [76]. Besides rich domestic reserves, relatively low potential of renewable energy sources [76] combined with prolonged and uncertain efforts to introduce nuclear power plant [77–79], secure the leading position of coal in the Polish electricity generation.

However, due to ageing power stations [80] and international schemes of combating the CO_2 emission [28,29], the demand on introducing highly efficient industries operating on lignite is constantly rising. Effective dewatering of this moisture-abundant fuel is one of the preconditions for satisfying the need formulated in such a way. As mentioned in chapter 2, the application of superheated steam, especially in the configuration enabling the recovery of water-vapor phase change heat, emerges as an opportunity to raise the quality of coal and gain benefits in the fields of economy, environmental protection and energy security. Pikon and Mujumdar claimed that *Superheated steam seems to provide all the required advantages but few vendors have developed these technologies for coal and for large-scale operations necessary. The*

31

drying conditions will need to be optimized for specific grades of coal and also the utilization of the product [25]. However, the literature concerning the drying properties of lignite from Polish deposits is limited [39,40] and no extensive coverage had been reported so far. Hence, researching the fundamental properties related to superheated steam drying seems well grounded for prospective types of lignite to be upgraded using this branch of drying technology.

The goal of this work is to investigate the influence of various groups of properties on the drying characteristics and behavior of the Polish lignite in the atmosphere of superheated steam. The comprehensive research, involving experimental trials and numerical modelling of drying, takes the thermophysical parameters into account (e.g. thermal conductivity, specific heat) together with properties related to the drying technology, such as equilibrium moisture content or bulk density, and features related to physical structure of examined material. For the sake of acquiring the broad perspective on the features of drying in superheated steam, the coal originated in divergent geological circumstances has been selected for the study.

CHAPTER 4

Methodology of experimental procedure of lignite drying in superheated steam

4.1 Lignite samples

All lignite samples used in the experimental procedure were cut out by knife from a randomly chosen lignite block as a coarse particles and smoothed in order to obtain the required size. Accurate preparation was achieved by rolling the lignite on a metal plate with round holes of decreasing diameter (Fig. 4.1). The precise size of the holes was provided by cutting them in an electric discharged machining process.
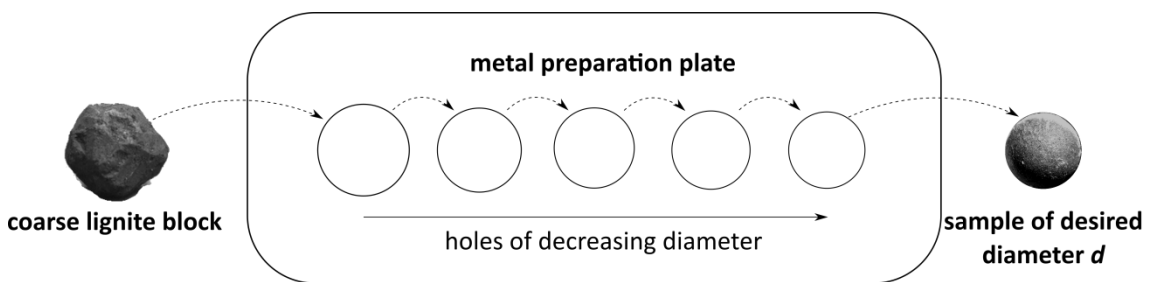
Figure 4.1 Scheme of preparation of the experimental samples

The samples utilized in the examination were split into four size groups: 2.5, 5, 10 and 30 mm in diameter. Table 4.1 presents dimensions of the examined objects, assuming the 2.5 mm sample's relative dimensions are equal to 1.

Table 4.1 Dimensions of samples used in the experiment

sample diameter	relative diameter	relative area	relative volume	relative mass (experimental average)
d [mm]	$d/d_{2.5}$	$A/A_{2.5}$	$V/V_{2.5}$	$m/m_{2.5}$
2.5	1	1	1	1
5	2	4	8	7.85
10	4	16	64	65.78
30	12	144	1728	1765.76

According to the relative values, the volume of samples can vary over three orders of magnitude. From the statistical point of view, taking averaged density as a factor, the mass relation should be analogical. They exhibit slight deviation from the expected relative value, though. Lignite belongs to organic-rich sedimentary rocks. Moreover, it is classified as a low-rank coal, which means the coalification processes did not progress as highly as in anthracite or even bituminous coal. Therefore, the structure of this fuel is strongly heterogeneous, with visible insertions of plant matter.

4.1.1 Sample of 30 mm

The initial weight of the particle of 30±0.05 mm in diameter was approximately 17-17.5 g. In the object prepared in the manner described two holes were made with a 0.3 mm drill: 15 mm and 7.5 mm in depth, respectively. Inside each drilling a K-type thermocouple was placed to allow for temperature measurement in the central point (referred to as "center") as well as the halfway point between the surface and the center of the sample ("midpoint"). The thermocouples fulfilled the Japan Industrial Standard Class 2 with temperature deviation ±2.5 $^{\circ}$C. They consisted of 0.09 mm wires made of chromel and alumel and insulated with silica-based material. Following the installation

of the thermocouples, an adhesive ceramic agent was put near the orifice of both drillings to ensure a stable position for the wires inside the sample.

The polyester thread, passed through the sample interior and fixed by the knot on the bottom side, was used to suspend the sphere in the test chamber. Its hydrophobic properties prevented the water absorption which would disturb the measurement of the weight. The object prepared for the examination is visible in Fig. 4.2.A.

4.1.2 Sample of 10 mm

The result of polishing the coarse particle into 10±0.05 mm sphere was an object of around 0.6-0.7 g in weight. The drill used for the thermocouple installation was thinner: 0.2 mm. However, the idea of temperature measurement was realized in an analogical way: in the midpoint and center, which in that case lied 2.5 mm and 5 mm below the surface, respectively. The K-type thermocouples, prepared from chromel/alumel wires of 0.08 mm in diameter were insulated and fixed to the orifice in the same way as for the largest sample.

In case of 10 mm sample, the mass of the sample was low enough, not to require additional hanging thread – it was suspended on two thermocouples only. On the other hand, to stabilize the position of the particle inside the test chamber and reduce the impact of fluid flow on the weight measurement, the thermocouples were rolled on a thin glass rod, that carried the sample weight onto an electronic balance. The results of the preparation is visualized schematically in Fig. 4.2.B. Figure 4.3 presents the photograph of a 10 mm sample prepared for the examination.

4.1.3 Sample of 5 mm

The weight of the 5±0.05 mm sample after the polishing was approximately 0.06-0.08 g. Due to the small volume, the sample was equipped with only one

thermocouple, which tip measured the temperature 2.5 mm inside the sphere, in the geometrical center of the particle. The wire was curved and inserted from side to the lignite. For the sake of low mass of the sample, no adhesive agent was needed to stabilize the connection between wire and coal.

Besides above-mentioned differences, the preparation of 5 mm object did not differ from 10 mm sphere. The particle ready for the experiment is shown in Fig. 4.2.C.

4.1.4 Sample of 2.5 mm

The sample of 2.5±0.0069 mm was characterized with by far the lowest mass of the entire set, around 0.01 g (10 mg). In order to neutralize influence of electronic balance sensitivity on the results (±0.1 mg), four samples were dried altogether, increasing the weight of the examined object.

The preparation of the sphere was performed using the same method as previously described. The 0.1 mm drill was used to make a hole for a same-sized suspension wire. In this case, no thermocouple was applied, due to inability of precise installation. Temperature measurement was realized only by means of thermography. The suspension wires, inserted from bottom to spheres were put into quadrilateral hollow handle on the end of the glass rod. The manner of hanging 2.5 mm sample is exhibited in Fig. 4.2.D.
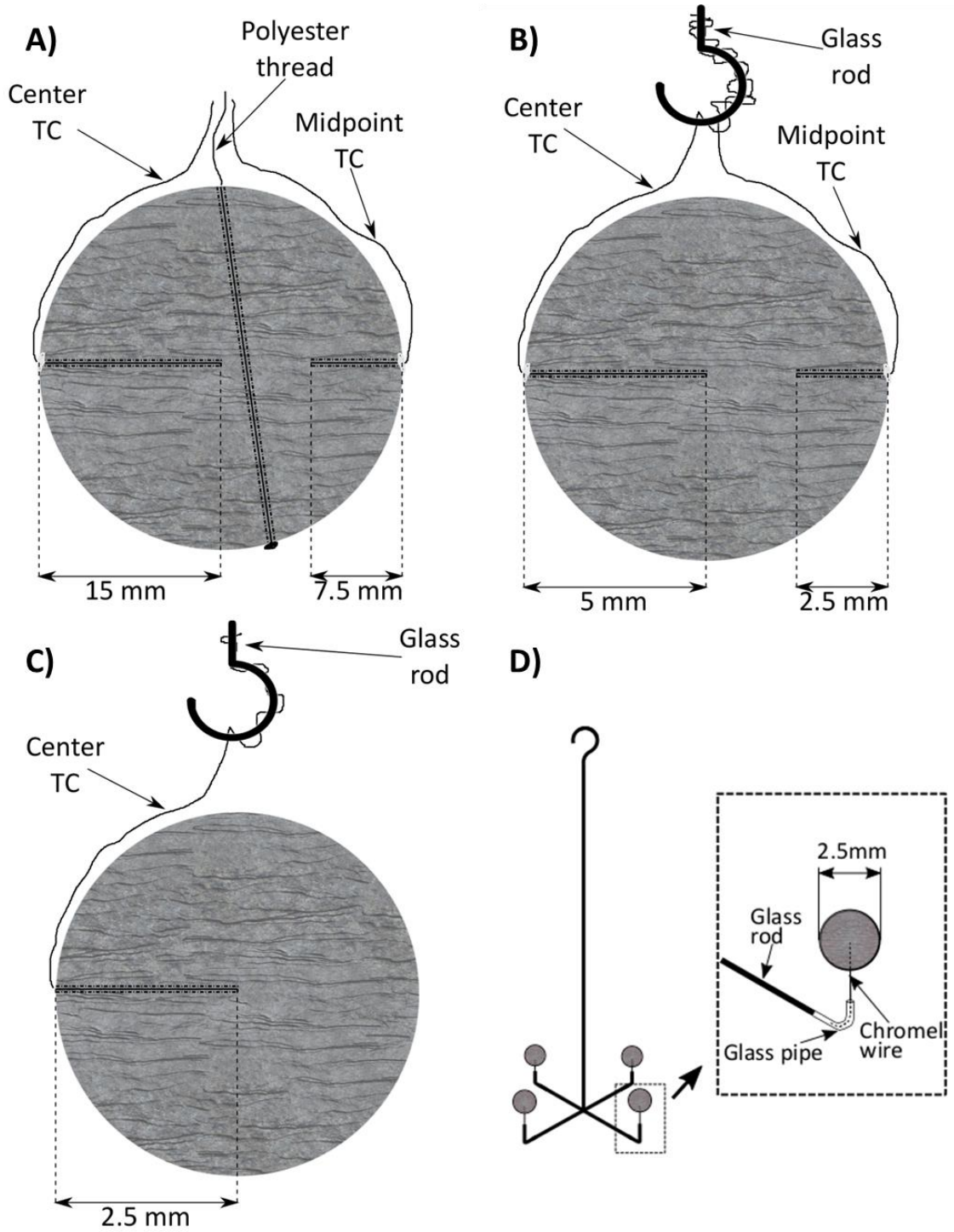
Figure 4.2 Lignite samples of A) 30 mm, B) 10 mm, C) 5 mm, D) 2.5 mm in diameter

Figure 4.3 Sample of 10 mm ready for the test (white adhesive agent visible on sides).

4.1.5 Variability of the samples

The natural diversity of lignite structure mentioned in section 4.1 was examined by gaining insight into the individual features of the samples used in the experiment. Over 120 drying tests conducted for each of 4 sizes were taken into consideration.

Figure 4.4 illustrates the relationship between water share and density of experimental objects prior to drying. Water percentage is defined as a ratio between mass of water in the present state and the initial mass of lignite, which consists of initial mass of water and invariable mass of dry coal:

$$WP^i = \frac{m_w^i}{m_w^0 + m_c} \qquad (4.1)$$

Note that in certain cases of this work, an indicator of water share (WS) is used, which denominator refers to the present mass of the sample, thus, including the instantaneous mass of water:

$$WS^i = \frac{m_w^i}{m_w^i + m_c} \qquad (4.2)$$
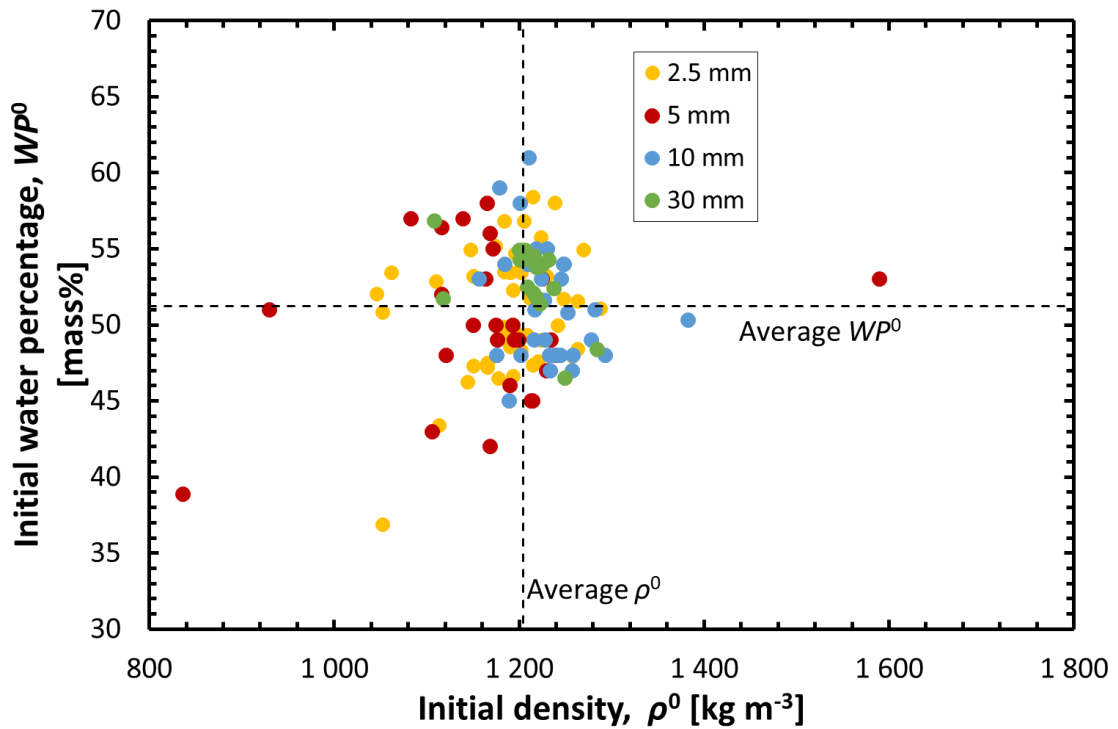
Figure 4.4 Correlation between density and initial water percentage of the samples

Table 4.2 contains statistical information on the objects presented in Figure 4.4. A global average density equaled 1.205 kg m^{-3}, while the initial water percentage was averaged on 51.25%. According to the value of relative standard deviation (RSD), the samples of 30 mm in diameter exhibit the smallest deviation from the mean value. This observation is related to the impact of contamination within structure of randomly

picked lignite particles, which is vastly enhanced with a decline in the sphere size. Therefore, the investigation of large objects, as more representative for the specific coal seam, is substantiated.

In the case of 2.5 mm samples the tendency described above does not apply. Those samples were weighed and dried in groups of four, thus, statistically, the deviation of their parameters is neutralized.

Table 4.2 Initial values of density and water percentage

diameter *d* [mm]	initial density ρ^0 [kg m^{-3}]		initial water percentage WP^0 [mass%]	
	average value	*RSD*	average value	*RSD*
2.5	1.187	4.6%	51.18%	7.7%
5	1.167	10.2%	50.01%	9.6%
10	1.222	5.3%	51.39%	7.3%
30	1.215	2.5%	52.86%	5.9%

4.2 Experimental setup

Once the preparation of the sample was complete, the object was placed in the apparatus, where the superheated steam drying took place. Figure 4.5 presents the setup of experimental equipment. Table 4.3 summarizes the commercial resources installed in the drying system or used for the measurements. The cylindrically-shaped test section, where the sample remained throughout the test, was the core of the drying system. The diameter of cylinder base was 133 mm, and the height equaled 152 mm. In order to maintain desired temperature of steam, the test section was thermally insulated and heated from 3 sources: on its bottom, around the outer side wall and at the top cover.
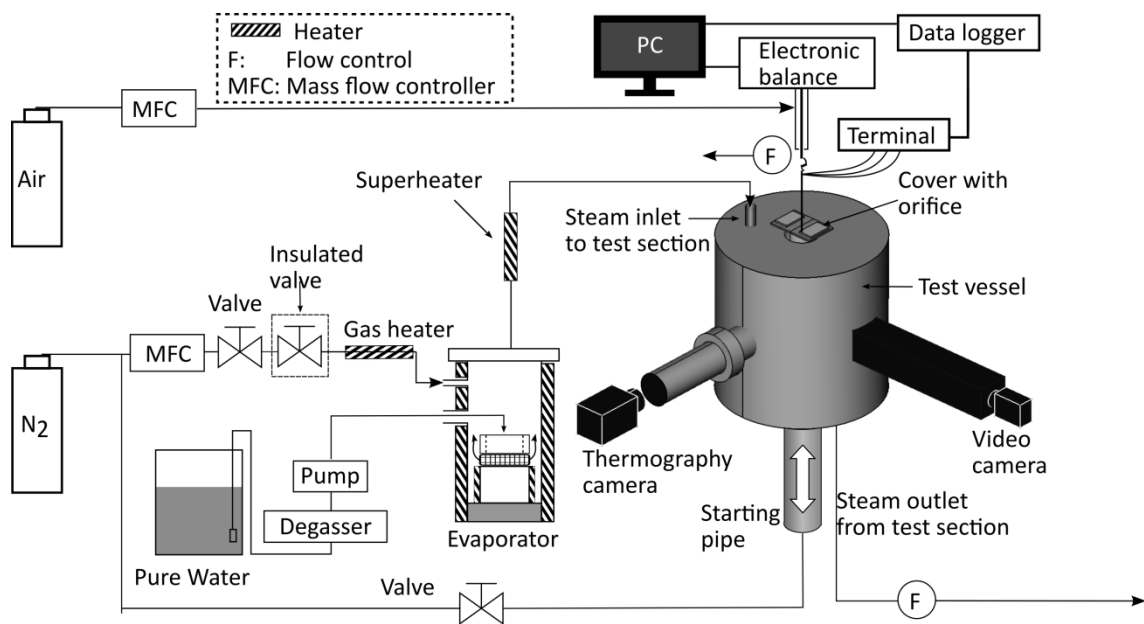
Figure 4.5 Scheme of experimental setup

The supply of steam to the test section was realized through the water line, which started at the pure water tank. Water was transported by liquid delivery pump, which drew it out from the tank, passed through the degasser and driven to the evaporator. There it was turned to steam. The steam run through the pipe of the superheater, located over the test section. The evaporator was equipped with two heaters: one placed around its enclosure and the other inside the vessel core, while the superheater was wrapped by the heating wire along its entire length.

Table 4.3 Commercial resources used for drying or measurement

item	producer/model
video camera	HDRCX170, SONY
thermography camera	R-300, NEC/Avio
black body spray	THI-1B, Tasco Japan
polymethylpentene film	Japanese Consumers' Cooperative Union
electronic balance	HR-200, A&D
degasser	DGU-20A3, Shimadzu Co. Ltd.
liquid delivery pump	LC-20AT, Shimadzu Co. Ltd.

The superheated steam was supplied into the top part of the test cylinder through a baffle plate. That solution aimed for a maximal possible dispersion of the steam in the entire volume of the vessel. At the bottom of the test chamber, a fan exhausted the gas from the drying system. Another fan was located next to the top of the cylinder in order to draw out the minor part of the steam (3-5% of the total amount) which was leaking through the orifice. Such implementation was applied in order to control the pressure inside the cylinder and thus, ensure the laminar flow and atmospheric condition. The orifice itself was used to pass the thread on which the sample was hanged into the test section.

During the experiment, the data on sample weight and temperature were continuously collected. Basing on this information, the drying characteristics were constructed.

In addition to thermocouples described in sections 4.1.1-4.1.3 (no thermocouples were installed in 2.5 mm objects), the thermography camera was applied to monitor the temperature of sample's surface. The device was equipped with infrared bolometers detecting the wavelength from 8 to 12 µm. To provide the reliable temperature measurement, an optical path was applied to connect the thermography camera and the window in the test cylinder. In the path, the polymethylpentene film, 10 µm thick, was located at an inclination of 10° to avoid infrared reflection. Due to temperature resistance of 180 $^{\circ}$C (above the highest superheated steam temperature) and average transmittance of 90% in the range of wavelengths from 8 to 12 µm, the film ensured appropriate conditions for performing the measurements. The optical path was additionally heated to prevent the steam condensation on its interior as well as the film and to reduce heat loss from the test section. It was also painted with black body spray, characterized with emissivity of 0.94. Constant test section temperature and constant

42

emissivity, together with sample characteristic temperature points obtained from the drying characteristics (initial water evaporation at 100 $^{\circ}$C, thermal equilibrium between sample and steam at the end) constituted the set of assumptions for thermography calibration. The detailed insight in the configuration of surface temperature measurement by means of thermography is provided in Fig. 4.6.
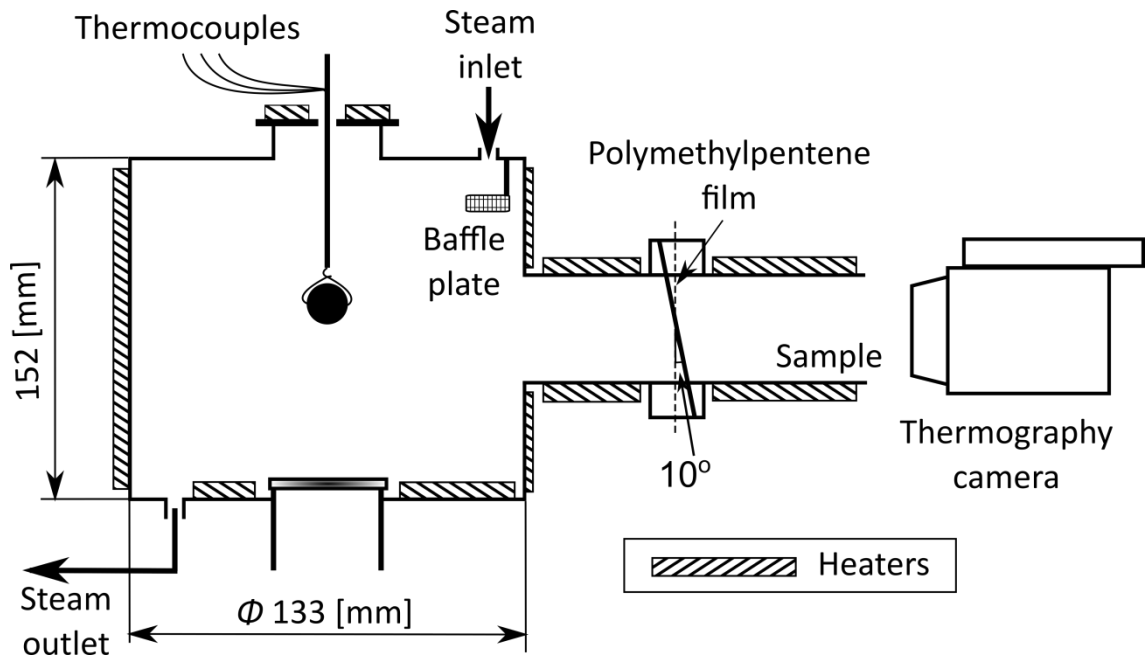
Figure 4.6 Side view on thermography measurement devices

The weight of the sample during the test was measured with an electronic balance, which resolution was equal to 0.1 mg. The glass rod with the sample was hanged on a thin metal bar which was connected directly to the balance. Protection of from the external influence was provided by an acrylic cylinder surrounding the metal bar. Air supply at the rate of 0.6 dm^3 min^{-1} was used within the acrylic component for the purpose of stable temperature and flow, a desirable factors for accurate weight measurement.

The setting of the sample within the test section was performed with the starting pipe lifted to the inside of the test chamber in order to isolate the object and control the

exact moment when it was exposed to the superheated steam. At that time, the starting pipe was filled with nitrogen. The second line of nitrogen supply reached the test section. This gas was used after the completion of superheated steam drying in order to remove any residual moisture from lignite. Both nitrogen and air were stored in the cylinders, compressed into 14.7 MPa, regulated into 0.2 MPa and fed to the system using mass flow controllers.

In order to observe the lignite sample during the experimentation, especially in terms of condensation in the first phase and shrinkage combined with cracking in the later stages of drying, the video camera was used. Its optical path led to the test cylinder and was situated perpendicularly to the optical path of thermography camera, what allowed for simultaneous observation of various aspects of the drying process. For the same reasons as in the case of surface temperature measurement, the glass window separating test section from the optical path of the camera was operated by additional heat source.

The auxiliary steps were taken for the purpose of protection of the measurement and drying devices from the environmental influence. The air flow in the vicinity of the electronic balance was reduced by a protective polyvinyl chloride enclosure that surrounded the entire apparatus. To minimize the effects of static electricity the air humidifier operated within the enclosure to maintain relative humidity above 45%, zero-ground cables were installed, and the antistatic spray was applied frequently.

4.3 Procedure of superheated steam drying

There were four experimental conditions applied in terms of superheated steam temperature: 110, 130, 150 and 170 ^{o}C. Maintaining the steam temperature below 180 ^{o}C purposed on preventing the lignite from volatilization and chemical decomposition of its functional groups [81,82]. Such approach ensured that the change in weight is induced solely by moisture removal.

The heating of the test chamber and auxiliary heaters listed in section 4.2 was done under the nitrogen flow. As the demanded test temperature was reached within the chamber, the gas supply was switched to superheated seam. In order to achieve steam input to the test section at an average velocity of 0.02 m s^{-1}, the water flow to the evaporator was set at 8 cm^3 min^{-1}. Under those circumstances, the Reynolds number averaged on the temperature range was 2.3, 4.6, 9.2 and 27.6 for 2.5, 5, 10 and 30 mm samples, respectively. Due to occurrence of laminar flow around the sample, the accurate weight measurement was possible.

Once the stabilization of the thermal conditions within test chamber was achieved, the sample was placed inside. As mentioned in the previous section, a hollow cylindrical object, so-called "starting pipe", was used under nitrogen flow to set the sample in the test section without immediate exposition to superheated steam. The beginning of proper drying took place in the moment of pulling the pipe down.

From that moment on, the data on sample mass m, and temperature profile T, was simultaneously collected in 1 s intervals. The superheated steam drying was decided to be completed once the changes in weight did not exceed around 0.01% of the dried sample weight per minute. When such a state occurred, the flow of steam was replaced by the supply of nitrogen to the drying zone. The amount of residual water within the sample was determined by the decrease in weight attained during that period.

This mass is related to the equilibrium moisture content, which is attained a sufficiently long time under specific process conditions, such as a drying medium, pressure and temperature [83]. For each sample size, more than dozen of experimental attempts in order assure repeatability and reproducibility of the results.

The mass of sample after the two-step drying process described in the paragraph above was assumed the mass of dry coal in lignite, m_c. Subsequently, the total or initial mass of water in lignite, m_w^0, was equal to the total decline in sample mass during the test, what is quantitatively expressed as the difference between the initial mass of the particle, m^0, and the mass of dry coal.

$$m_w^0 = m^0 - m_c \qquad (4.3)$$

Relying on the obtained values, the essential drying indicators used for the description were described. Dry basis moisture content, X, is expressed at a certain time instance i, as a ratio of the current mass of water, m_w^i [kg], and the mass of coal achieved after drying, m_c [kg].

$$X^i = \frac{m_w^i}{m_c} \qquad (4.4)$$

In order to gain insight into the speed of drying, the time derivative of moisture content was calculated and described as a drying rate:

$$DR^i = \frac{dX^i}{dt} \qquad (4.5)$$

CHAPTER 5

Experimental analysis of lignite drying in superheated steam

5.1 Comprehensive analysis of the general drying characteristics of lignite exposed to superheated steam

The insight into superheating steam drying of a lignite particle was described with reference to particular stages of the process. The temperature profile and mass of the sample as well as the drying indicators introduced in the previous chapter: moisture content and drying rate, were plotted along time to discuss the features of the process.

On the basis of video recording, the features of change in sample surface were evaluated and discussed together with the images of the object captured during the test. More details related to observation of the examined object are given in section 5.3.

The abovementioned components of drying behavior analysis were supplemented with deliberation on the mechanism of water evaporation. As discussed in chapter 2, moisture in lignite can be roughly divided into free and bound water, depending on the manner in which each type is removed from the porous structure.

As an exemplary case used for the sake of discussion, the instance of 5 mm sample exposed to superheated steam of 170 ^{o}C was used. The entire drying can be separated into consecutive stages: {1} preheating period, {2} constant drying rate period (CDRP), {3,4} decreasing drying rate period (DDRP) consisting of two phases and {5} final drying period. The drying behavior in particular parts is shown in Fig. 5.1.
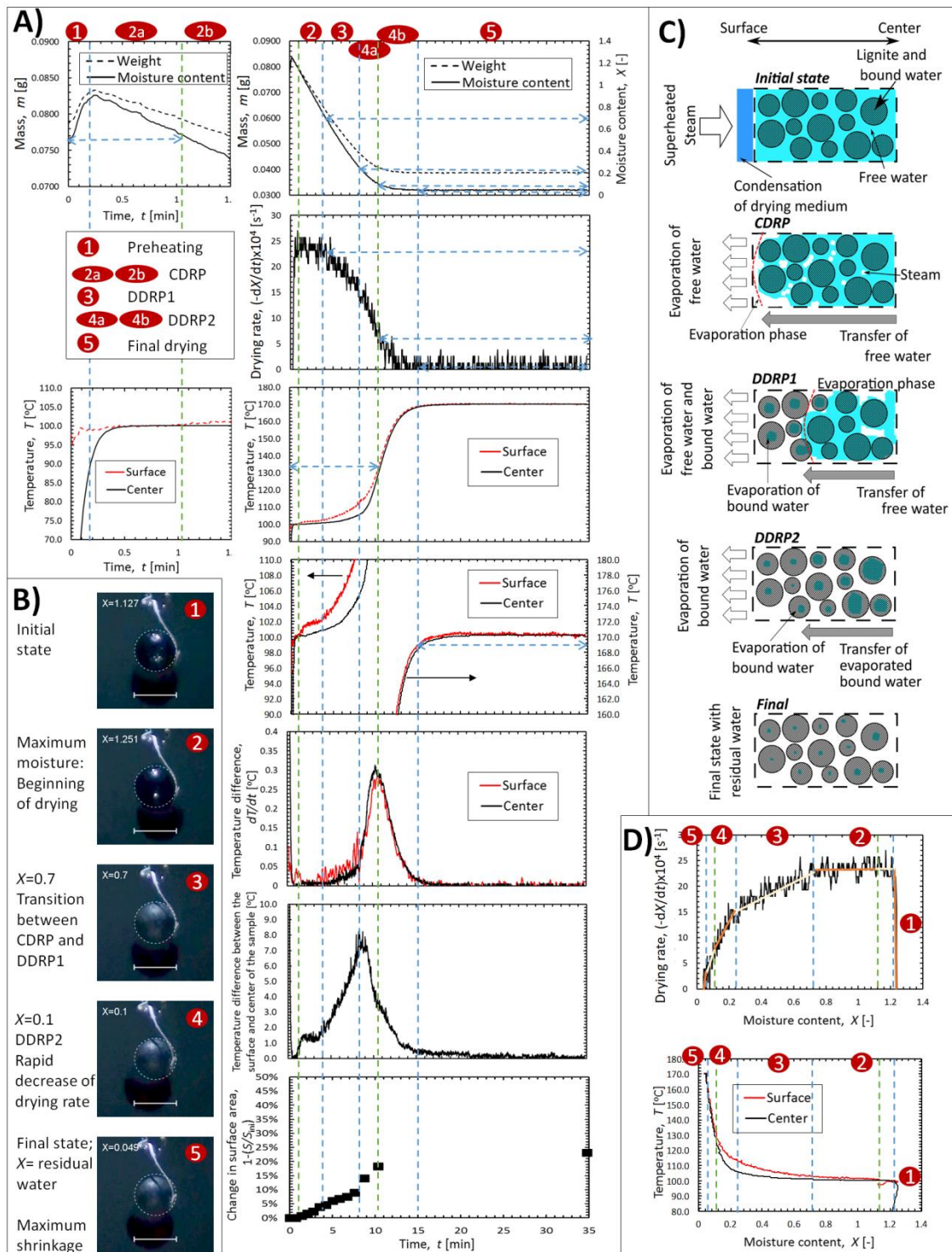
Figure 5.1 Drying behavior of 5 mm sample at 170 °C, in relation to: A) changes of drying indicators in time, B) changes in object's appearance, C) stages of water removal, D) changes of drying indicators in the function of moisture content.

5.1.1   Preheating period

In the beginning of drying, the exposition of cold sample to the superheated steam atmosphere induces condensation on its surface. The mass of the particle increases and so does the moisture content. The drying rate, consequently, achieves negative value for that reason. The temperature of the surface suddenly increases to reach the saturation temperature of 100°C, followed shortly by the temperature of the center. The end of this period is indicated by moisture content curve achieving its maximum level.

5.1.2   Constant drying rate period (CDRP)

The stage of CDRP is distinguished by the rate of drying stabilized at the invariable value. During the initial phase of this period, marked as {2a} in Fig. 5.1, the removal of water condensed in the preheating period is in progress. At this point the center temperature reaches 100 ^{o}C. This subperiod ends when the moisture from the surface is evaporated. It is indicated by stepwise ascend of the surface temperature into value slightly exceeding 100 ^{o}C and its subsequent gradual increase. The exact moment is determined by the experimental conditions, such as drying medium temperature and object diameter.

In the latter subperiod of CDRP {2b}, the difference of heat transferred to the sample and heat consumed on evaporation of water in the vicinity of the surface contributes to the increase of temperature in the surface region. Due to slowly inclining temperature gradient between surface and center of the particle, the heat is propagated to the lignite interior. Still, the evaporation occurs in the proximity of the surface, what is induced by capillary forces acting on the free water, which diffuses from the core of the sphere (Fig. 5.1.C). The value of drying rate, which remains constant, is defined by

the amount of heat exchanged with the superheated steam (Fig. 5.1.D). The decrease in sample diameter becomes observable, however, it is not significant at that stage. The constant drying rate period ultimately ends when the drying rate level decline is observed and the rapid incline in surface temperature occurs.

5.1.3 Decreasing drying rate period 1 (DDRP 1)

As mentioned in the end of previous paragraph, the DDRP, marked as {3} in Fig. 5.1, starts when the drying rate is in decline. Therefore, mass and moisture content of lignite decrease more gradually than in the previous period. The mechanism of drying alters in this stage, with evaporation border shifting towards the sample core (Fig. 5.1.C). The vaporization and resulting water content gradient entail movement of water in the form of multi-phase flow of liquid and gas. Over that period the hygroscopic bound water starts to be removed from the sample, what consumes larger amount of heat than required for the free water. As mentioned in chapter 2, the enthalpy change for the desorption of bound water, removed above the saturation temperature of 100 ^{o}C is correlated with the value of moisture content (see Fig. 2.2). The dewatering of lignite during this stage results in formation of gaps and crevices between dry matter, leading to cracking of the sphere's structure and volumetric shrinkage (Fig. 5.1.B). The first part of DDRP is decided to be finished when the rate of center temperature increase exceeds that of surface temperature, what is indicated by the highest difference between those two.

5.1.4 Decreasing drying rate period 2 (DDRP 2)

The decrease of dewatering rate in the first phase {4a} of DDRP 2 achieves the maximum level regarding the entire process, signalized by the steep inclination of drying rate chart. Evaporation of bound water is still in progress and the cracks already

formed tend to collapse due to shrinkage of the object (Fig. 5.1.B). The phase marked as {4a} terminates as the rate of temperature change reaches its peak value.

During the second phase {4b}, the rate of temperature alteration declines continually, accompanied by further reduction of the drying rate level. The decreasing drying rate period comes to an end when the temperatures within the sphere equalizes with the temperature of the superheated steam (Fig. 5.1.A).

5.1.5   Final drying period

Though the temperature is no longer subject to observable changes, the evaporation of tightly bonded water continues until the equilibrium moisture content is reached, which value is a function of the drying medium temperature [15]. The drying rate becomes close to none, as the bound water poses great challenge in terms of feasibility of its removal.

This stage takes the longest time to be finished and produces only a minor upgrade of the coal quality, what matches the general trend that subsequent periods of drying consume larger amounts of heat with smaller measurable effect. Thus, drying of coal to such a low moisture content value occurs mostly in the research endeavors [25]. In terms of industrial practice, though, the most crucial stages of drying are the CDRP and DDRP1.

5.2   Analysis of superheated steam drying characteristics obtained at various experimental conditions

In this section the drying characteristics of samples are presented. They include experimental trials conducted for samples of 2.5, 5, 10 and 30 mm at superheated steam temperatures of 110, 130, 150 and 170 ^{o}C. Among the numerous attempts performed for each combination of those two parameters, three representative cases were selected.

They are presented altogether in figures corresponding to the particular sample diameters and superheated steam temperatures. Changes of three kinds of indicators in time were taken into consideration: moisture content, drying curve and profile of temperature. The latter consists of three compounds: surface, midpoint and center temperature in the case of 30 and 10 mm objects, as described in chapter 4. Samples of 5 mm in diameter were deprived of midpoint temperature measurement, and the temperature of the smallest category of particles was measured on the surface only.

Figures 5.2 to 5.5 illustrate experimentally obtained drying curves for 2.5, 5, 10 and 30 mm lignite particles, respectively. In order to reduce the impact of electronic balance measurement oscillations and improve the legibility of the charts, the values of drying rate were averaged on a time frames ranging from 15 to 120 s, depending on the drying conditions. The charts representing the correlation of drying rate and moisture content are shown in regard to size dependence (Fig. 5.6) and temperature dependence (Fig. 5.7). Still, the amplitude of drying rate level for the sample of 2.5 mm is the most explicit among the entire set of object diameters, due to the high relative ratio of resolution of the balance (0.1 mg) to the mass of the examined sphere.

The fundamental conclusion drawn from the analysis of experimental drying curves is that increase in gas temperature and decrease in object size enhance the rate of dewatering. As a consequence, the time required for the completion of the process becomes shorter. Regarding temperature difference between surface and center temperatures, for 5 mm particles it is barely recognizable throughout the process, regardless the temperature scenario. Meanwhile, the two largest categories of object display significant gap in the temperature profile, especially during DDRP1. The tests conducted for samples of relatively high initial moisture content are characterized with elevated drying rate and delayed incline of the measured temperatures.
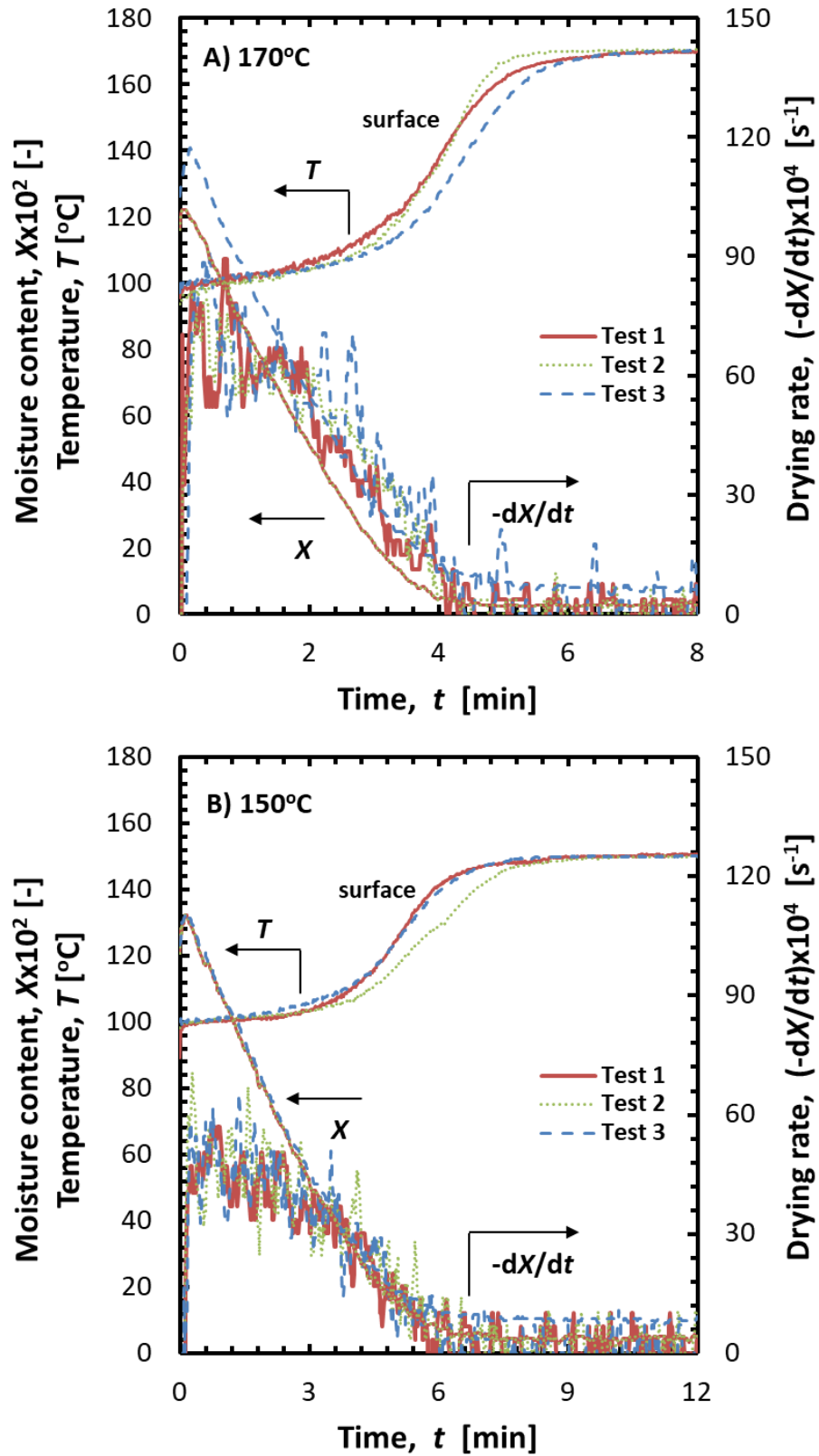
Figure 5.2.1 Experimentally obtained drying characteristics of 2.5 mm sample at test temperatures of A) 170 ^{o}C, B) 150 ^{o}C
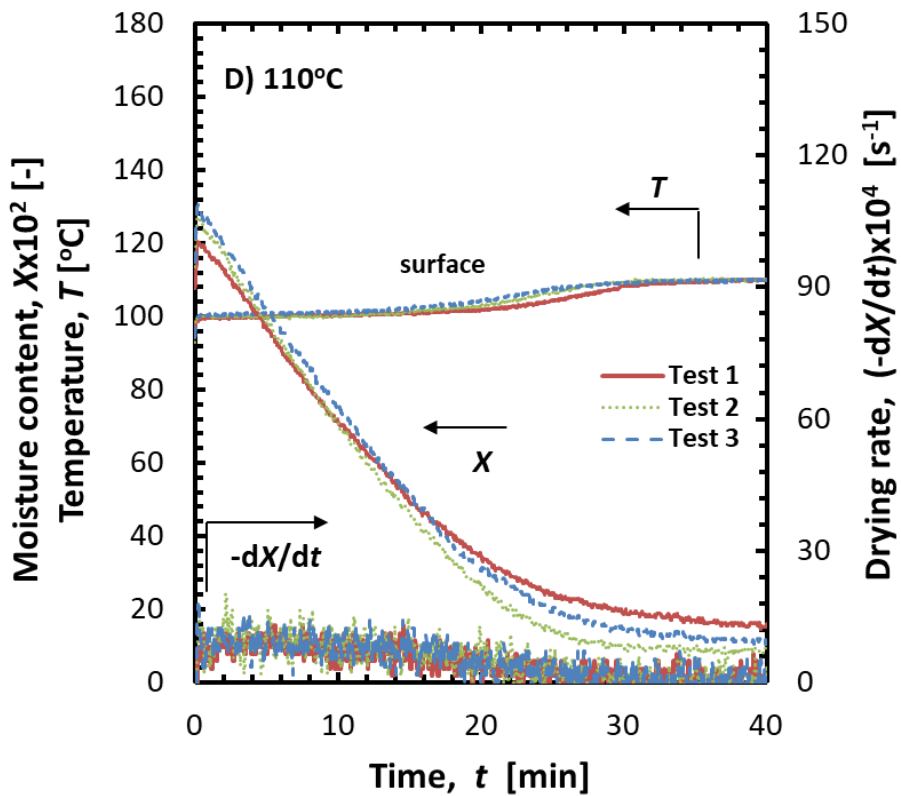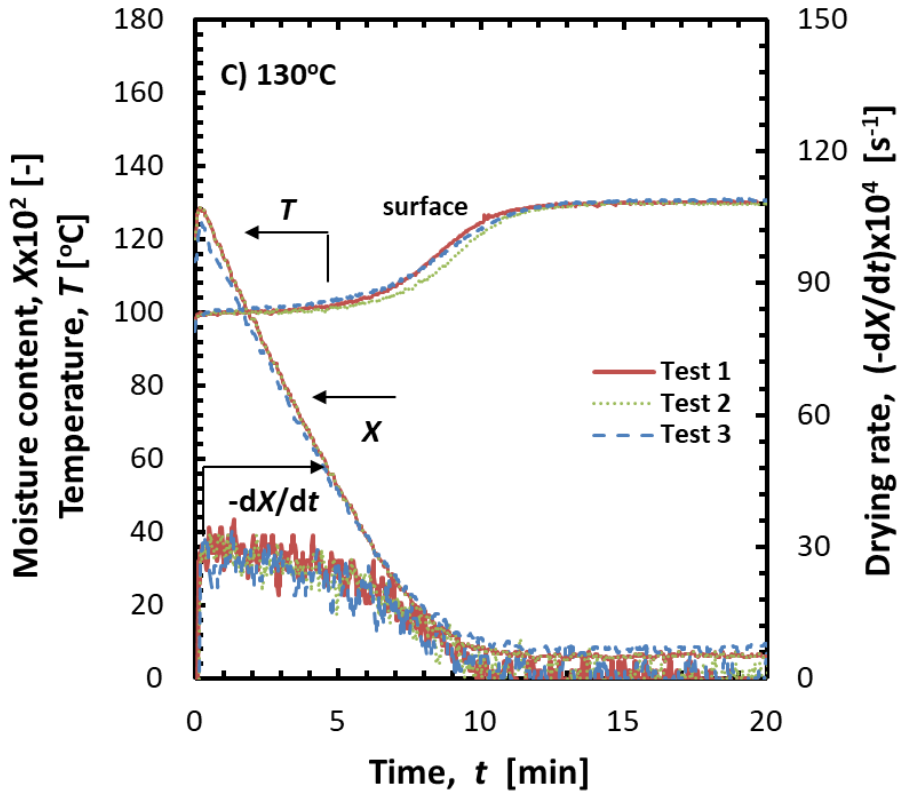
Figure 5.2.2 Experimentally obtained drying characteristics of 2.5 mm sample at test temperatures of C) 130 °C, D) 110 °C
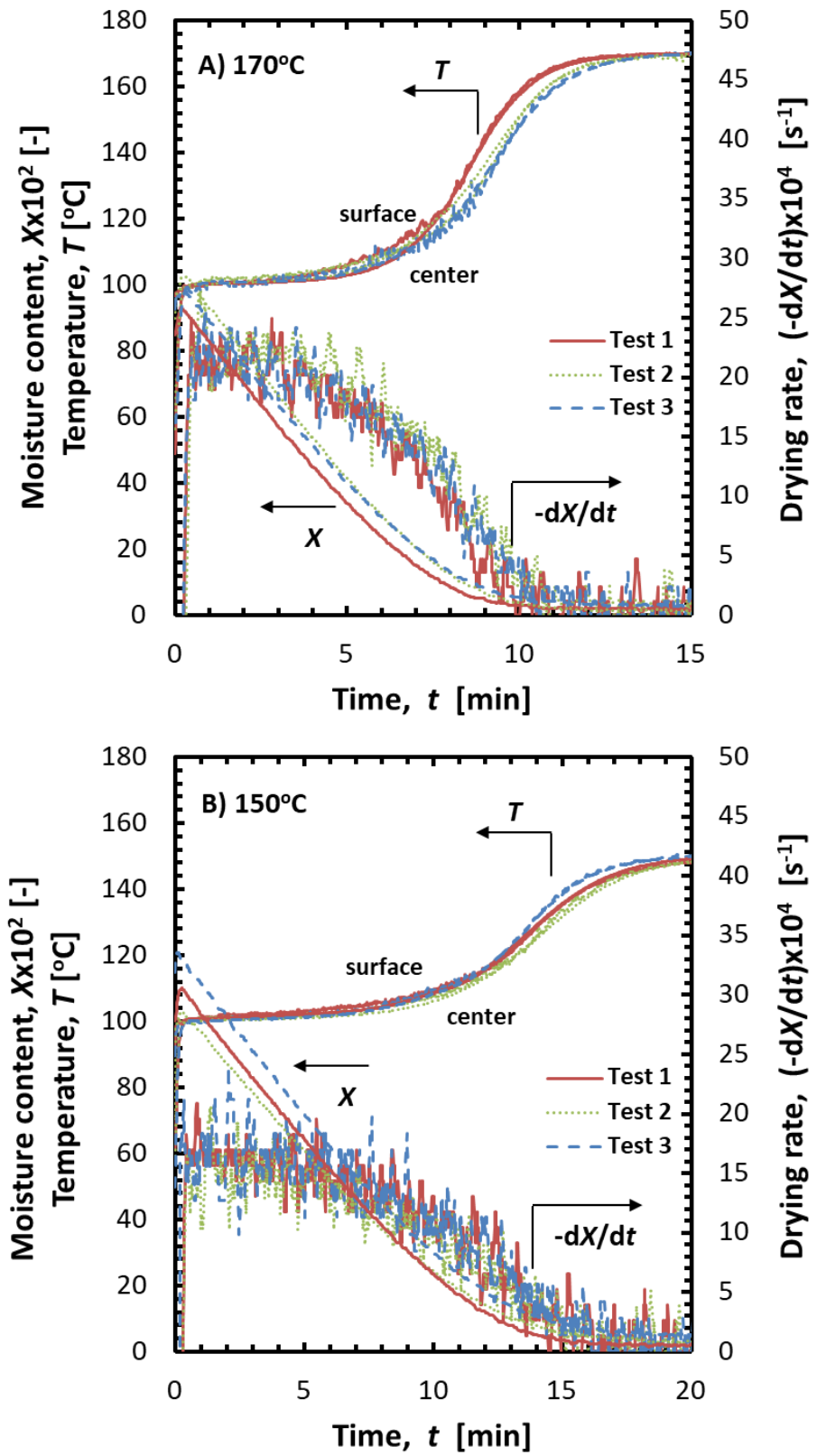
Figure 5.3.1 Experimentally obtained drying characteristics of 5 mm sample at test
temperatures of A) 170 ^{o}C, B) 150 ^{o}C
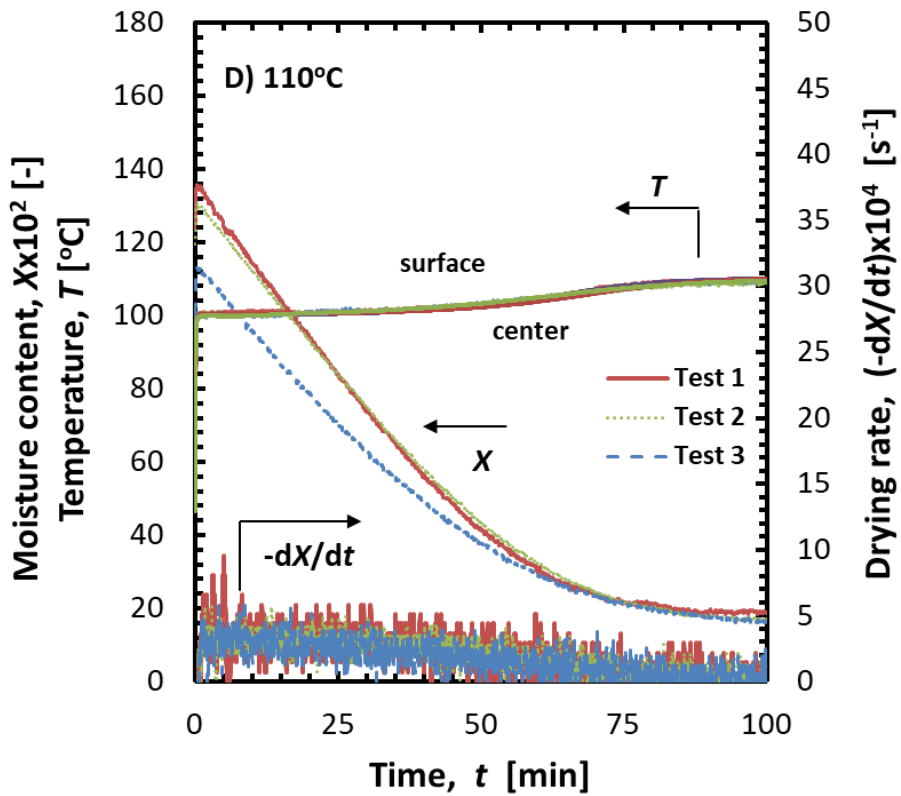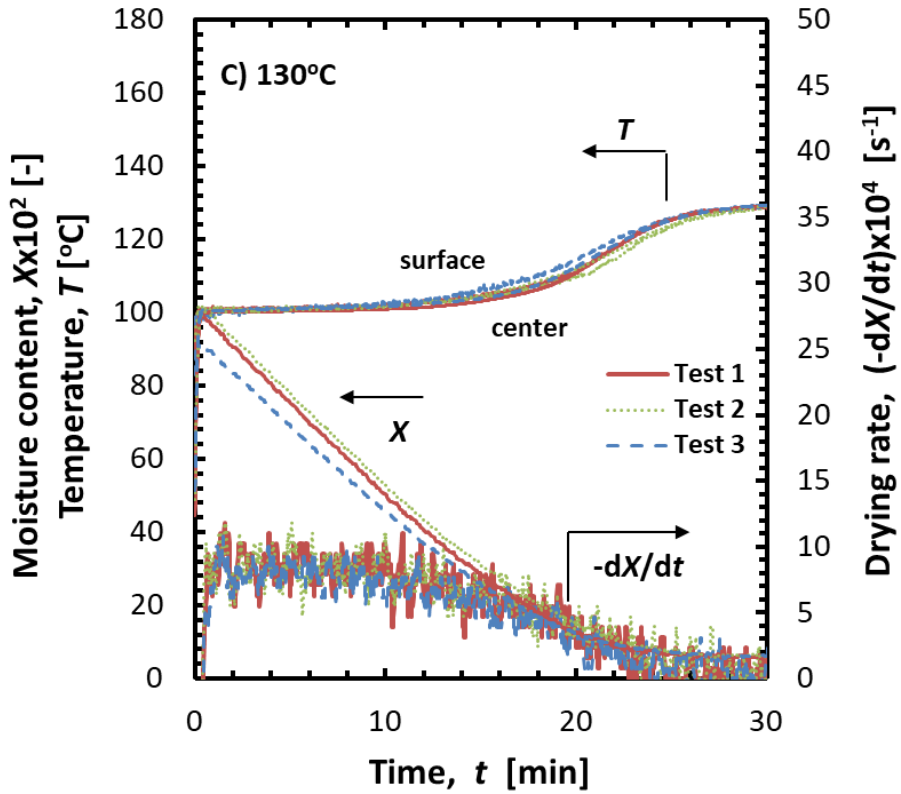
Figure 5.3.2 Experimentally obtained drying characteristics of 5 mm sample at test temperatures of C) 130 ^{o}C, D) 110 ^{o}C
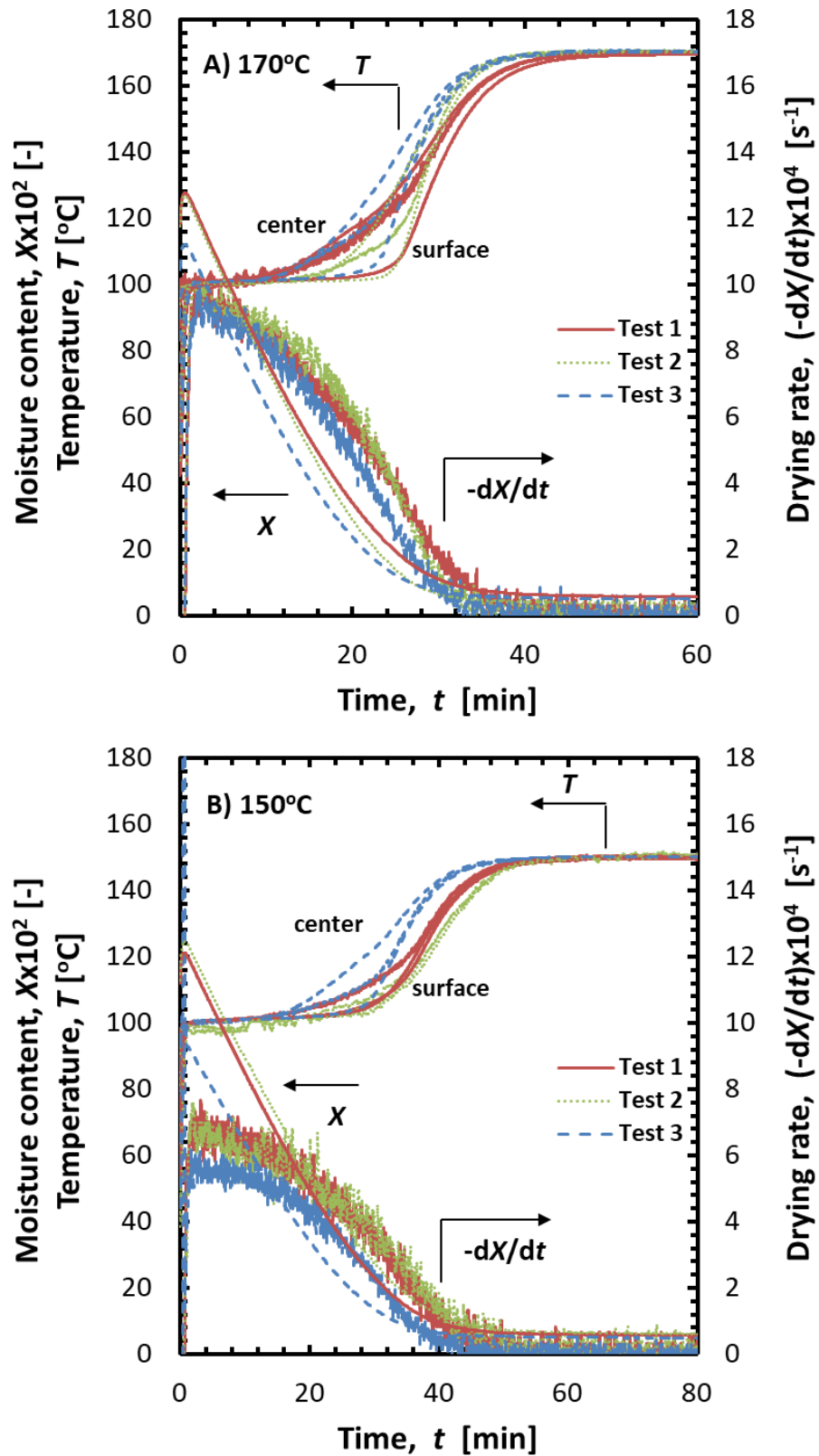
Figure 5.4.1 Experimentally obtained drying characteristics of 10 mm sample at test temperatures of A) 170 $^{\circ}$C, B) 150 $^{\circ}$C
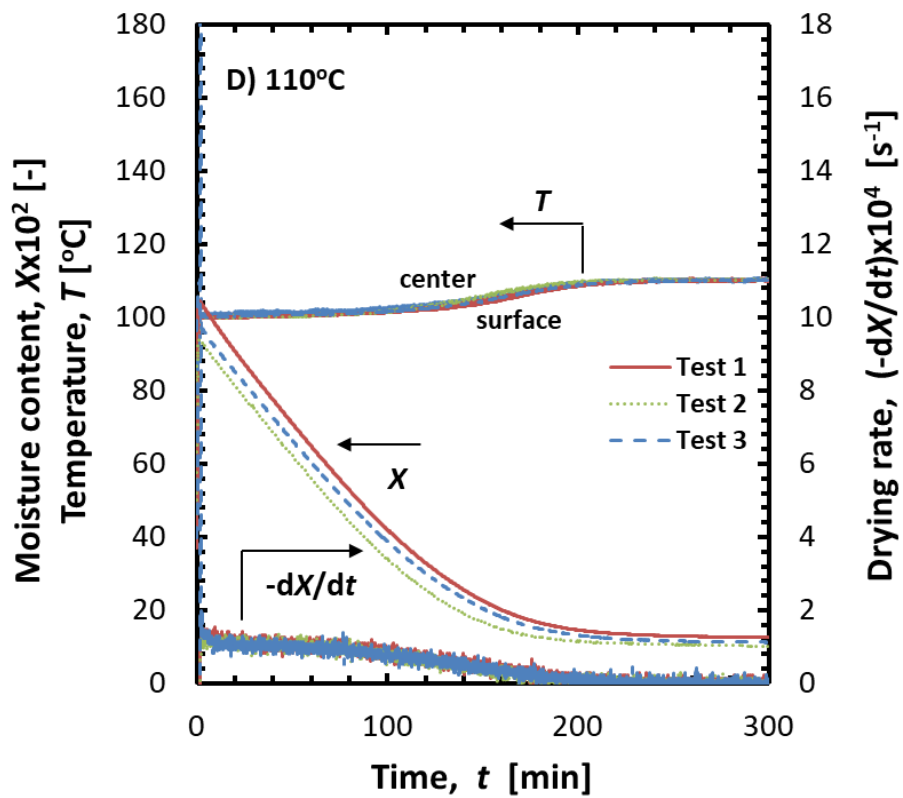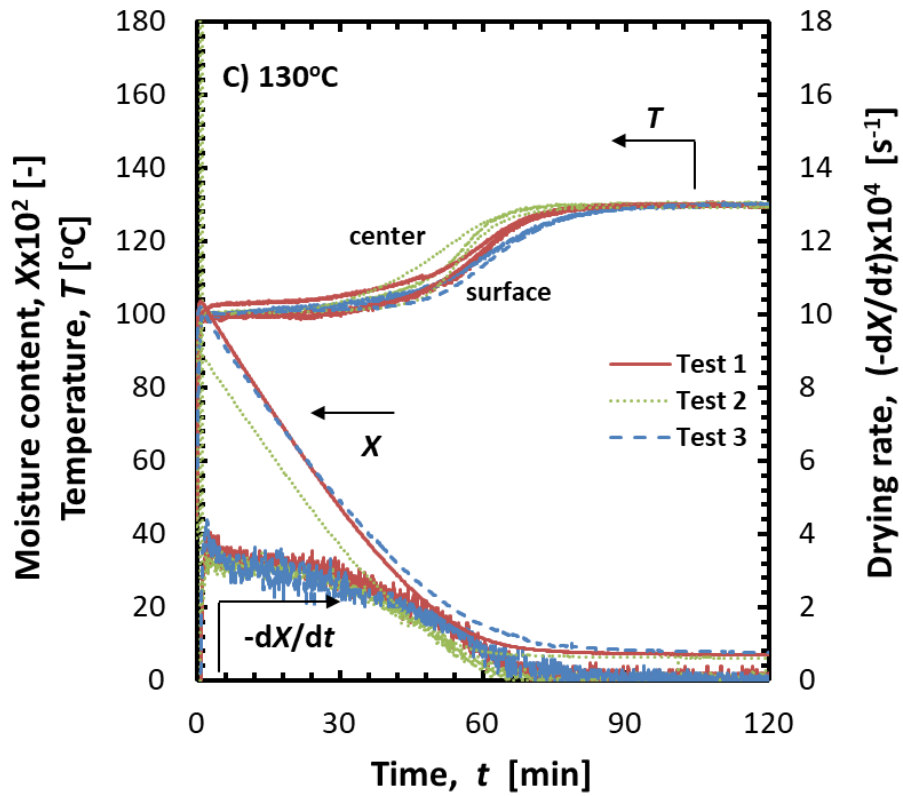
Figure 5.4.2 Experimentally obtained drying characteristics of 10 mm sample at test temperatures of C) 130 $^{\circ}$C, D) 110 $^{\circ}$C
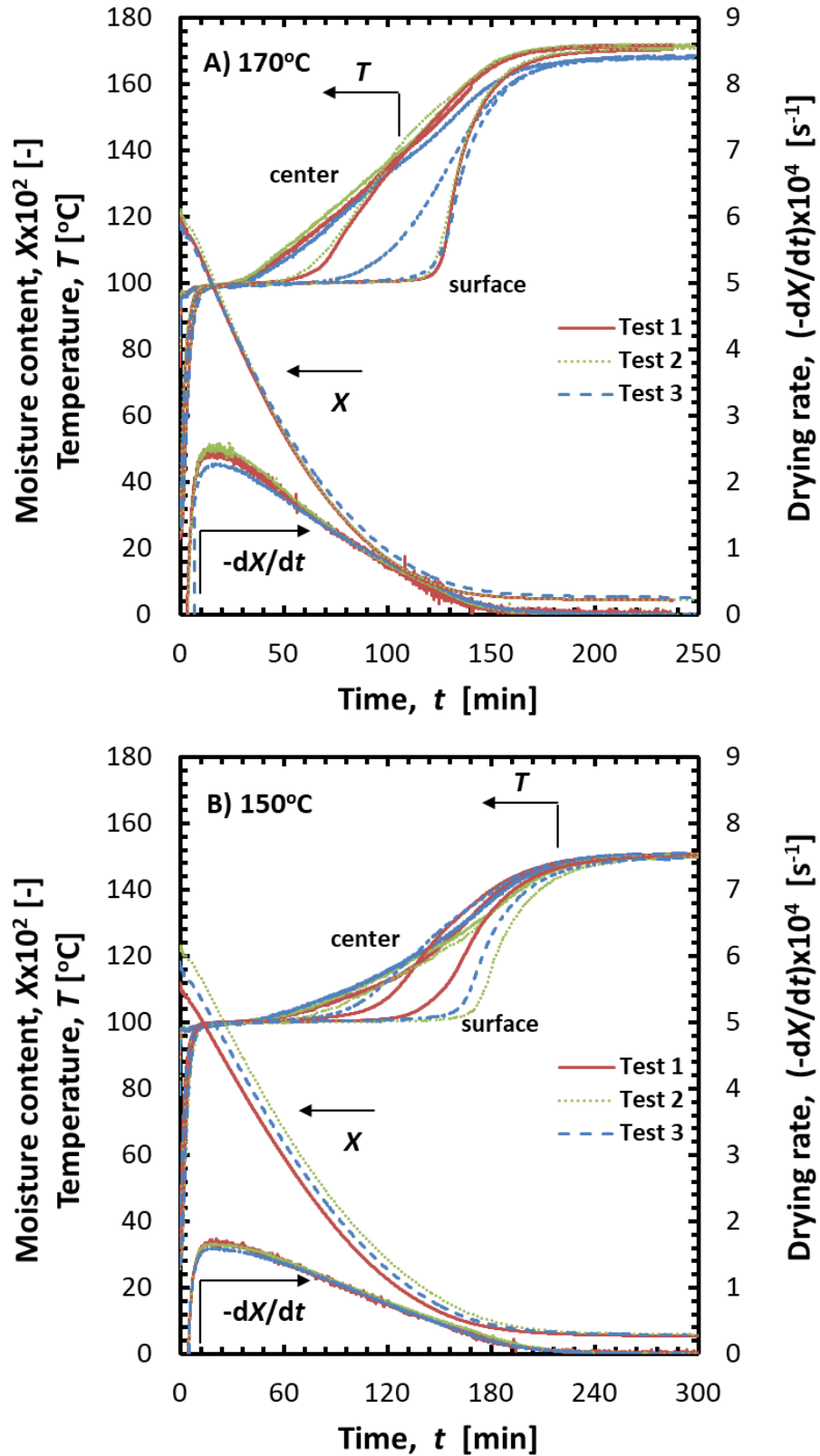
Figure 5.5.1 Experimentally obtained drying characteristics of 30 mm sample at test temperatures of A) 170 ^{o}C, B) 150 ^{o}C
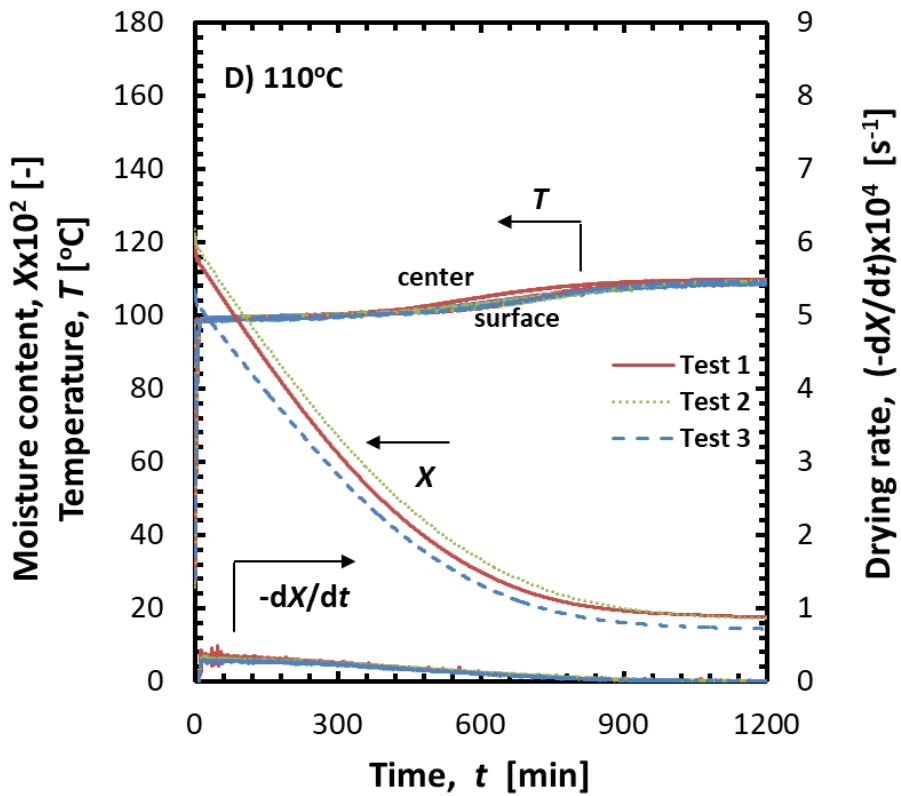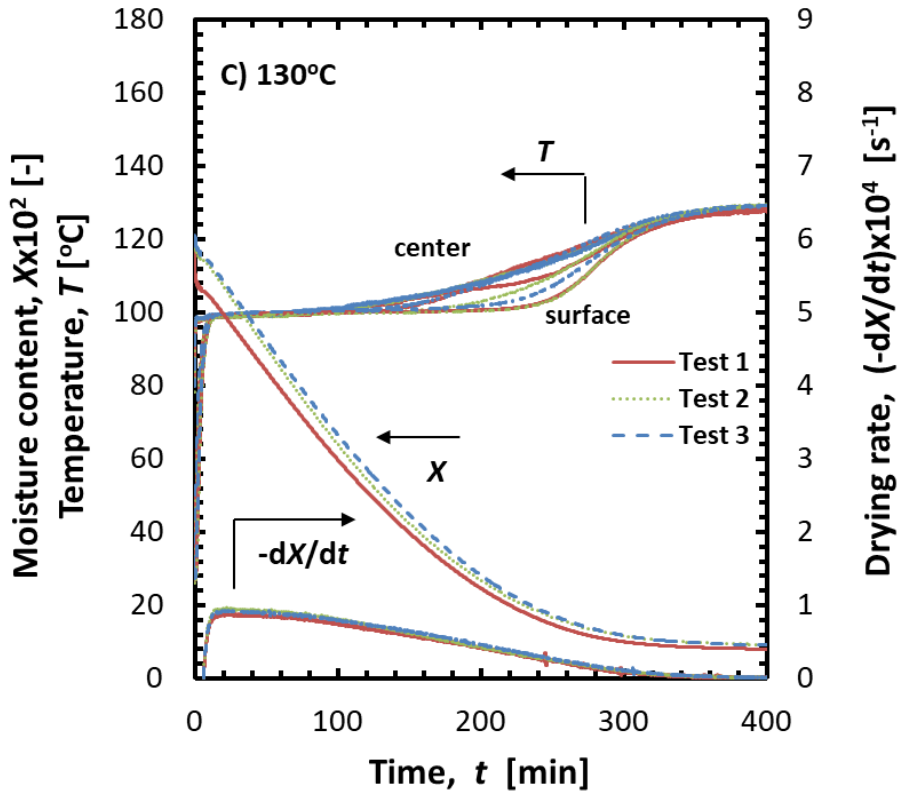
Figure 5.5.2 Experimentally obtained drying characteristics of 30 mm sample at test temperatures of C) 130 $^{\circ}$C, D) 110 $^{\circ}$C
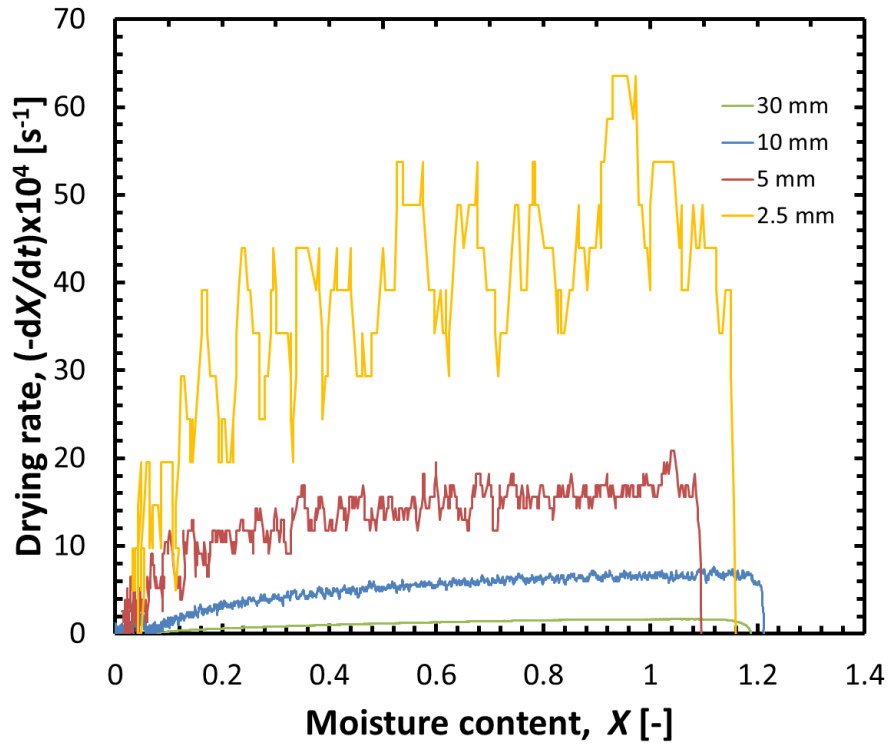
Figure 5.6 Experimentally obtained correlation of drying rate and moisture content for drying at 150 ^{o}C of samples of various diameters
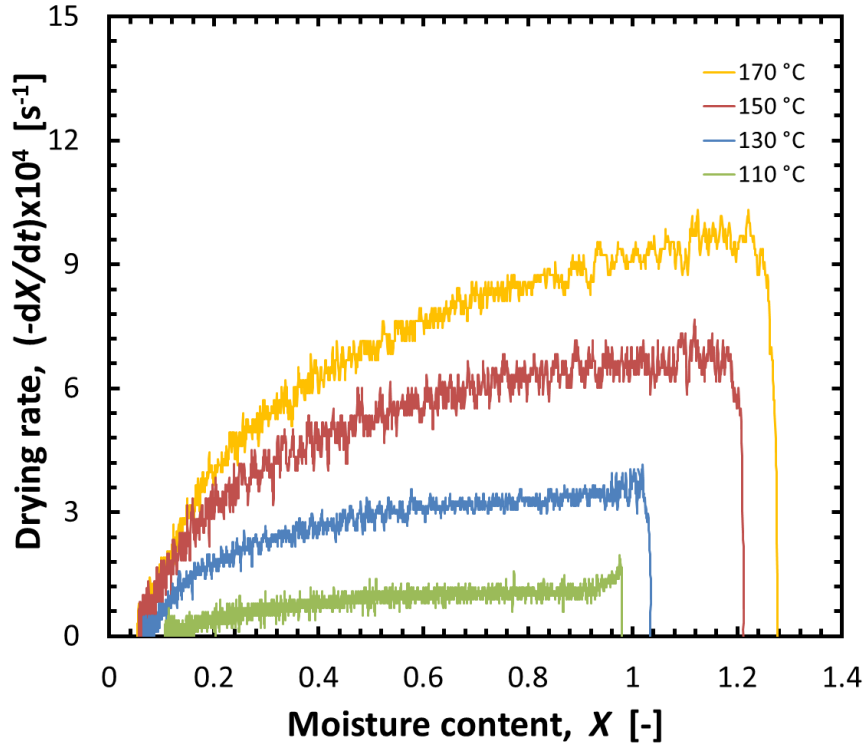
Figure 5.7 Experimentally obtained correlation of drying rate and moisture content for drying of 10 mm sample at various steam temperatures

Tables 5.1 to 5.4 present the information on the individual and averaged time of superheated steam drying for the experimental attempts included in Fig. 5.2 to 5.5. The average values were used to work out the approximation formula for drying time as a function of steam temperature and reciprocal of sample diameter. The equation is presented in section 7.3 and compared with the value of time of the drying process derived by means of numerical analysis (see Eqs. (7.2) and (7.3)).

Table 5.1 Experimental time of drying for samples of 30 mm

steam temperature	experimental drying time $t_{dry,exp}$ [min]			
T_a [°C]	Test 1	Test 2	Test 3	average
170	200.3	195.9	198.2	198.1
150	262.8	265.0	261.3	263.0
130	393.4	379.7	398.9	390.7
110	962.1	1076.3	1029.8	1022.7

Table 5.2 Experimental time of drying for samples of 10 mm

steam temperature	experimental drying time $t_{dry,exp}$ [min]			
T_a [°C]	Test 1	Test 2	Test 3	average
170	76.0	73.1	68.0	72.4
150	81.1	92.7	74.8	82.9
130	200.0	226.5	224.2	216.9
110	316.8	346.0	394.0	352.3

Table 5.3 Experimental time of drying for samples of 5 mm

steam temperature	experimental drying time $t_{dry,exp}$ [min]			
T_a [°C]	Test 1	Test 2	Test 3	average
170	12.7	13.2	13.2	13.0
150	20.0	23.7	19.7	21.0
130	28.5	30.0	30.5	29.7
110	92.5	104.3	120.0	105.6

Table 5.4 Experimental time of drying for samples of 2.5 mm

steam temperature	experimental drying time $t_{\mathrm{dry,exp}}$ [min]			
T_{a} [$^{\mathrm{o}}$C]	Test 1	Test 2	Test3	average
170	6.4	6.2	6.1	6.2
150	10.6	9.6	8.6	9.6
130	16.2	17.3	16.8	16.7
110	43.8	38.3	47.0	43.0

5.3 Observation of lignite appearance during superheated steam drying

As introduced in chapter 4, each experimental attempt was recorded using video camera. Owing to that, the observations of phenomena concerning physical appearance of the sample's surface and shape could be possible. Objects of 5, 10 and 30 mm were taken into consideration, as the 2.5 mm objects on a quadrilateral handle (see Fig. 5.8) were too small to observe significant impact of drying on their structure.

In Fig. 5.9, the images are shown in regard to 10 mm sample dried at various temperatures. They were captured at the start and the end of drying as well as at the certain values of declining moisture content.
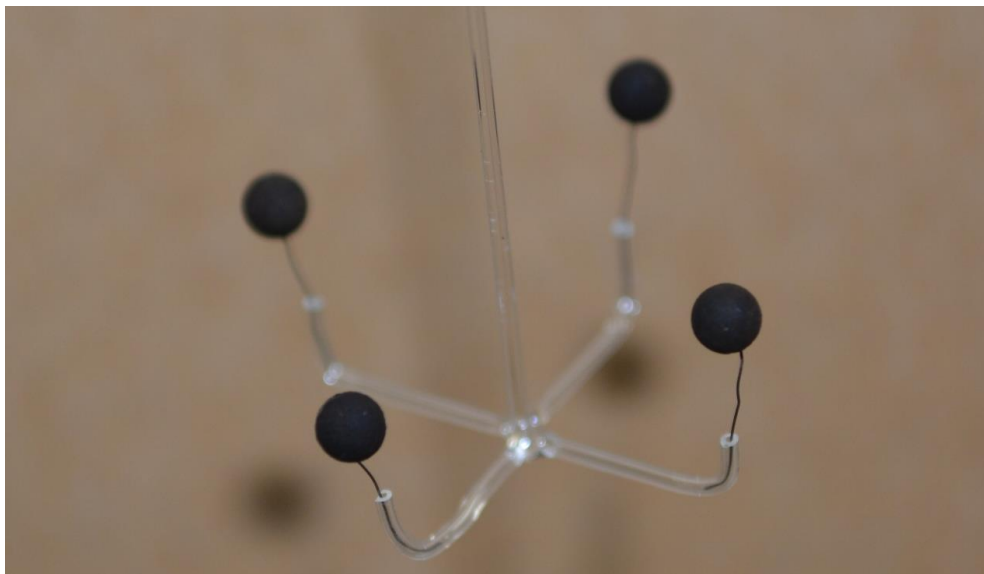
Figure 5.8 Photograph of the set of 2.5 mm lignite samples prepared for the test
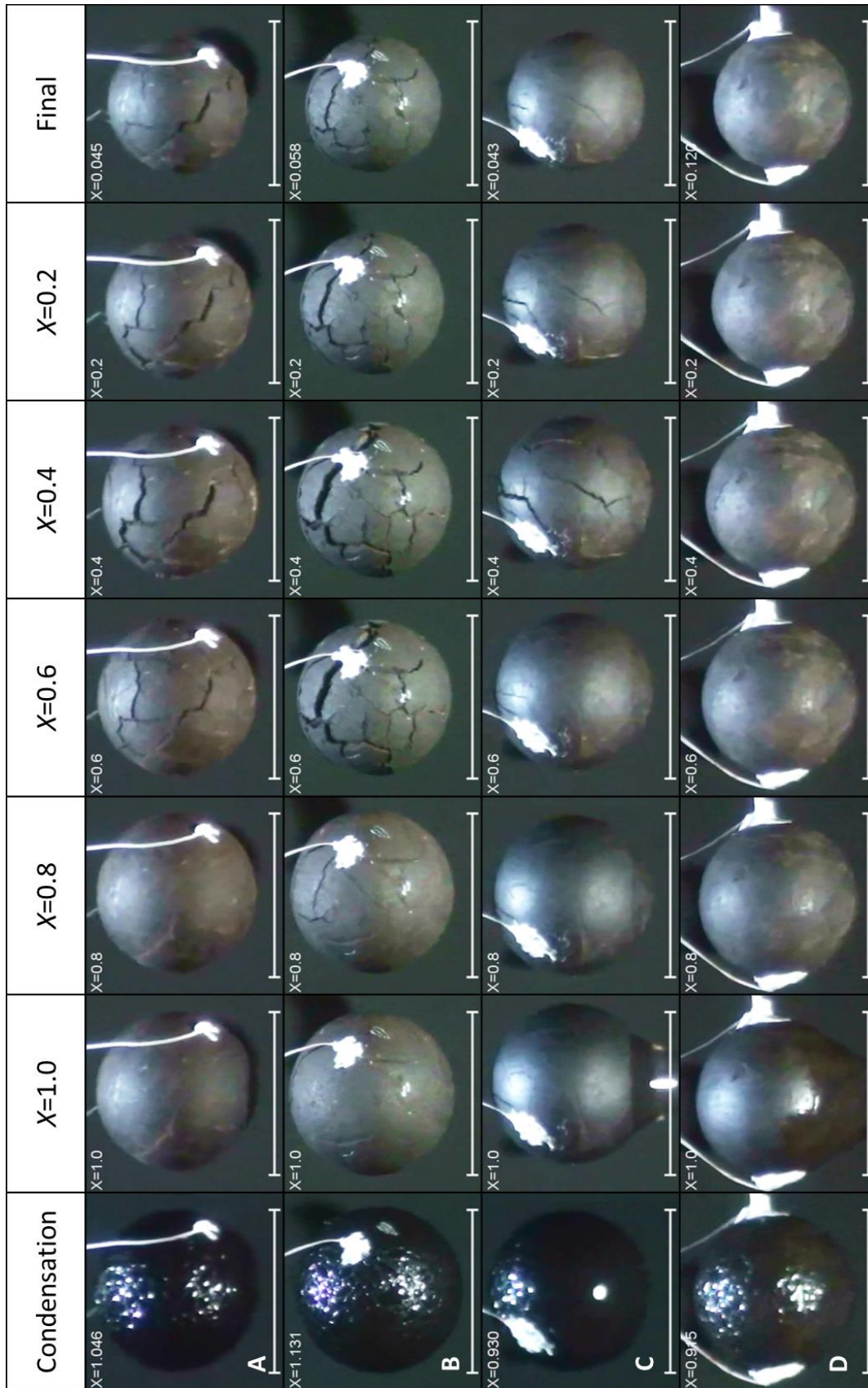
Figure 5.9 Observation of 10 mm sample dried at A) 170, B) 150, C) 130 and D) 110 ^{o}C

Judging from the images, considerable fracturing of the surface occurred principally for the cases of higher steam temperatures (150 and 170 ^{o}C). The first signs of cracking were spotted when the moisture content declined by around 0.2 with reference to the initial value, what is approximately related to the end of CDRP. In the case of 130 ^{o}C the changes in the structure of the surface were also observed, however they occurred later ($X \approx 0.5$) and did not exhibit such significant impact. As indicated by Fig. 5.4.2.D, the temperature gradient along the radius of lignite sphere dried at 110 ^{o}C is minor, therefore removal of water from the consecutive regions of the sample is not followed by occurrence of high thermal stress, what limits the surface deformation.

The influence of structural deformation is noticeable also in terms of uniformity of the drying characteristics (see Fig. 5.2 - 5.5). Experimental attempts conducted in lower test temperatures (110, 130 ^{o}C) are following the similar pattern for all three categories of drying indicators. Meanwhile, the repeatability of tests for higher temperature of superheated steam is slightly disrupted and the unexpected oscillations of the drying curves are more likely to occur.

Figure 5.10 illustrates the appearance of the samples of different diameters dried at the fixed steam temperature of 150 ^{o}C. Although a major circumferential crack is observable in the case of 10 mm object, the fragmentation of 30 mm sphere seems even more considerable. The movement of the dry shell zone towards the center of the sphere generates stress, which enhances with the increase of sample diameter. The loss of lump strength results in the emergence of cracks. Bulk pieces of organic matter and foreign inclusions, characteristic for low rank coals, occur more likely in objects of larger volume. They boost the mentioned disorder induced by thermal stresses. In accordance with this deliberation, the exemplary particle of 5 mm in diameter does not exhibit such vast fracturing of the surface as the larger counterparts presented in series A and B.
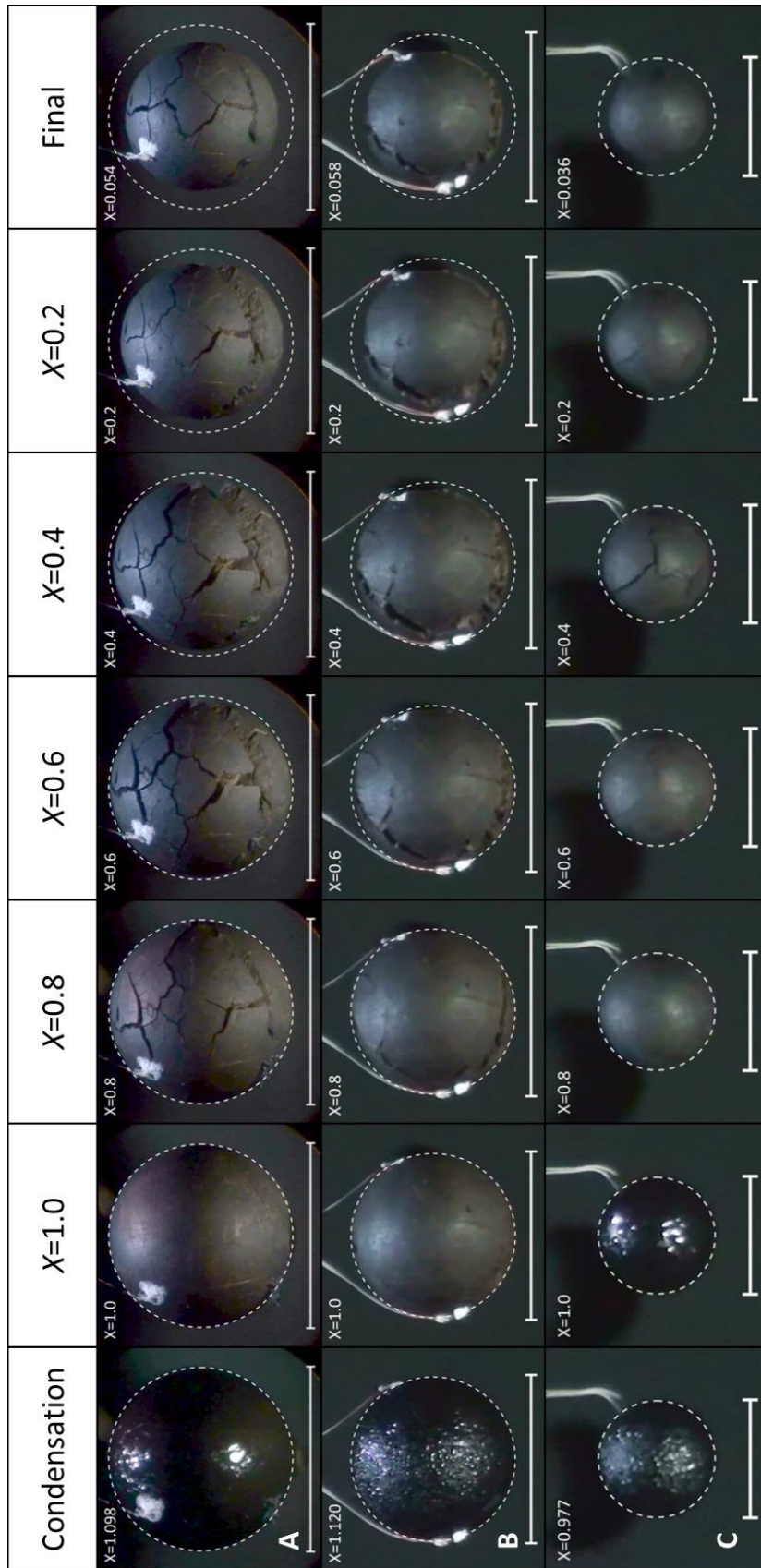
Figure 5.10 Observation of A) 30, B) 10 and C) 5 mm sample dried at 150 °C

66

The phenomenon of cracking is thought to be fostered by the coal shrinkage which occurs as the pieces of organic matter collapse into empty spaces previously occupied by water. In each image series of Fig. 5.10, a dashed line circle was inserted to mark the shape of the sample at the beginning of particular drying attempt. Allardice et al. claimed that removal of capillary water, which begins around the moisture content of 0.7 is accompanied by shrinkage [84]. It is consistent with first symptoms of shape change in the picture corresponding to X equal to 0.6. However, at the moisture content level of around 0.4, the gap between the dashed line and the sample becomes explicit, regardless the size of the object.

The observed decline in the sample diameter due to drying was applied to evaluate the volumetric shrinkage of the samples. In Tab. 5.5 the average values of final shrinkage are gathered for various drying conditions. In Fig. 5.11, the volumetric decline for corresponding scenarios are related to gradually regressing moisture content. The intensive shrinkage in the late DDRP contributes to the sealing of the previously emerged cracks, as shown in the two last columns of Fig. 5.9 and 5.10. In general, the steam temperature did not influence the total shrinkage. Yet, the individual determinants of the samples did. For instance, the tests for 5 mm at 130 and 170 $^{\circ}$C exhibited lower initial moisture content than the global average. Meanwhile, 30 mm objects, underwent irreversible and asymmetric deformation which precluded the gaps from sealing.

Table 5.5 Average total volumetric shrinkage of lignite ($1-V/V^0$)

steam temperature	sample diameter d [mm]		
T_a [$^{\circ}$C]	30	10	5
170	28%	40%	35%
150	37%	40%	43%
130	37%	41%	33%
110	39%	35%	36%
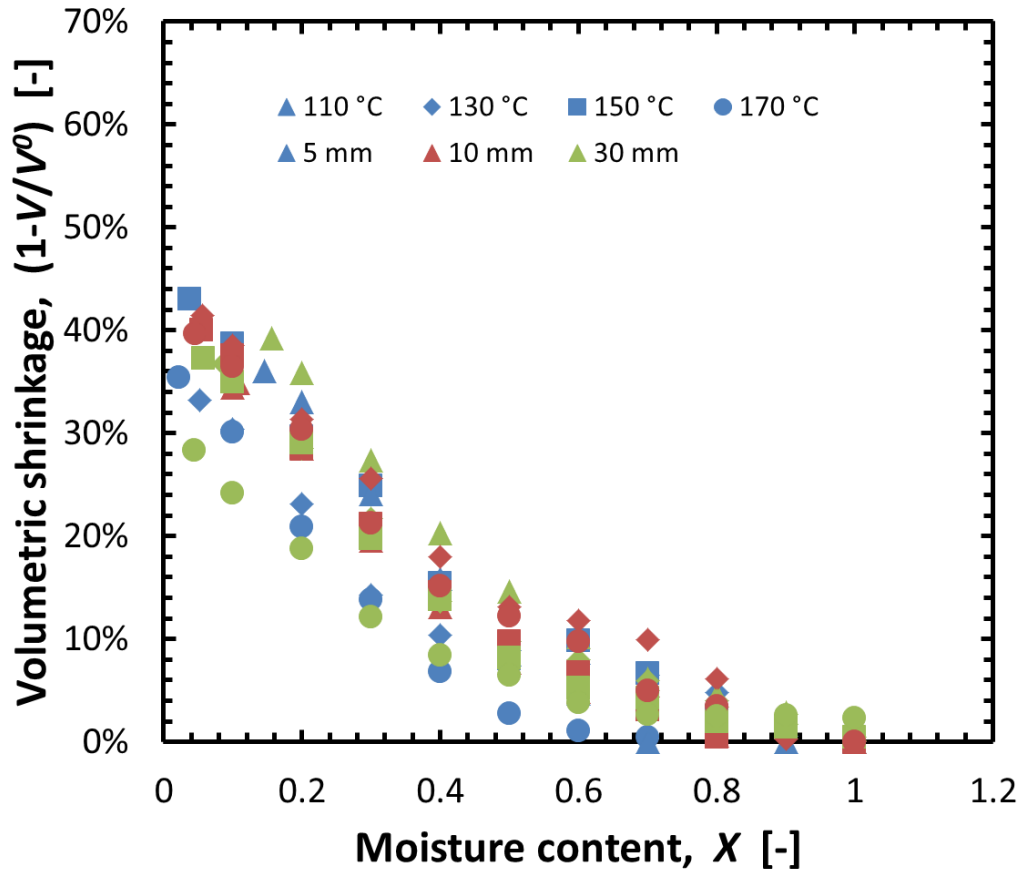
Figure 5.11 Average shrinkage of the samples in the drying process

Another kind of phenomenon observed by video recording was formation and falling of the droplets. In the beginning of every test, steam condensed on the cold lignite surface. In case the aggregate rate of condensation and diffusion to the surface exceeded the rate of drying for long enough, the surface tension of water was too low to balance the gravitational force. Then, the water hemisphere that was forming on the bottom of the sample tipped off in the form of droplet. In Fig. 5.9.C, a water hemisphere, seconds before exceeding the critical mass, is visible at the moisture content of 1.0.

The reduction of lignite mass and thus moisture content related to falling droplets was noted on the drying charts. The particles of different diameters varied in terms of droplet formation. No sudden decrease of weight was observed in drying of 2.5 and 5 mm objects, as the rate of condensation was low comparing to the drying rate. In

the case of 10 mm spheres, a single droplet was observed in some drying instances, for all test temperatures except 170 °C, at which the speed of dewatering was too high. The phenomenon was most noticeable in experiments performed with 30 mm samples. The alternating periods of gradual mass increase followed by rapid decline occurred several times at the entire range of steam temperatures, as presented in Fig. 5.12. The end of condensation was observed when the weight of the sample decreased below the initial value by 2.0%, 1.6%, 1.3% and 1.5% for drying tests at 110, 130, 150 and 170 °C, respectively. It suggests that both condensation and exudation of moisture from the lignite interior contributed to formation of the surface layer. The shrinkage, cracking and droplet formation during superheated steam drying of Belchatow lignite was discussed in regard to 5 and 10 mm samples in [85], while for 30 mm objects in [86].
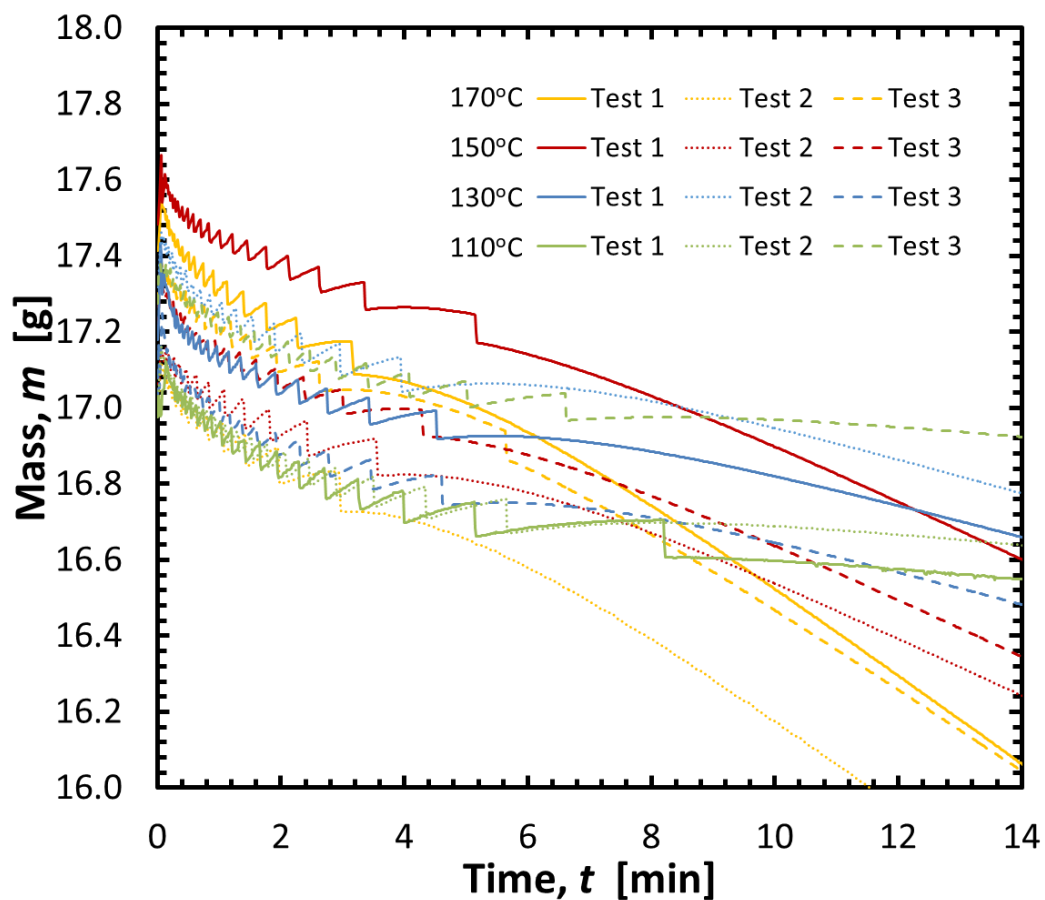
Figure 5.12 Falling of water droplets in the initial drying period of 30 mm sample

5.4 The influence of the structural features of lignite on the properties related to superheated steam drying

5.4.1 Geological origin and contents of coal from Belchatow and Turow lignite mines

In order to determine the potential impact of specific coal properties, including those related to its geological origin, the additional experimentation was performed. A series of lignite batches extracted from the deposits currently exploited by Belchatow and Turow mines were subject to superheated steam drying tests.

The Belchatow deposit originated in lower Miocene (23 – 5 million years ago) in the area formerly covered (throughout Mesozoic) by a warm sea. The seams, to which the Belchatow resources are attributed to, are categorized as the 3rd group of Scinawa Lignite Seam (SLS-3) [87]. The deposit has the form of widely spread thick layer. The Belchatow lignite mine area currently includes three mining fields: Belchatow, Szczercow and Kamiensk. Batches of lignite that were taken into consideration were extracted from Szczercow (batch B1) and Belchatow (batches B2 and B3) fields. The place of origin is visualized in the Fig. 5.13.

The investigated lignite batches from Turow mine came from two seams. Batches T1 and T3 were excavated from Seam I, placed in the stratigraphic group of SLS-3 (same as Belchatow), while batch T2 originated in Seam II, which belongs to the Lusatian Lignite Seam (LLS-2), located more shallow in the cross-sectional profile. The latter group formed between lower and middle Miocene [87]. The geographical and geological location of the batches is presented in Fig. 5.14.
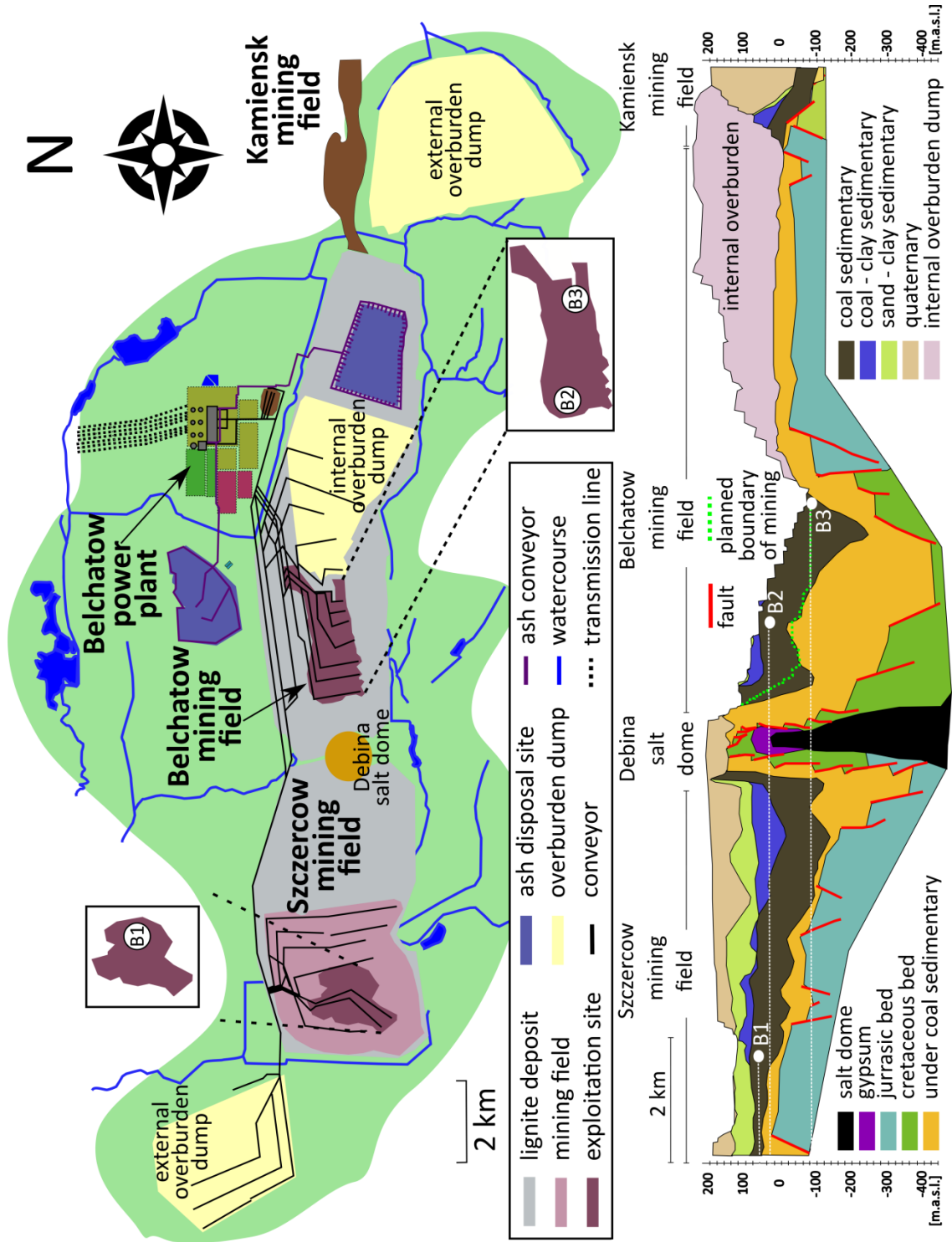
Figure 5.13 Map and cross section of Belchatow lignite mine and its surroundings [88]
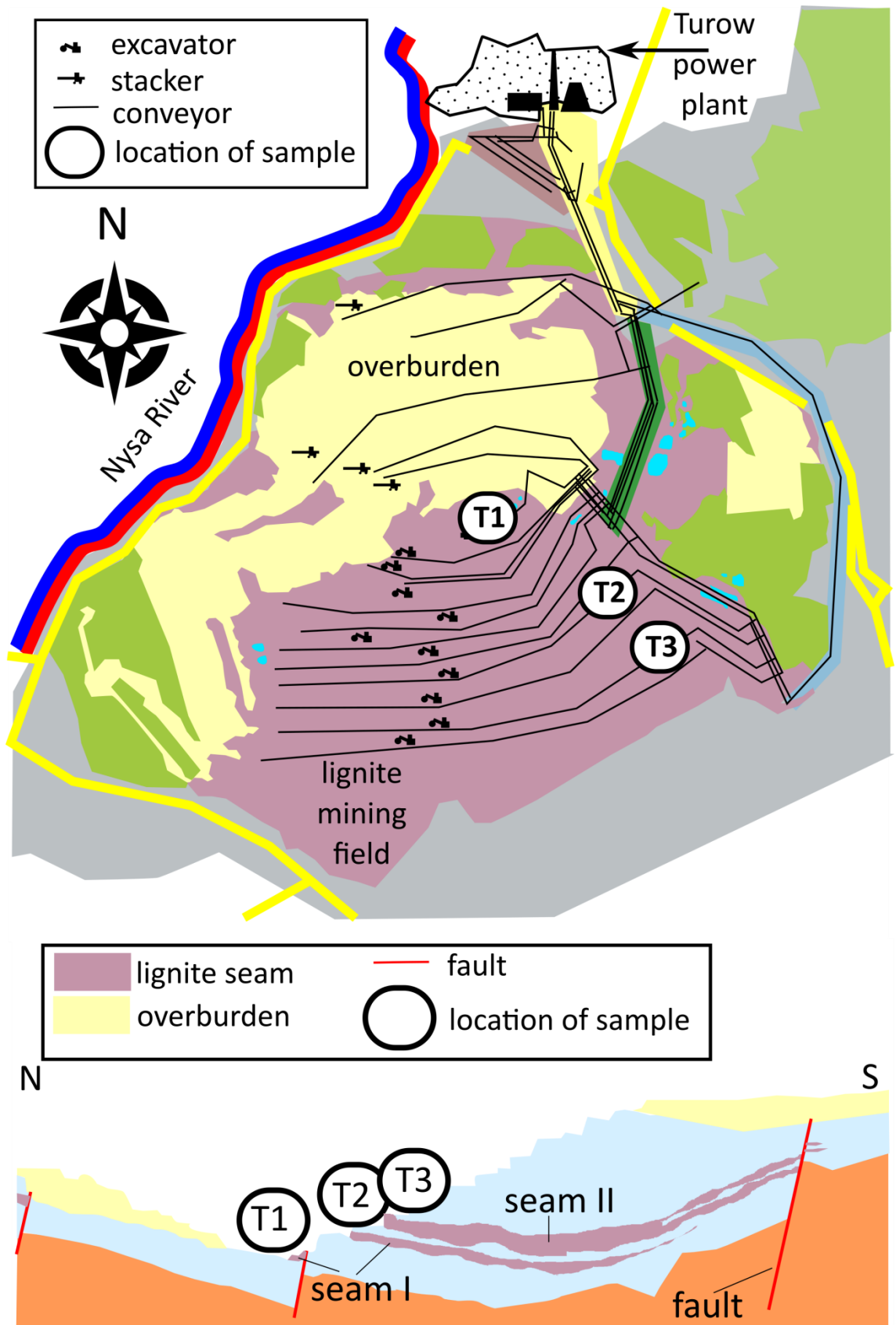
Figure 5.14 Map and cross section of Turow lignite mine and its surroundings [89]

The results of proximate and ultimate analyses of introduced lignite batches are presented in Tab. 5.6. For comparison, the corresponding values of the B2013 coal, investigated in the major part of this work are given. The expected properties of drying for two analyzed groups vary significantly, primarily due to large gap in water content. Turow lignite from batches T2 and T3 is characterized with considerable combined share of carbon and hydrogen, approaching 70% of the dry coal mass, what is reflected by high calorific value of these coals. Yet, this single parameter does not determine the quality of coal in power generation. For instance, ash content do not directly influence the drying kinetics (except reducing water percentage), but its content and composition are crucial, for instance in terms of IGCC system operation [90]. Around 1/4 of lignite is taken by volatiles, what may be profitable for gasification in the mentioned technology.

Table 5.6 Proximate and ultimate analyses for the lignite samples from Belchatow (B1, B2, B3, B2013) and Turow (T1, T2, T3) mines

coal batches	B2013	B1	B2	B3	T1	T2	T3
properties	**proximate analysis (as-received basis) [mass%]**						
total moisture	51.60	52.50	52.60	52.80	34.60	44.20	42.80
surface moisture	43.00	39.40	39.30	37.10	19.80	21.80	23.70
inherent moisture	8.60	13.10	13.30	15.70	14.80	22.40	19.10
fixed carbon	16.78	15.85	14.72	18.45	14.70	21.25	21.94
volatile matter	24.14	25.48	24.58	25.05	23.78	31.13	29.41
ash	7.48	6.22	7.99	3.74	26.92	3.42	5.79
contents	**ultimate analysis (dry basis) [mass%]**						
C	56.90	57.30	54.50	62.00	37.60	64.50	61.40
H	4.51	4.76	4.76	4.74	3.60	5.70	5.15
O	22.32	24.13	23.19	24.60	16.91	22.84	22.55
N	0.68	0.51	0.53	0.74	0.43	0.68	0.58
S (combustible)	0.19	0.26	0.10	0.06	0.30	0.50	0.17
ash	15.40	13.00	16.90	7.90	41.20	6.10	10.20
calorific value	**higher heating value (dry basis) [MJ kg^{-1}]**						
HHV_c	22.34	23.13	22.32	24.41	15.51	27.44	25.88

5.4.2 Effect of geological structure on initial moisture and density of lignite

The general influence of geological origin on the drying-related properties can be discussed with reference to two major coal lithotypes existing in lignite structure, xylitic and detritic coal. The lithotype is determined by prevalence of particular ingredients. Detritic coal (see Fig. 5.15.A) occurs in the form of fine-graded, crumble groundmass (detritus), which originated primarily from herbaceous plants as well as wood of deciduous shrubs and trees. In the macroscale, detritic coal is rather uniform, of distinguishable components smaller than 1 cm [91]. Xylitic coal (see Fig. 5.15.B), on the other hand, is composed of elongated woody remnants, in the form of pieces of branches, thin trunks or roots. Due to impregnation with resin which is produced by coniferous plants, the preservation of original structure is more likely to occur. The fragments of xylites in this type of coal exceed 1 cm [91]. The coals consisting of both structural components are denominated as xylo-detritic (over 50% of detritus) and detro-xylitic (over 50% of xylites) [92].

Figure 5.15 Representative cases of A) xylitic and B) detritic coal

In the studies of Romanian coal from Oltenia region [93], a correlation between lithotype and main qualitative parameters of coal was discussed. The significant dependence between coal lithotype and the ash content was observed. Xylitic coals were claimed to exhibit the lowest mineral content. The transient forms, xylo-detritic and

detro-xylitic coals, were characterized with larger share of ash contamination, while the largest values were obtained for detritic and clayed coals.

A several dozens of lignite samples made of Turow lignite were measured in terms of initial density and water share. In Fig. 5.16, the measurement results are presented, in regard to T1, T2 and T3 coal batches, formed in 5 and 10 mm spheres. The range of WS^0 is spread widely between 25 and 55% for all analyzed batches. Properties are distributed in two separated regions especially for T3 lignite, with a considerable number of objects, ranging significantly in initial water while having the alike initial density. In the case of T2, a transient group between samples of high and low density is observed. The trend for T1 lignite is rather blur, still, a certain amount of samples exhibiting low density and high moisture content is presented, similarly to T3, which originated within the same lignite seam. In general, the results may follow the correlation indicated in previous paragraph, as shown in Fig. 5.16.D. The highest moisture was remarked for xylitic coals, which evince low ash contamination and thus low density. The density rises at the expense of initial water content, what is specific feature of detritic coals. Still, some measurements resulted in remote and extreme values of both parameters, probably marking the objects prepared from highly contaminated footwall region of the lignite batch.

In conclusion, the knowledge on prevailing lithotype in the particular lignite type might be useful for predicting some properties related to fuel preparation. Initial water share and density, which gives the hint on ash content, are taken into account not only in terms of drying, but also the assignment of appropriate technology of combustion or gasification.
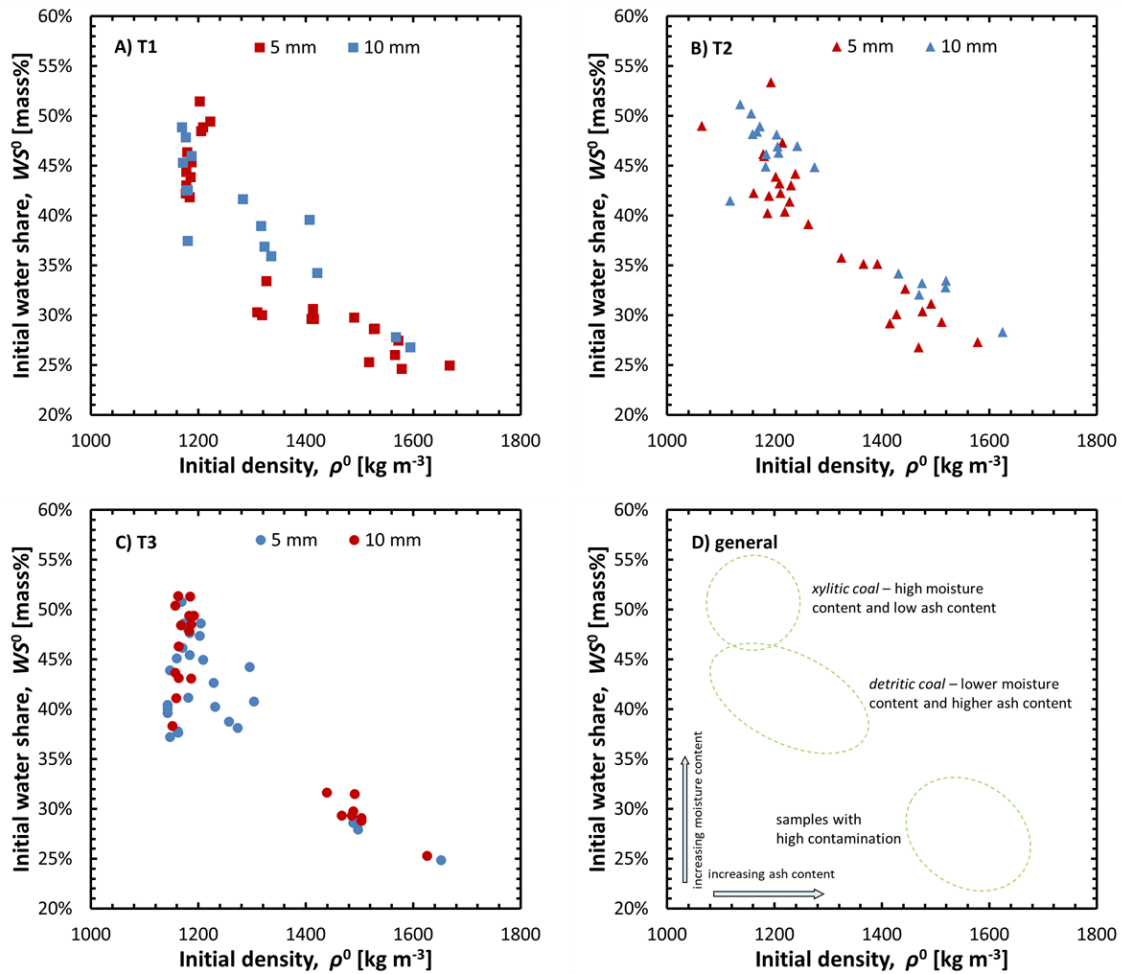
Figure 5.16 Correlation between initial density and water share for coal batches A) T1, B) T2, C) T3, combined with D) general observations

5.4.3 Effect of ash contamination on the drying behavior

The correlation between detailed individual properties of coal sample and the drying behavior are discussed on the example of T1 batch. Note that this lignite is characterized with by far the highest mineral contamination (Tab. 5.6). It is related to location from where that batch was extracted – the footwall of the seam. Due to proximity of other rocks formed of non-organic mineral matter, the high level of contamination, in the form of ash, is observed. The components of ash, are mostly silica and metal oxides, of higher molecular mass and density than water or carbon, therefore

the share of the two latter components is reduced in objects of significant ash contamination. Moreover, the inclusions of foreign material within lignite diminish the uniformity of the batch, what contributes to incline in randomness of drying properties and decline in experimental repeatability.

Figure 5.17 contains the drying characteristics for three tests performed for randomly chosen samples made of T1 batch, split into time charts of mass, moisture content, drying rate and temperature profile. Although they originated within 4 m section of a geological profile, their drying properties differ in significant manner. The major reason is the difference of moisture content, as presented with other drying indicators in Tab. 5.7.
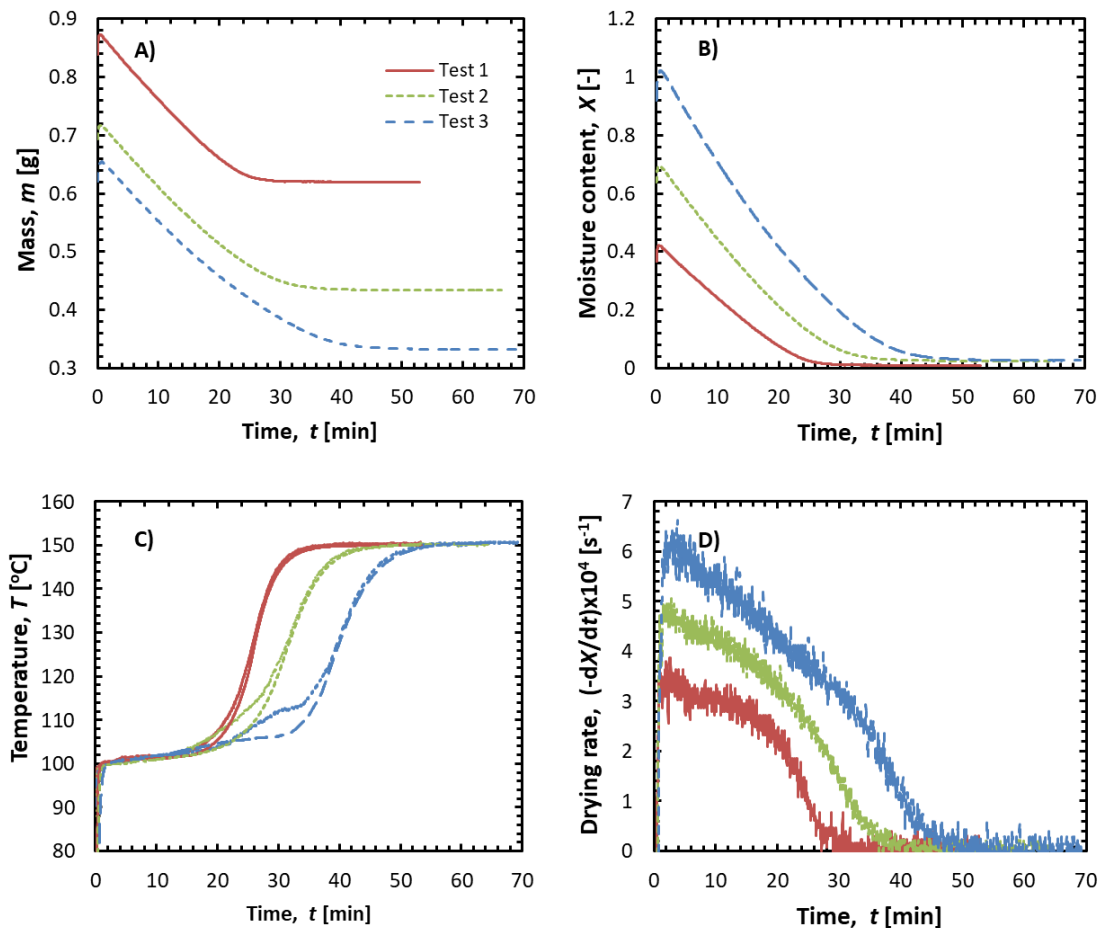
Figure 5.17 Exemplary drying characteristics of 10 mm samples made from T1 lignite, dried at 150 °C: A) mass, B) temperature profile, C) moisture content, D) drying rate

Table 5.7 Selected drying indicators of exemplary T1 samples

indicator	Test 1	Test 2	Test3
initial water share [mass%]	26.8	38.9	47.9
drying time [min]	42.1	57.6	58.2
peak drying rate [s^{-1}]	3.37×10^{-4}	4.69×10^{-4}	6.07×10^{-4}

The sample used in Test 1 was characterized by the lowest moisture content, therefore the period of preheating as well as CDRP ends sooner than the other two cases. For the same reason, the increase of surface and center temperatures (midpoint was omitted for the sake of chart's clarity) occurs the earliest, and so does the termination of the drying process. In addition, the small temperature difference is observed between surface and center curves, what might be attributed to the relatively high thermal diffusivity of this sample. This parameter is directly influence by moisture share, because water has the highest heat capacity among lignite components. With the assumption of constant volume of all three samples, the one used in Test 1 exhibits the highest mass and hence density. In relation to lowest water share, this correlation is consistent with the trend presented in Fig. 5.16.

The moisture content is also a key factor in levels of volumetric shrinkage achieved by drying. The spheres examined in Test 1, Test 2 and Test 3 lost 7.7%, 18.3% and 40.7% of their initial volume, respectively. In objects abundant in water, the volumetric ratio of internal pores and crevices is high. For they are subject to collapsing during dewatering, the potential of shrinkage under these circumstances is also significant.

5.4.4 Sensitivity analysis of physical properties of lignite on the drying parameters

The individual features of coal particles discussed in section 5.4.3 may strongly impact the observed drying behavior and thus blur the conclusions one can draw from the analysis of superheated steam drying charts. For that reason, a sensitivity analysis is required with reference to the physical properties of lignite. On the assumption of constant drying rate and invariable volume in the initial period of drying, such analysis was performed for CDRP. The formula for drying rate may be derived from the equations (B.3) and (B.4) in Appendix B and expressed as:

$$\left(-\frac{dX}{dt}\right)_{CDRP} = \frac{6h(T_a - T_1)}{L\rho_b} \frac{1}{d} \tag{5.1}$$

where ρ_b [kg m^{-3}] is a dry bulk density, expressed as a ratio of dry coal mass and initial volume of the sample:

$$\rho_b = \frac{m_c}{V^0} \tag{5.2}$$

To bind the dry bulk density with initial water share, one needs to express the latter as:

$$WS^0 = \frac{V_w^0 \rho_w}{V_w^0 \rho_w + V_c \rho_c} = \frac{1}{\frac{V_c}{V_w^0}\frac{\rho_c}{\rho_w} + 1} \tag{5.3}$$

where ρ_w equals 1000 kg m^{-3}. Equation (5.2) can be formulated in regard to (5.3) as:

$$\rho_b = \frac{\rho_c}{\frac{V_w^0}{V_c} + 1} = \frac{\rho_c}{\frac{\rho_c}{\rho_w}\frac{WS^0}{1 - WS^0} + 1} \tag{5.4}$$

In Fig. 5.18, the correlation of the initial water share and drying rate is presented for 10 mm samples of each lignite batch dried in superheated steam of 170 ^{o}C. The curves represent theoretical correlations between density of dry matter and the rate of

drying in accordance with the model in Eq. (5.1). The concentration of markers related to Belchatow lignite (B2013, B1, B2, B3) is contrasted with dispersion of Turow data points (T1, T2, T3). That fact arises from the lower contamination and more homogenous structure within Belchatow coal. However, the empirical data markers fit the general dependence obtained by calculation.

Figures 5.19 and 5.20 illustrate the correlation between dry bulk density and drying rate achieved for objects of different diameter and various drying temperature, respectively. The good agreement between theoretical and experimental results proves the validity of the model equation and confirms it may be applied for explanation of the physical properties of lignite applied for superheated steam drying. The wide dispersion of dry bulk density of Turow lignite is even more explicit and opposed to compact tendency evinced by the objects prepared using Belchatow coal.
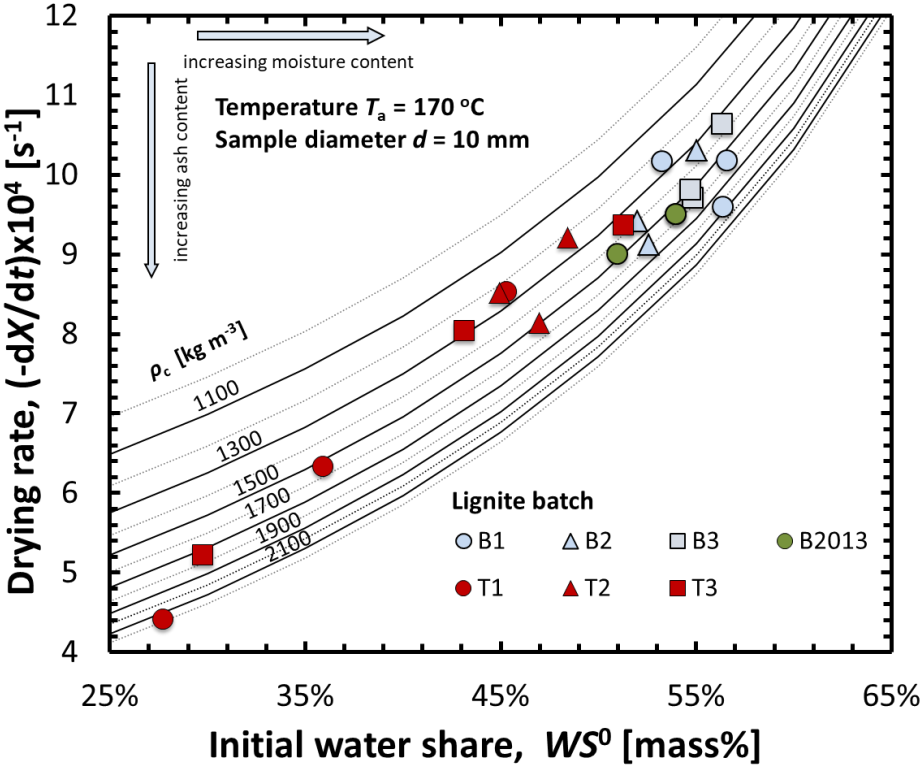
Figure 5.18 Impact of initial water share and density of lignite on the drying rate
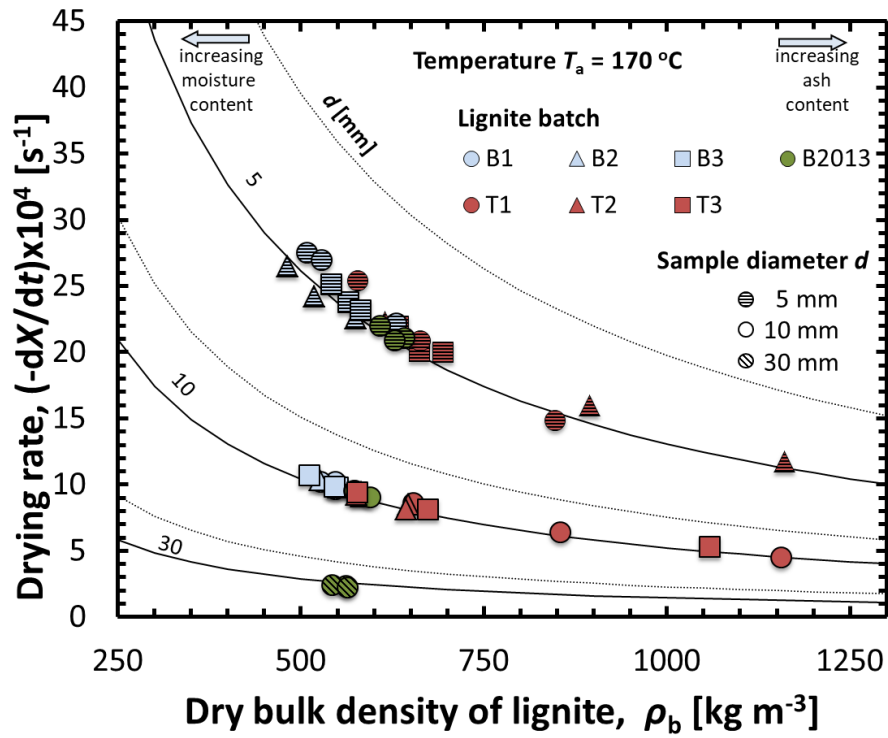
Figure 5.19 Impact of dry bulk density of lignite and particle size on the drying rate
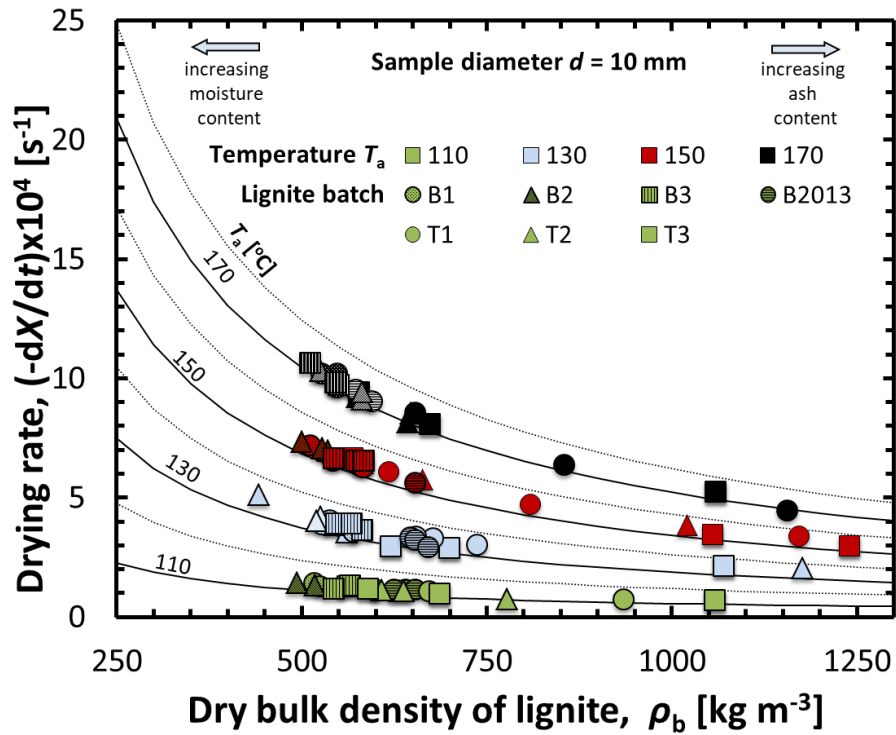
Figure 5.20 Impact of dry bulk density and steam temperature on the drying rate

5.4.5 Effect of geological structure on residual moisture content

The equilibrium moisture content, understood as amount of residual water remaining after drying at a certain temperature is a property of a material and drying environment. It is related to isobar sorption curve, which is a function of relative vapor pressure [15]. The increase in the temperature of the superheated steam is connected with decline of the relative humidity over the surface exposed to drying, hence, more water can be absorbed by the drying medium. Klutz et al. claimed that lignite cannot be "overdried" in the superheated steam, because once the equilibrium moisture content is reached, it cannot be further decreased [94].

The equilibrium moisture content was investigated for samples of Belchatow and Turow lignite, relying on the sample mass after superheated steam drying, prior to removal of residual water in nitrogen atmosphere. In case of the latter coal, the samples of low ash contamination, assumed on the basis of initial water share above a threshold value of 36%, were taken into consideration.

In order to approximate the temperature dependence of equilibrium moisture at certain conditions, one needs to adapt a general model represented by the class of functions. Tang and Cenkowski [95], relying on experience in investigating the equilibrium moisture content for various materials, proposed the following formula:

$$X_{eq} = k_1 \times \exp\left[k_2 \left(T - 100 \right)^{k_3} \right] \tag{5.5}$$

where parameters k_1, k_2 and k_3 can be determined using the experimental data. Though they claimed that Eq. (5.5) cannot be used to describe behavior of brown coals, as they exhibit enhanced moisture absorption capacity below 140 $^{\circ}$C [95], the formula was found to fit the experimental results for both categories of lignite above the temperature of 110 $^{\circ}$C.

The exact empirical equation for the coal from Belchatow mine is formulated as:

$$X_{eq} = 4.77 \times \exp\left[-2.36(T-100)^{0.179}\right] \tag{5.6}$$

In the case of T1, T2 and T3 coals, the model can be expressed in the following manner:

$$X_{eq} = 44.79 \times \exp\left[-4.41(T-100)^{0.127}\right] \tag{5.7}$$

Empirically derived equations (5.6) and (5.7) were applied in the numerical model of drying for batches of different origin. The results are presented in section 7.5. Note that the function of equilibrium moisture content below 110 ^{o}C was adapted from [73] as:

$$X_{eq} = 0.706/(T-98.6) + 6.23 \times 10^{-3} \tag{5.8}$$

In Fig. 5.21 the averaged experimental values of residual water for Belchatow and Turow lignite are presented together with the curves representing the model formulas (5.6) and (5.7). As can be seen, due to generally lower moisture content related to lower porosity of structure, Turow coal can store less water than Belchatow in an equilibrium state. For comparison, the results of experimental research on equilibrium moisture content of different materials were presented, including lignite [73,96], spent grains [95], ceramic spheres [97], wood chips [98] and paper pulp [99]. According to the experimental data, lignite exhibits considerably higher equilibrium moisture content at certain temperatures than other compared materials. It is related to developed internal surface of pores, where vast amount of moisture can be stored. At the opposite end of the spectrum ceramic spheres can be found as a material of non-capillary porous structure which can store barely any moisture at the equilibrium state.
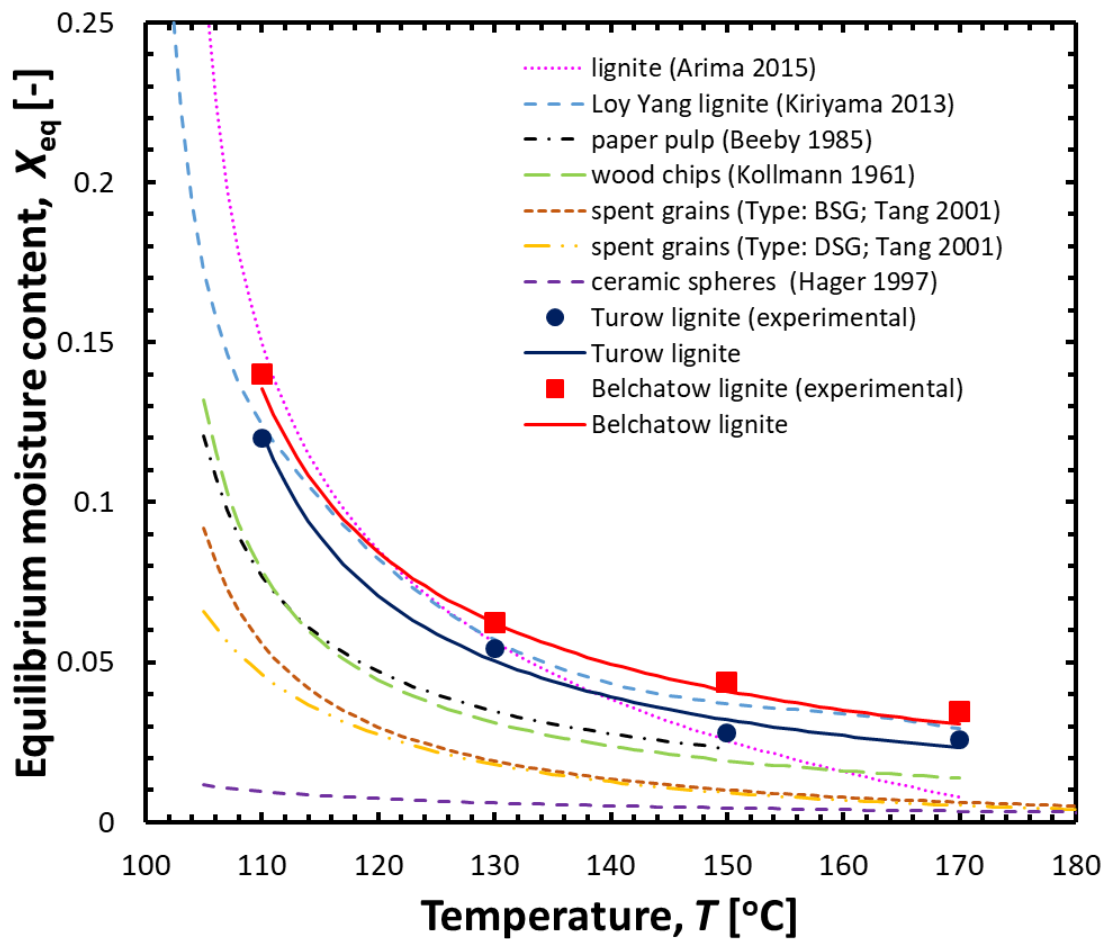
Figure 5.21 Comparison of equilibrium moisture content for Belchatow and Turow lignite with different lignite types [73,96] and other materials [95,97–99].

It is expected that the structural differences of lithotypes may impact the absorption capacity of lignite. Thus, further studies concerning size and distribution of pores are desirable to assess the relation between residual moisture and nature of lignite.

More details on dependencies between individual properties of Belchatow and Turow lignite can be found in [88,100,101]. The studies discuss the applicability of abovementioned coals not only in terms of superheated steam drying, but also regarding innovative technologies of energy production such as integrated gasification combined cycle (IGCC).

CHAPTER 6

Mathematical model of lignite drying in superheated steam

6.1 Physical model

The physical model of drying is represented by a sphere, that comprises three phases of coal. Each of them is characterized with different thermophysical properties: dry coal matter, free water and bound water.

Dry coal matter is a mixture of solid immobile substances: primarily carbon, carbohydrates and ash. Those lignite ingredients are not subject to evaporation. The drying temperature, as mentioned in the experimental section was limited in order to preclude volatilization and decomposition of chemical structure. For those two reasons, the total mass of dry coal does not vary through the drying process.

The total amount of water within coal is divided according to the mechanism of evaporation. Free water is assumed to evaporate at the saturation temperature, which is 100 $^{\rm o}$C under atmospheric pressure. Meanwhile, bound water, which represents the moisture kept tightly within the coal structure, turns to steam above 100 $^{\rm o}$C.

The model was constructed on the assumption that the object is a perfect sphere of isotropic properties. The parameters related to dry coal matter, i.e. density $\rho_{\rm c}$, specific heat $c_{\rm c}$ or thermal conductivity $\lambda_{\rm c}$, are temperature-independent, and thus remain invariable during drying process. On the contrary, analogical properties of water exhibit significant dependence on temperature. For that reason, empirical formulas for those

85

quantities, valid within process temperature range, were applied. What is more, evaporation and diffusion alter the moisture content in lignite interior (along the radius), what impacts the resultant values of particular properties. Coal in drying process is also subject to shrinking, what changes its geometry, affecting heat and mass transfer.

The essential material parameters applicable in the model are given in Tab. 6.1.

Table 6.1 Selected properties of coal applied in the simulation
(lignite types: B2013 – Belchatow, Y – Yallourn, LY – Loy Yang)

parameter	lignite	value	source
initial moisture content X^0	B2013	1.05	experimental average, equal to WS=51.25%
density (dry coal) ρ_c	B2013	1536 kg m^{-3}	experimental average
specific heat (dry coal) c_c	B2013	1246 J kg^{-1} K^{-1}	commissioned research
thermal conductivity (dry coal) λ_c	B2013	0.33 W m^{-1} K^{-1}	auxiliary in-house tests (Appendix A)
heat transfer coefficient h from steam of temperature T_a[^{o}C] to sphere of diameter d[m]	B2013	$(2.38\times10^{-4}/d\text{-}9.17\times10^{-2})\times T_a$- $-(2.99\times10^{-2}/d\text{-}5.43)$ W m^{-2} ^{o}C^{-1}	thermodynamically derived in Appendix B
equilibrium moisture content X_{eq}	Y	$0.71/(T_n\text{-}98.58)+0.006$	in range 100-114.1 ^{o}C, adapted from [73]
	B2013	$4.77\times\exp[2.36\times(T_n\text{-}100)^{0.18}]$	in range 114.1-170 ^{o}C, experimental data
enthalpy change of bound water evaporation ΔH	Y	$2.93\times10^6\text{-}6.76\times10^5\times$ $\times\exp[-0.08\times(T_n\text{-}100)]$ J kg^{-1}	adapted from [73]
linear shrinkage $1\text{-}l/l_{ini}$	LY	$-0.27\times(V_w/V^0_w)^3+0.66\times$ $\times(V_w/V^0_w)^2\text{-}0.55\times(V_w/V^0_w)+0.16$	adapted from [73]
diffusion coefficient of free water D	LY	3.0×10^{-9} m s^{-2}	adapted from [73]

Certain chemical and physical properties on Belchatow coal, have not been reported in the literature. Thus, for the purpose of simulation, appropriate parameters were adapted from other lignite types. The data marked as B2013 in the table relate to the specific lignite experimental batch from Belchatow mine. They are either acquired from auxiliary studies, calculated on experimental data or received from commissioned research.

6.2 Mathematical formulation

6.2.1 Heat transfer

The above-mentioned isotropy of the properties allowed for the application of one-dimensional model of transient heat transfer, along the sample radius. The temperature field under those conditions, is described by Eq. (6.1):

$$c(r,t)\rho(r,t)\frac{\partial T(r,t)}{\partial t} = \nabla \cdot \left(\lambda(r,t)\nabla T \right) - \dot{q}_V \tag{6.1}$$

where $\dot{q}_V$ represents volumetric heat sink (negative heat source) [W m^{-3}] which reflects heat loss by evaporation of free and bound water (sections 6.3.3.3 and 6.3.3.4). The first contribution of the right-hand side of Eq. (6.8) may also be presented as:

$$\nabla \cdot \left(\lambda(r,t)\nabla T \right) = \frac{1}{r^2}\frac{\partial}{\partial r}\left[r^2\lambda(r,t)\frac{\partial T(r,t)}{\partial r} \right] \tag{6.2}$$

The initial condition is equal to:

$$T(r,t)\big|_{t=0} = T^0 = 40\ °C \tag{6.3}$$

The boundary conditions represent the transfer of heat from the steam to the surface of a sample and the symmetry condition, respectively:

$$-\lambda \frac{\partial T(r,t)\big|_{r=r_1}}{\partial r} = h(r_1,T_a)\left[T_a - T_1(t)\right] \tag{6.4}$$

$$\frac{\partial T(r,t)\big|_{r=0}}{\partial r} = 0 \tag{6.5}$$

Heat transfer coefficient h in Eq. (6.4) is a function of steam temperature (the surrounding space around the sample is fulfilled with steam) and sample diameter. It was derived in Appendix B with consideration for heat transfer mechanisms of convection and radiation. The obtained empirical formula is shown in Tab. 6.1.

6.2.2 Mass transfer

As mentioned in section 6.1, the mass transfer phenomena during drying are limited to water. Thus, the general transport equation governing the water transfer and evaporation in coal sample is formulated by Eq. (6.6).

$$\frac{\partial \rho_{b,w}(r,t)}{\partial t} = \nabla \cdot \left(-D\nabla \rho_{b,w}(r,t)\right) - \dot{\rho}_{b,w,evap} \tag{6.6}$$

where $\rho_{b,w}$ is a bulk density or mass concentration of water within lignite [kg m^{-3}] and D stands for diffusion coefficient of free water [m^2 s^{-1}]. The first contribution on the right hand side is a diffusion term, while the second expresses the evaporative flux of water concentration.

Considering the formula (6.7) the initial condition can be expressed by Eq. (6.8):

$$\rho_{b,w} = \frac{m_w}{V}\frac{m_c}{m_c} = \frac{m_w}{m_c}\frac{m_c}{V} = X\rho_c \tag{6.7}$$

$$\rho_{b,w}(r,t)\big|_{t=0} = X^0\rho_c = 1.05 \times 1536 = 1612.8 \, \text{kg m}^{-3} \tag{6.8}$$

The values of initial moisture content X^0 and dry coal density ρ_c are taken from Tab. 6.1.

6.3 Numerical model

6.3.1 Discretization scheme

6.3.1.1 Heat transfer

In order to obtain algebraic formulas from differential equations, the control-volume method was used [102,103]. Assume element n within a sphere, which volume is V_n and area equals to A_n. Eq. (6.1) can be integrated on this element as:

$$\int_{V_n} c(r,t)\rho(r,t)\frac{\partial T(r,t)}{\partial t}dV = \int_{V_n} \nabla\cdot\left(\lambda(r,t)\nabla T\right)dV - \int_{V_n} \dot{q}_V dV \qquad (6.9)$$

The term related to conduction in Eq. (6.8), over the application of Gauss integral theorem, might be expressed as:

$$\int_{V_n} \nabla\cdot\left(\lambda(r,t)\nabla T\right)dV = \int_{A_n} \mathbf{n}\cdot\left(\lambda(r,t)\nabla T\right)dA \qquad (6.10)$$

where $\mathbf{n}$ is a normal vector.

Thermal conductivity λ_n, density ρ_n, and specific heat c_n over the entire element n are assumed to be constant at a certain time instance. Thus, apparent values dependent of volume fraction of coal and steam are used in the calculation domains in each time step. On that assumption, Eq. (6.9) and (6.10) might be transformed to:

$$\int_{V_n} c(r,t)\rho(r,t)\frac{\partial T(r,t)}{\partial t}dV = V_n\rho_n c_n \frac{\partial T_n}{\partial t} \qquad (6.11)$$

and:

$$\int_{A_n} \mathbf{n}\cdot\left(\lambda(r,t)\nabla T\right)dA = \sum\left(\dot{Q}_{in,n} - \dot{Q}_{out,n}\right) \qquad (6.12)$$

where the right side of Eq.(6.12) represent heat fluxes conducted into and out of layer n.

Transformation of the integral in Eq. (6.12) and separation of its variables produce a formula for the heat input by conduction to the layer n:

$$\frac{\dot{Q}_{in,n}}{4\pi} \int_{r_{n-1}}^{r_n} \frac{\partial r}{r^2} = -\lambda \int_{T_{n-1}}^{T_n} \partial T \qquad (6.13)$$

Assuming $T(r_n) = T_n$ and $T(r_{n-1}) = T_{n-1}$, the integration on the interval $[r_{n-1}, r_n]$ is performed. The outcome, with regard to thermal resistance of a spherical element, is equal to:

$$\dot{Q}_{in,n} = \frac{T_{n-1} - T_n}{R_{n,n-1}} = \frac{T_{n-1} - T_n}{\dfrac{r_n - r_{n-1}}{4\pi r_{n-1} r_n \lambda_{n,n-1}}} \qquad (6.14)$$

In the case of conduction between two adjacent layers of different thermal conductivity values, the heat resistance $R_{n,n-1}$ between their central points is equal to sum of heat resistances along the segment b_n and b_{n-1}. Introduction of interface radius $r_{int,n,n-1}$ between layers n and $n-1$ is required:

$$\dot{Q}_{in,n} = \frac{T_{n-1} - T_n}{R_{n-1} + R_n} = \frac{T_{n-1} - T_n}{\dfrac{r_{int,n,n-1} - r_{n-1}}{4\pi r_{int,n,n-1} r_{n-1} \lambda_{n-1}} + \dfrac{r_n - r_{int,n,n-1}}{4\pi r_n r_{int,n,n-1} \lambda_n}} = \frac{4\pi r_{int,n,n-1}\left(T_{n-1} - T_n\right)}{\dfrac{b_{n-1}}{r_{n-1}\lambda_{n-1}} + \dfrac{b_n}{r_n \lambda_n}} \qquad (6.15)$$

The heat output from layer n is equal to heat input to layer $n+1$:

$$\dot{Q}_{out,n} = \frac{4\pi r_{int,n+1,n}\left(T_n - T_{n+1}\right)}{\dfrac{b_n}{r_n \lambda_n} + \dfrac{b_{n+1}}{r_{n+1} \lambda_{n+1}}} \qquad (6.16)$$

6.3.1.2 Mass transfer

According to the scheme of the discretization of heat transfer equations introduced in the previous section, Eq. (6.6) can be integrated over the volume of element n.

$$\int_{V_n} \frac{\partial \rho_{b,w}(r,t)}{\partial t} dV = \int_{V_n} \frac{\partial}{\partial r}\left(-D\frac{\partial \rho_{b,w}(r,t)}{\partial r}\right) dV - \int_{V_n} \dot{\rho}_{b,w,evap} dV \tag{6.17}$$

What is equal to:

$$\frac{\partial m_w(r,t)}{\partial t} = \int_{A_n} \mathbf{n} \cdot \left(-D\frac{\partial \rho_{b,w}(r,t)}{\partial r}\right) dA - \dot{m}_{w,evap} \tag{6.18}$$

The first contribution on the right hand side represent the Fick's law and may be expressed as sum of diffusion fluxes into and out of the layer n:

$$\int_{A_n} \mathbf{n} \cdot \left(-D\frac{\partial \rho_{b,w}(r,t)}{\partial r}\right) dA = \sum \left(\dot{m}_{b,w,in,n} - \dot{m}_{b,w,out,n}\right) \tag{6.19}$$

The direction of water transfer within lignite is opposite to the direction of heat transfer. The evaporation of water proceeds from the surface to the core of the sphere, enhancing the water concentration gradient that induces diffusion. The diffusion coefficient of free water, D, which value is given in Table 6.1, is assumed constant over the entire volume and drying process [73]. Integrating LHS of Eq. (6.19) from r_{n-1} to r_n with the assumption of $\rho_{b,w}(r_n) = \rho_{b,w,n}$ and $\rho_{b,w}(r_{n-1}) = \rho_{b,w,n-1}$, the water diffused out of the layer n equals:

$$\dot{m}_{out,n} = D\frac{4\pi r_{n-1} r_n \left(\rho_{b,w,n} - \rho_{b,w,n-1}\right)}{r_{n-1} - r_n} \tag{6.20}$$

Substitution of water concentration according to Eq. (6.7) produces:

$$\dot{m}_{\text{out},n} = D \frac{4\pi r_{n-1} r_n \rho_{\text{b,c},n} \left(X_n - X_{n-1} \right)}{r_{n-1} - r_n}$$

(6.21)

Analogically, the diffusion input to layer n is equal to the output from layer $n+1$, thus:

$$\dot{m}_{\text{in},n} = D \frac{4\pi r_n r_{n+1} \rho_{\text{b,c},n} \left(X_{n+1} - X_n \right)}{r_n - r_{n+1}}$$

(6.22)

6.3.2 Particular discretization assumptions

The following assumptions of the discretization supplement those introduced in the previous sections of this chapter:

- The elements (layers) were distributed uniformly along the radius, establishing a series of concentric spherical shells characterized with initial width equal to $2b$. In the case of extreme elements, number 1 and N+1, the initial width was equal to b in order to avoid overlapping of control-volume balances (Fig. 6.1).

- The number of model segmentation was set equal to 50, what provides the acceptable accuracy of numerical prediction for each sample size taken into account in the present work. (Appendix C)

- Convergence of the simulation was judged with reference to values of two quantities observable in the experiment: weight and temperature. In the case of former, the sufficient condition was the stepwise decrease lesser than 0.01% of the dry coal mass, while the latter was assumed stable when the difference between the drying medium and center of the sphere became lower than 10^{-2} $^{\circ}$C.

92

- The explicit method of simulation was performed, therefore stability criterion was adapted with regard to a specific value of the time step width Δt:

$$\Delta t < \frac{(\Delta x)^2}{2\alpha} \qquad (6.23)$$

where α stands for thermal diffusivity [$m^2\ s^{-1}$]

The time step width Δt was adjusted to the conditions. By default, it was equal to 10^{-3} s. Nonetheless, to ensure stability, for samples smaller than 5 mm in diameter, its value was 10^{-4} s and for objects of diameter lesser than 1.5 mm, the time step width equaled 10^{-5} s.

- At the beginning of iteration $i+1$, the values of variables attained at the end of the previous iteration i are overwritten with the counter $i+1$. This does not concern the quantities, which symbols are preceded by Δ sign. Those quantities are representatives of the non-cumulative mass and heat flows between the layers and are calculated for each time instance repetitively. The general rule is also not applicable for material properties of water, e.g. specific heat or density, which are updated subsequently with regard to the current temperature of the layer. The graphical interpretation of the numerical simulation process is presented in Appendix F.
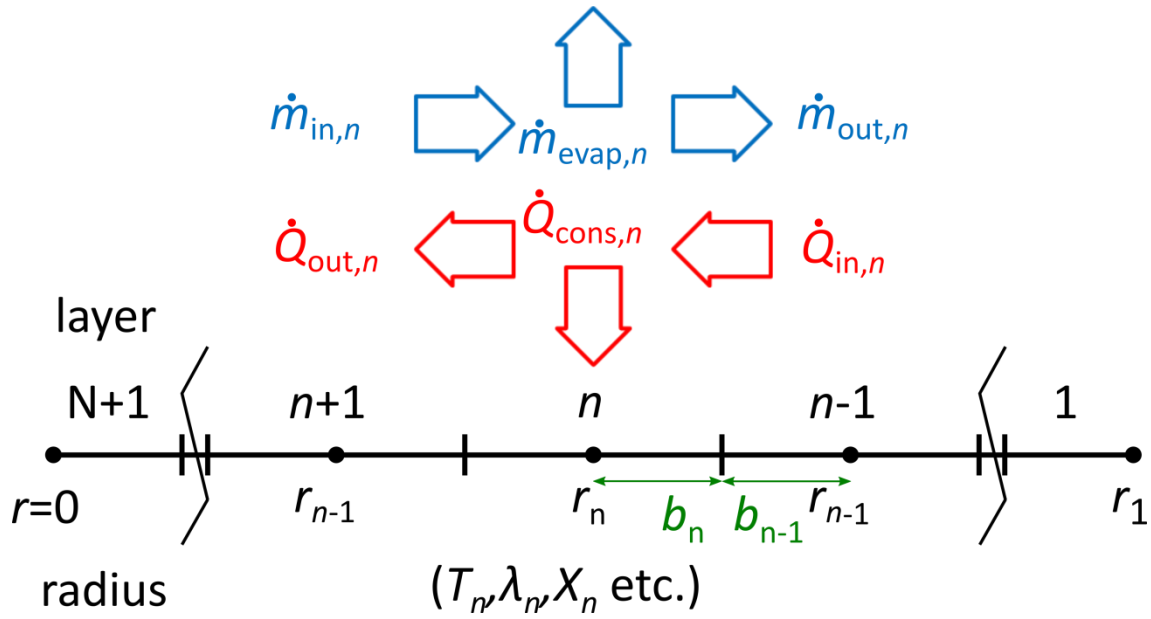
Figure 6.1 Distribution of elements within a lignite sphere

6.3.3 Specificity of particular drying stages

Throughout the process of superheated steam drying, the specificity of heat and mass transfer was subject to change, according to occurrence of water and temperature level as the most influential factors. The numerical model was prepared in accordance to the assumptions pointed out previously in this chapter. Its structural segmentation was designed with respect to varying modes of dewatering. Different sets of numerical equations are applicable to consecutive drying stages, as described in the following subsections. Still, the heat conduction between adjacent layers, followed the same pattern for all stages. The numerical formula, prepared basing on Eq. (6.15) is presented in Eq. (6.24).

$$\Delta Q_{n,\text{in}}^{i} = \frac{4\pi r_{n,n+1,\text{int}}^{i}}{b_{n-1}^{i}\big/\big(\lambda_{n-1}^{i} r_{n-1}^{i}\big) + b_{n}^{i}\big/\big(\lambda_{n}^{i} r_{n}^{i}\big)}\big(T_{n-1}^{i} - T_{n}^{i}\big)\Delta t \qquad (6.24)$$

6.3.3.1 Condensation of water on the surface

In the initial stage of drying, the temperature of the dried object is lower than

saturation temperature. For that reason, on the coal surface a condensation of water occurs. The entire heat input to the sample is determined by this phenomenon, what is expressed by Eq. (6.25):

$$\Delta Q_{1,\text{in}}^i = h_{\text{cond}} 4\pi \left(r_1^0\right)^2 \left(100 - T_1^i\right)\Delta t \tag{6.25}$$

The consumption of heat within the layer n at that time induces increase in the temperature of dry coal and internal moisture.

$$\Delta Q_{\text{cons},n}^i = \left(c_{\text{c}} m_{\text{c},n} + c_{\text{w},n}^i m_{\text{w},n}^i\right)\Delta T_n^i \tag{6.26}$$

6.3.3.2 Evaporation of water from the surface

When the temperature of the surface of the coal sample reaches 100 °C, the amount of heat transferred to the sample becomes proportional to the difference in temperature between the superheated steam and saturation temperature of water, what is reflected by Eq. (6.27).

$$\Delta Q_{1,\text{in}}^i = h 4\pi \left(r_1^i\right)^2 \left(T_{\text{a}} - 100\right)\Delta t \tag{6.27}$$

In this stage of drying, the water film formed by condensation and exudation, remained on the surface. This period, especially for larger samples, was characterized by a tendency of subsequent forming and falling of water droplets. It happened because the surface tension was outweighed by the gravitational force attracting the water hemisphere on the bottom part of the surface. The model of droplet formation was adapted from the other study [74].

6.3.3.3 Evaporation of free water

After the removal of water from the surface, the heat is driven to the object

according to the same mechanism. The value of the heat input, however, becomes proportional to the difference between the temperatures of steam and surface, the latter of which exceeds 100 $^{\circ}$C and gradually increases (Eq. (6.28)).

$$\Delta Q_{1,in}^{i} = h4\pi \left(r_{1}^{i} \right)^{2} \left(T_{a} - T_{1}^{i} \right) \Delta t \tag{6.28}$$

In terms of evaporation, water on the surface and free water inside the sample are subject to the same mechanism. The relation between heat stored within the layer n and the evaporated mass of water from this layer can be formulated as:

$$\Delta Q_{cons,n}^{i} = \Delta m_{evap,n}^{i} L \tag{6.29}$$

where L represents the latent heat of evaporation, equal to 2.256 MJ kg^{-1}.

As mentioned in section 6.3.1.2, due to evaporation of water, moisture content gradient occurs between the layers. The gradient induces water transport between the layers. The numerical representation of Eq. (6.22) describing the transfer mechanism of free water, is illustrated by Eq. (6.30).

$$\Delta m_{trans,in,n}^{i} = -D\rho_{c} 4\pi r_{n}^{i} r_{n+1}^{i} \frac{X_{n}^{i} - X_{n+1}^{i}}{b_{n}^{i} + b_{n+1}^{i}} \Delta t \tag{6.30}$$

6.3.3.4 Evaporation of bound water

As the temperature of a particular layer exceeds 100 $^{\circ}$C, the free water evaporation is signalized to be finished. The only remaining type of moisture in the coal sample at this time is bound water. It is tightly entwined within the structure of lignite, thus its removal requires greater input of heat than free water evaporation. The evaporation rate of bound water at a particular time instance is limited. For that reason, the surplus of heat input is allocated on raising the coal temperature. The simple

96

evaporation mechanism relying on constant latent heat is substituted by the manner utilizing enthalpy change of bound water evaporation ΔH. This approach applicable at that stage might be expressed as a function of temperature within the layer n. When bound water evaporation occurs, the heat consumption is determined by Eq. (6.31).

$$\Delta Q^i_{\text{cons},n} = \left[c_c m_{c,n} + c^i_{w,n} \left(m^i_{w,n} - \Delta m^i_{\text{evap},n} \right) \right] \Delta T^i_n + \Delta m^i_{\text{evap},n} \Delta H^i_n \qquad (6.31)$$

6.3.3.5 Change of sample size due to shrinkage

The decrease in moisture content to the level of around 0.6 [84] is accompanied by visible change in the particle size. Such a level of moisture content is typical for the period bound water is being evaporated from shallow parts of coal, when the core temperature is significantly above 100 $^{\circ}$C. Therefore, the dependency on moisture content was applied to formulate a shrinkage equation implemented to influence the sample diameter in the numerical simulation. The equation is presented in Table 6.1.

CHAPTER 7

Numerical analysis of lignite drying in superheated steam

7.1 Comparison of empirical and numerical results of single-particle drying

The outcome of the numerical simulation was juxtaposed with the experimental results presented in chapter 5. Identically, the results were presented as the time charts of the moisture content, drying rate and temperature profile. In the figures involving drying characteristics obtained both experimentally and numerically, the midpoint temperature was deliberately omitted for the sake of clarity. In the case of samples of 5, 10 and 30 mm, the surface and center temperature were included in the graphs, while for the smallest particles of 2.5 mm, only surface temperature was measured and therefore presented. Each simulation case was coupled with a single experimental attempt. Figures 7.1, 7.2, 7.3 and 7.4 illustrate characteristic drying curves for 2.5, 5, 10 and 30 mm lignite particles, respectively. The results contained in this section were presented in [104].
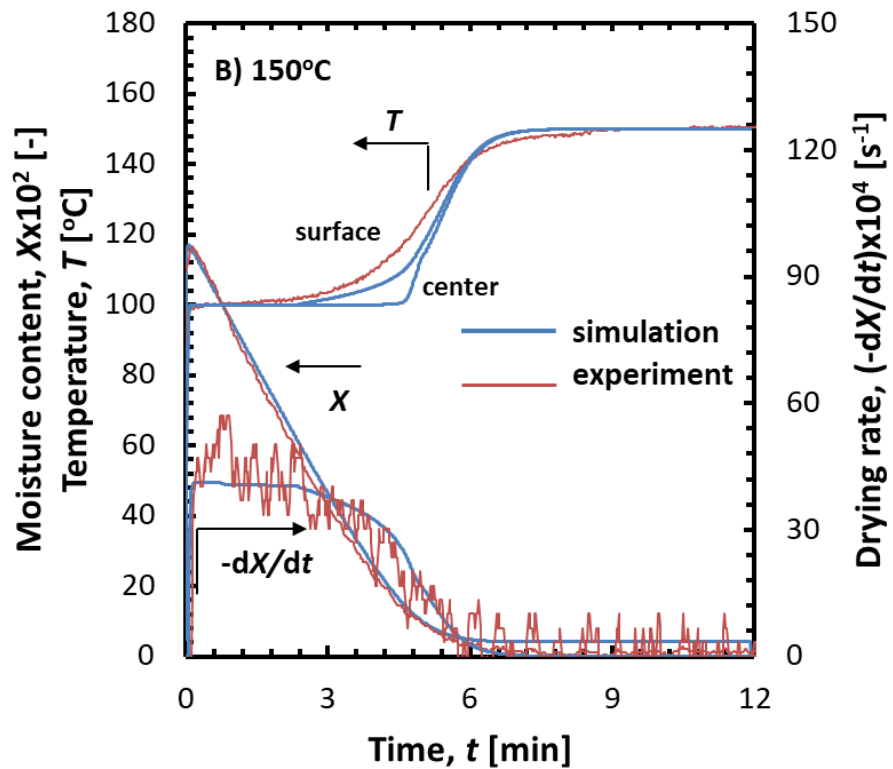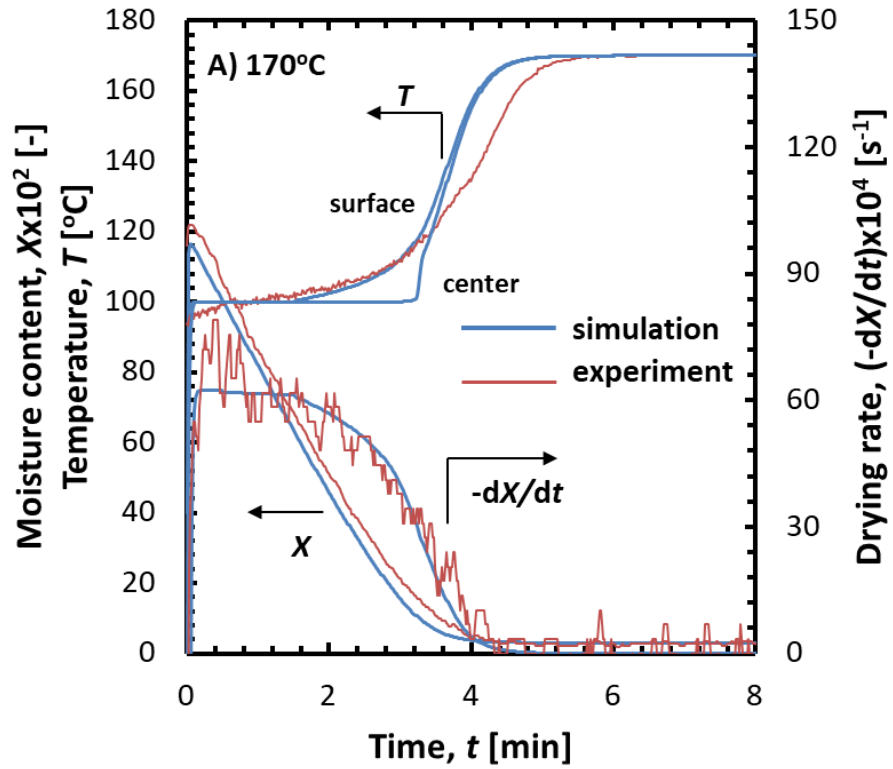
Figure 7.1.1 Comparison of experimentally and numerically obtained drying characteristics of 2.5 mm sample at test temperatures of A) 170 ^{o}C, B) 150 ^{o}C
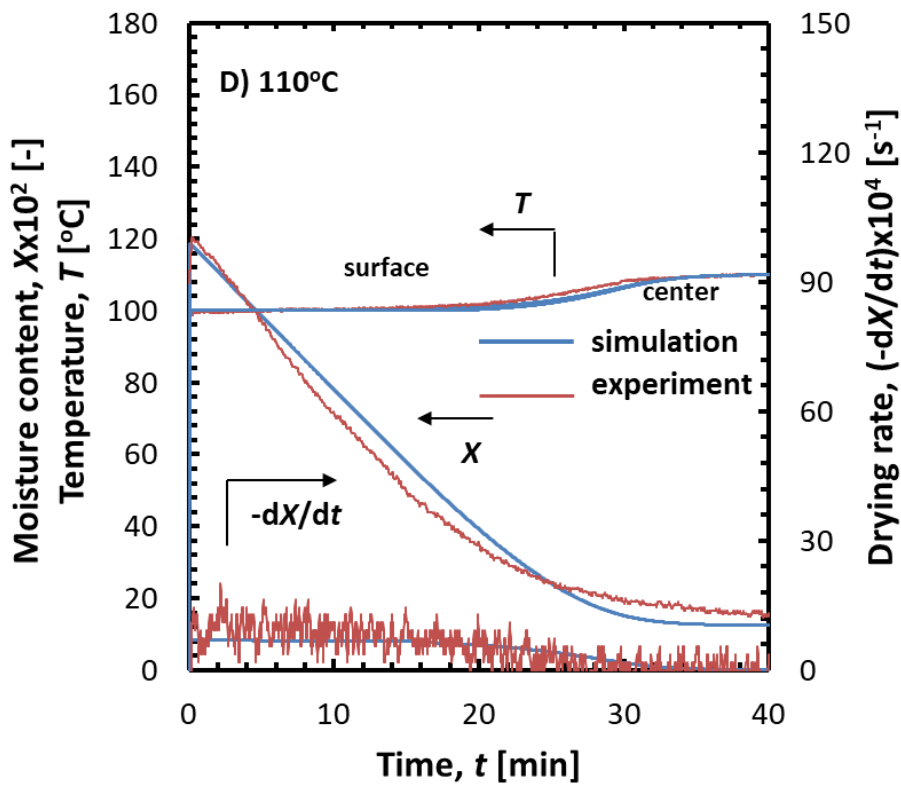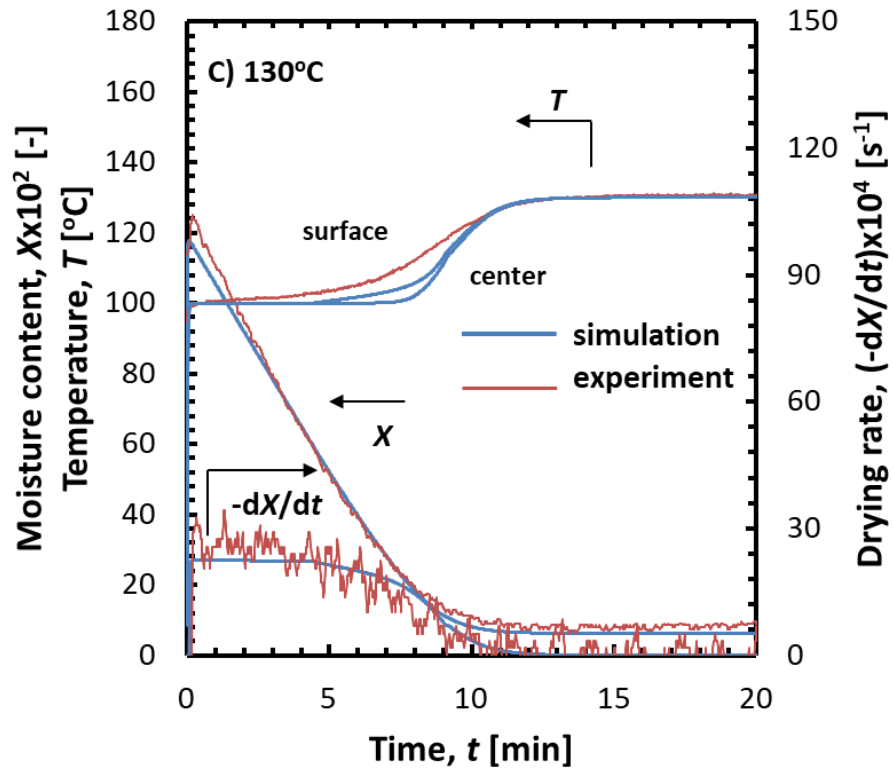
Figure 7.1.2 Comparison of experimentally and numerically obtained drying characteristics of 2.5 mm sample at test temperatures of C) 130 $^{\circ}$C, D) 110 $^{\circ}$C
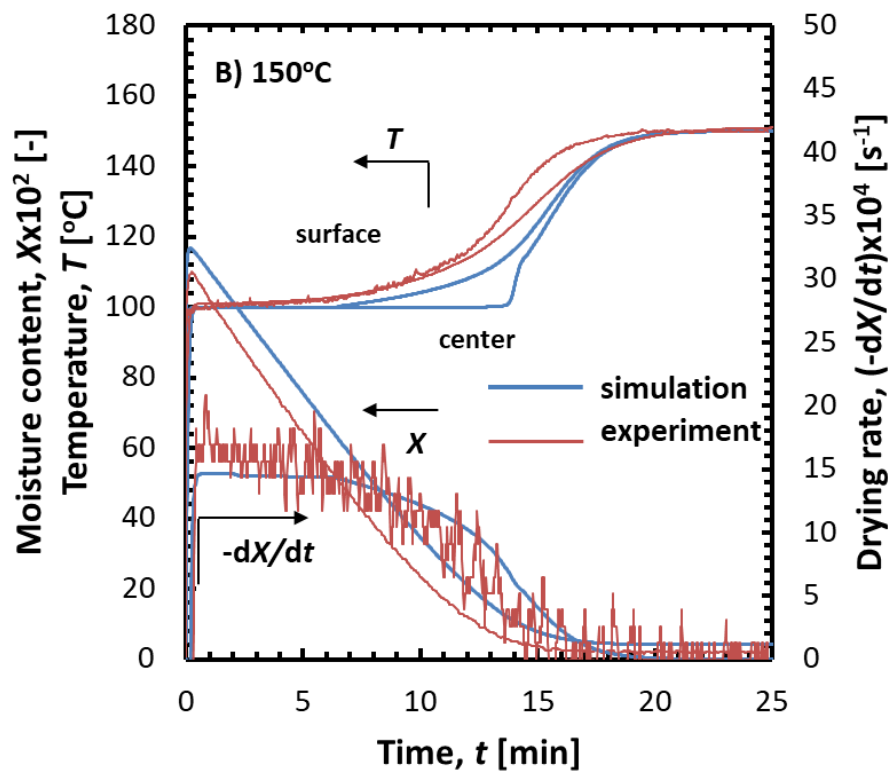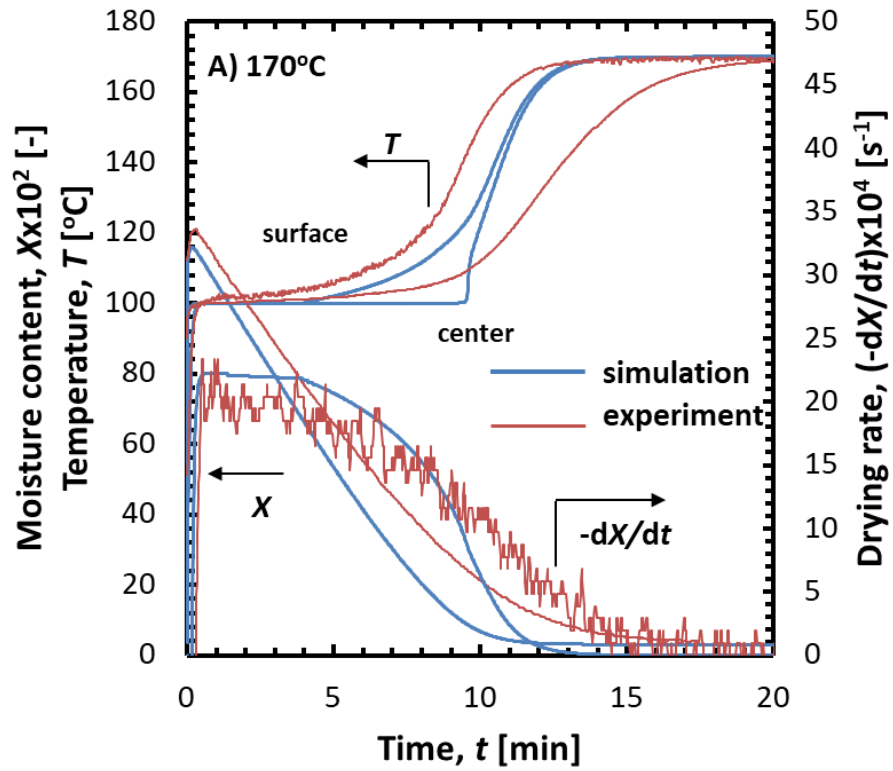
Figure 7.2.1 Comparison of experimentally and numerically obtained drying characteristics of 5 mm sample at test temperatures of A) 170 $^{\circ}$C, B) 150 $^{\circ}$C
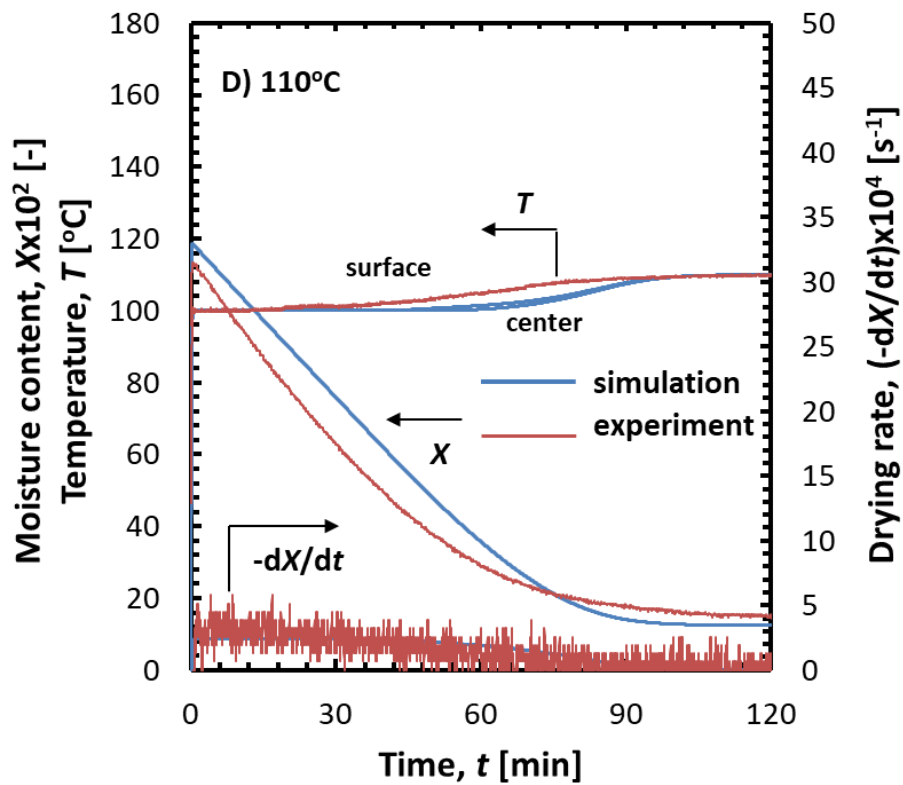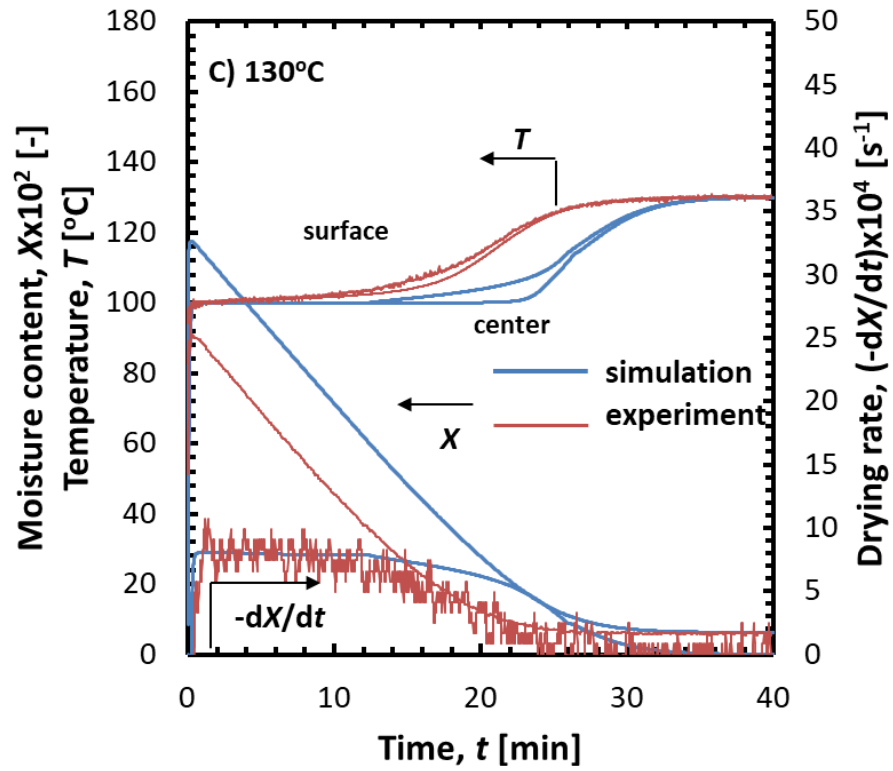
Figure 7.2.2 Comparison of experimentally and numerically obtained drying characteristics of 5 mm sample at test temperatures of C) 130 $^{\circ}$C, D) 110 $^{\circ}$C
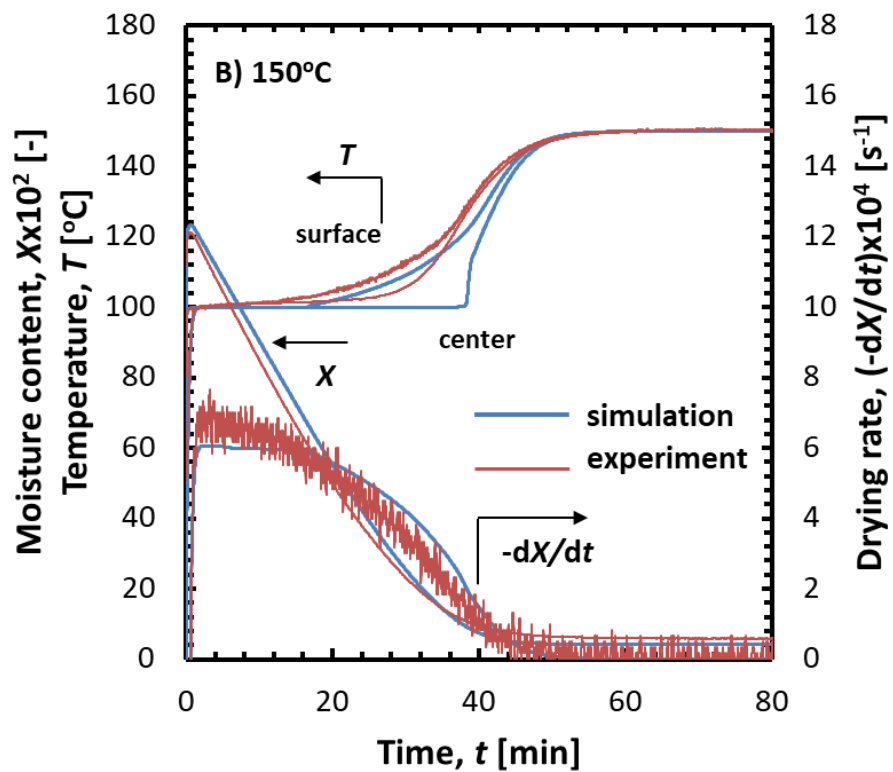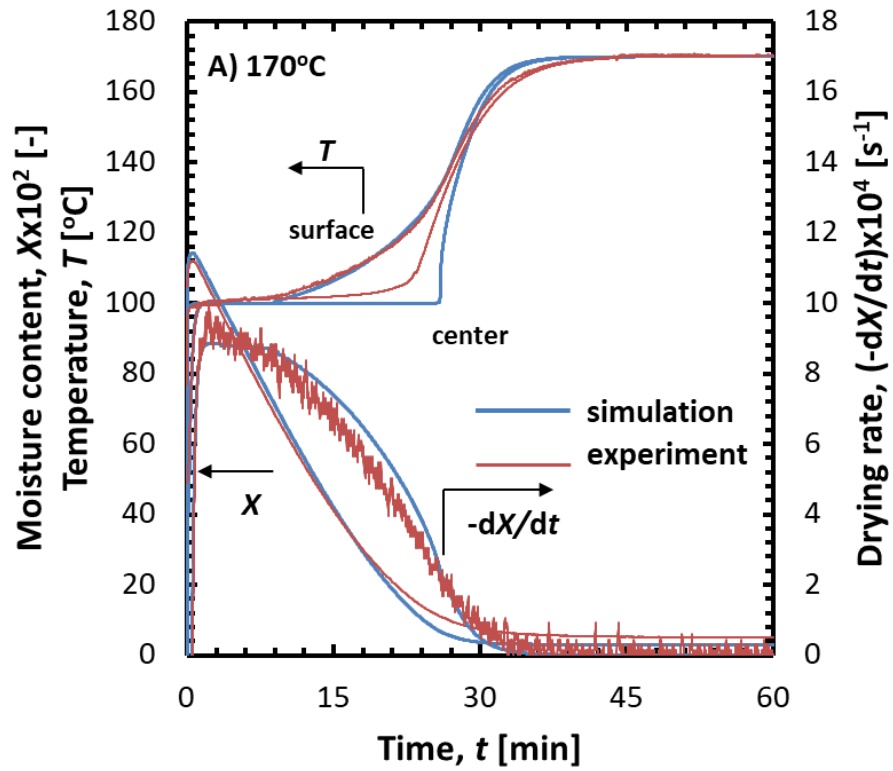
Figure 7.3.1 Comparison of experimentally and numerically obtained drying characteristics of 10 mm sample at test temperatures of A) 170 $^{\circ}$C, B) 150 $^{\circ}$C
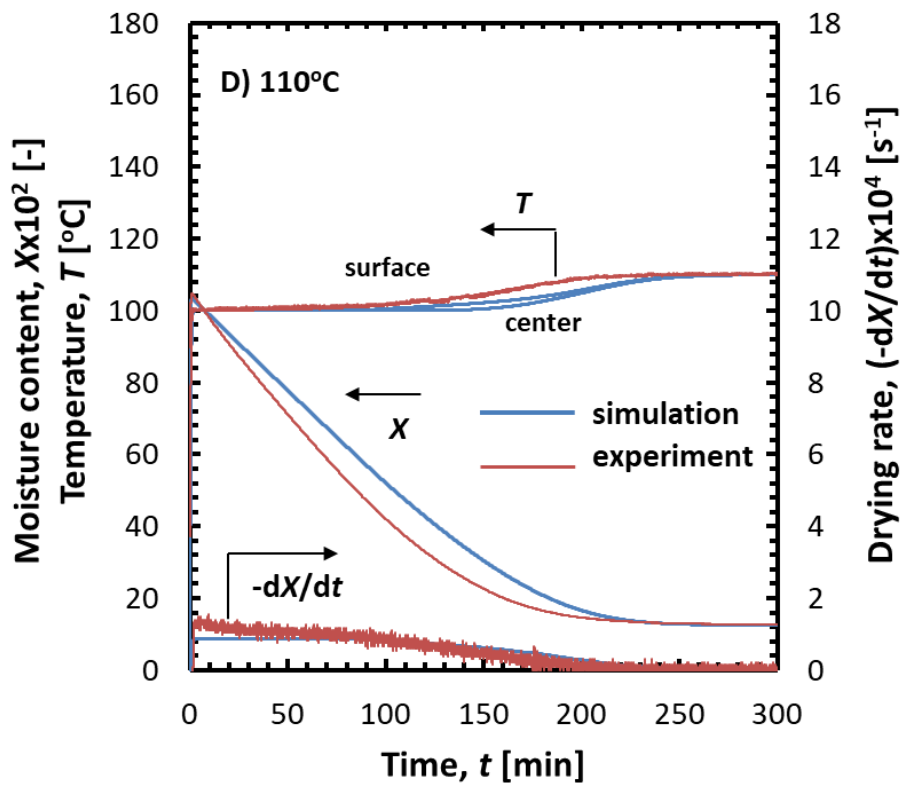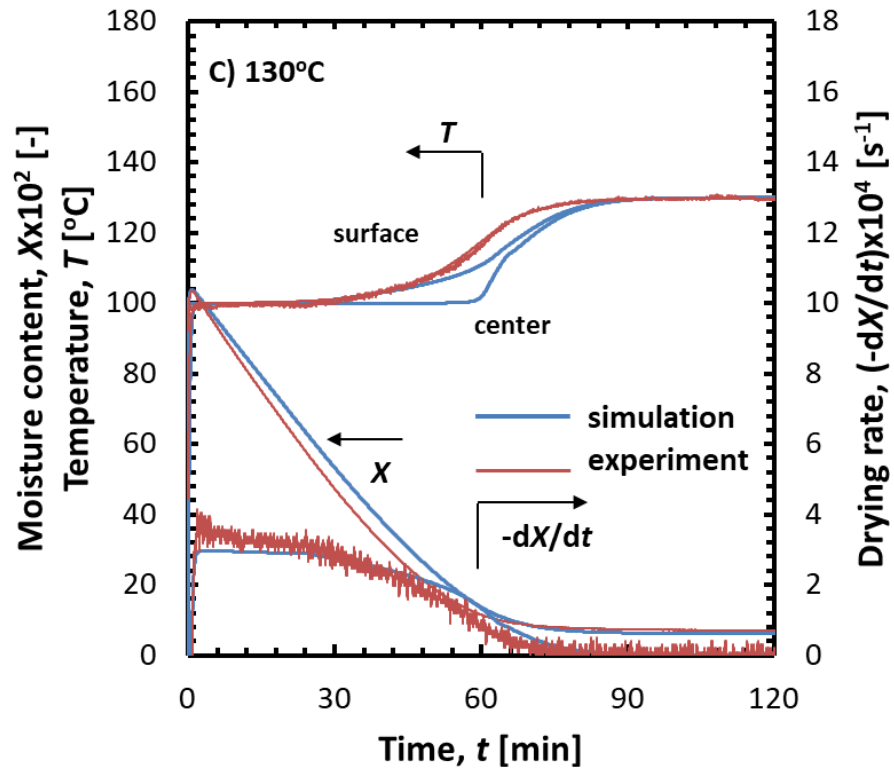
Figure 7.3.2 Comparison of experimentally and numerically obtained drying characteristics of 10 mm sample at test temperatures of C) 130 ^{o}C, D) 110 ^{o}C
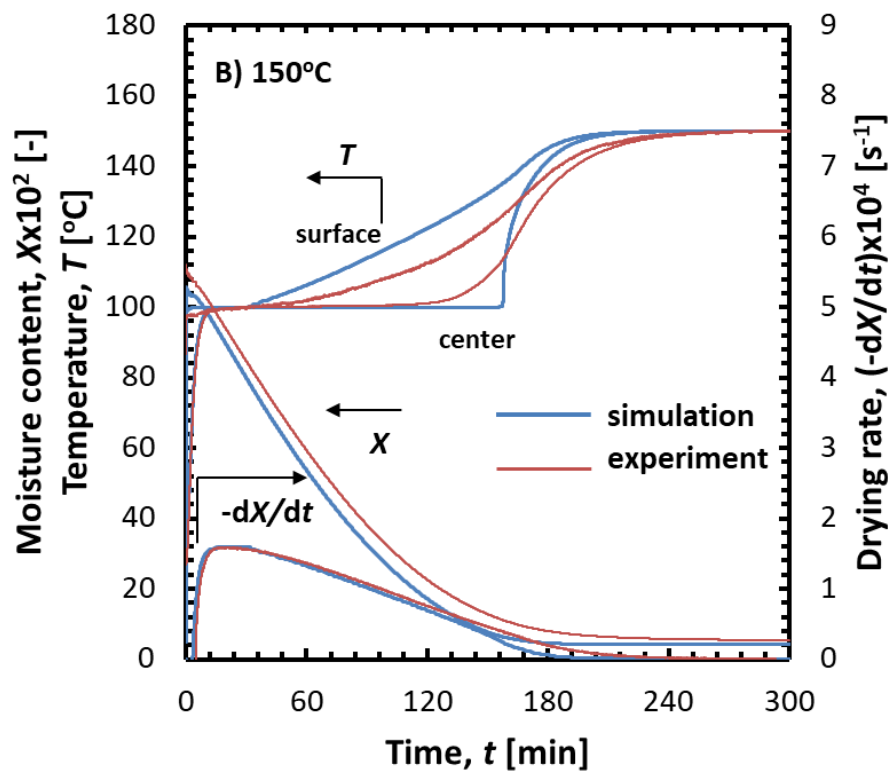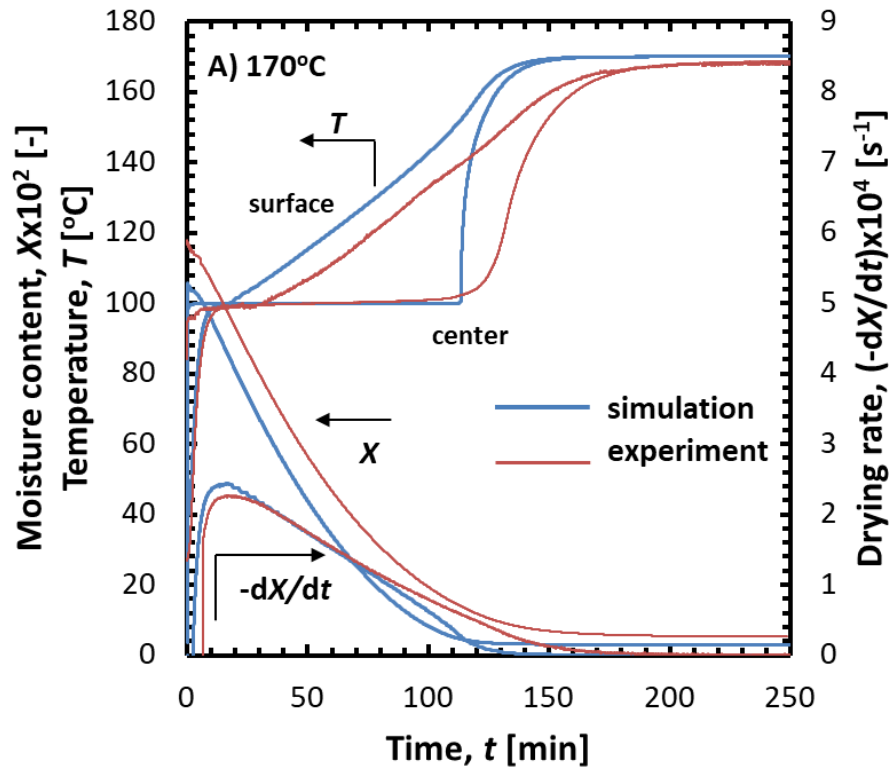
Figure 7.4.1 Comparison of experimentally and numerically obtained drying characteristics of 30 mm sample at test temperatures of A) 170 ^{o}C, B) 150 ^{o}C
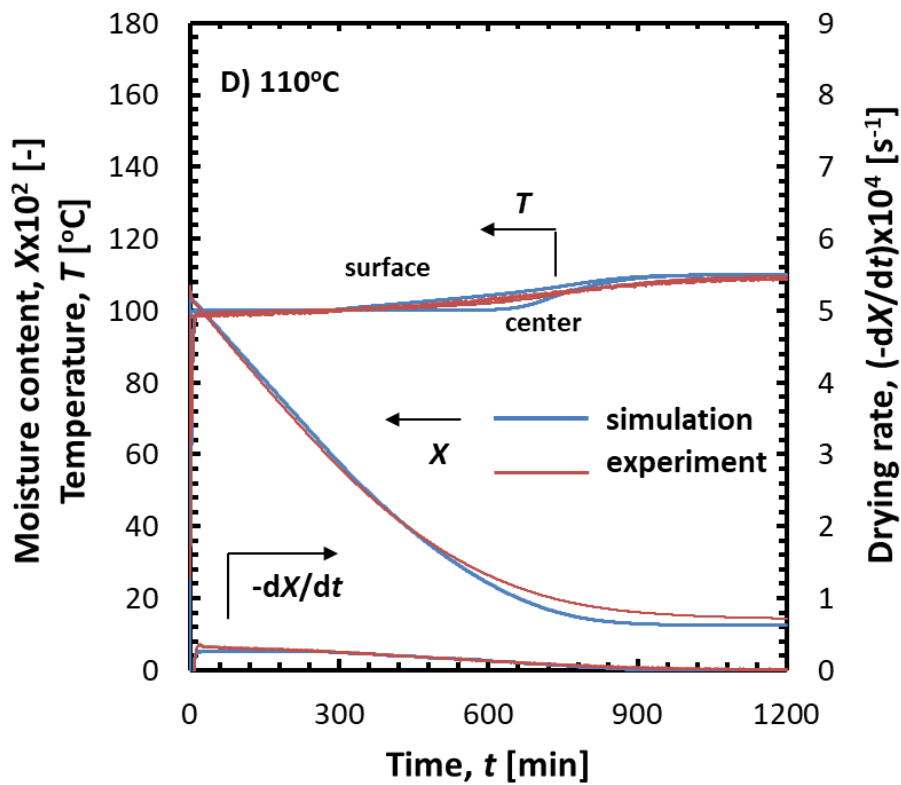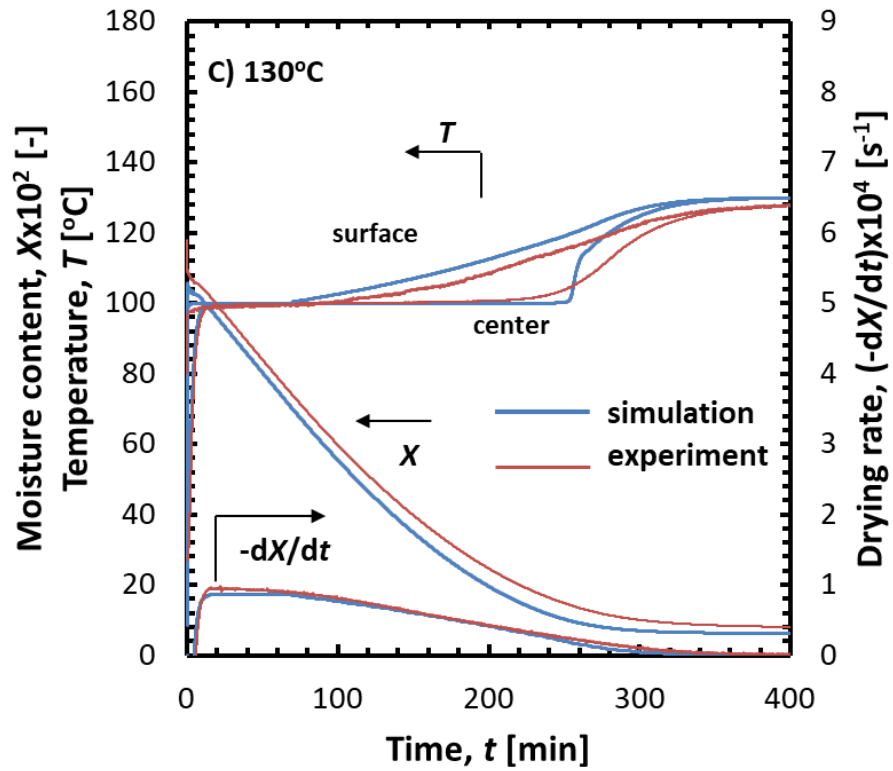
Figure 7.4.2 Comparison of experimentally and numerically obtained drying characteristics of 30 mm sample at test temperatures of C) 130 $^{\circ}$C, D) 110 $^{\circ}$C

In general, the simulated increase in lignite temperature, particularly the one indicating the center of the sphere, was more sharp and occurred later than in the empirical attempts. According to the adapted model, the temperature of particular layer could increase above 100 $^{\mathrm{o}}$C only if the free water has been completely removed from it. The inconsistence of calculated and directly achieved temperature profile might be attributed to the uniformity of the structure assumed in the simulation and its disorder enhanced by the actual processes of deformation and cracking. Those processes may influence the threshold between the free and the bound water, thus, diversifying the pace at which the moisture is diffused and evaporated within the different cross-section of the particle subject to experimental efforts.

7.2 Prediction of temperature dependence on the drying performance

The quantification of particular drying indicators, gathered in Tab. 7.1 was performed on the basis of another set of computations, within the same superheated steam temperature range, but applying the interval of 10 $^{\mathrm{o}}$C. The objective of such approach was to evaluate the impact of the drying medium temperature on the performance of superheated steam drying procedure.

Table 7.1 Indicators applied for drying performance evaluation

indicator	symbol	description
drying time	t_{dry}	time required for completion of drying
peak drying rate	$(-\mathrm{d}X/\mathrm{d}t)_{\mathrm{max}}$	highest level of the drying rate
duration of constant drying rate period	t_{CDRP}	period when the drying rate remains at a stable value
time of free water removal	t_{free}	instance when the center temperature exceeds 100 $^{\mathrm{o}}$C for the first time
peak temperature difference	$\Delta T_{1,51,\mathrm{max}}$	largest difference between the surface and center temperatures

The values of indicators obtained for particular temperatures of superheated steam are shown for samples of 30, 10, 5 and 2.5 mm in Tab. 7.2, 7.3, 7.4 and 7.5, respectively.

Table 7.2 Predicted values of drying indicators for 30 mm sample

T_a [°C]	t_{dry} [min]	t_{CDRP} [min]	$(-dX/dt)_{max}$ $\times 10^{-4}$ [s^{-1}]	t_{free} [min]	$\Delta T_{1,51,max}$ [°C]
170	193.3	9.4	2.44	110.7	51.7
160	225.6	12.7	2.00	133.0	43.1
150	271.9	17.3	1.58	148.3	34.7
140	342.7	30.6	1.22	180.9	26.6
130	460.7	54.3	0.92	224.6	18.9
120	695.0	107.7	0.55	298.3	11.4
110	1216.4	284.5	0.26	478.2	4.3

Table 7.3 Predicted values of drying indicators for 10 mm sample

T_a [°C]	t_{dry} [min]	t_{CDRP} [min]	$(-dX/dt)_{max}$ $\times 10^{-4}$ [s^{-1}]	t_{free} [min]	$\Delta T_{1,51,max}$ [°C]
170	46.4	7.1	8.89	24.5	32.3
160	54.9	9.5	7.31	27.9	26.2
150	67.2	13.2	5.83	32.7	20.6
140	85.9	18.6	4.45	39.4	15.3
130	117.7	28.1	3.18	49.9	9.7
120	180.7	47.3	2.02	70.2	5.0
110	328.8	106.0	0.96	129.8	1.8

Table 7.4 Predicted values of drying indicators for 5 mm sample

T_a [°C]	t_{dry} [min]	t_{CDRP} [min]	$(-dX/dt)_{max}$ $\times 10^{-4}$ [s^{-1}]	t_{free} [min]	$\Delta T_{1,51,max}$ [°C]
170	17.6	3.2	22.24	8.4	22.5
160	20.9	4.3	18.31	9.6	18.1
150	25.6	5.8	14.63	11.3	13.8
140	32.8	8.0	11.20	13.7	9.3
130	45.0	11.8	8.02	17.6	5.7
120	69.2	19.4	5.09	25.4	3.0
110	126.4	42.4	2.42	48.7	1.1

Table 7.5 Predicted values of drying indicators for 2.5 mm sample

T_a [^{o}C]	t_{dry} [min]	t_{CDRP} [min]	$(-dX/dt)_{max}$ $\times 10^{-4}$ [s^{-1}]	t_{free} [min]	$\Delta T_{1,51,max}$ [^{o}C]
170	6.1	1.1	62.32	2.7	16.3
160	7.3	1.6	51.39	3.1	12.7
150	8.9	1.9	41.13	3.7	9.0
140	11.4	2.9	31.55	4.5	6.0
130	15.6	4.2	22.65	5.8	3.7
120	23.9	6.7	14.42	8.5	2.0
110	43.7	15.0	6.87	16.7	0.8

The time of drying t_{dry} predicted in the simulation exhibit the sudden increase when the temperature is close to 100 ^{o}C. To give an example, the extension of the drying process by around 80% for samples of all sizes is expected when the steam temperature is changed from 120 to 110 ^{o}C.

The maximum value of the drying rate $(-dX/dt)_{max}$ is calculated at the temperature of 170 ^{o}C, what is related to the highest heat flux between the surrounding gas and the object. The peak values of the drying rate for corresponding temperatures were around 26 times higher when comparing the drying of smallest sample to the largest one.

Those values was simulated during the period, when dewatering is the most intense – the constant drying rate period (CDRP). The stage of constant drying exhibited similar share in the total duration of the process for the samples of 2.5, 5 and 10 mm, where it ranged from circa 1/6 (170 ^{o}C) to circa 1/3 (110 ^{o}C). The analogical boundary values for the largest, 30 mm, object were computed at around 1/20 and 1/4, respectively.

More uniform pattern was observed when analyzing the instance of total free water removal, t_{free}. For the entire range of examined objects, free water was predicted to be evaporated slightly before 40% of the entire drying time. As the steam temperature inclined, this relative value was slightly delayed. However, for smaller samples occurred a little sooner. The exact values of $t_{\text{free}}/t_{\text{dry}}$ ratio were 44.3%, 47.7%, 52.8% and 57.3% with relation to increasing order of sphere sizes.

The last indicator is the highest calculated difference between center and surface of the sphere. As the free water gradually moves to the more shallow layers and the front of evaporation descends towards the core of the sphere, a temperature gradient occurs. Below the front of evaporation the lignite remains at the temperature of 100 $^{\text{o}}$C, while the shallow layers, where the bound water is being removed is increasing its temperature. The larger the sample is, the higher peak difference can be obtained. The instance of highest temperature is slightly postponed in regard to the time of free water evaporation. Though maximal temperature gradient, understood as ratio of peak temperature difference and the radius is higher for the smaller samples, the time of exposition for significant thermal stress is supposed to bring about more serious damage in the structure of large samples, especially for high temperature of the superheated steam.

7.3 Quantitative verification of computed values

In order to comprehensively analyse the coherence of the computational and empirical results, the values of two indicators introduced in the previous section were compared. The approximation of heat transfer coefficient h_{apr}, derived in Appendix B, was used to predict the peak value of the drying rate, according to Eq. (7.1).

$$\left(-\frac{dX}{dt}\right)_{max,apr} = \frac{h_{apr}\left(T_a - T_1\right)\pi d^2}{L \cdot m_c} \tag{7.1}$$

The same approximation of heat transfer coefficient was implemented in the numerical model and the maximum value of drying rate was found in the simulation. Those two manners were correlated to experimental method of calculating drying rate, relying directly on the electronic balance indication, as shown in Fig. 7.5. Since the approximated and simulated values depend on the same approximation of heat transfer coefficient, the trend lines are almost identical, with consideration of accuracy of the numerical computation. Due to individuality of the dried objects, the empirical results are distributed in some range.
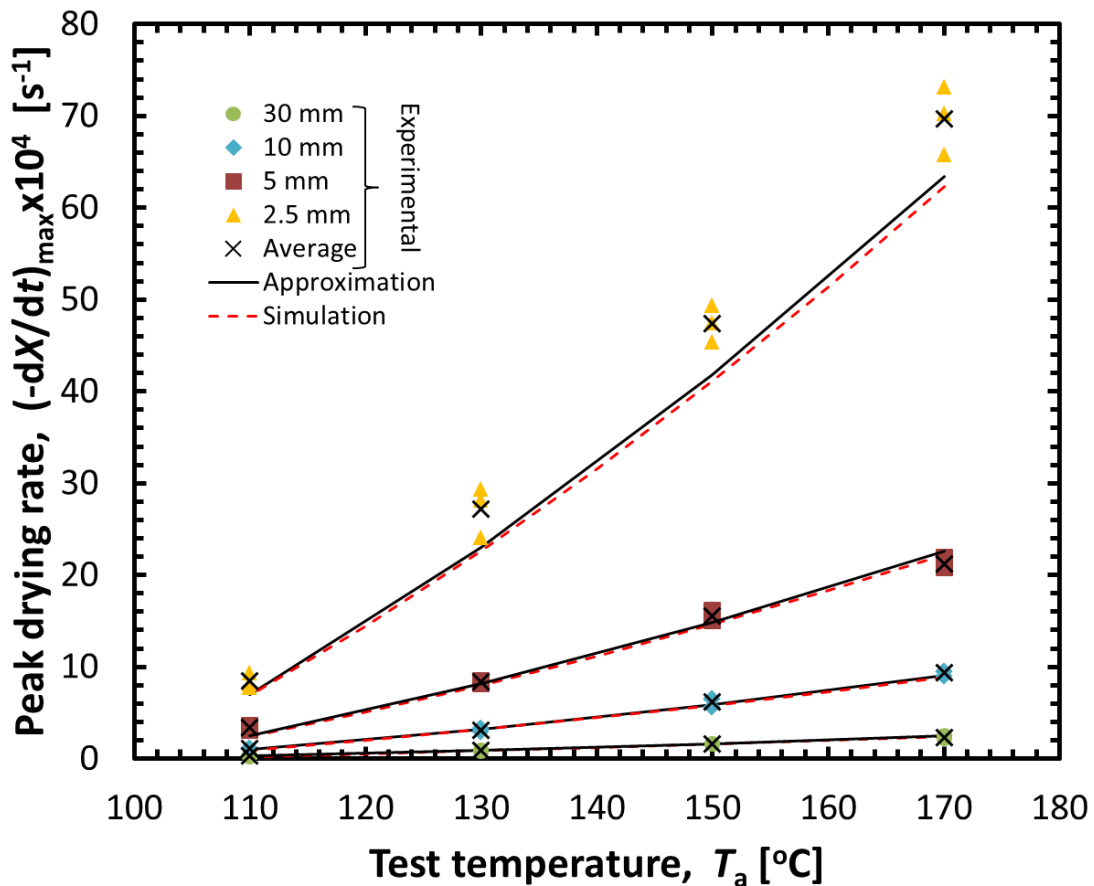
Figure 7.5 Maximum values of drying rate obtained from the experiment, the approximation formula and the numerical simulation

112

The model of approximation for the total time of drying was proposed relying on the dataset of actual experimental attempts. Proposed as a function of superheated steam temperature and reciprocal of sample diameter, initially for 5 and 10 mm [85], it was adjusted to the objects of the remaining sizes. Two models of approximation were taken into consideration, as given in Eq. (7.2) and (7.3).

$$t_{\mathrm{dry,apr}} = 1.93 \times 10^7 \exp\left[\frac{-5.73 \times 10^{-3}}{d} - 7.48 - \left(\frac{1.0 \times 10^{-5}}{d} + 2.74 \times 10^{-2}\right)T_{\mathrm{a}}\right] \qquad (7.2)$$

$$t_{\mathrm{dry,apr}} = 2.0 \times 10^7 \exp\left[\frac{-8.33 \times 10^{-3}}{d} - 6.88 - \left(\frac{4.0 \times 10^{-5}}{d} + 2.52 \times 10^{-2}\right)T_{\mathrm{a}}\right] \qquad (7.3)$$

The former was derived with use of experimental drying time values, while the latter excluded the smallest category of particles, 2.5 mm. They were assessed using a marker of normalized mean absolute error (*NMAE*), calculated for each particle category, as formulated in Eq. (7.4). The benchmark used in calculating this indicator is the averaged experimental value of drying time, $t_{\mathrm{dry,exp,avg}}$, in a certain conditions (steam temperature, sample size). In denominator, the value of 4 stands for number of experimental conditions, with regard to the steam temperature (110, 130, 150, 170 $^{\mathrm{o}}$C).

$$NMAE = \frac{\sum \dfrac{\left|t_{\mathrm{dry,exp,avg}} - t_{\mathrm{dry,apr}}\right|}{t_{\mathrm{dry,exp,avg}}}}{4} \qquad (7.4)$$

The values of *NMAE* are collected in Tab. 7.6. According to the values of normalized mean absolute error, Eq. (7.2) estimates the drying time more appropriately for categories of 30, 10 and 5 mm, but exhibits a large deviation from the experimental outcome in the case of smallest object. Therefore, the second model of approximation,

described in Eq. (7.3), was decided to be applied for estimating the time of drying for 2.5 mm lignite particles. An illustration of drying time, approached in different manners, analogically to previously presented drying rate, is shown in Fig. 7.6.

Table 7.6 Accuracy of two proposed models of drying time approximation

diameter d [mm]	model 1 - Eq. (7.2) *NMAE*	model 2 - Eq. (7.3) *NMAE*
30	0.16*	0.50
10	0.15*	0.23
5	0.32*	0.57
2.5	0.84	0.12*

* - selected model of approximation
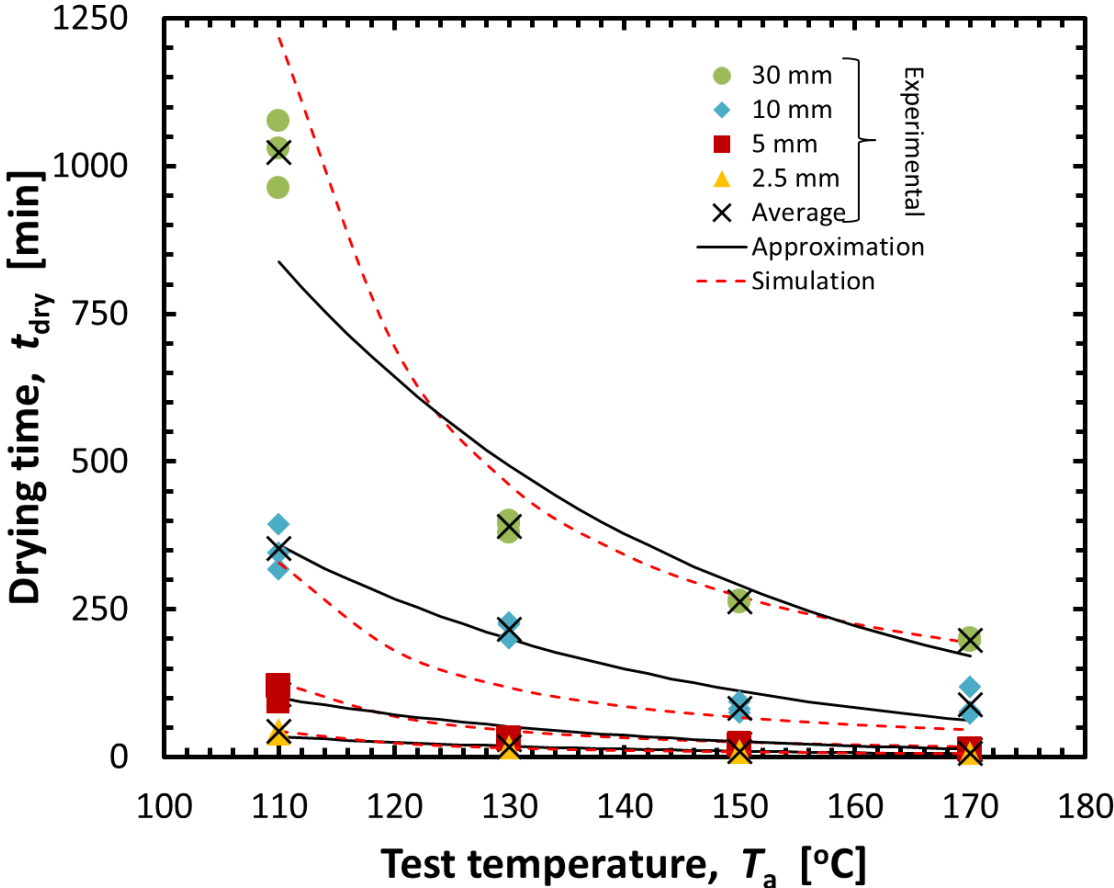
Figure 7.6 Drying time values obtained from the experiment,
the approximation formula and the numerical simulation

The data used for estimation of the drying rate and time, in regard to various methods of calculation were included in [85,86].

7.4 Visualization of temperature field within the lignite sphere during superheated steam drying

Besides utilization of the temperature profile as a function of time for selected regions of the sphere, the graphical representation of temperature field on its cross-section was prepared. As mentioned in the description of the mathematical foundations, the one-dimensional modelling of the drying parameters along the radius was applied. For that reason, the standard simulation results needed to be transformed in order to represent the planar coordinates of the sphere's cross-section. That objective was achieved with the application of the in-house data processing utility described in Appendix E. Relying on processed data sets, an open source application ParaView was used to prepare the graphic files.

Figure 7.7 illustrates the temperature distribution of temperature within the sample of 30 mm, during simulated process of drying at 150 ^{o}C. The corresponding images represent the particular values of decreasing moisture content, averaged on the entire particle. The spacing between the values is not equal, as the major of the water removal concerns the free water, which is evaporated from the particular layer at the constant temperature of 100 ^{o}C. The last two cases in Fig. 7.7, K and L, represent the moments of drying when the drying rate turns zero and the temperature of sample achieves convergence with the temperature of superheated steam, respectively.
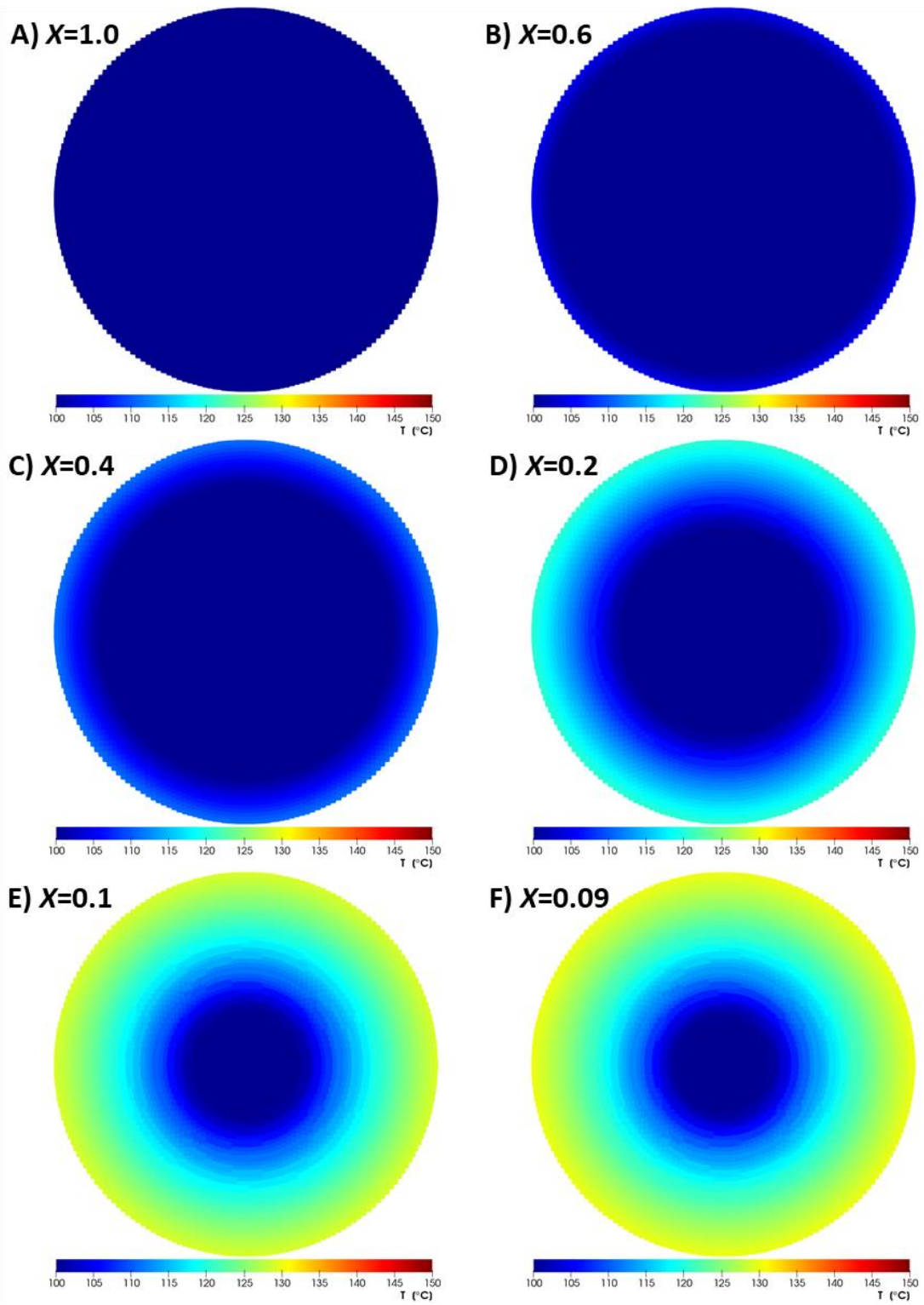
Figure 7.7.1 Simulated temperature field in 30 mm object dried at 150 $^{\circ}$C (part one)
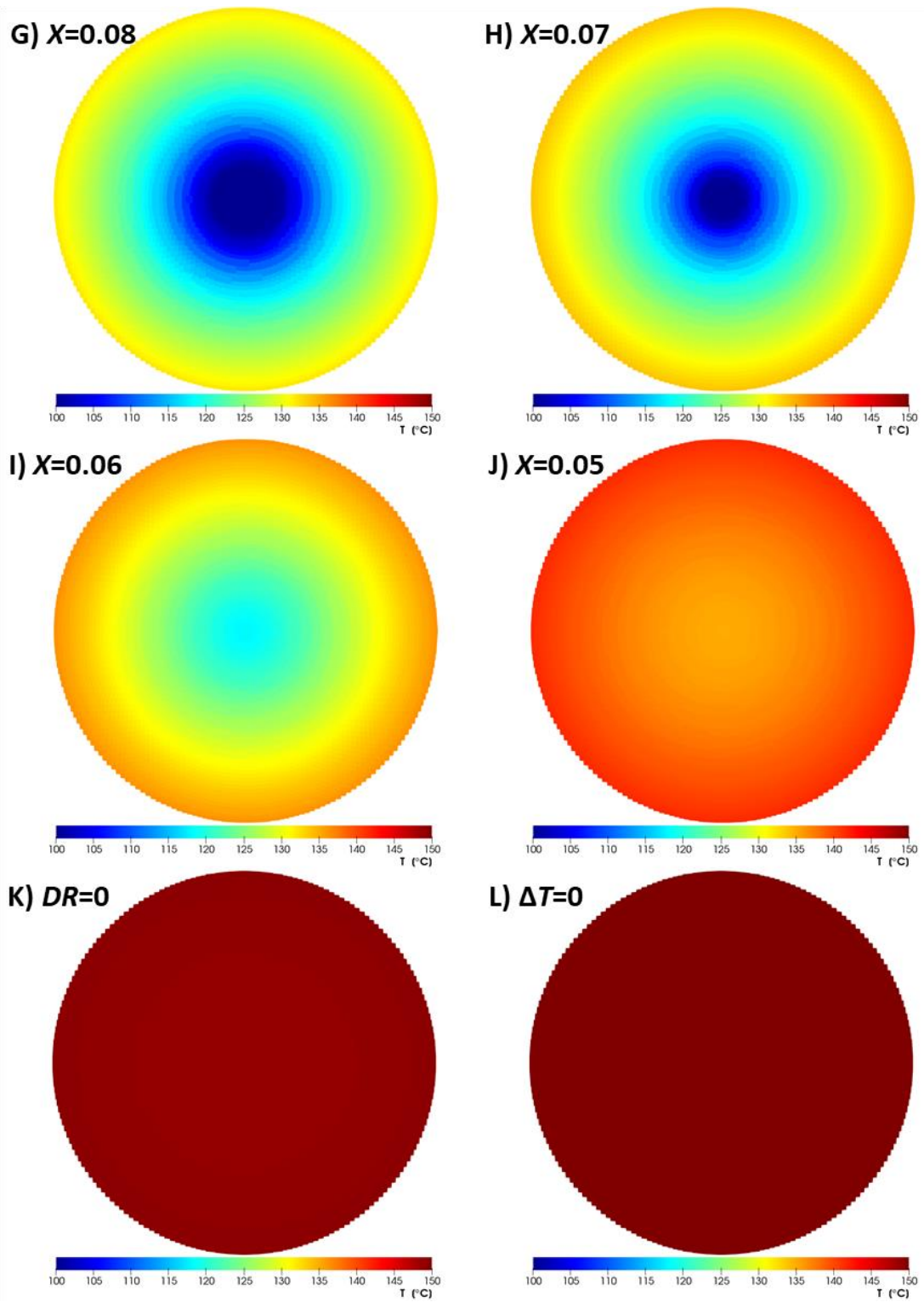
Figure 7.7.2 Simulated temperature field in 30 mm object dried at 150 ^{o}C (part two)

Analogical set of images was captured for the case of 10 mm sample dried at the superheated steam of identical temperature of 150 ^{o}C. They are shown in Fig. 7.8.

A) *X*=1.0
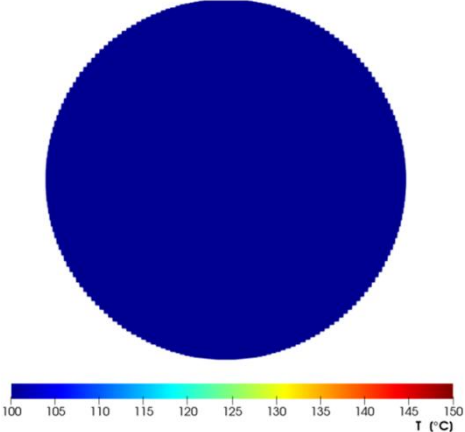
B) *X*=0.6
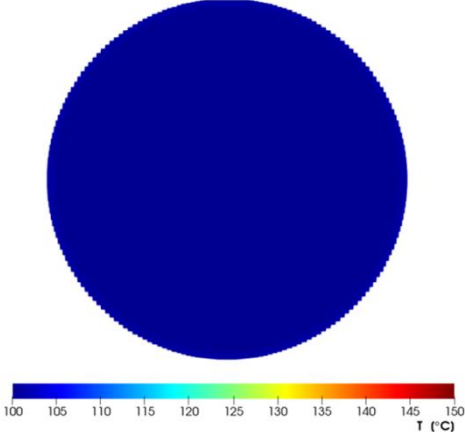
C) *X*=0.4
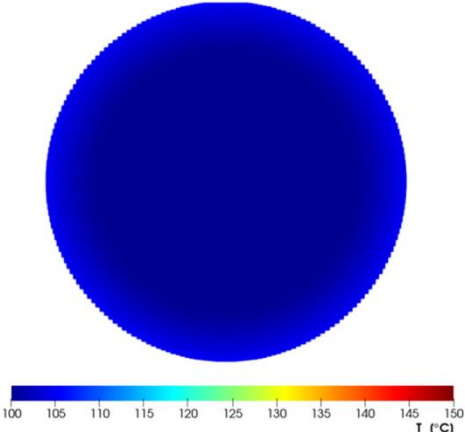
D) *X*=0.2
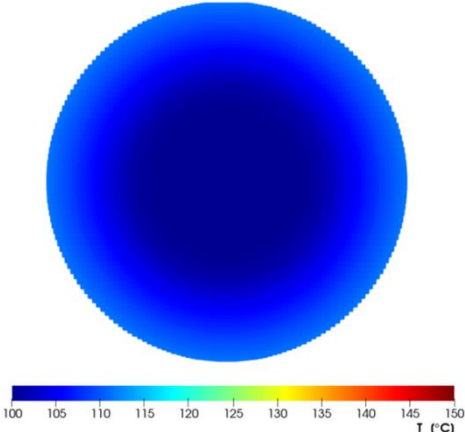
E) *X*=0.1
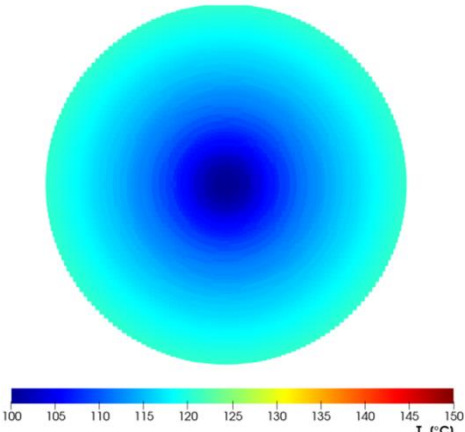
F) *X*=0.09
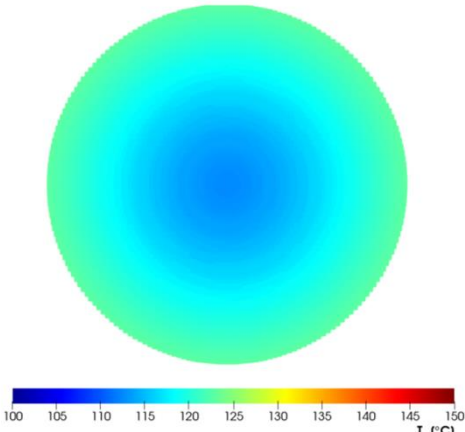
Figure 7.8.1 Simulated temperature field in 10 mm object dried at 150 ^{o}C (part one)
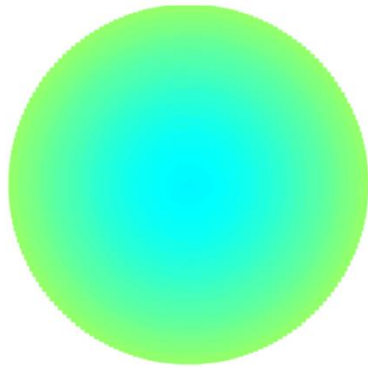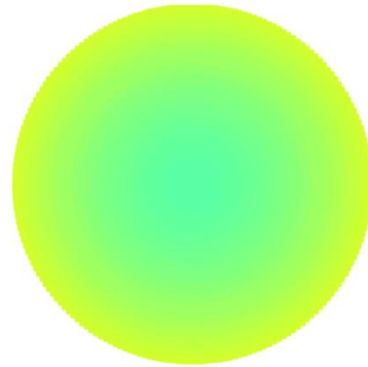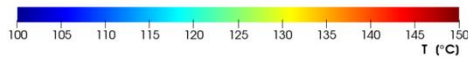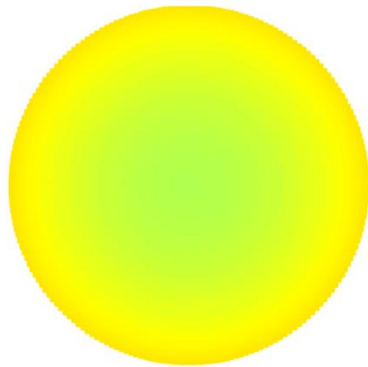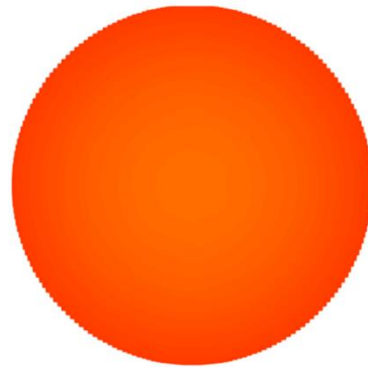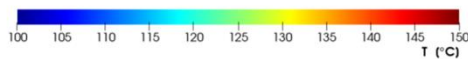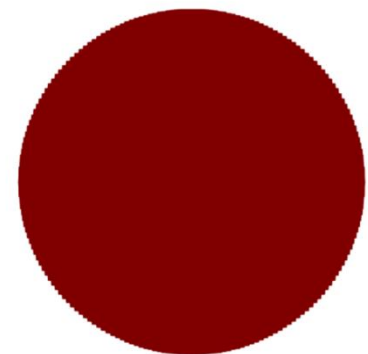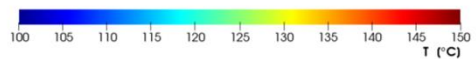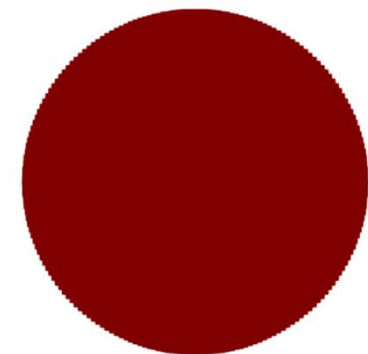
Figure 7.8.2 Simulated temperature field in 10 mm object dried at 150 $^{\circ}$C (part two)

The patterns of heating presented for the simulation of drying for 10 and 30 mm

samples exhibit considerable differences. First of all, the temperature distribution is

more uniform throughout the entire process in the case of 10 mm object, what is related to the size margin of the objects. In Fig. 7.9, the correlation of decreasing moisture content and the simulated difference of temperature between surface and center is presented for two sample diameters discussed in this section. Note that when the mass of water equalizes the mass of dry part ($X=1$), the center temperature of the larger object is still below 100 ^{o}C. The sample of 30 mm tends to achieve larger temperature disparity for the corresponding levels of decreasing moisture content, though the peak value is attained relatively later in terms of level of dewatering. In general, it occurs around the time instance of free water removal. In the case of 10 mm particle it is related to moisture content of 0.1 (Fig. 7.8.E), while the bigger object achieves the maximum difference at moisture content level of around 0.07 (Fig. 7.7.H).
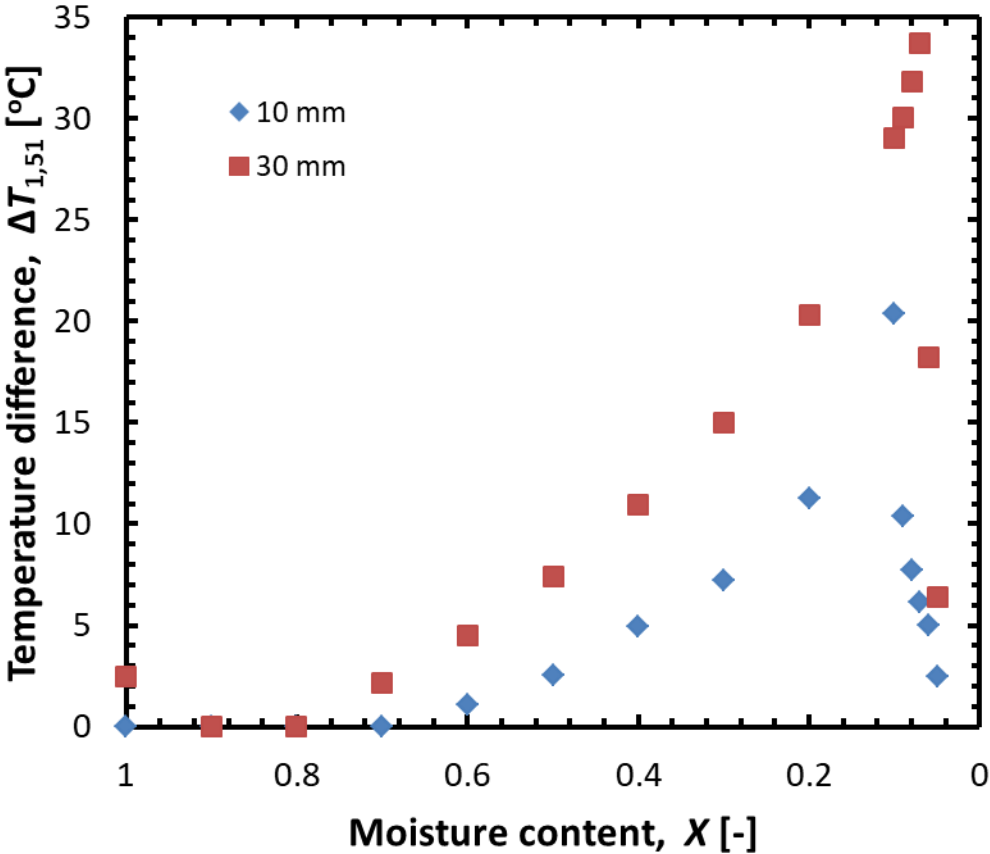
Figure 7.9 Simulated temperature difference between surface and center of 10 mm and 30 mm samples dried at 150 ^{o}C

7.5 Influence of variability of fundamental parameters of superheated steam drying process on the drying kinetics

7.5.1 Simulated drying kinetics of lignite from various deposits

According to the studies performed on Polish lignite [88,89], diverse material properties are exhibited by coal from different locations or even excavation spots within one deposit. Experimental results presented in chapter 5 also proved the diversification of the drying behavior among the samples from different lignite seams. In this section the results of numerical simulation performed for coals denominated B1, B2, B3 (Belchatow lignite) as well as T1, T2, T3 (Turow lignite) are presented.

In Tab. 7.7, the material properties that differed between particular batches, were presented. The parameters that were not included in this table, were assumed equal for all six coals, same as in Tab. 6.1. The first two properties, initial water share and density, were evaluated as average experimental values. For each test, they were calculated depending on the mass of the sample before and after drying in superheated steam. The values of specific heat for each type of coal were obtained in commissioned examination performed by an external company. The investigation was conducted according to the Japanese Industrial Standard (JIS K 0129). In order to find value of thermal conductivity, a series of auxiliary experiments was conducted for each coal designation, as described in Appendix A.

Figure 7.10 presents the drying kinetics obtained by the simulation for lignite categories listed in Tab. 7.7. They were prepared for the exemplary case of 10 mm sample exposed to superheated steam at 170 $^{\circ}$C. Parts on the left-hand side (A-C) correspond to Belchatow lignite, while the panels on the right (D-F) illustrate drying behavior of coal from Turow lignite mine.

Table 7.7 Selected material properties of Belchatow and Turow lignites

Parameter	Unit	B1	B2	B3	T1	T2	T3
initial water share WS^0	mass%	52.5	52.6	52.8	38.7	44.2	42.8
density (DBC) ρ_c	kg m^{-3}	1468	1378	1523	1569	1578	1561
specific heat (DBC) c_c	J kg^{-1} K^{-1}	1202	1181	1197	1324	1439	1461
thermal conductivity (DBC) λ_c	W m^{-1} K^{-1}	0.22	0.23	0.48	0.50	0.39	0.47
equilibrium moisture content X_{eq}	[-]	$4.8\times\exp[-2.4(T\text{-}100)^{0.18}]$			$44.8\times\exp[-4.4(T\text{-}100)^{0.13}]$		

The major visible difference between Belchatow and Turow drying characteristics is the shape of drying rate curve. There are two criteria of this aspect. First is the highest level of the drying rate. Due to higher total moisture level, Belchatow samples attain significantly higher level of the drying rate. The second one is the duration of above mentioned maximum. In case of Belchatow samples dried at the higher temperatures, a distinct period of constant drying rate is exhibited. Meanwhile, Turow lignite achieves the maximal drying rate level, what is followed by almost immediate decline of the value. Such a short constant drying rate period (CDRP) is caused by quick evaporation of the free water in the vicinity of the surface. This phenomenon is reflected by relatively early growth of surface temperature above the saturation temperature (100 ^{o}C).

Although the total moisture of B1, B2 and B3 coal is much higher than those of T1, T2 and T3, the difference in the drying time is not reflected proportionally, as the numbers in the Tab. 7.8 indicate. Results of simulation for B2013 coal (Tab. 7.3) were put in the table for reference. The reason is the vital importance of the initial stage of drying, when the speed of dewatering is kept at the highest rate. The duration of CDRP at 150 ^{o}C in exemplary case of 10 mm B3 sample is around 3.5 times longer than for T1 in analogical conditions. As mentioned, drying of Belchatow lignite is much more effective than Turow during this period.
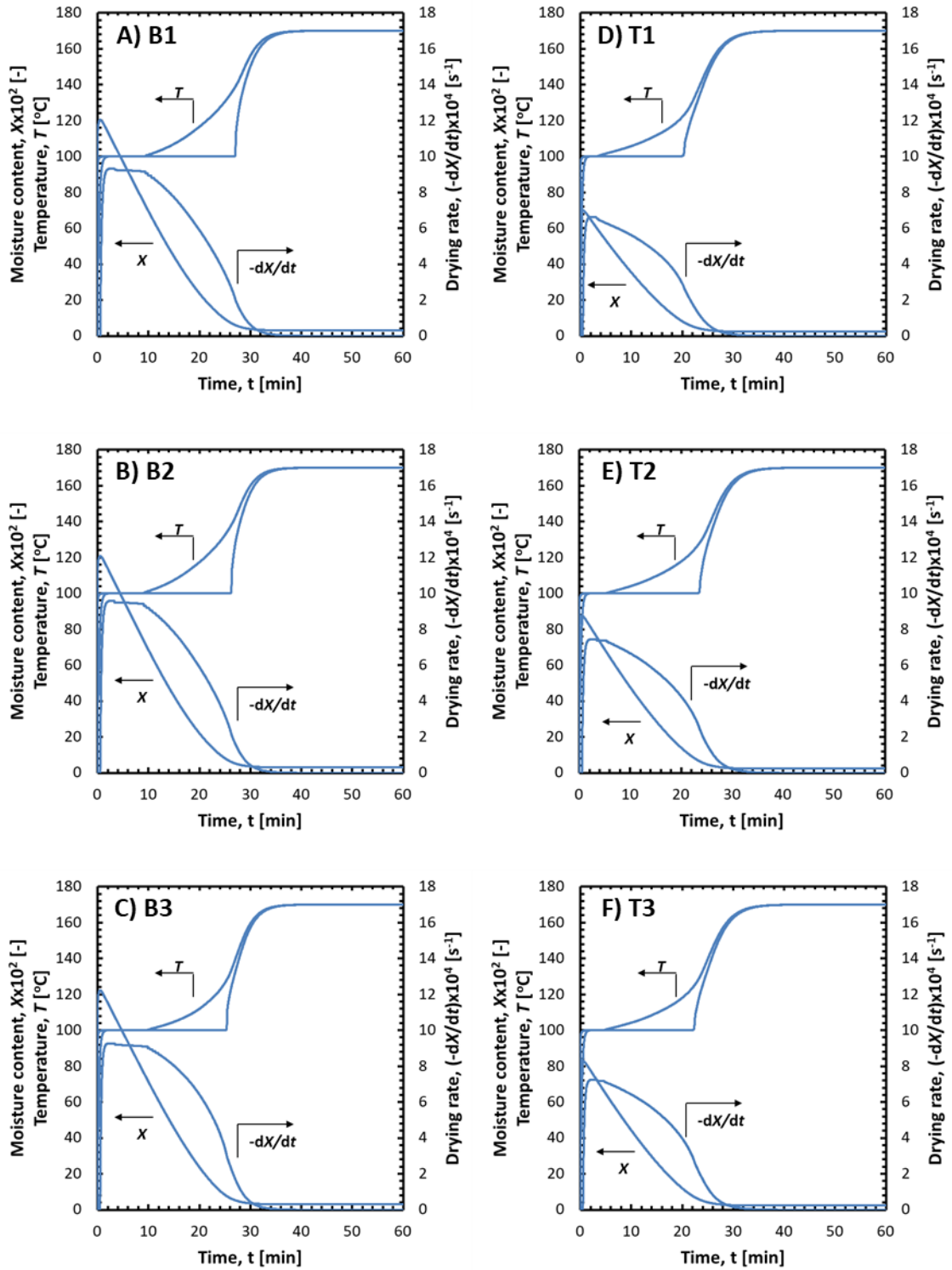
Figure 7.10 Drying behavior of 10 mm sample at test temperature of 150 ^{o}C obtained numerically for lignite batches from Belchatow (A-C) and Turow (D-F) mines

Table 7.8 Comparison of main simulation indicators for
10 mm samples of different coal types dried at 150 ^{o}C

lignite	t_{dry} [min]	t_{CDRP} [min]	$(-dX/dt)_{max}$ $\times 10^{-4}$ [s^{-1}]	t_{free} [min]	$\Delta T_{1,51,max}$ [^{o}C]
B3	65.0	14.7	6.08	32.6	17.5
T1	65.7	4.3	4.34	21.1	13.4
B2013	67.2	13.2	5.83	32.7	20.6

Figure 7.11 represents comparison of numerical and empirical drying characteristics for the scenarios. The analogical curves seem well matched to each other in the case of B3. The agreement in case of T1 lignite is not as good. It might be justified by the fact that that lignite batch was extracted from the footwall of the coal seam, where high contamination from the adjacent rocks occurs. Therefore, the overall distribution of properties for singular objects made of this coal is relatively wide, what directly induces the drying behavior, promoting the instances of drying kinetics deviated from the averaged simulation.

The direct comparison between simulation outcome for both lignite groups is presented in the Fig. 7.12. Concluding from the curves, the higher initial moisture content is usually followed by higher maximum of the drying rate, as most of the moisture contained within coal is the free water, subject to uninhibited evaporation during the early period of drying. Note that the initial stage of drying, when due to condensation of water on the sample surface, the level of drying rate remains below zero, is not visible in the chart. Omission of this part is substantiated by clarity of this figure.
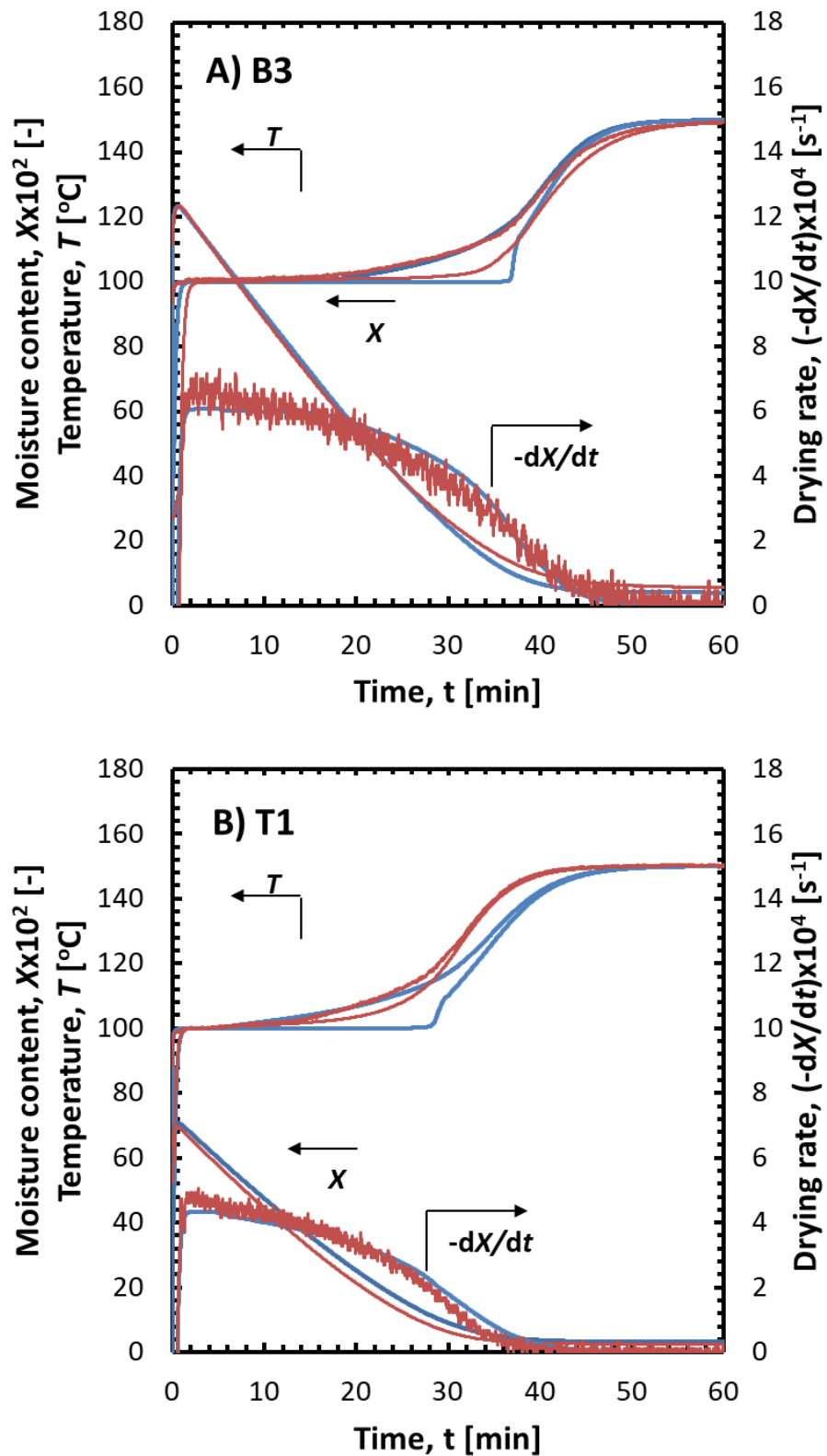
Figure 7.11 Comparison of drying characteristics of 10 mm sample at 150 $^{\circ}$C obtained numerically and experimentally for A) B3, B) T1 lignite batches
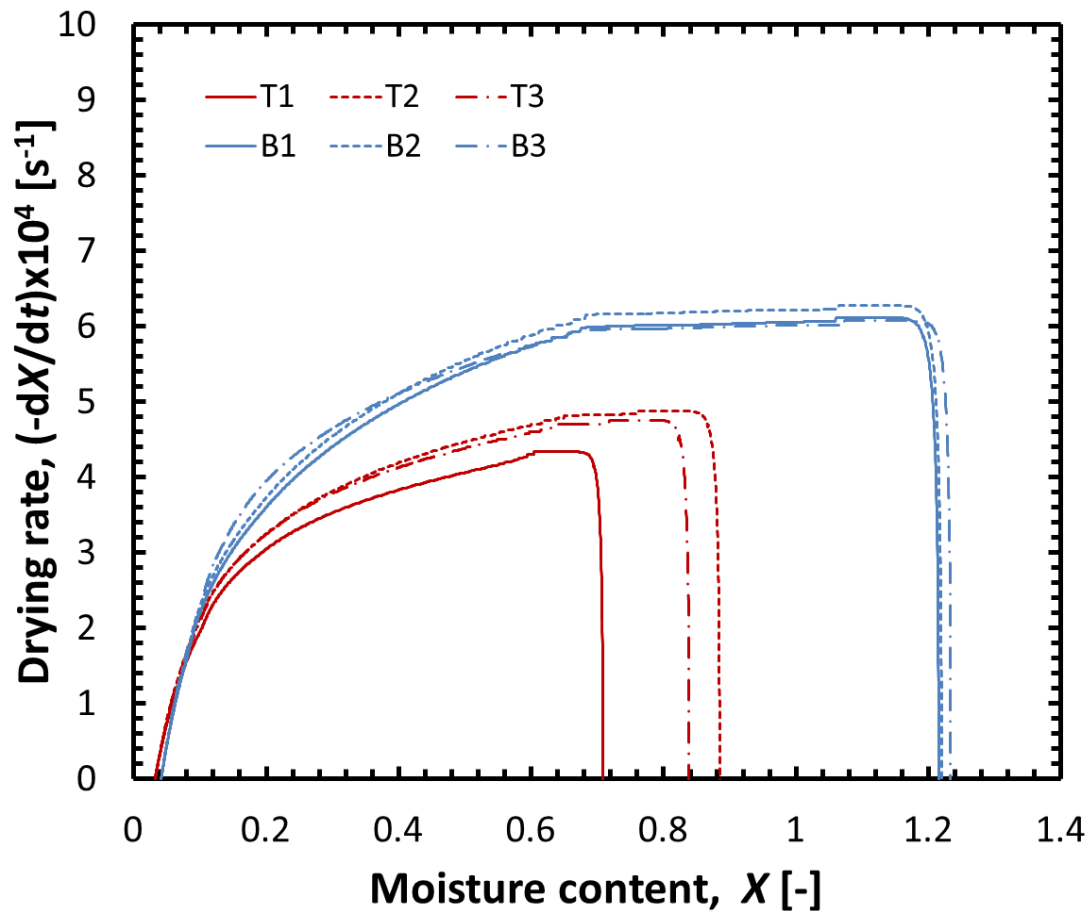
Figure 7.12 Numerically obtained correlation of drying rate and moisture content for 10 mm samples of Turow and Belchatow lignite dried at test temperature of 150 $^{\circ}$C

7.5.2 Sensitivity analysis of the drying kinetics in regard to process parameters

As indicated previously, the drying characteristics derived both experimentally and numerically differ significantly in regard to the type of fuel subject to superheated steam drying. For that reason, the preparation of general sensitivity analysis of the drying model is substantiated. The application of previously verified numerical model facilitates such an investigation, enabling the simulation of drying with variable process properties. The main objective of such an approach is to determine the parameters, which modifications impact the process of superheated steam drying in the most crucial manner.

126

The sensitivity analysis was performed mainly in regard to material properties of lignite, as listed in Tab. 6.1, however to obtain the proper overview, the factors independent from the material or even the object were taken into consideration as well. The full list of parameters subject to investigation is presented in Tab. 7.9. The numbers gathered in the table are base (reference) values of the parameters. In the simulation attempts, each quantity was gradually increased by 10%, 30% and 50% at once, with other parameters remaining fixed (*ceteris paribus* rule). As a result, four sets of simulated drying characteristics were produced. The only exception concerned temperature of superheated steam. For analyzing the variability of other parameters, its value was fixed at 150 ^{o}C. However, the investigation of temperature modification itself was performed with reference value of 110 ^{o}C. Under such condition, all applicable cases fall into the range of actual experimental settings, with 165 ^{o}C as a maximum.

Table 7.9 Parameters used in sensitivity analysis of the numerical model

parameter	reference value	origin	type
density (DBC) ρ_c	1536 kg m^{-3}	averaged experimental values	
initial water share WS^0	51.25 mass%		
thermal conductivity (DBC) λ_c	0.33 W m^{-1} K^{-1}	commissioned research	material properties
specific heat (DBC) c_c	1246 J kg^{-1} K^{-1}		
apparent free water transfer coefficient D	3×10^{-9} m^2 s^{-1}	empirical value	
sample diameter d	0.01 m	experimental conditions	extensive property
superheated steam temperature T_a	150 (110) ^{o}C		external parameter

The analysis was done basing on the time charts involving correlations of the moisture content, drying rate and temperature profile, similarly as in basic simulation. In this particular part, each of the characteristic drying quantities was illustrated using a reference curve and three auxiliary curves, representing the increased values of a particular parameter.

The indicators selected for quantitative evaluation of the simulation outcome were the following quantities: drying time t_{dry}, peak drying rate $-(dX/dt)_{max}$, time of free water removal t_{free} and the maximum difference in temperature between center and surface of the sample $\Delta T_{1,51,max}$.

Fig. 7.13.1.A shows the influence of density of lignite on the drying kinetics. Among major factors related to the density of coal, ash content may be distinguished. Generally, significant content of mineral compounds is correlated with elevated value of specific weight. That observation is connected with relatively low density of lignite's substantial ingredients: carbon, volatile matter and water in comparison to metal oxides that ash is mostly composed of. Still, the precise estimation of coal density should also take the ash composition into account, as normally several chemical compounds constitute its ash content [101]. An slight decline in the drying rate and a minor postponement of free water removal (from 33 to 36 minutes) is observed following the increase in density. Contrarily, the difference of surface and center temperature rises to 21.7 ^{o}C from the initial 20.6 ^{o}C. The total time of drying is extended by around 1/6 of the reference value, from 67.2 to 77.8 minutes.

In Fig. 7.13.2.B the influence of the initial water share on the process is exhibited. Note that curves of +30% and +50% equivalent to WS^0 at the level of 66.6% and 76.9%, respectively, may only have the theoretical meaning, because water share in lignite rarely exceeds 65%. The simulated incline in the water share, though, induces a

considerable rise in the peak drying rate. As the larger amount of water needs to be evaporated from the lignite, t_{free} exhibits approximately direct proportion to the initial water share. In the last cases, the temperature difference escalates to 29.9 ^{o}C.

The sensitivity analysis in regard to thermal conductivity as a parameter was presented in Fig. 7.13.2.C. The modifications of the reference value do not produce any changes in the top level of drying rate. The removal of free water and the termination of the process are remarked insignificantly sooner, as the transfer of heat through the sphere is simulated at a slightly higher, especially in the late stages of drying, when the dry part of coal possesses a greater share in the entire particle. The indicator most sensitive on thermal conductivity modification is the temperature gradient. Abovementioned increase in heat transfer rate reduces the difference of temperature between the extreme layers. The values of this indicator were computed at 20.6, 19.7, 18.2 and 16.9 ^{o}C for base and auxiliary cases, respectively.

The impact of specific heat alterations was presented in Fig. 7.13.3.D. The rise in value of this property, even as high as 50% in regard to reference case, does not influence the drying indicators in a significant way. For instance, the drying time extends by around 8% in the maximal specific heat scenario. It should be taken into account even in this extreme case, the specific heat of dry coal (1869 J kg^{-1} K^{-1}) is below half of the corresponding parameter of water (4180 – 4210 J kg^{-1} K^{-1} within the analyzed temperature range). This is the reason that the larger influence on heat accumulation during drying is exerted by wet phase of a lignite particle.

Among material properties analyzed in terms of sensitivity analysis, the apparent free water transfer coefficient, D, can be listed as well. Its value is related to the complexity of porous structure within lignite. The drying kinetics with regard to this parameter as a variable are exhibited in Fig. 7.13.3.E. The values of the indicators

remain virtually invariable, what is also reflected on their graphical representation. The instance of free water removal completion, which is the only indicator subject to any change, for subsequently increased value of *D* occurs 1%, 3% and 4% earlier than in the reference case. It can be explained by higher efficiency of free water transport to the vicinity of sample's surface. The temperature of shallow layers is generally higher than the sample core, what elevates the rate of evaporation relating to the water stored inside and thus reduces the time required for free water removal.
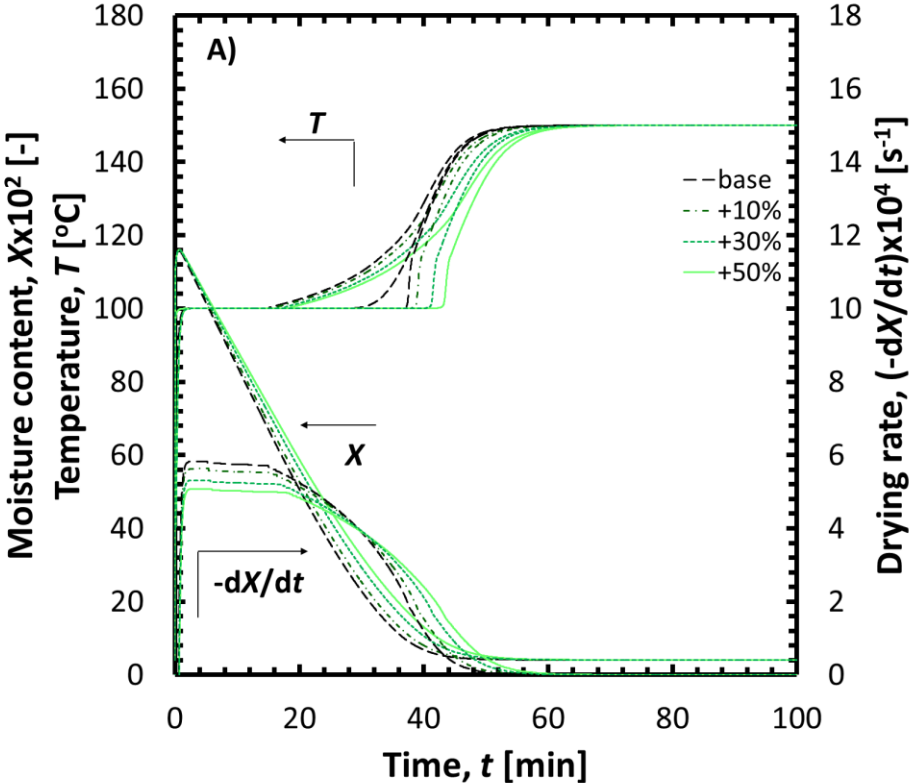
Figure 7.13.1 Numerical simulation of drying parametrized for: A) density
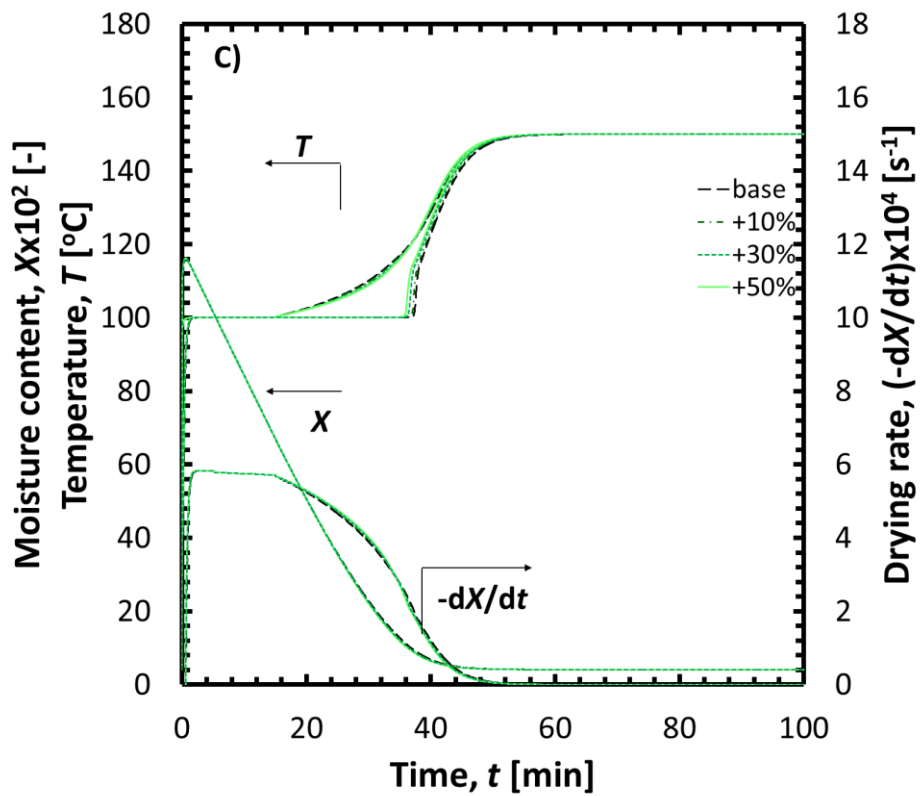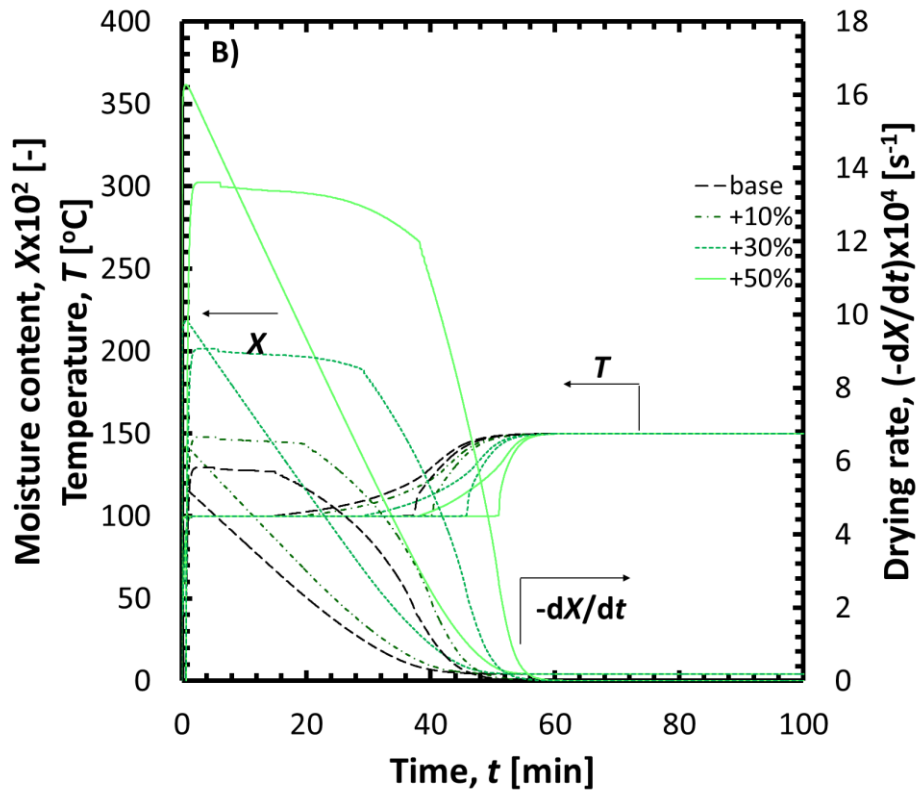
Figure 7.13.2 Numerical simulation of drying parametrized for:
B) initial water share, C) thermal conductivity
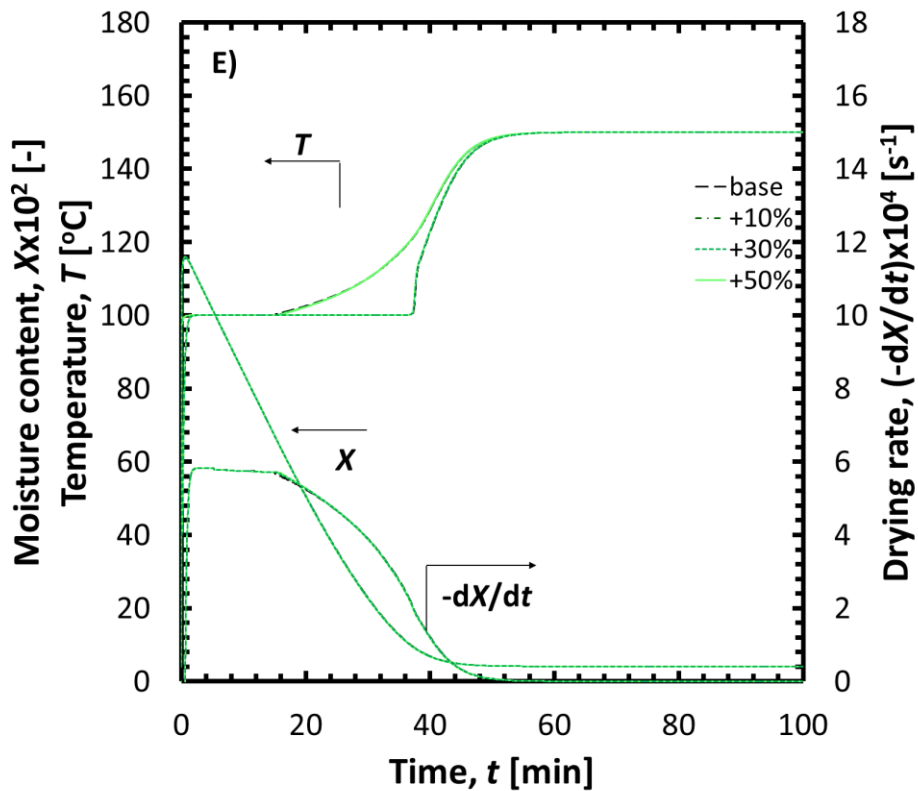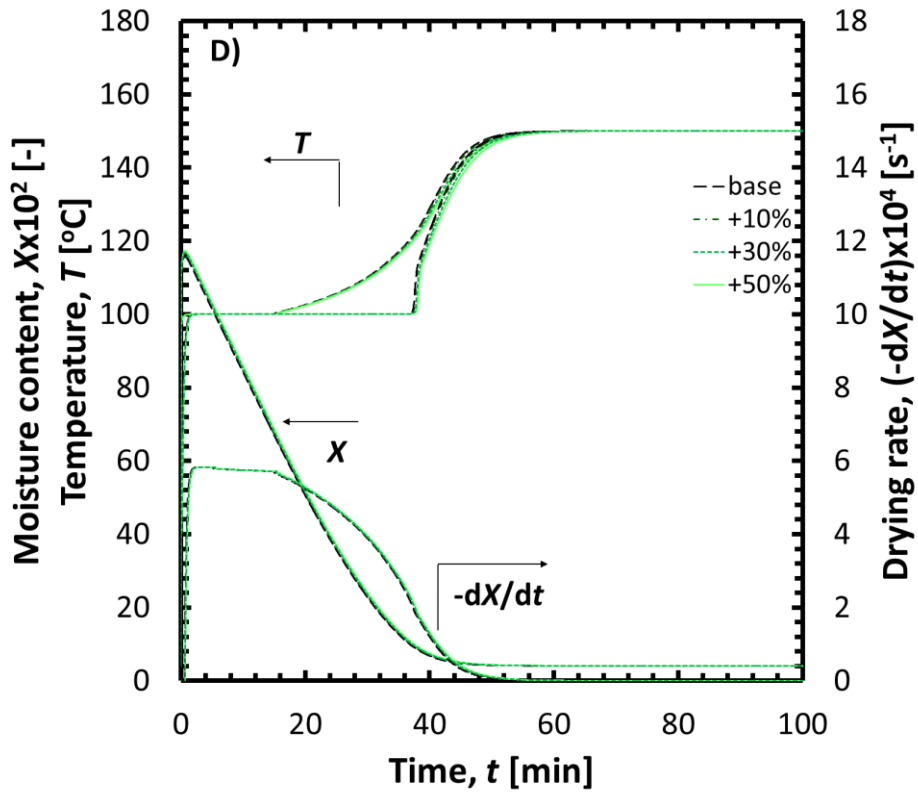
Figure 7.13.3 Numerical simulation of drying parametrized for:
D) specific heat, E) apparent water transfer coefficient

132

Besides investigating the material properties, that can be classified as intensive parameters of the process, additional quantities independent from the structure of lignite were taken into consideration. The correlation of drying kinetics and sample diameter as well as superheated steam temperature have been previously discussed in a number of studies, in regard to experimental attempts [85,88,105] and relying on results of the numerical simulation [86,106]. Those studies, though, involved a range of experimental condition, as described in chapter 4. In this section, the base values were set for particle diameter and steam temperature at 10 mm and 110 $^{\circ}$C, respectively. The pattern of stepwise increase was assumed the same as for material properties.

Drying curves for samples of various diameters are presented in Fig. 7.14.1.A, exhibiting strong dependence of size on the drying behavior. The rate of increase in the case of t_{free} and t_{dry} in comparison to the base curve is similar. For the 11 and 13 mm scenarios both values are higher than reference case by 14% and 37%, respectively. Only for the largest sample simulation, a small disparity was observed, evinced by increase of times required for the removal of free water by 65% and for the completion of drying by 62%. The drying rate achievable during CDRP was simulated at 3.52 s^{-1} in the case of 15 mm object, which is nearly 40% lower than base value. The least considerable impact of diameter incline concerns the extreme temperature difference. Its rise was simulated at 5%, 15% and 24%, respectively.

Fig. 7.14.2.B visualizes the influence of superheated steam temperature enhancement. Due to large disparity of analyzed instances in terms of drying time, the abscissae axis is limited to initial 100 minutes of the process. The ratio of peak temperature differences in extreme cases exceeds 16 (29.2 $^{\circ}$C against 1.8 $^{\circ}$C), which is the most considerable change among all indicators. The significant rise, regarding the period when the peak value of drying rate occurs as well as the value itself is also

observed. The predicted time required for the completion of drying is 329, 172, 79 and 50 minutes for 110, 121, 143 and 165 $^{\circ}$C of superheated steam temperature, respectively.

On the whole, the degree to which variability of material properties influences drying kinetics is diversified. The most important in these terms is the total share of water within coal, followed by density and thermal conductivity. Regarding parameters independent from the material, the simulation of superheated steam drying displayed high sensitivity to changes both in object size and drying medium temperature. For more details, refer to [107].
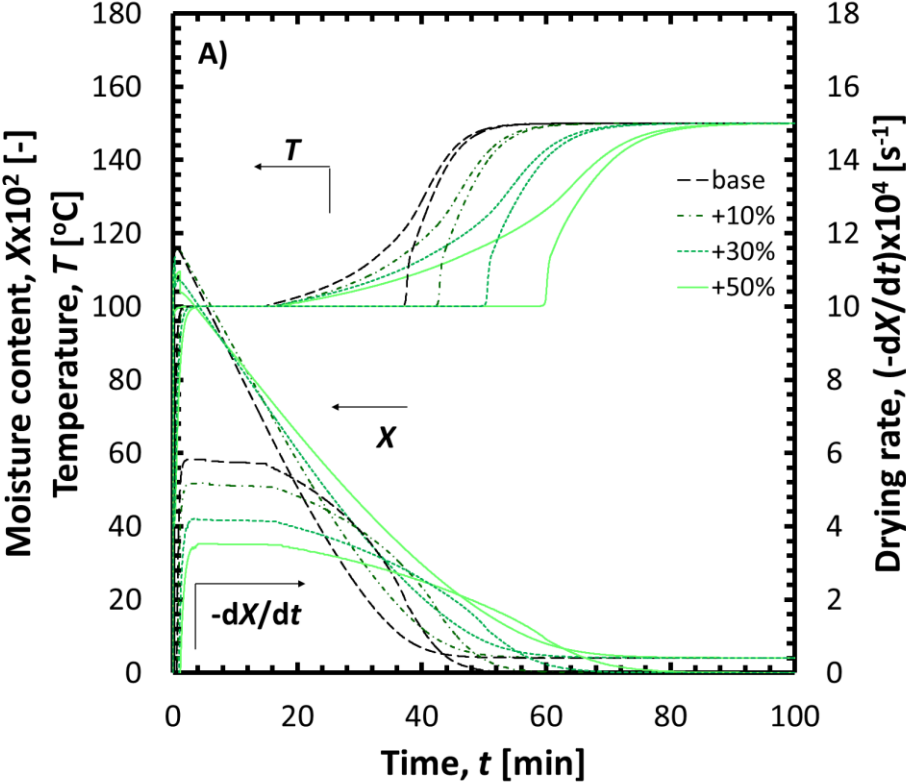
Figure 7.14.1 Numerical simulation of drying parametrized for: A) sample diameter
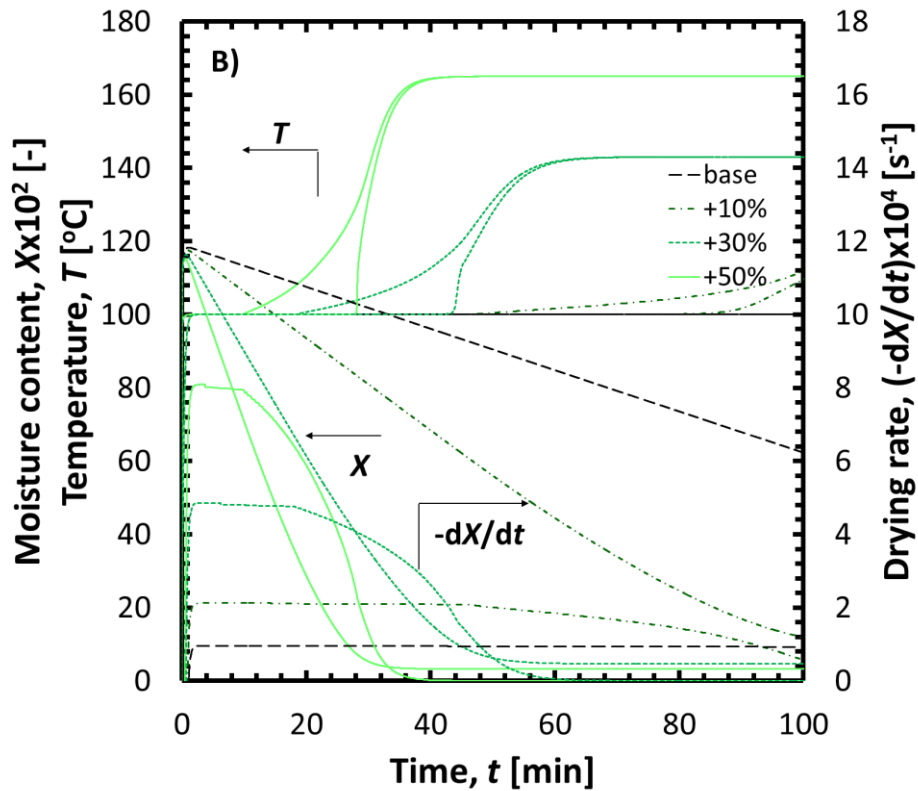
Figure 7.14.2 Numerical simulation of drying parametrized for:
B) superheated steam temperature

7.6 Simulation of multi-particle drying

The actual conditions determining the operation of the drying system assume diversification of coal assortment that is supplied to the dryer. Hence, it is reasonable to gain insight into drying behavior in regard to a batch of multiple particles characterized with different dimensions.

The drying behavior of mixed lignite batch was previously analyzed and discussed regarding the experimental results in regard to four arbitrarily adapted scenarios [105]. In this section, the diameter of coal particles was assumed to follow the Rosin-Rammler formula (Eq.(7.5)), frequently utilized to model the size distribution in fractionized mineral matter [108,109].

$$f(d) = 100 \times \exp\left[\left(-\frac{d}{d_e}\right)^B\right] \qquad (7.5)$$

The equation (7.5) results in a mass percent ratio of particles characterized with diameter larger than d to the total mass of a particular coal group. Characteristic particle size for the group is represented by d_e, while B stands for a uniformity constant equal 1 [74]. For the sake of asymptotical character of the function in Eq.(7.5) (the value tends to zero as the diameter approaches infinity), the variable of d_{max} is introduced to embody the diameter, over which only 1% of the mass distribution in each group occurs. To simplify the model of fragmentation, that top part is neglected and not taken into calculations. The remaining part is divided into 10 groups, where the first accounts for 9 percent of the total mass distribution and groups numbered 2 to 10 represent 10% of the total mass distribution per each.

The chart illustrating the negative of derivative of $f(d)$ is shown in Fig. 7.15 for the scenario of d_{max} equal to 80 mm. The triangular markers on the bottom axis represent the mean diameter of a particle in each lignite group. Equation (7.6) describes the derivative curve in the particular form visible in Fig. 7.15.

$$-f'(d) = 5.76 \times \exp\left(-\frac{d}{17.37}\right) \qquad (7.6)$$

According to the industrial standards applied by the producer of both Belchatow and Turow coal [110,111], there are three basic lignite assortments. They correspond to the maximum diameter values of 40, 80 and 300 mm and were denominated as "fine", "medium" and "thick", respectively. The representative diameter for each group of the particular assortment is given in Tab. 7.10.
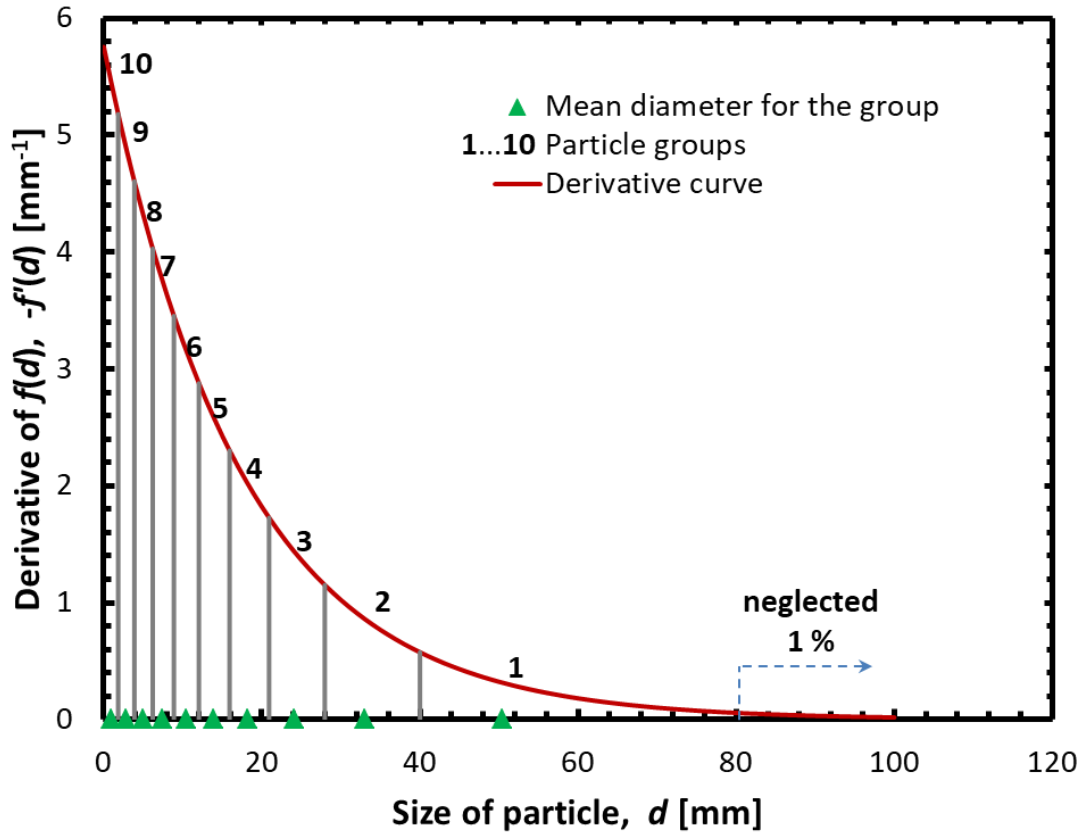
Figure 7.15 Size distribution of particles in lignite groups (d_{max}=80 mm)

Table 7.10 Representative diameters of particle groups in various lignite assortments

representative diameter [mm]	lignite assortment		
	fine	medium	thick
d_{max}	40	80	300
group 1	25.19	50.38	188.95
group 2	16.48	32.96	123.59
group 3	12.04	24.08	90.31
group 4	9.12	18.24	68.39
group 5	6.94	13.88	52.02
group 6	5.19	10.39	38.95
group 7	3.74	7.48	28.06
group 8	2.50	5.00	18.74
group 9	1.41	2.82	10.59
group 10	0.45	0.89	3.34

The initial 60 minutes of medium coal drying is presented in Fig. 7.16. The moisture content predicted for the particular groups, marked by dashed line, is plotted together with curves of moisture content and drying rate of the multi-particle simulation. The drying rate of the entire assortment declines in a stepwise manner, what is related to the state of attained by particles of subsequently declining representative diameter at the decreasing drying rate periods of drying.
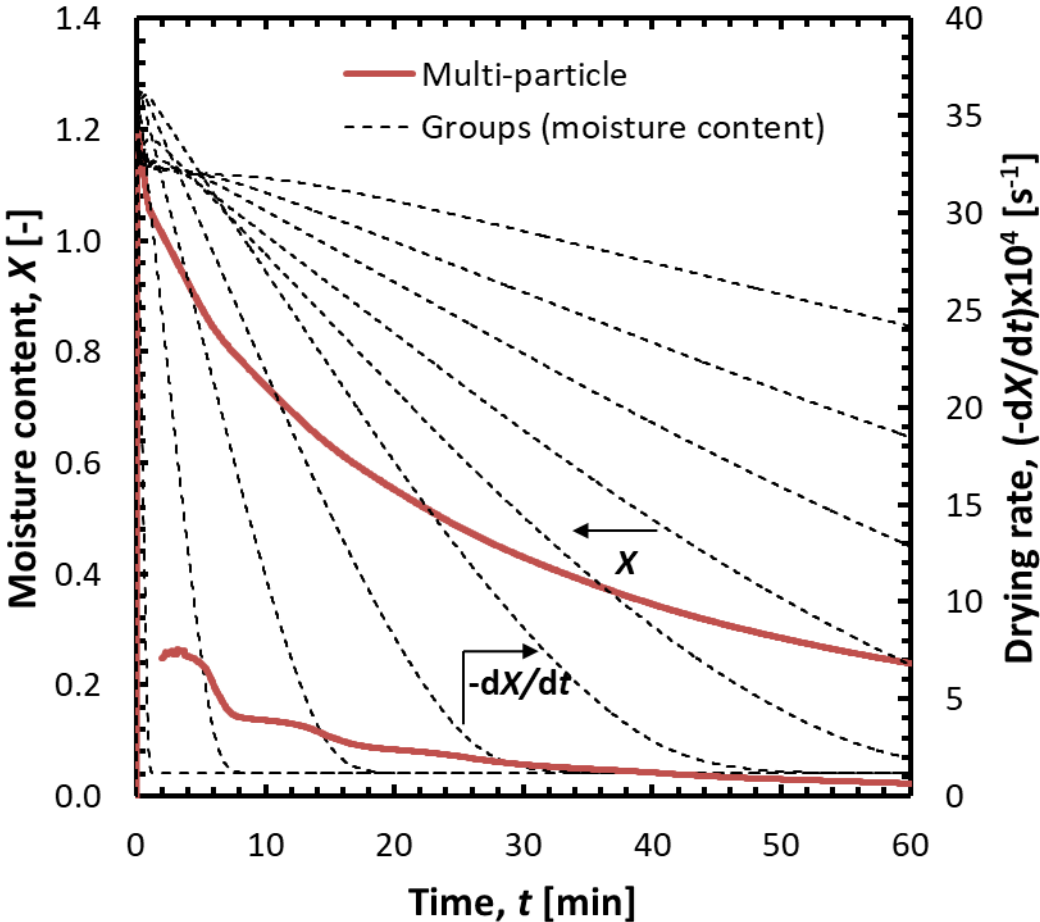
Figure 7.16 Individual and collective drying curves (medium lignite)

The simulation of drying for particles of coal grouped in assortments was presented altogether in the form of drying rate curve plotted against decreasing moisture content. The speed of evaporation is significantly influenced by the composition of a lignite batch [105]. When the assortment is characterized with prevailing share of relatively small particles (less than 10 mm in diameter) the peak drying rate is elevated what entails the steep shape of the correlation chart. All curves exhibit irregularities in the vicinity of initial (highest) moisture content, what is related to a simulated series of water droplets formed on the surface that happened to fall down in the condensation period of drying. This phenomenon, enhanced particularly in the case of medium and thick coal, was observed frequently in the experimentation conducted for spheres of 30 mm [86] and occasionally in drying of other samples [85].

7.7 Impact of drying on the efficiency of power generation

7.7.1 Assumptions

In order to analyze the influence of superheated steam drying on the optimization of power generation, two indicators were used: carbon dioxide emission per generated unit of electricity and thermal efficiency of the power plant. The evaluation of these two quantities requires insight into composition of lignite. In Tab. 7.11 the constituents of B2013 coal relevant in terms of calorific value evaluation, alongside the general category of "remaining dry part", were presented. The percentage of each elemental component, carbon and hydrogen, was reported in an outsourced professional investigation on the basis of dry coal. Then it was recalculated to share appropriate to as-received form of fuel ("raw coal" column).

Table 7.11 Components of B2013 lignite relevant to evaluation of calorific value

component [mass%]	dry coal	raw coal
water share *WS*	-	51.60
carbon *C%*	56.90	27.54
hydrogen *H%*	4.51	2.18
remaining dry part	38.59	18.68

The calculated emission of carbon dioxide relies on the stoichiometry of elemental carbon combustion. Per each 12 kg of combusted carbon, 44 kg of carbon dioxide is formed. Taking it into account and assuming that carbon in lignite is subject to complete combustion, the formulation of CO_2 emission per mass unit is given as:

$$\{CO_2\_kg\}^i = \frac{44}{12} C\%_c \left(1 - WS^i\right)$$

(7.7)

The superscript *i* correlates the water share *WS* down to which lignite has been dried at a certain instance of the process with the estimated CO_2 emission.

Two quantities are commonly applied to describe the thermal effect of fuel combustion. *HHV* understood as "higher heating value" stands for the total amount of heat generated on burning the mass unit fuel, on the assumption that heat loss does not occur through the evaporation of neither water present in the fuel nor produced parallel to the combustion. The *HHV* at the air-dried state of coal can be used to obtain the analogical parameter for the dry coal:

$$HHV_c = \frac{HHV_{ad}}{1 - WS_{ad}}$$

(7.8)

According to the commissioned investigation, mentioned earlier in this section, the

air-dried B2013 is characterized with *HHV* equal to 19.08 MJ kg^{-1} and 14.6 mass% of water share. Applying formula (7.8), the higher heating value for the dry coal is 22.34 MJ kg^{-1}. Hence, the general formula on *HHV* at the current state of water share is:

$$HHV^i = HHV_c\left(1 - WS^i\right)$$ (7.9)

Relying on the evaluated *HHV*, the lower heating value (*LHV*) might be expressed as the higher heating value diminished by the heat required for evaporation of inherent moisture as well as water synthesized from the oxidant and hydrogen stored within dry part of coal. According to stoichiometry, 36 kg of water is formed with 4 kg of hydrogen as a substrate of synthesis. Thus, *LHV* related to coal of a certain water share may be expressed as:

$$LHV^i = HHV^i - L\left[WS^i + 9H\%_c\left(1 - WS^i\right)\right]$$ (7.10)

Then, electricity generation per mass unit regarding the fuel characterized with particular value of *LHV* is in direct proportion to thermal efficiency of the power generation unit.

$$E\_kg^i = LHV^i \times \eta_{LHV,\text{raw}}$$ (7.11)

Consequently, the function from Eq. (7.7) describing CO_2 emission might be recalculated to represent emission per electricity generation unit.

$$\left\{CO_2\_kWh\right\}^i = \frac{\left\{CO_2\_kg\right\}^i}{E\_kg^i} \times 3.6$$ (7.12)

Note that thermal efficiency data provided by power generation companies tend to rely on *LHV* of utilized fuel [112,113], while the scientific publication often correlate

the emission ratio and thermal efficiency taking *HHV* into account [114,115]. Considering these facts, the thermal efficiency calculated using both representations of fuel's calorific value might be given as:

$$\eta_{HHV}^{i} = \frac{LHV^{i} \times \eta_{LHV,\mathrm{raw}}}{HHV^{i}} \qquad (7.13)$$

The decline in water share induce rise in *LHV* and *HHV*, as presented in Fig. 7.17. All but one pair of data points are displaced with a water share interval of 5%, whereas the last is assigned to 3.94% of residual water share (equivalent to 1.98% of residual water percentage), a value characteristic for superheated steam drying at 150 °C. The initial disparity between higher (10.21 MJ kg^{-1}) and lower heating values (8.56 MJ kg^{-1}) reduces during the process, attaining the lowest level of 0.97 MJ kg^{-1} at the final. That margin is justified mostly by the hydrogen content, because the theoretical gap, achievable for the dry lignite (elliptical selection) is equal to 0.97 MJ kg^{-1}.
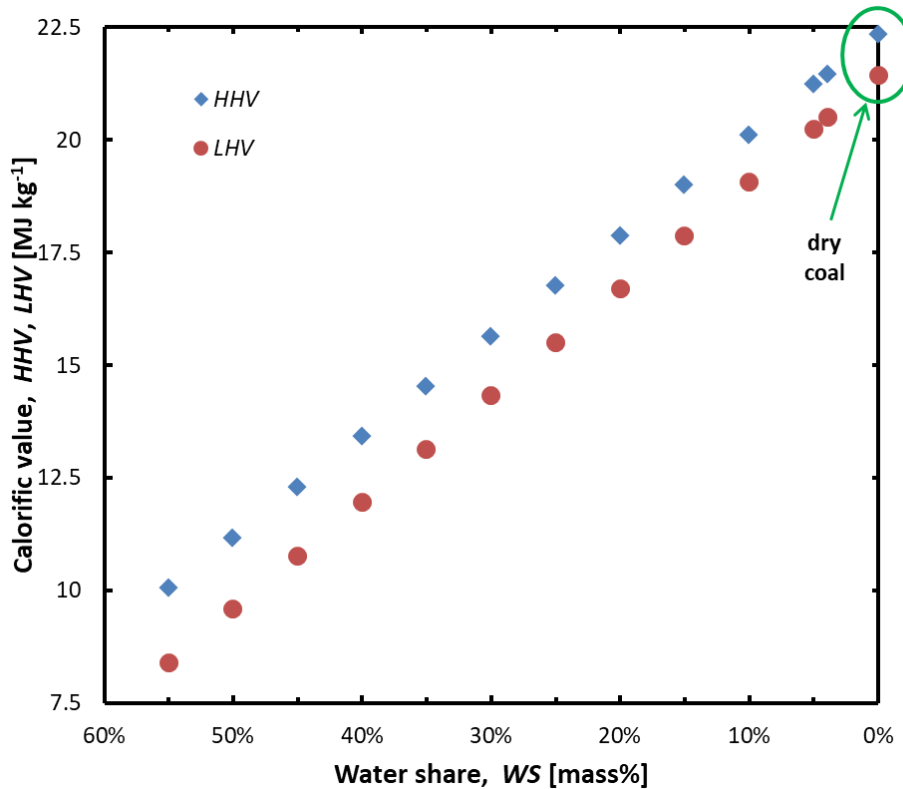
Figure 7.17 Simulated increase in calorific value of lignite due to drying at 150 °C

The application of high-calorific fuels is beneficial in economical as well as ecological aspect. Reduction of water content by drying may contribute to those benefits. Fig. 7.18 illustrates the feasibility of carbon dioxide emission in regard to operational parameters of power generation units. The information on the Polish coal-fueled power generation units, in reference to which the illustration was prepared, is provided in Tab. 7.12. Scenarios 1 and 2 relate to units utilizing lignite, while the last represent a unit of the power plant fueled by bituminous coal.
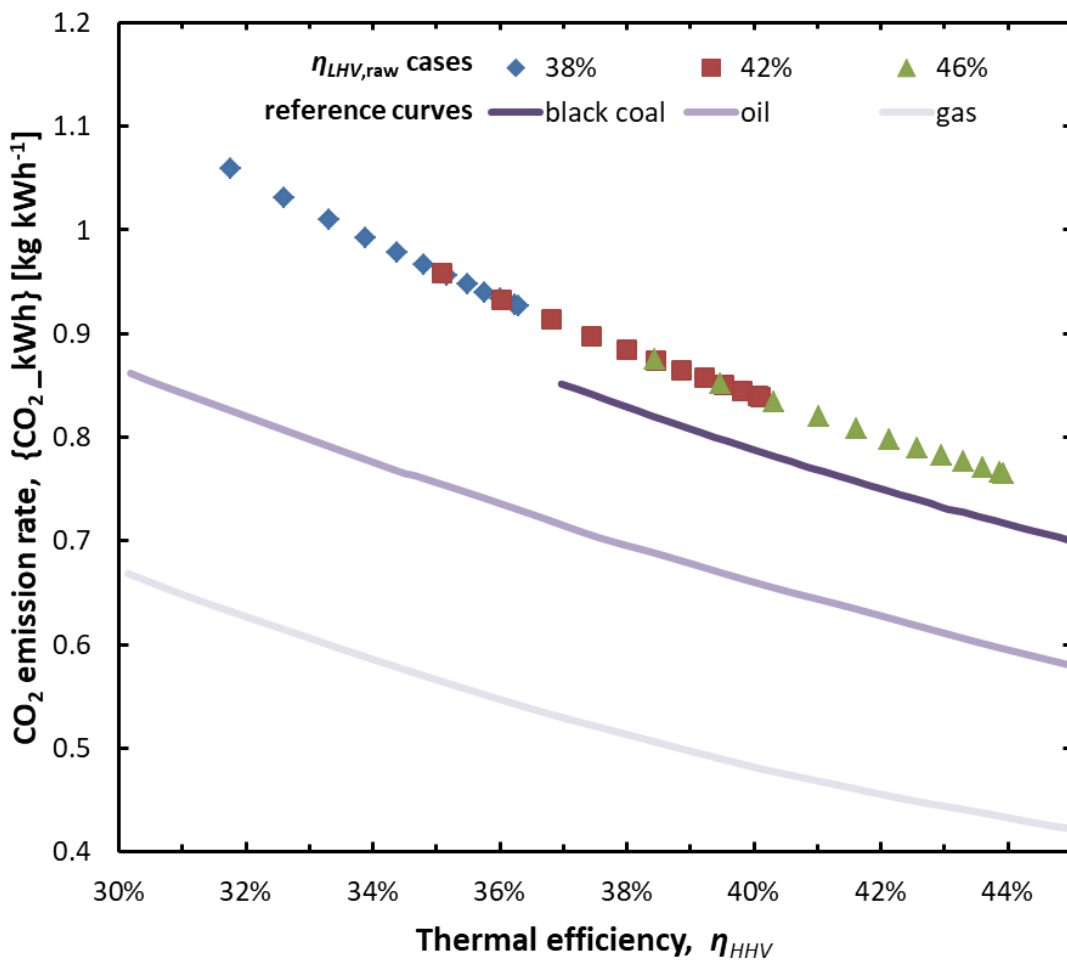
Figure 7.18 Dependence between carbon dioxide emission rate and thermal efficiency of exemplary power plants operating on fossil fuels [114,116]

Table 7.12 Reference cases applied to CO_2 reduction analysis [112,117]

scenario	thermal efficiency $\eta_{LHV,\text{raw}}$	refers to power generation unit	electricity output	commissioned
1	38%	Belchatow No. 1-12	370 MW	1980s
2	42%	Belchatow No. 14	858 MW	2011
3	46%	Kozienice No. 11	1075 MW	2017

On the horizontal axis of Fig. 7.18, the thermal efficiency on *HHV* is shown, according to Eq. (7.13). Corresponding data points in each scenario are distributed in regard to water share value according to the same pattern as in Fig. 7.17. The reference trends below data markers illustrate the tendencies of carbon intensity applicable for bituminous (black) coal [116], oil and natural gas [114]. The estimated CO_2 emission for raw coal in the case of 38% in thermal efficiency is equal to 1.054 kg kWh^{-1}, what is coherent value with information on average actual emission published in 2015 by the operator of Belchatow power generation complex (1.069 kg kWh^{-1}) [118]. The levels of emission attained for raw coal in scenarios 2 and 3 are 0.954 and 0.871 kg kWh^{-1}. Due to utilization of the same simulation results in all cases, the total decrease in the emission rate in comparison to initial level is 12.1%. Still, the displacement of data points becomes more tight as the share of water declines, therefore a claim can be made that the most beneficial period in terms of lifting the environmental and technical efficiency of the power generation unit falls into the initial stage of drying. The trend exhibited by the data points, together with three reference curves, agree with the general rule that combustion of fuels characterized with higher hydrogen-to-carbon ratio results in lower level of carbon emission.

7.7.2 Influence of input coal assortment on calorific value of lignite

As it was already stated (Fig. 7.6), the decline in object size entails considerable reduction of time required to complete the drying process. For that reason, the utilization of the grinder (expressed by its heat consumption) which prepares the fuel for the drying, followed by combustion or gasification, is rewarded by diminishing of the time and energy input to the dryer. In this section, the latter component of this interdependence is presented. In order to determine the impact of coal fragmentation on the potential of its heating value's enhancement, three multi-particle scenarios introduced in section 7.5 were investigated.

In Fig. 7.19 the simulated progress of drying for various lignite batches was presented in correlation to the increasing *LHV*. The largest improvement of coal quality is observed in the initial stage of the process. In order to double the lower heating value of raw lignite (8.56 MJ kg^{-1}), circa 30 minutes is required for fine coal, twice as much for medium coal and over 400 minutes for thick coal. This disparity between coal assortments grows as the process continues. To give an example, if the target level is 18 MJ kg^{-1} (equivalent to *WS*≈14% and *WP*≈8%), the difference between fine and medium coal equals 47 minutes. Whether the objective rises to 20 MJ kg^{-1} (water share around 14%, water percentage around 8%), the difference extends to approximately 2 hours.

Taking the deliberations above into account, the application of finest possible grains of coal is the most beneficial in terms of enhancement of calorific value. However, the fragmentation of lignite requires work provided by the grinder. Thus, for global analysis of the power generation unit efficiency, the loss side should also be discussed, with the evaluation of power input required for achieving the demanded size of grain.
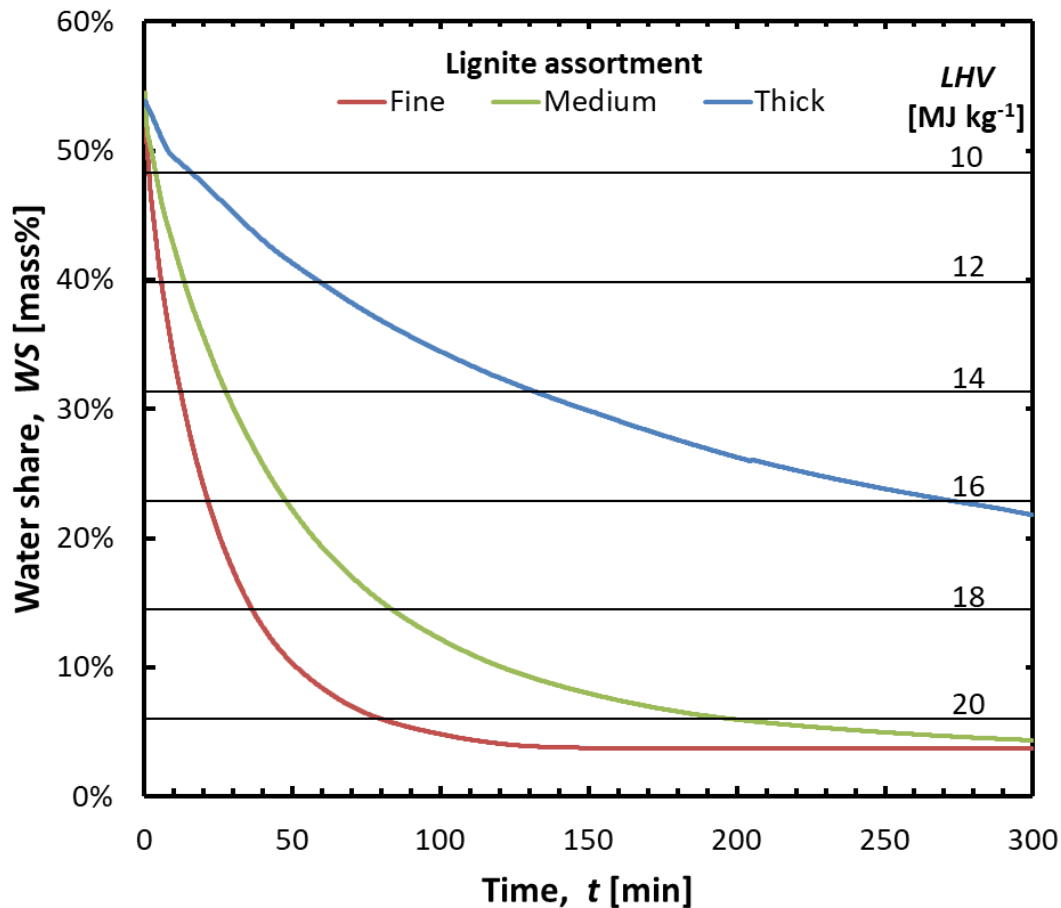
Figure 7.19 Simulated increase of lower heating value for various lignite assortments dried at 150 °C

7.7.3 Influence of process parameters variability on calorific value of lignite

The selected parameters analyzed in terms of numerical model's sensitivity (section 7.5.2) on their modifications were adapted to gain insight into their influence on upgrading the calorific value of lignite. The time dependencies of water share and *LHV* for two material properties (density, initial water percentage) and sample size are illustrated and discussed in this part. The adapted case is 10 mm particle dried at 150 °C.

Figure 7.20 presents the abovementioned correlations in regard to dry coal density. It should be taken into consideration that value HHV_c is fixed in that case for the purpose of discussion only, as the actual density is a derivative of dry coal contents,

which ratio influences the heating value of coal. The gap in upgrading of the lower heating value expands between particular scenarios as the process continues. For instance, achieving of 12 MJ kg^{-1} consumes between 21.6 and 24.7 minutes, whereas drying oriented on obtaining lignite of 18 MJ kg^{-1} is predicted to last from 32.7 to 37.6 minutes. The first quarter hour induces a 0.54 MJ kg^{-1} difference between extreme cases. After another 15 minutes, the simulated level of *LHV* for reference curve reaches 17.03 MJ kg^{-1} and the coal characterized with theoretical DBC density of 2304 kg m^{-3} attains 15.64 MJ kg^{-1}. At the 45-minute mark, the difference is reduced to the level of 0.5 – 0.6 MJ kg^{-1} and further decrease to reach the saturation level around one hour since the start of the process.
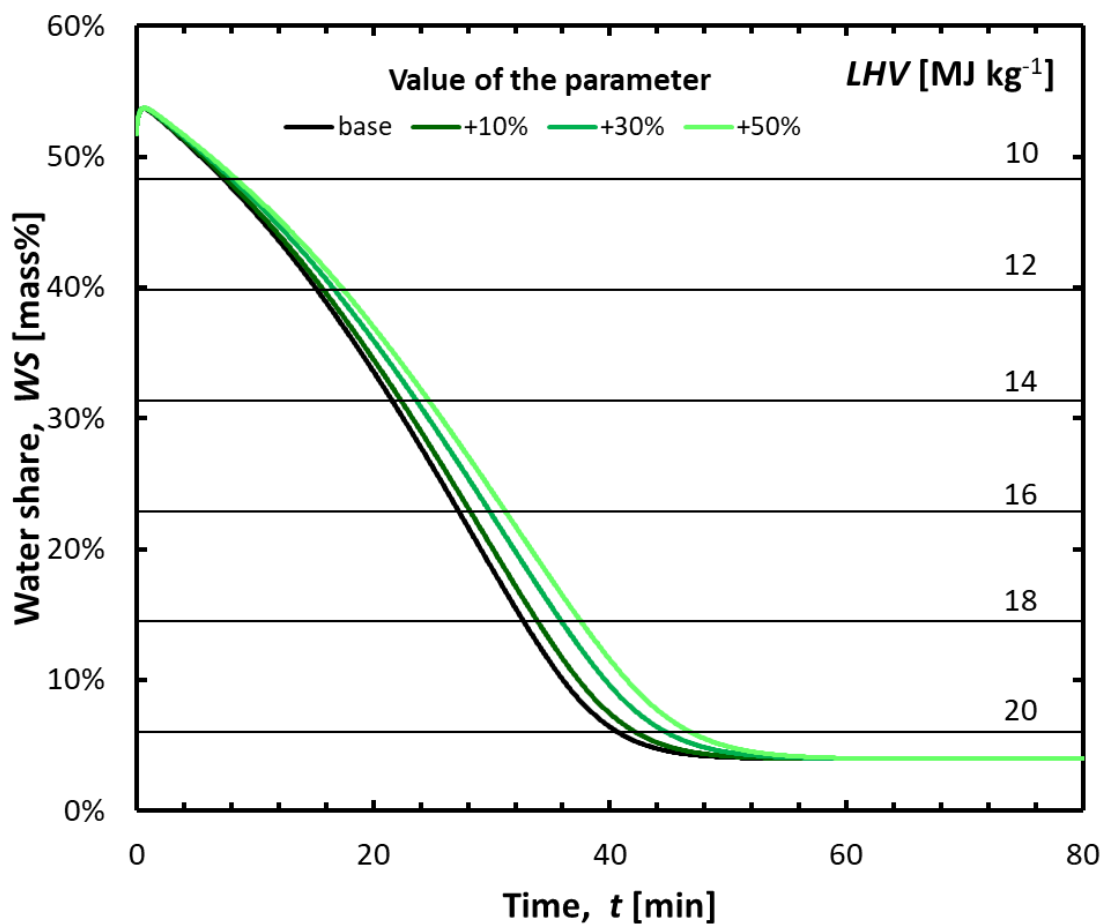
Figure 7.20 Simulated increase of lower heating value for variable dry base coal density

In Fig. 7.21, the chart of water share against time was shown for initial water share as a parameter. As explained in section 7.5, scenarios of +30% and +50% may have only theoretical meaning. Because of diverse share of water in raw coal, the initial values of *LHV* differ considerably in the particular cases, with the minimum level of 3.16 MJ kg^{-1}. Half an hour of simulated drying results in 9 MJ kg^{-1} of difference between curves representing the lowest and highest initial moisture content. After 45 minutes of the process this disparity diminishes to 4 MJ kg^{-1} and another 5 minutes entails the reduction to 1 MJ kg^{-1}. Comparing the +10% scenario with reference case, the time required for preparation of fuel of 12 MJ kg^{-1} in *LHV* is 32% longer, whereas 18 MJ kg^{-1} is attained with 10% of surplus in drying time.
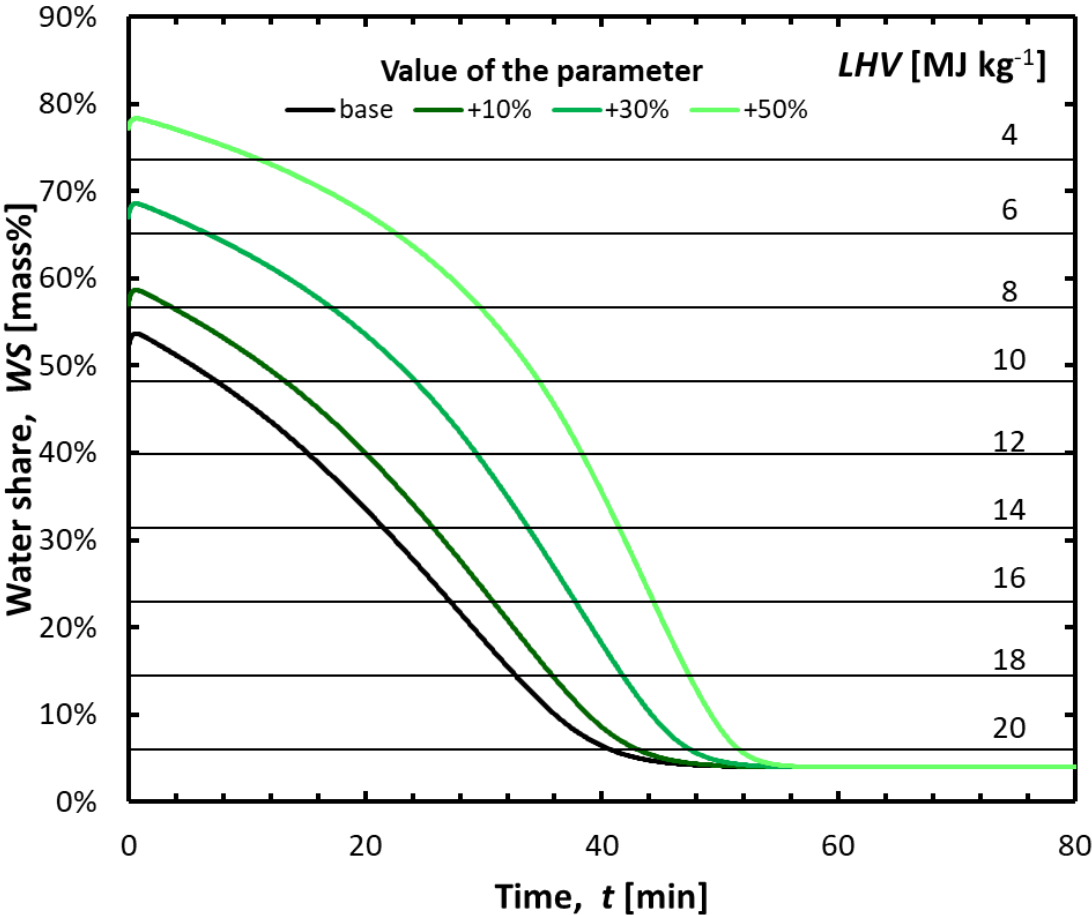
Figure 7.21 Simulated increase of lower heating value for variable initial water share

The final parameter investigated in this section is the particle diameter. The set of curves presented in Fig. 7.22 has an intersection around the 9th minute of the simulation. That fact is brought about by a sudden decline in water share relevant to the predicted fall of droplets from the surface of two largest objects (13 and 15 mm). The smaller samples may achieve the sooner increase of the calorific value. The 30-minute mark signalizes the level of *LHV* equal to 17.03, 15.76, 14.82 and 13.93 MJ kg^{-1} for base scenario and cases of subsequently increased sample diameter.
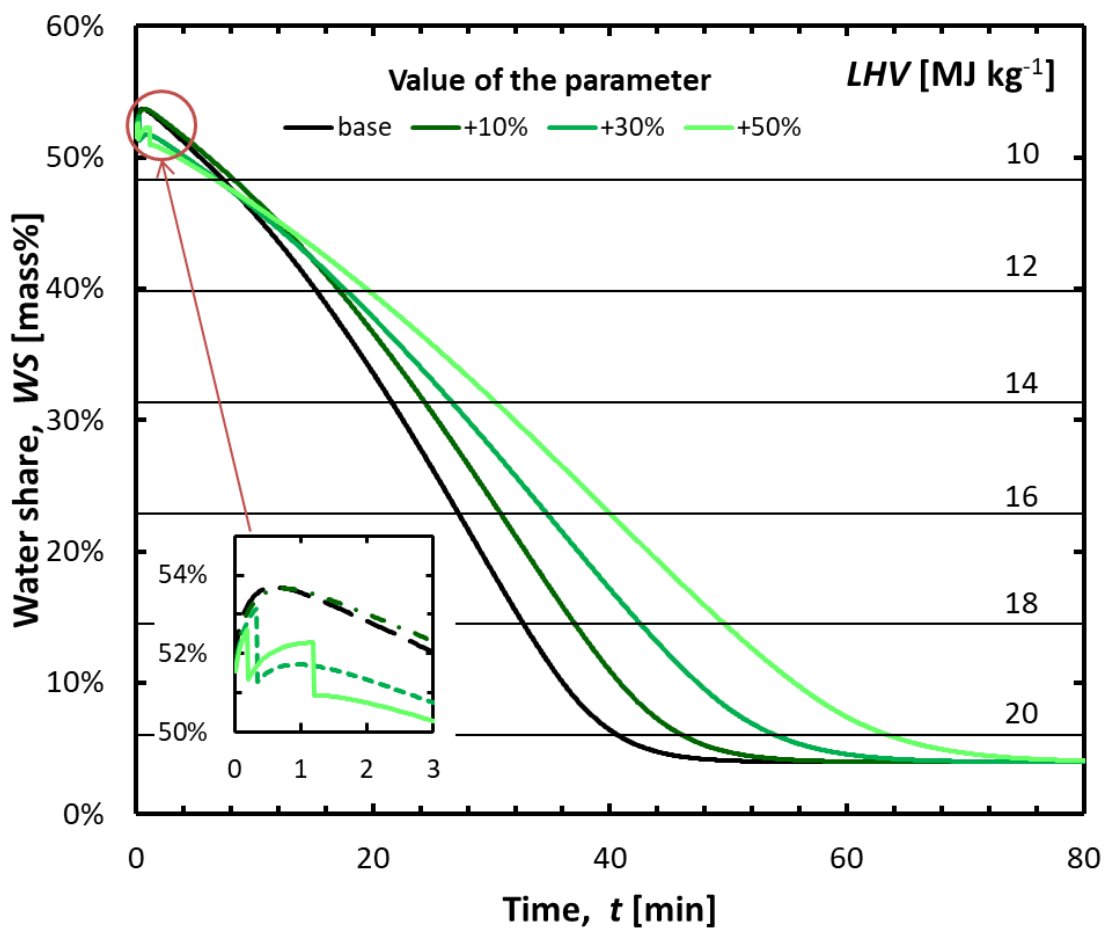
Figure 7.22 Simulated increase of lower heating value for variable sample diameter

In general, the influence of various initial water share on the calorific value enhancement is explicit mainly during the initial stage of drying, the impact of increased size becomes apparent after a certain time, whereas remaining material parameters, represented in this comparison by density, evince slight variation of *LHV* enhancement throughout the drying process.

CHAPTER 8

Summary

8.1 Conclusions

The analysis of drying properties of lignite exposed to superheated steam atmosphere was performed in relation to coals from Polish mines in Belchatow and Turow. The experimental attempts involved spherical objects of four diameters dried in the gaseous medium heated up to four various temperatures. The measurements of changing weight and temperature were used to prepare the drying characteristics, which included time charts of moisture content, drying rate and temperature of sample surface and interior. The fundamental correlations between sample size, steam temperature and drying indicators were formulated. The approximation formula was proposed to calculate expected time of drying as a function of two main experimental conditions. Moreover, the detailed analysis of the particular stages of drying was performed, considering the transport and evaporation of two general types of moisture in coal: free and bound water.

Applying the experimental results, a thermodynamic deliberation on the heat transfer between steam and coal during constant drying rate period was done, producing approximation equation on the heat transfer coefficient and the empirical formula on maximum level of the drying rate. The correlation between initial water share and initial density of lignite was confirmed and supplemented with an attempt to include the

prevailing coal lithotype in this interdependence. In terms of experimental repeatability, a negative impact of foreign inclusions from the adjacent rocks into lignite structure was observed. Relying on samples originated in different geological surroundings, the functions of equilibrium moisture content were elaborated. They were also used to successfully validate formulated general dependencies between material properties (water share, dry bulk density) and drying indicators such as rate of dewatering, with homogenous results distribution obtained for Belchatow coal and wide dispersion in the case of Turow lignite. Significantly sooner evaporation of water was found out for coal from Turow mine, comparing to its counterpart from the central part of Poland.

For the sake of comprehensive understanding of the drying process, observations of coal surface were performed with video recorder. Due to such approach, the acquisition of data on cracking, shrinkage and droplet formation was possible. The samples of larger size exhibited higher vulnerability on cracking. The expansion of sample surface and exposition of porous structure to the direct impact of the drying medium might enhance the rate of drying. The evaluation of shrinkage was performed, confirming the major influence of this phenomenon for water share below 40%.

On the assumption of isotropy of the properties within the coal sphere, a one dimensional mathematical model of drying was prepared. It used the concepts of the receding wet core and border of evaporation. The deliberation on heat and transfer phenomena occurring between lignite and superheated steam was conducted with reference to results of the previous studies on coal and other porous materials, tables of thermodynamic properties of water as well as the results of experimental investigation. The temperature distribution over the drying period was visualized, illustrating the increase of heating homogeneity with decline of the sample diameter. In order to determine decisive material properties of lignite, a sensitivity analysis of the drying

model was performed, indicating initial water share as the most sensitive parameter, followed by density and thermal conductivity of the dry coal matter. An attempt to determine the industrial applicability of divergent coal assortments was made, resulting in correlation curves between the fragmentation of lignite and potential of increase in calorific value. The required time of drying for attaining particular levels of lower heating value was also evaluated with regard to varying material parameters, such as density or water percentage.

The empirical trials and numerical simulations were supplemented with auxiliary activities aimed at achieving necessary information. They included, but were not restricted to in-house experimentations deriving the thermal conductivity, outsourced laboratory tests of heat capacity or transformation of numerical results with the application of self-made data processing utility. Some of these procedures are described in the Appendix section, following this chapter.

8.2 Recommendations

The present work focused mainly on analysis of fundamental properties of lignite on the kinetics of drying in superheated steam. However, the findings attained during the research inspired a series of questions for possible investigation in the future.

For instance, the investigation of relationship between issues of physical structure, exhibited by predominant lithotype, and attributes related to drying, triggered the interest in the manner of water storage in the porous structure of lignite. Although the porosity of coal has already been investigated by means of gas absorption [119] or X-ray irradiation [120], the nature of pores still evinces a research potential. A technique, which could be potentially applied to visualize the macro- and mesopores (larger than 2 nm) is known as FIB-SEM (focused ion beam combined with scanning electron

microscope). It was successfully applied to investigate the microstructure of electrodes in solid oxide fuel cells [121]. In the case of lignite, a detailed insight into its pores network is expected to be achieved, including the hollows without channel connection with the ambience (and therefore unreachable by the gas absorption methods). Still, it should be taken into consideration that the volume of interest in a single FIB-SEM measurement can include around several thousands of cubic micrometers. For that reason, a series of tests would be required to gain enough comparative material and draw some solid conclusions validated by the observation of various areas of the coal structure.

Another area discussed in this work in which a further investigation is desirable is the analysis of superheated steam drying in relation to raising the thermal efficiency. In this study an attempt was made to evaluate the increase in calorific value of lignite as a function of residence time in dryer operating on superheated steam. The results were related to possible impact on the efficiency and carbon intensity of the coal-fired power plants. However, only the gain side was discussed, without estimating the costs of decreasing the water content. Hence, a study on heat consumption by the dryer could be informative, preferably with regard to larger scale of the research. The latter aspect concerns also the fragmentation of coal. As indicated in this study, the assortment of dried material exhibits strong correlation with the rate of incline in the heating value. Therefore, besides drying equipment, the workload of the grinder preparing the fuel for further utilization should also be taken into account. By such means, indication of the optimal parameters of the fuel preparation system may be possible.

On the subject of technological dependences between fuel and energy conversion equipment, the complex feasibility study might be interesting follow-up of the fundamental research of lignite properties. It should involve all stages of fuel

154

utilization, from the production site to the ultimate physical and chemical transformation. However, the emphasis could be put on the stages of direct preparation and utilization of lignite. For instance, the lignite batches investigated in this work with regard to their drying properties were also examined for prospective gasification in IGCC technology. Whereas physical parameters related to heat and water transfer were mainly analyzed in the case of drying, the chemical composition of ash, determining the viscosity of molten slag was decided a critical aspect in feasibility of integrated coal gasification [101]. Combination of fuel property analyses related to various stages of its application may contribute to more effective allocation of resources by national economies seeking for effective power generation technologies relying on fossil fuels.

References

1. Andruleit H., Babies H. G., Fleig S., Ladage S., Meßner J., Pein M., Rebscher D., Schauer M., Schmidt S., von Goerne G.; *Energy Study 2016. Reserves, resources and availability of energy resources* (Industrial Report), Hannover, 2016.

2. Lindner E.; *Chemie für Ingenieure*, Lindner Verlag: Karlsruhe, 1993.

3. Hilt C.; Die Beiziehungen zwischen der Zusammensetzung und den technischen Eigenschaften der Steinkohle, *Bezirksvereinigung Verhandungen der Dtsch. Ingenieure Zeitschrift*, **17**, pp. 194–202, 1873.

4. Thomas L.; *Coal Geology*, Wiley-Blackwell: Chichester, 2013.

5. Patrycy A.; Wpływ produkcji energii elektrycznej w źródłach opalanych węglem brunatnym na stabilizację ceny energii dla odbiorców końcowych, *Górnictwo i Geoinżynieria (AGH J. Min. Geoengin.*, **35**, pp. 249–260, 2011.

6. Kicki J., Kozioł W.; Technologia eksploatacji złóż węgla brunatnego. In: *Surowce energetyczne*; Mokrzycki E. Ed.; Centrum PPGSMiE PAN: Kraków, 1996.

7. Kasztelewicz Z.; *Polskie górnictwo węgla brunatnego*, Związek Pracodawców "Porozumienie Producentów Węgla Brunatnego" w Bełchatowie: Bełchatów, 2004.

8. PGE Górnictwo i Energetyka Konwencjonalna S.A.; Kopalnia Węgla Brunatnego Bełchatów, Available online: http://www.kwbbelchatow.pgegiek.pl.

9. United Nations Framework Convention on Climate Change; Compilation and synthesis of fifth national communications. Executive summary, pp. 1–16, 2011.

10. Polskie Sieci Elektroenergetyczne; *Annual Report on the Polish Power System operation* (Industrial Report), 2016.

11. Pietraszewski A.; Polskie górnictwo węgla brunatnego w 2016 roku, *Węgiel brunatny*, pp. 10–21, 2017.

12. PGE Górnictwo i Energetyka Konwencjonalna S.A.; Oddział Elektrownia Bełchatów, Available online: https://elbelchatow.pgegiek.pl/ (accessed on Jan 21, 2018).

13. PGE Górnictwo i Energetyka Konwencjonalna S.A.; Oddział Elektrownia Turów, Available online: https://elturow.pgegiek.pl/ (accessed on Jan 21, 2018).

14. Zespół Elektrowni Pątnów-Adamów-Konin; ZE PAK, Available online: http://zepak.com.pl/pl/ (accessed on Jan 21, 2018).

15. Allardice D. J.; The Water in Brown Coal. In: *The Science of Victorian Brown Coal: Structure, Properties and Consequence for Utilization*; Durie R. A. Ed.; Butterworth-Heinemann Ltd.: Oxford, 1993.

16. Le Roux M., Campbell Q. P.; An investigation into an improved method of fine coal dewatering, *Miner. Eng.*, **16**, pp. 999–1003, 2003.

17. Karr C.; *Analytical methods for coal and coal products*, Academic Press: New York, 1978.

18. Karthikeyan M., Zhonghua W., Mujumdar A. S.; Low-rank coal drying technologies - Current status and new developments, *Dry. Technol.*, **27**, pp. 403–415, 2009.

19. Charrière D., Behra P.; Water sorption on coals, *J. Colloid Interface Sci.*, **344**, pp. 460–467, 2010.

20. Rao Z., Zhao Y., Huang C., Duan C., He J.; Recent developments in drying and dewatering for low rank coals, *Prog. Energy Combust. Sci.*, **46**, pp. 1–11, 2015.

21. Evans D. G.; The brown-coal/water system: Part 4. Shrinkage on drying, *Fuel*, **52**, pp. 186–190, 1973.

22. Mraw S. C., O'Rourke D. F.; Water in coal pores: The enthalpy of fusion reflects pore size distribution, *J. Colloid Interface Sci.*, **89**, pp. 268–271, 1982.

23. Lynch L. J., Webster D. S.; Effect of thermal treatment on the interaction of brown coal and water: a nuclear magnetic resonance study, *Fuel*, **61**, pp. 271–275, 1982.

24. Allardice D. J., Young B. C.; Utilisation of Low Rank Coals. In: *18th International Pittburgh Coal Conference*; 2001.

25. Pikon J., Mujumdar A. S.; Drying of Coal. In: *Handbook of Industrial Drying*; Mujumdar A. S. Ed.; CRC Press: Boca Raton, 2006.

26. Allardice D. J., Clemow L. M., Favas G., Jackson W. R., Marshall M., Sakurovs R.; The characterisation of different forms of water in low rank coals and some hydrothermally dried products, *Fuel*, **82**, pp. 661–667, 2003.

27. Domazetis G., Barilla P., James B. D., Glaisher R.; Treatments of low rank coals for improved power generation and reduction in Greenhouse gas emissions, *Fuel Process. Technol.*, **89**, pp. 68–76, 2008.

28. European Comission; EU Emissions Trading System, Available online: https://ec.europa.eu/clima/policies/ets_en (accessed on Jan 17, 2018).

29. United Nations; Kyoto Protocol, Available online: http://unfccc.int/kyoto_protocol/items/2830.php (accessed on Jan 18, 2018).

30. Agraniotis M., Koumanakos A., Doukelis A., Karellas S., Kakaras E.; Investigation of technical and economic aspects of pre-dried lignite utilisation in a modern lignite power plant towards zero CO_2 emissions, *Energy*, **45**, pp. 134–141, 2012.

31. Mujumdar A. S.; Part II - Description of Various Dryer Types. In: *Handbook of industrial drying*; CRC Press: Boca Raton, 2006.

32. Uslu T., Atalay Ü.; Microwave heating of coal for enhanced magnetic removal of pyrite, *Fuel Process. Technol.*, **85**, pp. 21–29, 2004.

33. Tahmasebi A., Yu J., Li X., Meesri C.; Experimental study on microwave drying of Chinese and Indonesian low-rank coals, *Fuel Process. Technol.*, **92**, pp. 1821–1829, 2011.

34. Ohm T. I., Chae J. S., Lim J. H., Moon S. H.; Evaluation of a hot oil immersion drying method for the upgrading of crushed low-rank coal, *J. Mech. Sci. Technol.*, **26**, pp. 1299–1303, 2012.

35. Kim H.-S., Matsushita Y., Oomori M., Harada T., Miyawaki J., Yoon S.-H., Mochida I.; Fluidized bed drying of Loy Yang brown coal with variation of temperature, relative humidity, fluidization velocity and formulation of its drying rate, *Fuel*, **105**, pp. 415–424, 2013.

36. Wang W.-C.; Laboratory investigation of drying process of Illinois coals, *Powder Technol.*, **225**, pp. 72–85, 2012.

37. Tahmasebi A., Yu J., Han Y., Zhao H., Bhattacharya S.; A kinetic study of microwave and fluidized-bed drying of a Chinese lignite, *Chem. Eng. Res. Des.*, **92**, pp. 54–65, 2014.

38. Agraniotis M., Karellas S., Violidakis I., Doukelis A., Grammelis P., Kakaras E.; Investigation of pre-drying lignite in an existing Greek power plant, *Therm. Sci.*, **16**, pp. 283–296, 2012.

39. Pakowski Z., Adamski R., Kwapisz S.; Effective diffusivity of moisture in low rank coal during superheated steam drying at atmospheric pressure, *Chem. Process Eng. - Inz. Chem. i Proces.*, **33**, pp. 43–51, 2012.

40. Michalski M.; Suszenie węgla brunatnego w złożu fluidalnym z wykorzystaniem niskotemperaturowego źródła ciepła (PhD Thesis), Politechnika Wrocławska, 2015.

41. Karthikeyan M., Zhonghua W., Mujumdar A. S.; Low-Rank Coal Drying Technologies—Current Status and New Developments, *Dry. Technol.*, **27**, pp. 403–415, 2009.

42. Fleissner H.; The drying of fuels and the Austrian coal industry, *Sonderdruck Spartwirtschaft*, **10/11**, 1927.

43. Bergins C.; Kinetics and mechanism during mechanical/thermal dewatering of lignite, *Fuel*, **82**, pp. 355–364, 2003.

44. Miura K., Mae K., Ashida R., Tamura T., Ihara T.; Dewatering of coal through solvent extraction, *Fuel*, **81**, pp. 1417–1422, 2002.

45. Fujitsuka H., Ashida R., Miura K.; Upgrading and dewatering of low rank coals through solvent treatment at around 350°C and low temperature oxygen reactivity of the treated coals, *Fuel*, **114**, pp. 16–20, 2013.

46. Iwai Y., Koujina Y., Arai Y., Watanabe I., Mochida I., Sakanishi K.; Low temperature drying of low rank coal by supercritical carbon dioxide with methanol as entrainer, *J. Supercrit. Fluids*, **23**, pp. 251–255, 2002.

47. Kanda H., Makino H.; Energy-efficient coal dewatering using liquefied dimethyl ether, *Fuel*, **89**, pp. 2104–2109, 2010.

48. Lockhart N. C., Hart G. H.; Electro-osmotic dewatering of fine suspensions: the efficacy of current interruptions, *Dry. Technol.*, **6**, pp. 415–423, 1988.

49. Rabie H. R., Mujumdar A. S., Weber M. E.; Interrupted electroosmotic dewatering of clay suspensions, *Sep. Technol.*, **4**, pp. 38–46, 1994.

50. Hausbrand E.; *Das Trocknen mit Luft und Dampf*, Springer-Verlag: Berlin, 1903.

51. Wenzel L., White R. R.; Drying Granular Solids in Superheated Steam Engineering development, *Ind. Eng. Chem.*, **43**, pp. 1829–1837, 1951.

52. Yoshida T., Hyodo T.; Evaporation of water in air, humid air, and superheated steam, *Ind. Eng. Chem. Process Des. Dev.*, **97**, pp. 207–214, 1970.

53. Kiiskinen H. T., Edelmann K. E.; Superheated Steam Drying of Paper Web, *Dev. Chem. Eng. Miner. Process.*, **10**, pp. 349–365, 2002.

54. Mujumdar A. S.; Superheated steam drying. In: *Handbook of Industrial Drying*; Mujumdar A. S. Ed.; CRC Press: Boca Raton, 2006.

55. Hoehne O., Lechner S., Schreiber M., Krautz H. J.; Drying of Lignite in a Pressurized Steam Fluidized Bed—Theory and Experiments, *Dry. Technol.*, **28**, pp. 5–19, 2009.

56. Potter O. E., Keogh A. J.; Cheaper power from high moisture brown coals, *J. Inst. Energy*, **52**, pp. 143–146, 1979.

57. Potter O. E., Beeby C. J., Fernando W. J. N., Ho P.; Drying brown coal in steam-heated steam-fluidised beds, *Dry. Technol.*, **2**, pp. 219–234, 1984.

58. Potter O. E., Keogh A. J.; Drying high-moisture coals before liquefaction or gasification, *Fuel Process. Technol.*, **4**, pp. 217–227, 1981.

59. Bongers G. D., Jackson W. R., Woskoboenko F.; Pressurised steam drying of Australian low-rank coals. Part 1. Equilibrium moisture contents, *Fuel Process. Technol.*, **57**, pp. 41–54, 1998.

60. Bongers G. D., Jackson W. R., Woskoboenko F.; Pressurised steam drying of Australian low-rank coals. Part 2. Shrinkage and physical properties of steam dried coals , preparation of dried coals with very high porosity, *Fuel Process. Technol.*, **64**, pp. 13–23, 2000.

61. Nunokawa M., Asano T.; Progress and utilization of Nakoso 250MW air-blown IGCC demonstration project, *JSME Mech. Eng. J.*, **1**, pp. 1–8, 2014.

62. Fushimi C., Kansha Y., Aziz M., Mochidzuki K., Kaneko S., Tsutsumi A., Matsumoto K., Yokohama K., Kosaka K., Kawamoto N., Oura K., Yamaguchi Y., Kinoshita M.; Novel Drying Process Based on Self-Heat Recuperation Technology, *Dry. Technol.*, **29**, pp. 105–110, 2010.

63. RWE Power; The WTA technology: An advanced method of processing and drying lignite (Commercial Brochure), pp. 1–6, 2013.

64. Tang Z., Cenkowski S., Muir W. E.; Modelling the Superheated-steam Drying of a Fixed Bed of Brewers' Spent Grain, *Biosyst. Eng.*, **87**, pp. 67–77, 2004.

65. Sa-Adchom P., Swasdisevi T., Nathakaranakule A., Soponronnarit S.; Mathematical model of pork slice drying using superheated steam, *J. Food Eng.*, **104**, pp. 499–507, 2011.

66. Morey R. V., Zheng H., Kaliyan N., Pham M. V.; Modelling of superheated steam drying for combined heat and power at a corn ethanol plant using Aspen Plus software, *Biosyst. Eng.*, **119**, pp. 80–88, 2014.

67. Liu Y., Kansha Y., Ishizuka M., Fu Q., Tsutsumi A.; Experimental and simulation investigations on self-heat recuperative fluidized bed dryer for biomass drying with superheated steam, *Fuel Process. Technol.*, **136**, pp. 79–86, 2015.

68. Chen Z., Wu W., Agarwal P. K.; Steam-drying of coal. Part 1. Modeling the behavior of a single particle, *Fuel*, **79**, pp. 961–973, 2000.

69. Chen Z., Agarwal P. K., Agnew J. B.; Steam drying of coal. Part 2. Modeling the operation of a fuidized bed drying unit, *Fuel*, **80**, pp. 209–223, 2001.

70. Looi A. Y., Golonka K., Rhodes M.; Drying kinetics of single porous particles in superheated steam under pressure, *Chem. Eng. J.*, **87**, pp. 329–338, 2002.

71. Olufemi B. A., Udefiagbon I. F.; Modelling the Drying of Porous Coal Particles in Superheated Steam, *Chem. Biochem. Eng. Q.*, **24**, pp. 29–34, 2010.

72. Zhang K., You C.; Experimental and Numerical Investigation of Convective Drying of Single Coarse Lignite Particles, *Energy & Fuels*, **24**, pp. 6428–6436, 2010.

73. Kiriyama T., Sasaki H., Hashimoto A., Kaneko S., Maeda M.; Experimental Observations and Numerical Modeling of a Single Coarse Lignite Particle Dried in Superheated Steam, *Mater. Trans.*, **54**, pp. 1725–1734, 2013.

74. Kiriyama T., Sasaki H., Hashimoto A., Kaneko S., Maeda M.; Size Dependence of the Drying Characteristics of Single Lignite Particles in Superheated Steam, *Metall. Mater. Trans. E*, **1**, pp. 349–363, 2014.

75. Kiriyama T., Sasaki H., Hashimoto A., Kaneko S., Maeda M.; Evaluation of Drying Rates of Lignite Particles in Superheated Steam Using Single-Particle Model, *Metall. Mater. Trans. E*, **3**, pp. 308–316, 2016.

76. Ministerstwo Gospodarki; *Polityka energetyczna Polski do 2030 roku* (Industrial Report), Warszawa, 2009.

77. Zmiany w PGE papierkiem lakmusowym dla polskiego atomu, Available online: http://energetyka.defence24.pl/297505,zmiany-w-pge-papierkiem-lakmusowym-dla-polskiego-atomu (accessed on Feb 16, 2016).

78. Maciążek P.; Kontrakt różnicowy zagrożony. Jaki model finansowania dla polskiego atomu?, Available online: http://energetyka.defence24.pl/266021,kontrakt-roznicowy-zagrozony-jaki-model -finansowania-dla-polskiego-atomu (accessed on Feb 16, 2016).

79. Elektrownia atomowa w Polsce. Decyzja o jej lokalizacji powinna zapaść za dwa lata, Available online: http://www.money.pl/gospodarka/wiadomosci/artykul/elektrownia-atomowa-w-p olsce-decyzja-o-jej,133,0,1717125.html (accessed on Feb 16, 2016).

80. Ministerstwo Gospodarki; *Prognoza zapotrzebowania na paliwa i energię do 2030 roku* (Industrial Report), Warszawa, 2009.

81. Umar D. F., Usui H., Daulay B.; Effects of Processing Temperature of Hot Water Drying on the Properties and Combustion Characteristics of an Indonesian Low Rank Coal, *Coal Prep.*, **25**, pp. 313–322, 2005.

82. Kopp O. C., Harris L. A.; Initial volatilization temperatures and average volatilization rates of coal - their relationship to coal rank and other characteristics, *Int. J. Coal Geol.*, **3**, pp. 333–348, 1984.

83. Molnar K.; Experimental Techniques in Drying. In: *Handbook of Industrial Drying*; Mujumdar A. S. Ed.; CRC Press: Boca Raton, 2006.

84. Allardice D. J., Chaffee A. L., Jackson W. R., Marshall M.; Water in Brown Coal and Its Removal. In: *Advances in the Science of Victorian Brown Coal*; Li C.-Z. Ed.; Elsevier Ltd.: Oxford, 2004.

85. Komatsu Y., Sciazko A., Zakrzewski M., Kimijima S., Hashimoto A., Kaneko S., Szmyd J. S.; An experimental investigation on the drying kinetics of a single coarse particle of Belchatow lignite in an atmospheric superheated steam condition, *Fuel Process. Technol.*, **131**, pp. 356–369, 2015.

86. Zakrzewski M., Komatsu Y., Sciazko A., Akiyama T., Hashimoto A., Shikazono N., Kaneko S., Kimijima S., Szmyd J. S., Kobayashi Y.; Comprehensive study on the kinetics and modelling of superheated steam drying of Belchatow lignite from Poland, *JSME Mech. Eng. J.*, **3**, pp. 1–12, 2016.

87. Widera M.; Changes of the lignite seam architecture — A case study from Polish lignite deposits, *Int. J. Coal Geol.*, **114**, pp. 60–73, 2013.

88. Sciazko A., Komatsu Y., Zakrzewski M., Akiyama T., Hashimoto A., Shikazono N., Kaneko S., Kimijima S., Szmyd J., Kobayashi Y.; Influence of geological variations on lignite drying kinetics in superheated steam atmosphere for Belchatow deposit located in the central Poland, *Therm. Sci.*, **20**, pp. 1185–1198, 2016.

89. Sciazko A., Komatsu Y., Zakrzewski M., Akiyama T., Hashimoto A., Shikazono N., Kaneko S., Kimijima S., Szmyd J., Kobayashi Y.; Experimental Attempts to Investigate the Influence of Petrographic Properties on Drying Characteristics of Lignite in Superheated Steam Atmosphere, *Energies*, **9**, 2016.

90. Komatsu Y., Sciazko A., Zakrzewski M., Akiyama T., Hashimoto A., Shikazono N., Kaneko S., Kimijima S., Szmyd J. S., Kobayashi Y.; Towards the improvement of thermal efficiency in lignite-fired power generation: Concerning the utilization of Polish lignite deposits in state-of-the-art IGCC technology, *Int. J. Energy Res.*, **40**, pp. 1757–1772, 2016.

91. Kwiecińska B., Wagner M.; *Atlas petrograficzny węgla brunatnego : litotypy i macerały*, Wydawnictwo JAK: Kraków, 2001.

92. Widera M.; Macroscopic lithotype characterisation of the 1st Middle-Polish (1st Lusatian) Lignite Seam in the Miocene of central Poland, *Geologos*, **18**, pp. 1–11, 2012.

93. Ticleanu N., Scradeanu D., Popa M., Milutinovici S., Popa R., Preda I., Ticleanu M., Savu C., Diaconita D., Barus T., Petrescu I., Dinulescu C., Maftei R.; The relation between the lithotypes of Pliocenne coals from Oltenia and thier main quality characteristics, *Bull. Czech Geol. Surv.*, **74**, pp. 169–174, 1999.

94. Klutz H.-J., Moser C., von Bargen N.; The RWE Power WTA process (Fluidized bed drying) as a key for higher efficiency, *Górnictwo i Geoinżynieria (AGH J. Min. Geoengin.*, **35**, pp. 147–153, 2011.

95. Tang Z., Cenkowski S.; Equilibrium moisture content of spent grains in supherheated steam under atmospheric pressure, *Trans. ASAE*, **44**, pp. 1261–1264, 2001.

96. Arima K., Tsuchiyama Y., Suzuki T., Sawatsubashi T., Kakigami H., Kinoshita M., Ishii H.; Drying Characteristics of Wet Brown Coal Particles in a Steam Fluidized Bed, *Kagaku Kogaku Ronbunshu*, **41**, pp. 100–106, 2015.

97. Hager J., Hermansson M., Wimmerstedt R.; Modelling steam drying of a single porous ceramic sphere: Experiments and simulations, *Chem. Eng. Sci.*, **52**, pp. 1253–1264, 1997.

98. Kollmann F. F. P.; High temperature drying: research, application and experience in Germany, *For. Prod. J.*, **11**, pp. 508–515, 1961.

99. Beeby C. J., Potter O. E.; Steam drying. In: *The 4th International Drying Symposium*; American Society of Chemical Engineers: Washington, D. C., 1985.

100. Sciazko A., Komatsu Y., Zakrzewski M., Akiyama T., Hashimoto A., Shikazono N., Kaneko S., Kimijima S., Szmyd J., Kobayashi Y.; Experimental Attempts to Investigate the Influence of Petrographic Properties on Drying Characteristics of Lignite in Superheated Steam Atmosphere, *Energies*, **9**, p. 371, 2016.

101. Komatsu Y., Sciazko A., Zakrzewski M., Akiyama T., Hashimoto A., Shikazono N., Kaneko S., Kimijima S., Szmyd J. S., Kobayashi Y.; Towards the improvement of thermal efficiency in lignite-fired power generation: Concerning the utilization of Polish lignite deposits in state-of-the-art IGCC technology, *Int. J. Energy Res.*, **40**, pp. 1757–1772, 2016.

102. Patankar S. V; *Numerical Heat Transfer and Fluid Flow*, Electro Skills Series, Hemisphere Publishing Corporation, 1980.

103. Szargut J.; *Modelowanie numeryczne pól temperatury*, Wydawnictwa Naukowo-Techniczne: Warszawa, 1992.

104. Zakrzewski M., Sciazko A., Komatsu Y., Akiyama T., Hashimoto A., Kaneko S.; Numerical analysis of single and multiple particles of Belchatow lignite dried in superheated steam, *Heat Mass Transf.*, **54**, pp. 2215–2230, 2018.

105. Komatsu Y., Sciazko A., Zakrzewski M., Fukuda K., Tanaka K., Hashimoto A., Kaneko S., Kimijima S., Szmyd J. S., Kobayashi Y.; Experimental and analytical evaluation of the drying kinetics of Belchatow lignite in relation to the size of particles, *J. Phys. Conf. Ser.*, **745**, pp. 032144-1–032144-8, 2016.

106. Zakrzewski M., Sciazko A., Komatsu Y., Akiyama T., Hashimoto A., Kaneko S., Kimijima S., Szmyd J. S., Kobayashi Y.; An experimental verification of numerical model on superheated steam drying of Belchatow lignite, *J. Phys. Conf. Ser.*, **745**, pp. 032145-1–032145-8, 2016.

107. Zakrzewski M., Sciazko A., Komatsu Y., Akiyama T., Hashimoto A., Kaneko S., Kimijima S., Szmyd J. S., Kobayashi Y.; The impact of fundamental properties of lignite on superheated steam drying in a single particle model. In: *Współczesne problemy termodynamiki*; Bury T., Andrzej S. Eds.; Wydawnictwo Instytutu Techniki Cieplnej: Gliwice, 2017.

108. Nsakala N. Y., Essenhigh R. H., Walker P. L.; Characteristics of chars produced from lignites by pyrolysis at 808 °C following rapid heating, *Fuel*, **57**, pp. 605–611, 1978.

109. Scaroni A. W., Walker P. L., Essenhigh R. H.; Kinetics of lignite pyrolysis in an entrained-flow, isothermal furnace, *Fuel*, **60**, pp. 71–76, 1981.

110. PGE Górnictwo i Energetyka Konwencjonalna S.A.; Sprzedaż węgla. Kopalnia Węgla Brunatnego Bełchatów., Available online: https://kwbbelchatow.pgegiek.pl/Oferta/Sprzedaz-wegla (accessed on Dec 18, 2017).

111. PGE Górnictwo i Energetyka Konwencjonalna S.A.; Oferta. Kopalnia Węgla Brunatnego Turów., Available online: https://kwbturow.pgegiek.pl/Oferta (accessed on Dec 18, 2017).

112. PGE GiEK S.A. Oddział Elektrownia Bełchatów - O oddziale, Available online: https://www.elbelchatow.pgegiek.pl/index.php/o-oddziale/ (accessed on Mar 21, 2017).

113. Sylwetki kotłów RAFAKO, Available online: http://www.rafako.com.pl/produkty/kotly/sylwetki/kotly-pylowe-przeplywowe2 (accessed on Mar 21, 2017).

114. Booras G., Holt N.; Pulverized coal and IGCC plant cost and performance estimates. In: *Gasification Technologies*; Washington, 2004.

115. Bilek M., Hardy C., Lenzen M., Dey C.; *Life-Cycle Energy Balance and Greenhouse Gas Emissions of Nuclear Energy in Australia* (Industrial Report), Sydney, 2006.

116. White D.; *Reduction in Carbon Dioxide Emissions: Estimating the Potential Contribution From Wind-Power* (Industrial Report), London, 2004.

117. Mistubishi Hitachi Power Systems Europe GmbH; First Boiler Column Fixed at the Kozienice 11 Power Plant, pp. 1–3, 2014.

118. Wskaźniki emisji za rok 2015, Available online: https://www.elbelchatow.pgegiek.pl/index.php/ochrona-srodowiska/wskazniki-e misji/ (accessed on Mar 22, 2017).

119. Mastalerz M., Drobniak A., Rupp J.; Meso- and micropore characteristics of coal lithotypes: Implications for CO2 adsorption, *Energy and Fuels*, **22**, pp. 4049–4061, 2008.

120. Zhao Y., Liu S., Elsworth D., Jiang Y., Zhu J.; Pore Structure Characterization of Coal by Synchrotron Small-Angle X-ray Scattering and Transmission Electron Microscopy, *Energy & Fuels*, **28**, pp. 3704–3711, 2014.

121. Brus G., Iwai H., Sciazko A., Saito M., Yoshida H., Szmyd J. S.; Local evolution of anode microstructure morphology in a solid oxide fuel cell after long-term stack operation, *J. Power Sources*, **288**, pp. 199–205, 2015.

References in Appendices A-F

122. *JSME Data Book: Thermophysical Properties of Fluids*, Japanese Society of Mechanical Engineers: Tokyo, 1983.

123. Pakowski Z.; *Projektowanie suszarek do suszenia parą przegrzaną*, Wydawnictwo Politechniki Łódzkiej: Łódź, 2011.

124. Fujii T., Honda T., Fujii M.; A numerical analysis of laminar free convection around an isothermal sphere: Finite-difference solution of the full Navier-Stokes and energy equations between concentric spheres, *Numer. Heat Transf.*, **7**, pp. 103–111, 1984.

125. Wiśniewski S.; *Wymiana ciepła*, Państwowe Wydawnictwo Naukowe: Warszawa, 1979.

126. Information processing - Documentation symbols and conventions for data, program and system flowcharts, program network charts and system resource charts, 1985.

Appendix A

Determination of thermal conductivity coefficient

A.1. Experimental setup and procedure

The experimental apparatus used for the determination of thermal conductivity is presented in Figure A.1. The water bath was heated to $80\,^{\circ}\text{C}$ and empty plastic balls were put to float on the water surface and provide the thermal insulation from the top of the vessel. The spherical lignite sample, suspended by the wire installed on the rack, was equipped with two thermocouples, similarly to the regular superheated steam drying experiments: one measuring the center and the other the midpoint temperature of the sphere. An auxiliary thermocouple was used to monitor the temperature of water, above the coal sample.

Starting on from the moment of the sample immersion in water, the acquisition of temperature data was performed every 1 second. It lasted until the center temperature reached the temperature of water level. In order to determine the value of thermal conductivity, the numerical simulation illustrating this heating process was conducted as described below.

Lignite from seven excavation spots was examined, four of which were located in Belchatow lignite complex (designated: B2013, B1, B2, B3) and three in Turoszow lignite complex (T1, T2, T3). For each lignite type, at least 4 tests were done and average results were assumed representative values of thermal conductivity coefficient.
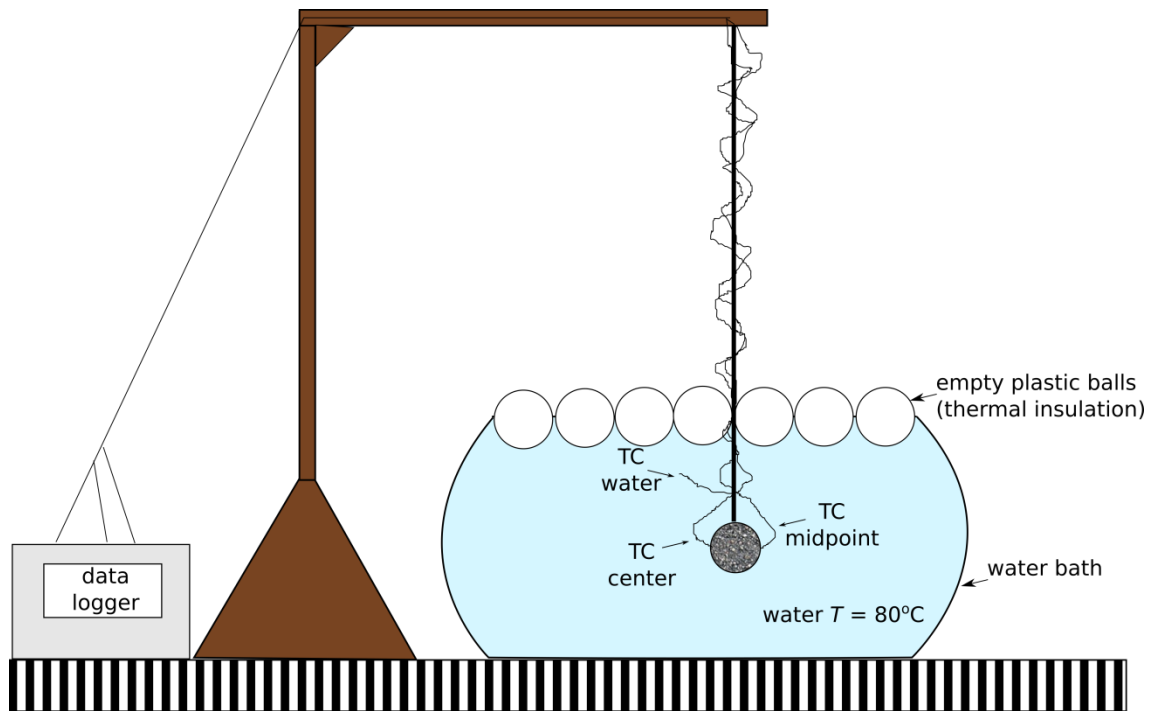
Figure A.1 Scheme of thermal conductivity measurement setup

A.2. Assumptions of the simulation

- The sample is a perfect sphere of isotropic properties, what makes the one-dimensional modelling along the radius possible.

- There are N spherical shells of stepwise decreasing diameter constituting the model of the sample. Each of them has equal width $2b$, besides the first and last, characterized with the half of the standard width: b. The N number was assumed 60 in this experimentation.

- The initial temperature of coal for each simulation attempt is adjusted to the actual experimental temperature measured by the thermocouples.

- Lignite contains two phases: water and dry coal, ratio of which is decided by average experimental value of initial moisture content X^0. The ratio remains invariable throughout the heating process.

- Specific heat, c_c, and thermal conductivity, λ_c of dry coal are material properties and are assumed constant for the specific type of lignite.

- Thermal conductivity of water, λ_w, exhibits temperature dependence [122]:

$$\lambda_w(T) = 8.71 \times 10^{-6} T^2 + 2.01 \times 10^{-3} T + 0.56 \qquad \text{(A.1)}$$

- The properties of lignite are resultant of corresponding dry coal and water properties, weighed regarding to mass fraction (moisture content) of both phases.
- The explicit method of simulation was applied. The stability condition was fulfilled, regarding the time step width Δt equal to 0.05 s. The temperature of the layer n in the time instance i is expressed as:

$$T_n^i = T_n^{i-1} + \left[\frac{\left(T_{n-1}^{i-1} - T_n^{i-1}\right) \times 4\pi \times r_{\text{int},n,n-1}}{b_n \times \left(\dfrac{1}{\lambda_{n-1}^{i-1} r_{n-1}} + \dfrac{1}{\lambda_n^{i-1} r_n}\right)} - \frac{\left(T_n^{i-1} - T_{n+1}^{i-1}\right) \times 4\pi \times r_{\text{int},n+1,n}}{b_{n+1} \times \left(\dfrac{1}{\lambda_n^{i-1} r_n} + \dfrac{1}{\lambda_{n+1}^{i-1} r_{n+1}}\right)} \right] \times \frac{c\Delta t}{m_n} \qquad \text{(A.2)}$$

Where $r_{\text{int},n,n-1}$ represents the radius of the interface between layers n and n-1, which is equal to the arithmetic mean of the radii of those adjacent layers.

A.3. Function of the objective

The solution of a problem introduced in this Appendix is a value which minimizes the function of the objective. The function, which variable is a value of thermal conductivity, is expressed in Eq. (A.3)

$$f(\lambda_c) = \frac{1}{2} \left(\sqrt{\frac{\sum_{i=0}^{DT} \left(T_{\text{mid,exp}}^i - T_{\text{mid,sim}}^i\right)^2}{DT}} + \sqrt{\frac{\sum_{i=0}^{DT} \left(T_{\text{cent,exp}}^i - T_{\text{cent,sim}}^i\right)^2}{DT}} \right) = \frac{RMSE_{\text{mid}} + RMSE_{\text{cent}}}{2} \qquad \text{(A.3)}$$

where the variances between temperature of midpoint and center measured experimentally and calculated in a simulation are taken into consideration. Thus, the contributions on the right-hand side of Eq. (A.3) represent root-mean squared error (RMSE) for midpoint and center temperature, respectively, giving the average RMSE as an result. The variable of DT is the number of simulation steps, which is the quotient of total simulation time (needed for attainment of thermal equilibrium between coal and water) and time step width:

$$DT = \frac{t_{sim}}{\Delta t} \tag{A.4}$$

The chart illustrating the determination of thermal conductivity coefficient is shown in Figure A.2. Each data point represent a value of either midpoint, center or average RMSE appropriate for singular simulation attempt. This particular case was performed for B1 lignite and came out with a value of 0.351 W m^{-1} K^{-1}.
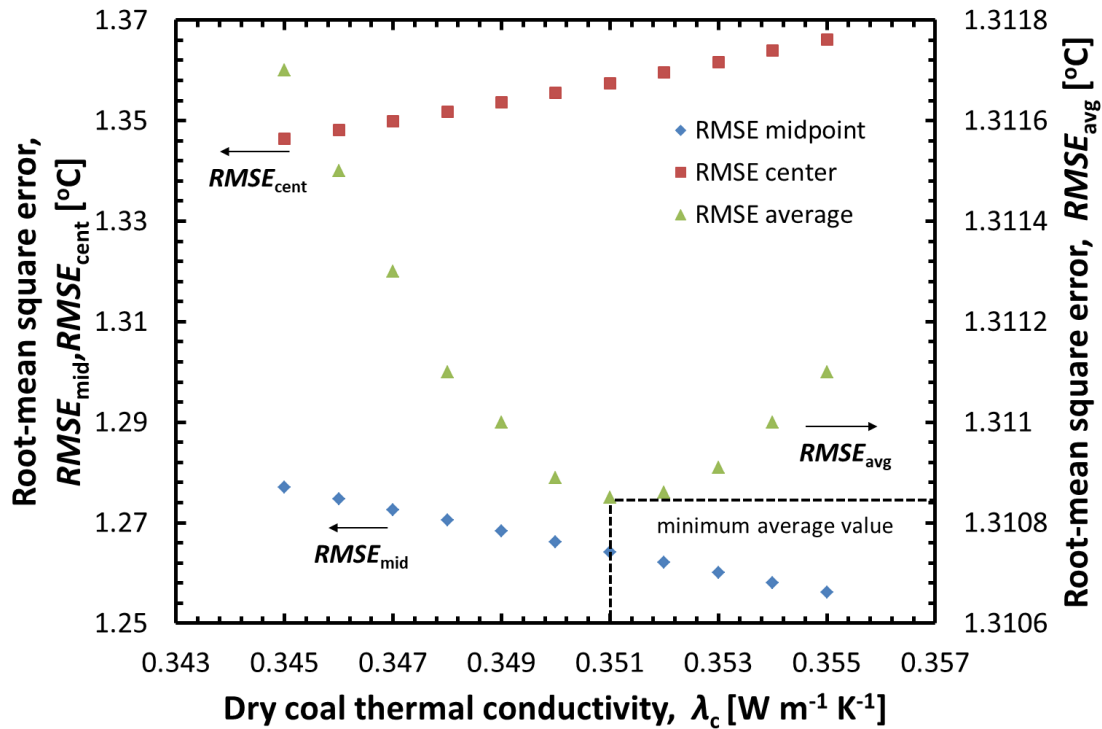
Figure A.2 Illustration of exemplary minimization of the function of the objective

Appendix B

Determination of heat transfer coefficient

B.1.   Derivation from experimental drying kinetics

On the assumption that changes in sample geometry are negligible during the constant drying rate period (CDRP), the heat transfer per unit area between the superheated steam and coal surface can be defined at this period as:

$$\dot{q} = h\left(T_{a} - T_{1}\right) \tag{B.1}$$

where $\dot{q}$ is the heat flux to the surface [W m^{-2}] and h is the heat transfer coefficient [W m^{-2} K^{-1}]. During the period of constant drying, the surface of the sample remains at a steady temperature T_1 = 100 $^{\circ}$C. The entire heat input to the sample at the CDRP is consumed for the evaporation of free water. Under those circumstances, the heat transfer per unit area of the sample surface, might be expressed by the following dependence on the evaporation rate υ:

$$\dot{q} = -L \cdot \upsilon = -L \cdot \frac{\mathrm{d}m_{w}}{A \cdot \mathrm{d}t} \tag{B.2}$$

where L is the latent heat of free water evaporation ($2.256{\times}10^{6}$ J kg^{-1}). The correlation between evaporation rate and drying rate DR is given by the following equation:

$$\upsilon = \frac{m_c}{A} \cdot DR = \frac{m_c}{A}\frac{\mathrm{d}X}{\mathrm{d}t} = \rho\varphi_c^0 \frac{d}{6}\frac{\mathrm{d}X}{\mathrm{d}t} \tag{B.3}$$

Combination of equations (B.1)-(B.3) produces the formula for the heat transfer coefficient as a function of the drying rate, valid during the CDRP:

$$h_{\text{exp}} = \frac{-L \cdot m_c}{\left(T_a - T_1\right)\pi d^2}\frac{\mathrm{d}X}{\mathrm{d}t} \tag{B.4}$$

B.2. Derivation with a linearized radiation equation

Another approach to obtaining the heat transfer coefficient involves deliberation on two mechanisms of heat transfer, convection and radiation, as in Eq.(B.5):

$$\dot{q} = \dot{q}_{\text{conv}} + \dot{q}_{\text{rad}} \tag{B.5}$$

The convective heat transfer is given as:

$$\dot{q}_{\text{conv}} = h_{\text{conv}}\left(T_a - T_1\right) \tag{B.6}$$

while the radiative term can be defined as:

$$\dot{q}_{\text{rad}} = \varepsilon_r \cdot \sigma \cdot \left[\left(T_a + 273.15\right)^4 - \left(T_1 + 273.15\right)^4\right] \tag{B.7}$$

The relative emissivity ε_r is equal to 0.887 [85], and σ stands for the Stefan-Boltzmann constant (5.67×10^{-8} W m^{-2} K^{-4}).

The heat flux in Eq. (B.5) can be expressed as a sum of coefficients multiplied by temperature difference:

$$\dot{q} = h_{\text{rad}}\left(T_a - T_1\right) + h_{\text{conv}}\left(T_a - T_1\right) \tag{B.8}$$

Hence, the apparent coefficient of radiative heat transfer can be expressed as in (B.9).

176

$$h_{rad} = \frac{\varepsilon_r \cdot \sigma \cdot \left[\left(T_a + 273.15\right)^4 - \left(T_1 + 273.15\right)^4 \right]}{T_a - T_1} \quad \text{(B.9)}$$

The convective term of the coefficient, for the low Reynolds number combined with the assumption of the laminar flow and natural convection, might be given as:

$$h_{conv} = Nu \frac{\lambda_a}{d} \quad \text{(B.10)}$$

where Nu represents the Nusselt number and λ_a is the thermal conductivity of the superheated steam. The dimensionless numbers and thermodynamic parameters leading to the derivation of the Nusselt number are listed in Tab. B.1.

Table B.1 Properties and dimensionless numbers used in derivation of h_{conv}

quantity	formula [source]
Nusselt number Nu	$2 + 0.760 \cdot C_T(Pr) \cdot Ra^m$ [123]
Prandtl number Pr	$\dfrac{\nu_a}{\alpha_a}$
Coefficient C_T	$\dfrac{3}{4} \times \left(\dfrac{Pr}{2.4 + 4.9\sqrt{Pr} + 5Pr} \right)^{\frac{1}{4}}$ [124]
Rayleigh number Ra	$Gr \cdot Pr$
Grashof number Gr	$\dfrac{9.81}{T_a}\left(T_a - T_1\right) \cdot \dfrac{d^3}{\nu_a^2}$
Coefficient m	$\dfrac{1}{4} + \dfrac{1}{4 + 8.2Ra^{0.095}}$ [124]
thermal conductivity of steam λ_a [W m^{-1} K^{-1}]	$-1.16 \times 10^{-7} \cdot T_a^2 + 5.17 \times 10^{-5} \cdot T_a + 0.0184$ [122]
kinematic viscosity of steam ν_a [m^2 s^{-1}]	$-2.04 \times 10^{-10} \cdot T_a^2 + 8.21 \times 10^{-8} \cdot T_a + 1.06 \times 10^{-5}$ [122]
thermal diffusivity of steam α_a [m^2 s^{-1}]	$2.48 \times 10^{-10} \cdot T_a^2 + 8.47 \times 10^{-8} \cdot T_a + 9.77 \times 10^{-6}$ [122]

Combination of the equations gathered in Tab. B.1 leads to the conclusion that convective heat transfer coefficient is a function of superheated steam temperature and diameter of the sample, while the term related to radiation depends only on the superheated steam temperature. Taking these facts into account, the approximated equation of the resultant heat transfer coefficient, can be formulated:

$$h_{apr} = \left(\frac{2.381 \times 10^{-4}}{d} + 9.173 \times 10^{-2} \right) T_a - \left(\frac{2.99 \times 10^{-2}}{d} + 5.43 \right) \tag{B.11}$$
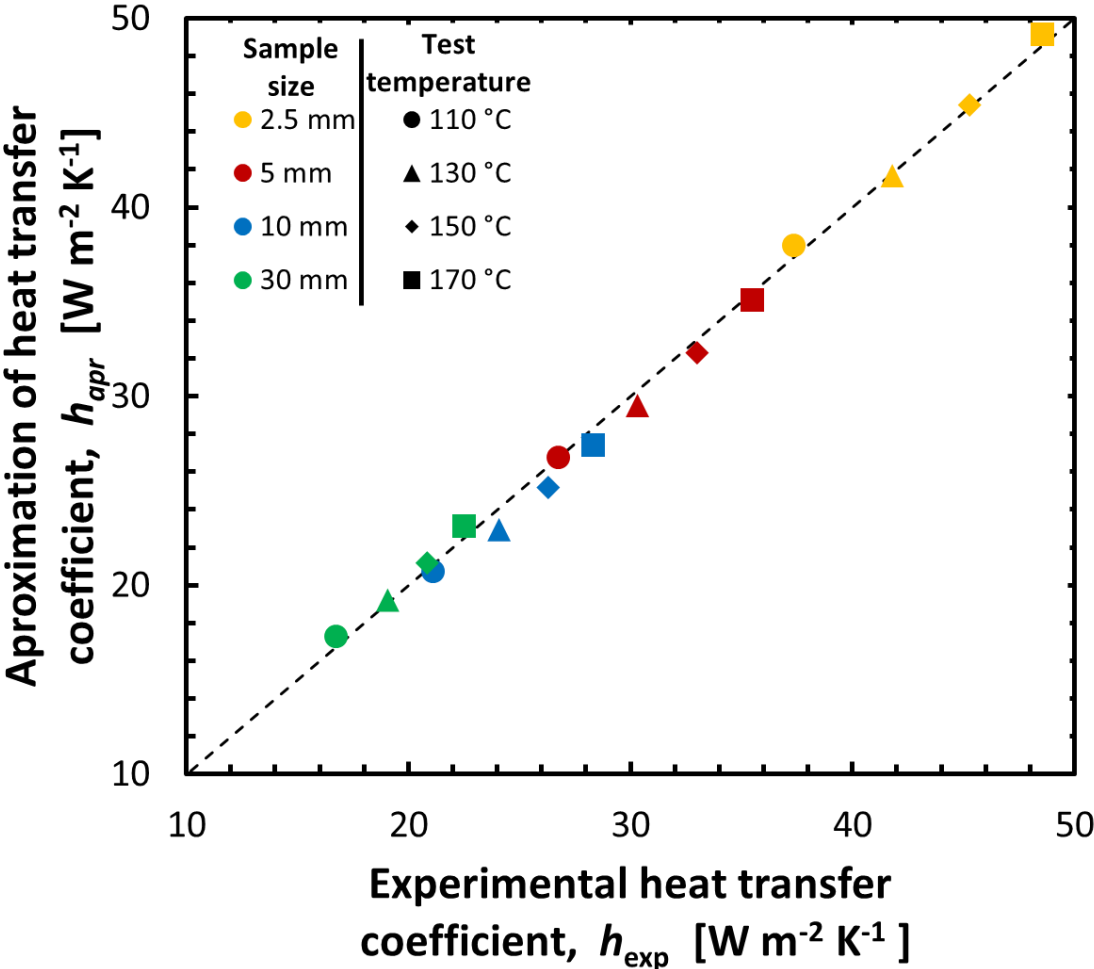
Figure B.1 Correlation of the heat transfer coefficient derived from exact and approximated equations

The values of heat transfer coefficient were calculated for the entire set of test temperatures and sample diameters using the approach presented in section B.1 and compared with linear approximation constructed in section B.2. The correlation of coefficients obtained in two methods is shown in Fig. B.1.

Appendix C

Optimization of model segmentation

C.1. Assumptions

In order to determine the appropriate number of elements within a spherical model of lignite, the drying simulation was performed for six segmentation cases: 6, 10, 30, 50, 100 and 200 layers. The diameter of modelled sample was 30 mm, as it was the largest size of object used in the experimentation, while the steam temperature was simulated at the level of 150 ^{o}C. Two conditions were taken into consideration: the number of simulation iterations required to achieve convergence and the real time elapsed for the completion of the simulation. The correlation of the conditions and the number of the elements within the sphere were shown in Fig. C.1 and Fig. C.2. The time of simulation had a direct, while the number of iterations inverse proportion to the number of layers.

The first criterion was objective and relied only on the construction of the model, with target temperature difference between superheated steam temperature T_a and center temperature of lignite T_{N+1} lesser than 5×10^{-6} ^{o}C. The second condition was CPU-dependent, thus, both sets of results were transformed into relative values with regard to the maxima. The absolute and relative values were gathered in Tab. C.1.
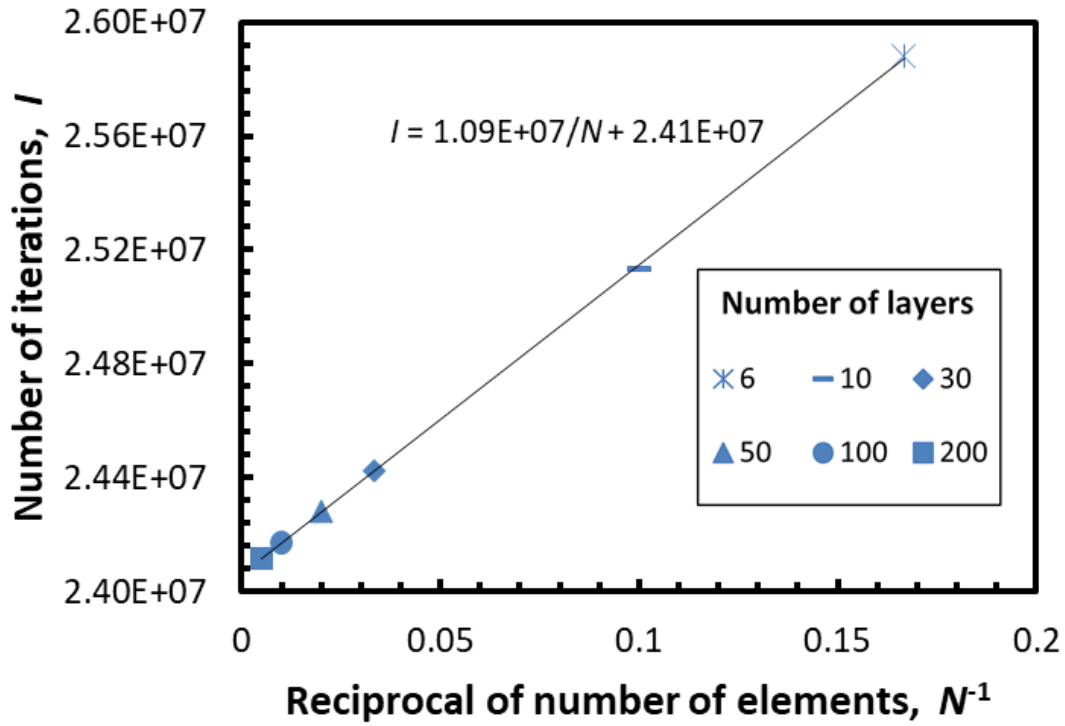
Figure C.1 Relation between number of layers and the number of simulation iterations
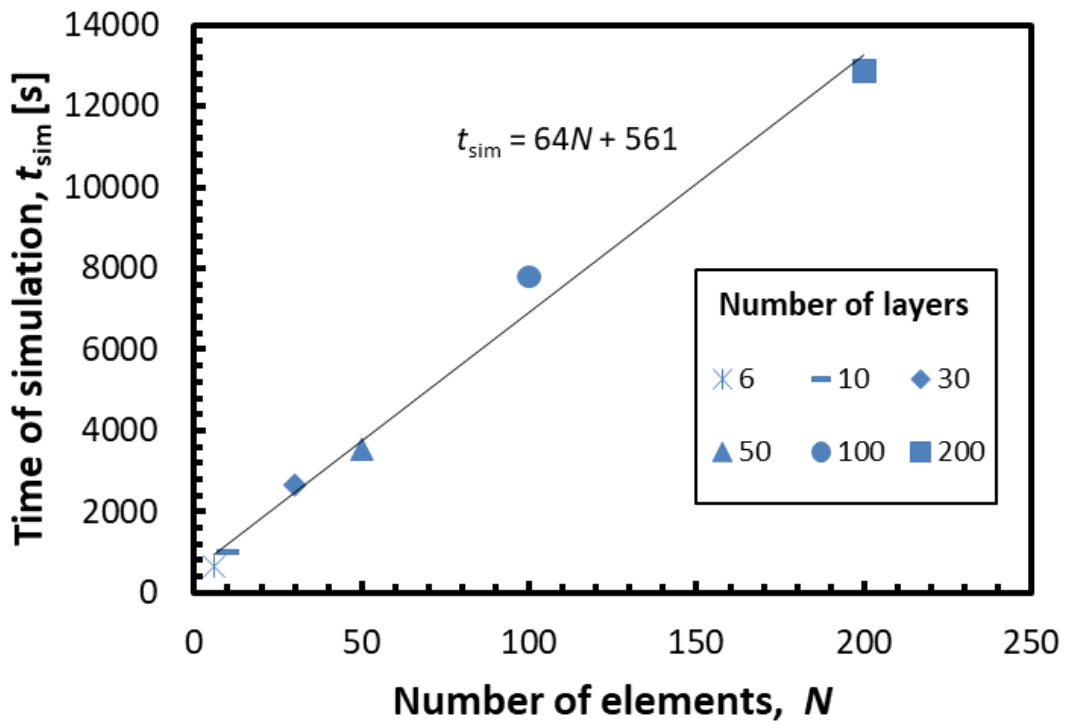
Figure C.2 Relation between number of layers and the time required for simulation

Table C.1 Absolute and relative values of both optimization criteria

number of layers N	number of iterations I		time of simulation t_{sim} [s]	
	absolute	relative	absolute	relative
6	25880559	1.000	647	0.050
10	25132360	0.971	1018	0.079
30	24424053	0.944	2659	0.207
50	24281146	0.938	3545	0.275
100	24171933	0.934	7796	0.606
200	24116066	0.932	12870	1.000

For the determination of optimal number of layers, the particular criteria were arbitrarily assigned to weights. The number of iterations is by far more important than the time of simulation, therefore 0.95 was given to the former, while 0.05 to the latter criterion. The relative values of I and t_{sim} were multiplied by the corresponding weights to form the function of the objective. The number of layers for which the minimum resultant value was obtained, $N=50$ was decided to be applied to the model. Figure X presents the results of the investigation.
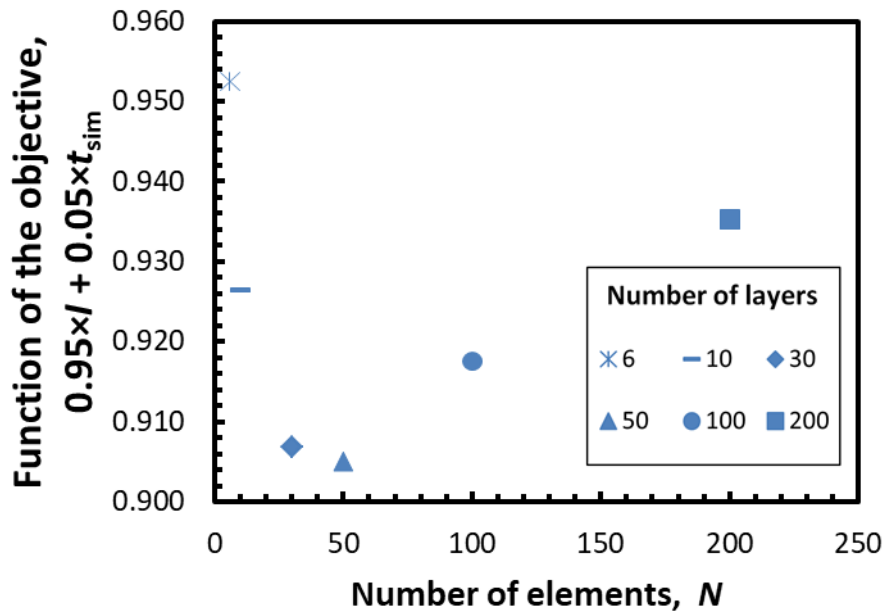
Figure C.3 Minimization of the function of the objective

Appendix D

Unsteady state heat transfer in lignite by means of conduction

D.1. Assumptions

For the sake of verification of the basic equations constituting the mathematical model of drying, the analytical solution of the transient heat transfer by conduction was calculated and compared with the numerical results. The comparison was simplified and limited to heating of dry coal ($X=0$) from the initial temperature $T^0 = 40$ ^{o}C to the temperature of surrounding medium $T_a = 150$ ^{o}C. Although heat transfer coefficient was calculated according to the equation derived for the superheated steam (Eq.(B.11)), no condensation of water on the surface was assumed. The object selected for comparison had 30 mm in diameter. The thermophysical quantities as well as dimensionless numbers applied for the analytical solution were gathered in Table D.1.

D.2. Analytical solution

The analytical solution was modeled using the approach of Wisniewski [125]. In order to describe unsteady heat transfer in lignite sphere, three auxiliary quantities were applied. The excess temperature is defined as:

$$\vartheta(r,t) = T_a - T(r,t) \tag{D.1}$$

Table D.1 Parameters used for the analytical solution of lignite heating

quantity	value	origin
diameter d	0.03 m	section 4.1
characteristic linear dimension R	0.015 m	$d\,/\,2$
superheated steam temperature T_a	150 °C	section 4.3
initial temperature T^0	40 °C	section 6.2.1
density (DBC) ρ_c	1536 kg m^{-3}	Tab. 6.1
thermal conductivity (DBC) λ_c	0.33 W m^{-1} K^{-1}	Tab. 6.1
specific heat (DBC) c_c	1246 J kg^{-1} K^{-1}	Tab. 6.1
heat transfer coefficient h	21.36 W m^{-2} K^{-1}	Eq. (B.11)
thermal diffusivity α_c	1.72×10^{-7} m^2 s^{-1}	$\lambda_c\,/\,(\rho_c \times c_c)$
Biot number Bi	0.971	$R \times h\,/\,\lambda_c$

The radius r was applied to define dimensionless radius r^+, with regard to characteristic linear dimension R:

$$r^+(r) = \frac{r}{R} \qquad (D.2)$$

To derive the dimensionless analogue in terms of time, Fourier number was used:

$$\text{Fo}(t) = \frac{\alpha t}{R^2} \qquad (D.3)$$

The problem of heating of the isotropic sphere, which is characterized with constant thermal conductivity, density and specific heat, might be expressed in the form of differential equation:

$$\frac{\partial\left[r\vartheta(r,t)\right]}{\partial t} = \alpha_c \frac{\partial^2\left[r\vartheta(r,t)\right]}{\partial r^2} \qquad (D.4)$$

with following boundary conditions:

$$-\lambda_c \frac{\partial \vartheta(R,t)}{\partial t} = h\vartheta(R,t) \qquad \text{for } r = R \tag{D.5}$$

$$\frac{\partial \vartheta(0,t)}{\partial t} = 0 \qquad \text{for } r = 0 \tag{D.6}$$

and initial condition:

$$\vartheta(r,0) = T_a - T(r,0) = \vartheta^0(r) \qquad \text{for } t = 0 \tag{D.7}$$

Taking into account the symmetry condition Eq. (D.6) and that the temperature of the center at any moment cannot be infinitely high, $\vartheta(0,t) \neq \infty$, the particular solution of Eq. (D.4) can be formulated as below:

$$\vartheta(r,t) = \frac{F}{r} \sin \frac{\beta r}{R} \exp(-\frac{\beta^2}{R^2} \alpha t) \tag{D.8}$$

where β represents an infinite sequence of roots of the characteristic equation (Eq. (D.9)) derived from the boundary condition (Eq. (D.5)).

$$\mathrm{tg}\beta = \frac{\beta}{1 - \mathrm{Bi}} \tag{D.9}$$

Coefficient F can be expressed with reference to β sequence in the formula:

$$F_m = \frac{2\vartheta^0 \left(\sin \beta_m - \beta_m \cos \beta_m \right) R}{\beta_m \left(\beta_m - \sin \beta_m \cos \beta_m \right)} \tag{D.10}$$

The general solution is the sum of particular solutions, presented in Eq. (D.8). Taking dimensionless radius r^+ and dimensionless time Fo into consideration, the general solution can be given:

$$\vartheta(r^+,\text{Fo})=\sum_{m=1}^{\infty}\frac{F_m}{Rr^+}\sin\beta_m r^+ \exp(-\beta_m^2\text{Fo}) \qquad (\text{D.11})$$

In order to calculate the temperature of the sphere at a certain time in the precise manner, the first six terms of a series expressed in Eq. (D.11) were used. The exact values of β were interpolated from the table of roots for specific values of Biot number, as shown in Tab. D.2.

Table D.2 Exertion from table of roots for Eq. (D.9) [125]

Bi	β_1	β_2	β_3	β_4	β_5	β_6
0.8	1.4320	4.6696	7.8284	10.9774	14.1230	17.2672
1.0	1.5708	4.7124	7.8540	10.9956	14.1372	17.2788
0.971	1.5505	4.7061	7.8503	10.9929	14.1351	17.2771

The values of r^+ for surface, midpoint and center were assumed 1, 0.5 and 10^{-6}.

D.3. Numerical solution

The numerical solution in simplified form, for heating of the lignite sphere, can be reduced to the following dependencies valid in time instance i:

- boundary conditions

$$\Delta Q_{1,n}^i = h4\pi r_1^2\left(T_a - T_1^i\right)\Delta t \qquad (\text{D.12})$$

$$\Delta Q_{N+1,\text{out}}^i = 0 \qquad (\text{D.13})$$

- initial condition

$$T^0 = 40\ ^\circ\text{C} \qquad (\text{D.14})$$

- heat conduction

$$\Delta Q^i_{n,\text{in}} = \frac{4\pi r_{n,n+1,\text{int}} \lambda_\text{c}}{\dfrac{b_{n-1}}{r_{n-1}} + \dfrac{b_n}{r_n}} \left(T^i_{n-1} - T^i_n \right) \Delta t \qquad (D.15)$$

- heat propagation

$$\Delta Q^i_{n+1,\text{in}} = \Delta Q^i_{n,\text{out}} \qquad (D.16)$$

- heat consumption

$$\Delta Q^i_{n,\text{in}} - \Delta Q^i_{n,\text{out}} = \Delta Q^i_{\text{cons},n} = c_\text{c} m_\text{c} \Delta T^i_n \qquad (D.17)$$

The combination of the formulas above lead to the equation describing the temperature of the sphere layers in the subsequent time instance $i+1$:

$$T^{i+1}_n = \frac{\Delta Q^i_{n,\text{in}} - \Delta Q^i_{n,\text{out}}}{c_\text{c} m_\text{c}} + T^i_n \qquad (D.18)$$

D.4. Comparison

The values of temperature were determined using both numerical and analytical method for the time step width of 1 s. The convergence criterion applied for the computational model of drying (difference between surrounding gas and center temperature equal to 5×10^{-6} °C) was fulfilled for numerical method after 9232 s (153.9 min). At that time, the corresponding value for analytical method was 5.7×10^{-6} °C.

Figures D.1, D.2 and D.3 present the temperature profile of the heated dry coal sphere, calculated analytically and numerically for surface, midpoint and center,

respectively. First 50 minutes of the process was shown in each case and the gaps between the curves are impossible to distinguish at the current scale of the charts.
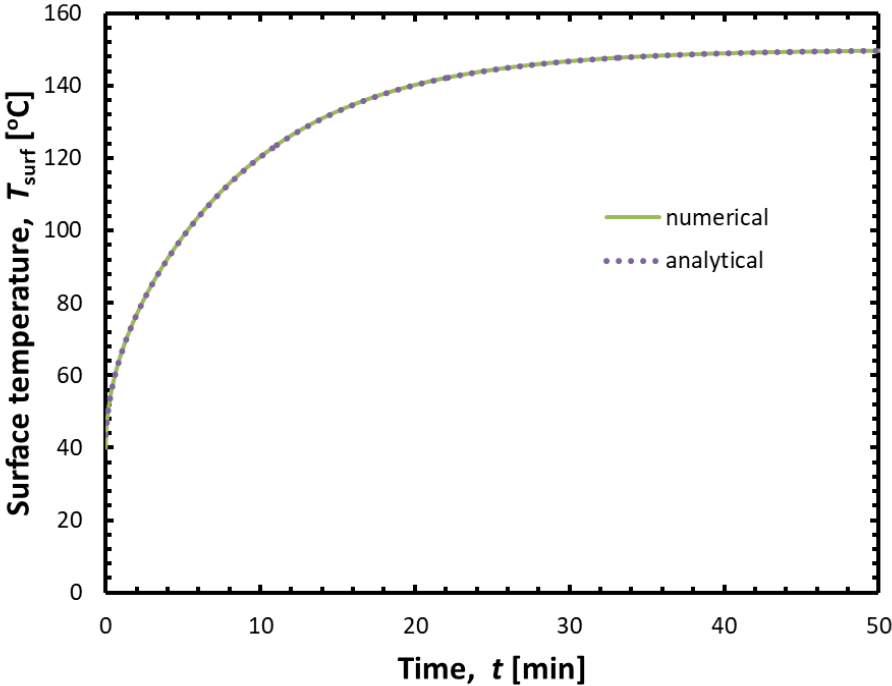
Figure D.1 Surface temperature of heated dry coal sphere determined in two methods
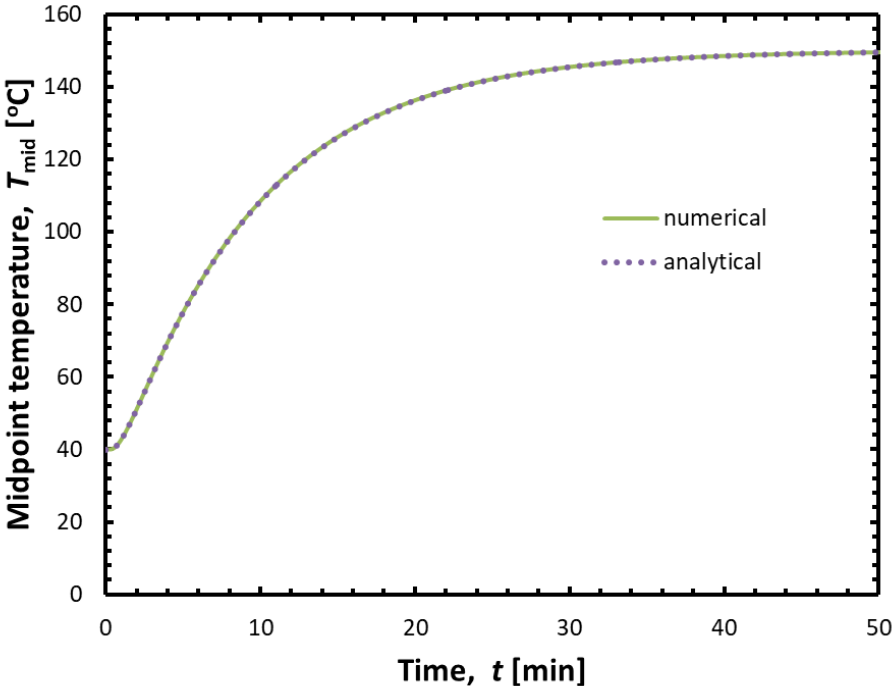
Figure D.2 Midpoint temperature of heated dry coal sphere determined in two methods
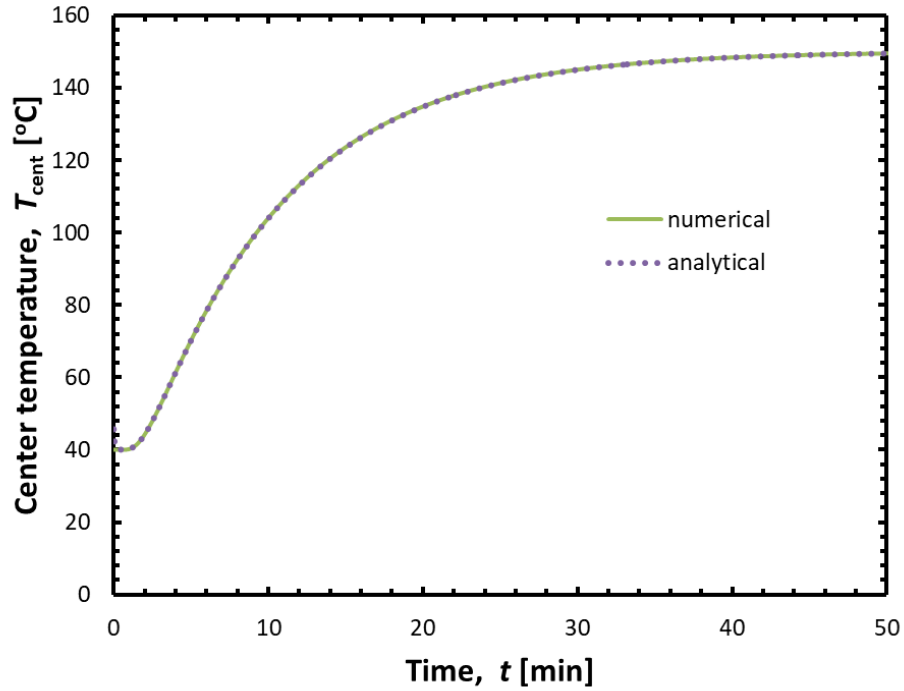
Figure D.3 Center temperature of heated dry coal sphere determined in two methods

In order to determine the coherence of acquired results, the root-mean squared error coefficient was calculated for all three pairs of output temperature data sets, according to the formula given in Eq. (D.19). In accordance with the statement in the first paragraph of this section, DT was equal to 9232. The corresponding values for surface, midpoint and center temperature of 0.0297 $^{\circ}$C, 0.0299 $^{\circ}$C and 0.0274 $^{\circ}$C were evaluated as satisfying to sustain the basic assumptions of numerical heat transfer applied in the drying model.

$$RMSE = \sqrt{\frac{\sum_{i=0}^{DT}\left(T_{numerical}^{i} - T_{analytical}^{i}\right)^{2}}{DT}} \qquad (D.19)$$

Appendix E

Coal temperature data processing utility

E.1. Assumptions

In this part, the idea, scheme of operation and source code listing of a utility, which prepares the input data for coal temperature visualization, is presented. Due to one-dimensional character of the numerical model, the simulation results are achieved as a single file containing values of temperature corresponding to the spherical layers along the sample radius (Fig. E.1). The subsequent rows of temperatures are separated by the simulation's time step or its multiplication (second, minute), accordingly to the total time of drying. In order to present the temperature distribution in a proper way, the transformation of simulation file into a series of output files is required. The files correspond to the particular time instances of the process. For each layer, a series of nodes, distributed symmetrically on the both sides of the geometrical center of the object on the OX axis. Their number depends on a layer diameter, therefore can be given as a function of layer's number. Every x coordinate of a node is used to calculate the y value, according to the Eq. (E.1). The parameter computed in this way is paired with its additive inverse for the sake of covering the mesh on the both sides of OX axis.

$$y = \sqrt{r_n^2 - x^2} \qquad\qquad (E.1)$$
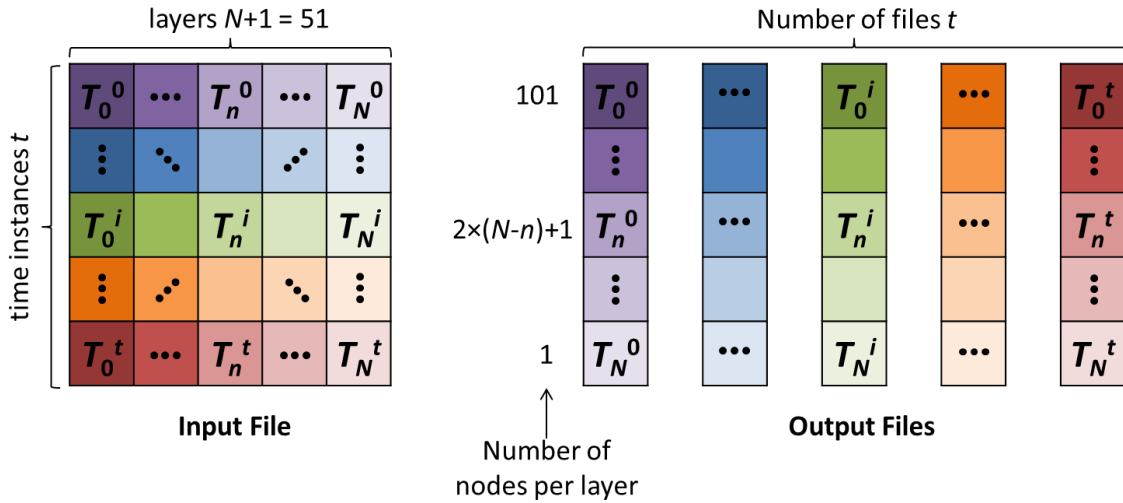
Figure E.1 Scheme of simulation results (source file) and output files applied for graphical representation of temperature distribution within lignite sphere

E.2.   Schematics of data transformation

The specificity of the task presented schematically in Fig. E.1 includes the following aspects:

- acquiring the detailed information about simulation time and segmentation count from the source file,

- reading the temperature values from the file and generating the temperature field,

- preparation of the mesh which contains all the layers of the model,

- combining the temperature field with round-shaped mesh,

- iterative storage of data into subsequent output files.

Due to the necessity of multiple data flows between files and program or between matrices/vectors containing values and Cartesian coordinate system, the application of structured programming, as in the program executing the simulation of superheated steam drying (C++ language), was supposed to be ineffective. Therefore,

the object programming was applied to address the problem of data transformation. This paradigm relates more adequately to the nature of mathematical objects, that digital representations of exchange information between each other. The graphical scheme of a utility constructed using Java language is presented in Fig. E.2.
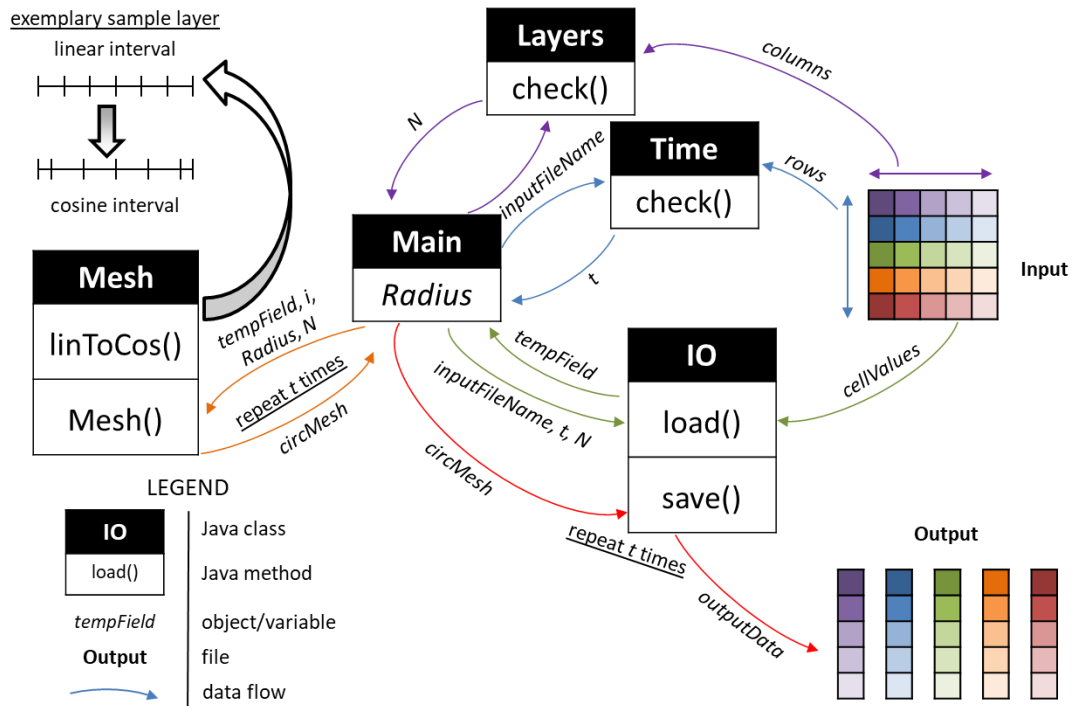
Figure E.2 Graphical scheme of operation and data organization in temperature data processing utility

It operates on five classes, which functioning is coordinated by the Main class. The only data kept within the Main class is the radius of modelled sample, distinguished by capital-letter name *Radius*. The order of operations performed by the program is following:

1. Main class passes the name of the input file (the one containing drying simulation results) to the Time and Layers classes. The two latter classes use check() method to read the number of rows and columns, and then store the acquired data in t and N variables, respectively.

2. Main class sends the input filename to the IO class, altogether with t and N values. Invoking load() method, IO class is able to get the values of input file and return them as a temperature field two-dimensional array (*tempField*).

3. Main class performs two operations for t times:

    a. passes the *tempField*, N and *Radius* variables, together with current time instance i to Mesh class, receiving the two-dimensional mesh *circMesh*, coupled with temperature variables,

    b. passes *circMesh* to IO class, which using save() method, stores it to the subsequent output files.

It should be noted that Mesh class, besides using own constructor to generate *circMesh*, applies also linToCos() method, which transforms the linear system of nodes in a particular layer into distribution described by trigonometric function. Thanks to such approach, the resultant mesh is refined near its edges, what guarantees fairly uniform distribution of the mesh points on the entire circular cross-section. The application of linear range the points of low y value are insufficiently represented in the mesh, especially near the circle border.

The output CSV files prepared in the manner described above were then loaded into ParaView application as described in section 7.4, which offers multiple possibilities of graphical representation of numerical data. Fig. E.3 illustrates the exemplary frame of the animation of the transient temperature distribution in the lignite dried with the use of superheated steam. The red rectangle symbolically encompass the input data vector for the current time instance, while the violet circle indicates the entire range of mesh points, being the result of temperature data processing utility operation.
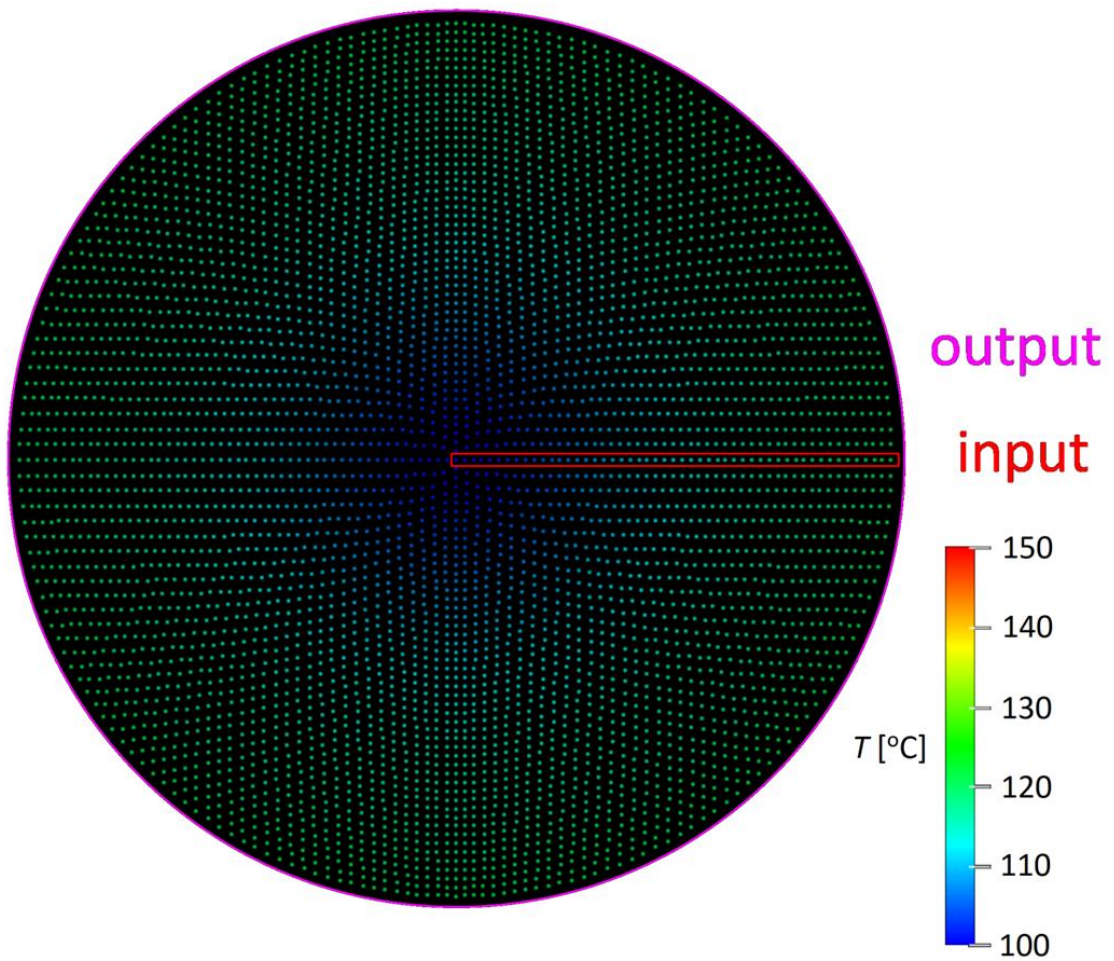
Figure E.3 Scheme of input and output data on the circular mesh (ParaView)

E.3. Code listing

Class Main

```java
public class Main {
public static void main(String[] args) {

File inputFileName = new File(System.getProperty("user.dir")+"\\"+"input.csv");
int N = SegmentationCheck.check(inputFileName);
// segments count(read from input file)
int layers = N+1;                    // layers (nodes) count
double Radius = 10.0/2.0;         //sample total radius
double interval = Radius/(double)N;//interval between layers along the radius
int t = TimeCheck.check(inputFileName);//time of simulation (read from input file)
```

```java
double [][] tempField = InputOutput.load(inputFileName, t, layers);


for (int i =0; i<=t;i++) {
MeshGrid circMesh = new MeshGrid(N,Radius,interval,tempField,i);


InputOutput.save(circMesh.getX(), circMesh.getY(), circMesh.getY_neg(),
circMesh.getZ(), circMesh.getT(), circMesh.getX_nod(), N, i);
                }
        }
}
```

Class Layers

```java
public class Layers {
static int check (File input){
int columns=0;


try (Scanner sc = new Scanner(input)){
        String layerLine = sc.nextLine();
        String []layerCount = layerLine.split(";");
        columns=layerCount.length;
        return columns-1;
} catch (IOException e) {
        e.printStackTrace();
        return columns;
                }
        }
}
```

Class Time

```java
public class Time {
static int check (File input){
int rows=0;


try (Scanner sc = new Scanner(input)){
while (sc.hasNextLine())
        {sc.nextLine();
        rows++;
```

```java
        }
        return rows-1;
} catch (IOException e) {
        e.printStackTrace();
        return rows;
            }
        }
}
```

Class IO

```java
public class IO {
public static void save (double[][] xMesh, double[][] yMesh, double[][] y_negMesh,
double[][] zMesh, double[][] TMesh, int[] nodes, int N, int t) {

String outputFileName = System.getProperty("user.dir")+"\\"+"output"+t+".csv";
File output = new File (outputFileName);

try(PrintWriter out = new PrintWriter(output)){
        out.print("x;y;z;T");
        out.println();
        for (int n=0;n<=N;n++)
                {for (int i=0;i<nodes[n];i++) {
                        double x=xMesh[i][n];
                        double y=yMesh[i][n];
                        double y_neg=y_negMesh[i][n];
                        double z=zMesh[i][n];
                        double T=TMesh[i][n];
                        out.print(x+";"+y+";"+z+";"+T);
                        out.println();
                        out.print(x+";"+y_neg+";"+z+";"+T);
                        out.println();
                }
        }
}catch (FileNotFoundException e) {
        e.printStackTrace();
            }
        }
public static double[][] load (File inputFileName, int t, int layers) {
```

```java
double[][]tempField = new double[t+1][layers];
try (Scanner sc = new Scanner(inputFileName)){
        int m=0;
        while (sc.hasNextLine()) {
                String line = sc.nextLine();
                String []data = line.split(";");
                for (int n=0;n<layers;n++)
                tempField[m][n]=Double.parseDouble(data[n]);
                m++;}
} catch (IOException e) {
        e.printStackTrace();
}
return tempField;
        }
}
```

Class Mesh

```java
public class Mesh{
private double [][]x,y,y_neg,z,T;
private int []x_nod;
Mesh(int N, double Radius, double interval, double[][]tempField,int currentTime)
{double []rad = new double[N+1];                         //radial coordinates
x_nod = new int[N+1];                                    //nodes count
for (int n=0;n<=N;n++){
        x_nod[n]=2*(N-n)+1;
        rad[n] = (double)(N-n)*interval;}

x = new double[x_nod[0]][N+1];          //rectangular abscissae
y = new double[x_nod[0]][N+1];          //rectangular ordinates
y_neg = new double[x_nod[0]][N+1];      //rectangular negative ordinates
z = new double[x_nod[0]][N+1];
//rectangular neutral coordinates (for 3D visualisation)
T = new double[x_nod[0]][N+1];
//temperatures corresponding to particular coordinates
for (int n=0;n<=N;n++){
        for (int i=0;i<x_nod[n];i++) {
                x[i][n]=-rad[n]+LinToCos(x_nod[n], interval,rad[n])[i];
                y[i][n]=Math.sqrt(rad[n]*rad[n]-x[i][n]*x[i][n]);
```

```java
                    y_neg[i][n]=-y[i][n];
                    z[i][n]=0.0;
                    T[i][n]=tempField[currentTime][n];}
        }
}


double []LinToCos (int nodes,double interval,double layerRad){
//casting linear abscissae range to trigonometric
double [] linNod = new double [nodes];
double [] cosNod = new double [nodes];
double [] arg = new double [nodes];
double x;


for (int i = 0;i<nodes;i++)
        {linNod[i] = interval*i;
        x=-layerRad+linNod[i];
        arg[i]=x*Math.PI/(2.0*layerRad);}


for (int i = 0; i<=(nodes-1)/2;i++)
        cosNod[i]=Math.cos(arg[i])*linNod[i];
for (int i = 0; i<(nodes-1)/2;i++)
        cosNod[nodes-1-i]=2*layerRad-Math.cos(arg[i])*linNod[i];


if (nodes==1) cosNod[0]=0.0;
return cosNod;  }


            public double[][] getX() {return x;}
            public double[][] getY() {return y;}
            public double[][] getY_neg() {return y_neg;}
            public double[][] getZ() {return z;}
            public double[][] getT() {return T;}
            public int[] getX_nod() {return x_nod;}

}
```

Appendix F

Computational algorithm of superheated steam drying

F.1. Assumptions

The algorithm of numerical model was prepared and presented in the form of the flowchart diagram, regarding to the mutually exclusive stages of the drying process, shown in sections F.2.2-F.2.5. The components of the diagram were illustrated in accordance with ISO standard [126], as indicated in Fig. F.1.

A) terminal

START

B) input/output

initial coal parameters
$c_c, d^0, D, \lambda_c, \rho_c, T^0, X^0$

C) process

$T_1^i = 100\ {}^\circ C$

D) predefined process

WATER TRANSFER

E) decision

CONDENSATION
$T_1 < 100\ {}^\circ C$
N

Y

F) flowline

G) off-page/on-page connector

A2   B1
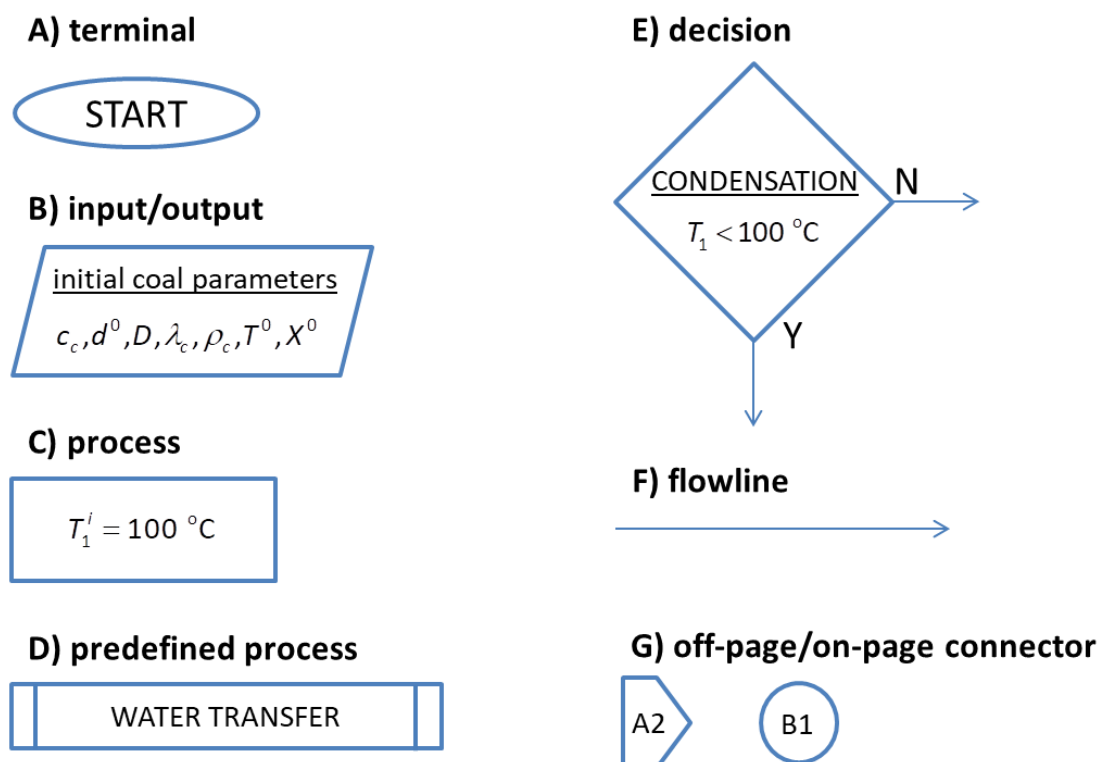
Figure F.1 Examples of the components used in the flowchart diagram
of numerical algorithm

F.2. Flowchart diagram

F.2.1 Initial calculations

START

initial coal parameters
$$c_c, d^0, D, \lambda_c, \rho_c, T^0, X^0$$

process parameters
$$\Delta t, t_{dry}, T_s$$

values overwrite
$$i = i + 1$$

output data
$$i \times \Delta t, m^i, T_1^i, T_{N/2+1}^i, T_{N+1}^i, X^i, DR^i, m_{surf}^i$$

convergence
$$T_a - T_{N+1}^i > 5 \times 10^{-6} \,°C$$

N → STOP

Y

calculating variable properties
$$c_{w,n}^i = c_{w,n}^i(T)$$
$$c_{s,n}^i = c_{s,n}^i(T)$$
$$d_n^i / d_n^0 = d_n^i / d_n^0(X)$$

calculating thermal conductivity
$$\lambda_{w,n}^i = \lambda_{w,n}^i(T)$$
$$\lambda_{s,n}^i = \lambda_{s,n}^i(T)$$
$$\lambda_n^i = \lambda_c \, \varphi_{c,n}^i + \lambda_{w,n}^i \varphi_{w,n}^i + \lambda_{s,n}^i \varphi_{s,n}^i$$

calculating global indicators of drying behaviour
$$m^i = \sum_{n=1}^{N+1}\left(m_{c,n}^i + m_{w,n}^i\right) + m_{surf}^i$$
$$X^i = \left[\sum_{n=1}^{N+1}\left(m_{w,n}^i\right) + m_{surf}^i\right] \bigg/ \sum_{n=1}^{N+1}\left(m_{c,n}^i\right)$$
$$DR^i = \left(X^{i-1} - X^i\right)\big/ \Delta t$$

A5

A1

204

F.2.2 Condensation stage

A1

CONDENSATION $T_1^i < 100\ ^\circ C$ —N→ A2

Y

$$\Delta Q_{surf,in}^i = h_{cond}\, 4\pi \left(r_1^i\right)^2 \left(100 - T_1^i\right)\Delta t$$
$$\Delta Q_{surf,out}^i = h_{avg}\, 4\pi \left(r_1^i\right)^2 \left(T_s - 100\right)\Delta t$$

$$\Delta Q_{1,in}^i = \Delta Q_{surf,in}^i$$
$$\Delta Q_{N+1,out}^i = 0$$

$i = 0 \vee m_{surf}^i > 0$ —N→

Y

B1

$$\Delta m_{cond}^i = \Delta Q_{surf,in}^i / L$$
$$\Delta m_{evap,surf}^i = \Delta Q_{surf,out}^i / L$$

$$m_{surf}^i = m_{surf}^i + \sum_{n=1}^{N+1}\left(\Delta m_{sw,n}^i\right) + \Delta m_{cond}^i - \Delta m_{evap,surf}^i$$
$$m_{sw,total}^i = m_{sw,total}^i + \sum_{n=1}^{N+1}\left(\Delta m_{sw,n}^i\right)$$
$$m_{cond,total}^i = m_{cond,total}^i + \Delta m_{cond}^i$$

$m_{surf}^i > m_{surf,crit}^i$ —N→

Y

$$m_{surf}^i = m_{surf}^i - m_{drop}^i$$

WATER TRANSFER

$$\Delta Q_{n,in}^i = \frac{4\pi r_{n,out}^i}{b_{n-1}^i / \left(\lambda_{n-1}^i r_{n-1}^i\right) + b_n^i / \left(\lambda_n^i r_n^i\right)}\left(T_{n-1}^i - T_n^i\right)\Delta t$$
$$\Delta Q_{n,out}^i = \Delta Q_{n+1,in}^i$$
$$\Delta Q_{n,cons}^i = \Delta Q_{n,in}^i - \Delta Q_{n,out}^i$$
$$T_n^i = \frac{\Delta Q_{n,cons}^i}{c_c m_{c,n} + c_{w,n}^i m_{w,n}^i} + T_n^i$$

B2

$$m_{w,1}^i = m_{w,1}^i + \sum_{n=1}^{N+1}\left(\Delta m_{sw,n}^i\right) + \Delta m_{cond}^i - \Delta m_{evap,surf}^i$$
$$X_1^i = \frac{m_{w,1}^i}{m_{c,1}}$$
$$\varphi_{w,n}^i = m_{w,n}^i / \left(V_n^i \rho_{w,n}^i\right)$$
$$\varphi_{s,n}^i = \varphi_{w,n}^0 - \varphi_{w,n}^i$$

$$\Delta m_{sw}^i = m_{w,n}^i - V_n^i \rho_{w,n}^i \varphi_{w,n}^i$$
$$m_{w,n}^i = V_n^i \rho_{w,n}^i \varphi_{w,n}^i$$
$$X_n^i = \frac{m_{w,n}^i}{m_{c,n}}$$

B1   B2

F.2.3 Surface evaporation stage

A2

SURFACE
EVAPORATION
$T_1^i \geq 100 \, ^\circ C$
$\wedge$
$m_{surf}^i > 0$

N   A3

Y

$$\Delta Q_{surf,in}^i = 0$$

$$\Delta Q_{surf,out}^i = h_{avg} 4\pi \left(r_1^i\right)^2 \left(T_s - 100\right) \Delta t$$

$$T_1^i = 100 \, ^\circ C$$

$$\Delta Q_{N+1,out}^i = 0$$

$$\Delta Q_{n,in}^i = \frac{4\pi r_{n,out}^i}{b_{n-1}^i / \left(\lambda_{n-1}^i r_{n-1}^i\right) + b_n^i / \left(\lambda_n^i r_n^i\right)} \left(T_{n-1}^i - T_n^i\right) \Delta t$$

$$\Delta Q_{n,out}^i = \Delta Q_{n+1,in}^i$$

$$\Delta Q_{1,in}^i = \Delta Q_{1,out}^i$$

$$\Delta Q_{n,cons}^i = \Delta Q_{n,in}^i - \Delta Q_{n,out}^i$$

$$T_n^i = \frac{\Delta Q_{n,cons}^i}{c_c m_{c,n} + c_{w,n}^i m_{w,n}^i} + T_n^i$$

$$\Delta m_{evap,surf}^i = \left(\Delta Q_{surf,out}^i - \Delta Q_{1,out}^i\right) \Big/ L$$

$$m_{surf}^i = m_{surf}^i - \Delta m_{evap,surf}^i$$
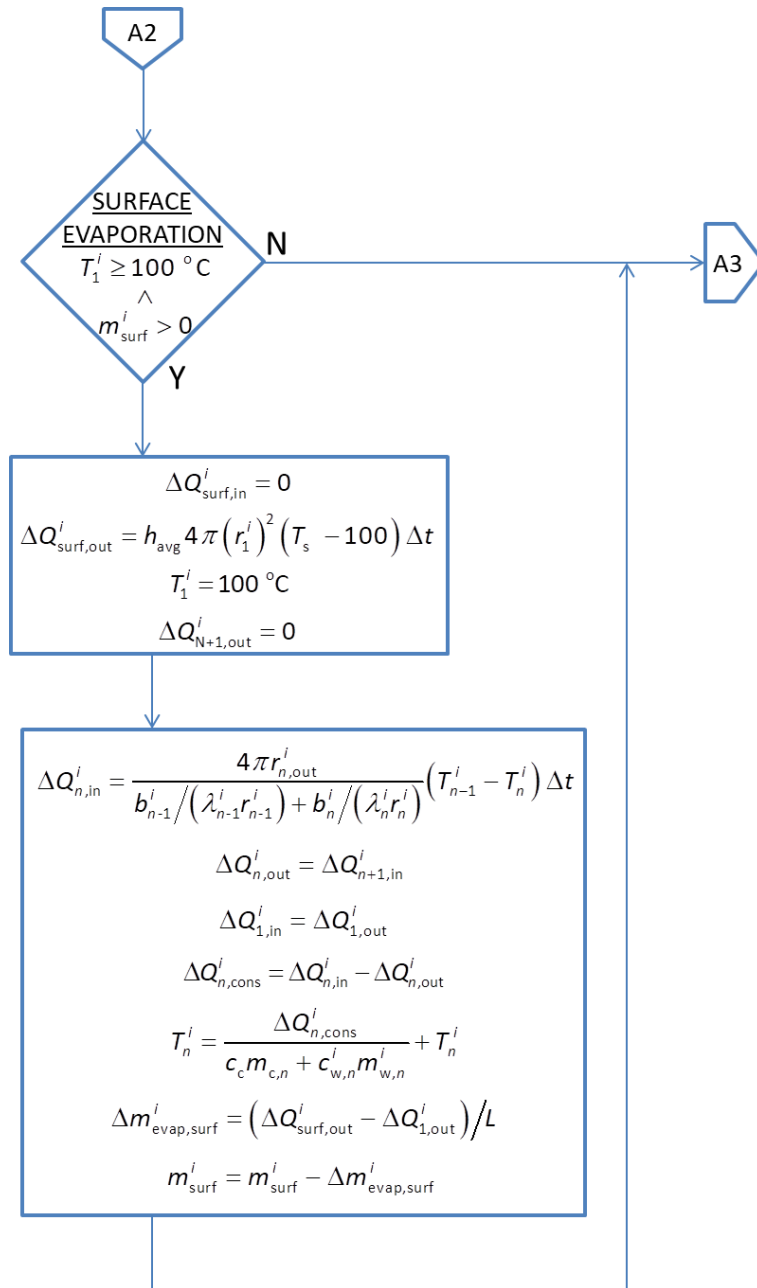
F.2.4 Drying 1 stage – free water occurring

A3

B3

B4

DRYING 1
$$T_1^i \geq 100\ ^{\circ}\mathrm{C}$$
$$\wedge$$
$$T_{N+1}^i < 100\ ^{\circ}\mathrm{C}$$
$$\wedge$$
$$m_{\text{surf}}^i = 0$$

N

Y

$$T_n^i = \frac{\Delta Q_{n,\text{cons}}^i}{c_c m_{c,n} + c_{w,n}^i m_{w,n}^i} + T_n^i$$

$$\varphi_{w,n}^i = m_{w,n}^i \big/ \left(V_n^i \rho_{w,n}^i\right)$$

$$\varphi_{s,n}^i = \varphi_{w,n}^0 - \varphi_{w,n}^i$$

$$X_n^i > X_{\text{eq}}(T = 100\ ^{\circ}\mathrm{C})$$

N

Y

$$X_1^i > X_{\text{eq}}(T = 100\ ^{\circ}\mathrm{C})$$

N

Y

$$T_1^i = 100\ ^{\circ}\mathrm{C}$$

$$T_n^i = 100\ ^{\circ}\mathrm{C}$$

$$\Delta m_{\text{evap},n}^i = \Delta Q_{n,\text{cons}}^i \big/ L$$

$$m_{w,n}^i = m_{w,n}^i - \Delta m_{\text{evap},n}^i$$

$$X_n^i = \frac{m_{w,n}^i}{m_{c,n}}$$

$$\varphi_{w,n}^i = m_{w,n}^i \big/ \left(V_n^i \rho_{w,n}^i\right)$$

$$\varphi_{s,n}^i = \varphi_{w,n}^0 - \varphi_{w,n}^i$$

$$T'^i_n = T_n^i$$
$$X_{\text{eq}} = X_{\text{eq}}\left(T'^i_n\right)$$

$$\Delta Q_{1,\text{in}}^i = 0$$
$$\Delta Q_{1,\text{out}}^i = h_{\text{avg}} 4\pi \left(r_1^i\right)^2 \left(T_s - 100\right)\Delta t$$
$$T_1^i = 100\ ^{\circ}\mathrm{C}$$
$$\Delta Q_{N+1,\text{out}}^i = 0$$

$$\Delta T_n^i \geq 10^{-14}\ ^{\circ}\mathrm{C}$$

N

Y

$$\Delta Q_{n,\text{in}}^i = \frac{4\pi r_{n,\text{out}}^i}{b_{n-1}^i \big/ \left(\lambda_{n-1}^i r_{n-1}^i\right) + b_n^i \big/ \left(\lambda_n^i r_n^i\right)} \left(T_{n-1}^i - T_n^i\right)\Delta t$$

$$\Delta Q_{n,\text{out}}^i = \Delta Q_{n+1,\text{in}}^i$$

$$\Delta Q_{n,\text{cons}}^i = \Delta Q_{n,\text{in}}^i - \Delta Q_{n,\text{out}}^i - \left(\Delta T_n^i - \Delta T_{n+1}^i\right)m_{\text{evap,total},n}^i c_{s,n}^i$$

$$X'_{\text{eq}} = X'_{\text{eq}}\left(T'^i_n\right)$$

$$\frac{dX}{dT}'_{\text{eq}} = \frac{dX}{dT}'_{\text{eq}}\left(T'^i_n\right)$$

$$\Delta H_{\text{evap},n}^i = \Delta H_{\text{evap},n}^i\left(T'^i_n\right)$$

$$T''^i_n = T'^i_n - \frac{\Delta Q_{n,\text{cons}}^i - \left(X_{\text{eq}} - X'_{\text{eq}}\right)m_{c,n}\Delta H_{\text{evap},n}^i}{\frac{dX}{dT}'_{\text{eq}} m_{c,n}\Delta H_{\text{evap},n}^i - \left(m_{c,n}c_c + m_{c,n}c_{w,n}^i \frac{X_{\text{eq}} + X'_{\text{eq}}}{2}\right)} - $$
$$-\frac{\left(T''^i_n - T_n^i\right)\left(m_{c,n}c_c + m_{c,n}c_{w,n}^i \frac{X_{\text{eq}} + X'_{\text{eq}}}{2}\right)}{\frac{dX}{dT}'_{\text{eq}} m_{c,n}\Delta H_{\text{evap},n}^i - \left(m_{c,n}c_c + m_{c,n}c_{w,n}^i \frac{X_{\text{eq}} + X'_{\text{eq}}}{2}\right)}$$

$$\Delta T_n^i = \left|T''^i_n - T'^i_n\right|$$

$$T'^i_n = T''^i_n$$

WATER TRANSFER

$$T_n^i < 100\ ^{\circ}\mathrm{C}$$

N

Y

B3

B4

A4

$$T_n^i = T''^i_n$$
$$\Delta m_{\text{evap},n}^i = m_{w,n}^i - m_{c,n}X'_{\text{eq}}$$
$$X_n^i = \frac{m_{w,n}^i}{m_{c,n}}$$
$$\varphi_{w,n}^i = m_{w,n}^i \big/ \left(V_n^i \rho_{w,n}^i\right)$$
$$\varphi_{s,n}^i = \varphi_{w,n}^0 - \varphi_{w,n}^i$$

F.2.5 Drying 2 stage – no free water occurring

A4

B5

DRYING 2

$T_{N+1}^{i} \geq 100\ ^{\circ}C$
$\wedge$
$m_{surf}^{i} = 0$

N

$X_n^i > X_{eq}(T = 100\ ^{\circ}C)$

N

Y

Y

$T_n^i = 100\ ^{\circ}C$

$\Delta m_{evap,n}^{i} = \Delta m_{evap,n}^{i} + \Delta Q_{n,cons}^{i}/L$

$m_{w,n}^{i} = m_{w,n}^{i} - \Delta Q_{n,cons}^{i}/L$

$\varphi_{w,n}^{i} = m_{w,n}^{i}/\left(V_n^i \rho_{w,n}^i\right)$

$\varphi_{s,n}^{i} = \varphi_{w,n}^{0} - \varphi_{w,n}^{i}$

$T\,''^{\,i}_n = T_n^i$
$X_{eq} = X_{eq}\left(T\,''^{\,i}_n\right)$

$\Delta T_n^i \geq 10^{-14}\ ^{\circ}C$

N

Y

$\Delta Q_{1,in}^{i} = 0$

$\Delta Q_{1,out}^{i} = h_{avg}\,4\pi\left(r_1^i\right)^2\left(T_s - 100\right)\Delta t$

$T_1^i = 100\ ^{\circ}C$

$\Delta Q_{N+1,out}^{i} = 0$

$\Delta Q_{n,in}^{i} = \dfrac{4\pi r_{n,out}^{i}}{b_{n-1}^i/\left(\lambda_{n-1}^i r_{n-1}^i\right) + b_n^i/\left(\lambda_n^i r_n^i\right)}\left(T_{n-1}^i - T_n^i\right)\Delta t$

$\Delta Q_{n,out}^{i} = \Delta Q_{n+1,in}^{i}$

$\Delta Q_{n,cons}^{i} = \Delta Q_{n,in}^{i} - \Delta Q_{n,out}^{i} - \left(\Delta T_n^i - \Delta T_{n+1}^i\right)m_{evap,total,n}^{i}c_{s,n}^i$

WATER TRANSFER

$X'_{eq} = X'_{eq}\left(T\,''^{\,i}_n\right)$

$\dfrac{dX'}{dT}_{eq} = \dfrac{dX'}{dT}_{eq}\left(T\,''^{\,i}_n\right)$

$\Delta H_{evap,n}^{i} = \Delta H_{evap,n}^{i}\left(T\,''^{\,i}_n\right)$

$T\,'''^{\,i}_n = T\,''^{\,i}_n - \dfrac{\Delta Q_{n,cons}^{i} - \left(X_{eq} - X'_{eq}\right)m_{c,n}\Delta H_{evap,n}^{i}}{\dfrac{dX'}{dT}_{eq} m_{c,n}\Delta H_{evap,n}^{i} - \left(m_{c,n}c_c + m_{c,n}c_{w,n}^i \dfrac{X_{eq} + X'_{eq}}{2}\right)} -$

$- \dfrac{\left(T\,''^{\,i}_n - T_n^i\right)\left(m_{c,n}c_c + m_{c,n}c_{w,n}^i \dfrac{X_{eq} + X'_{eq}}{2}\right)}{\dfrac{dX'}{dT}_{eq} m_{c,n}\Delta H_{evap,n}^{i} - \left(m_{c,n}c_c + m_{c,n}c_{w,n}^i \dfrac{X_{eq} + X'_{eq}}{2}\right)}$

$\Delta T_n^i = \left|T\,'''^{\,i}_n - T\,''^{\,i}_n\right|$

$T\,''^{\,i}_n = T\,'''^{\,i}_n$

B5

A5

$T_n^i = T\,''^{\,i}_n$

$\Delta m_{evap,n}^{i} = \Delta m_{evap,n}^{i} + m_{w,n}^{i} - m_{c,n}X'_{eq}$

$X_n^i = \dfrac{m_{w,n}^{i}}{m_{c,n}}$

$\varphi_{w,n}^{i} = m_{w,n}^{i}/\left(V_n^i \rho_{w,n}^i\right)$

$\varphi_{s,n}^{i} = \varphi_{w,n}^{0} - \varphi_{w,n}^{i}$

F.2.6 Water transfer procedure

WATER TRANSFER

START

$$\Delta m^i_{\text{trans,in},N+1} = 0$$

$X^i_{n+1} > X_{eq}(T = 100\ ^\circ C)$ — N → $\Delta m^i_{\text{trans,in},n} = 0$

Y

$$\Delta m^i_{\text{trans,in},n} = -D\rho_c\, 4\pi r^i_n r^i_{n+1}\, \frac{X^i_n - X^i_{n+1}}{b^i_n + b^i_{n+1}}\, \Delta t$$

$$\Delta m^i_{\text{trans,out},1} = 0$$
$$\Delta m^i_{\text{trans,out},n} = \Delta m^i_{\text{trans,in},n-1}$$
$$\Delta m^i_{\text{trans},n} = \Delta m^i_{\text{trans,in},n} - \Delta m^i_{\text{trans,out},n}$$
$$m^i_{w,n} = m^i_{w,n} + \Delta m^i_{\text{trans},n}$$

$T^i_n > 100^\circ C$ — N

Y

$\Delta m^i_{\text{trans},n}\, L < \Delta Q^i_{n,\text{cons}}$ — N

Y

$$m^i_{w,n} = m^i_{w,n} - \Delta m^i_{\text{trans},n}$$
$$\Delta Q^i_{n,\text{cons}} = \Delta Q^i_{n,\text{cons}} - \Delta m^i_{\text{trans},n}\, L$$
$$\Delta m^i_{\text{evap},n} = \Delta m^i_{\text{trans},n}$$

$$m^i_{w,n} = m^i_{w,n} - \Delta m^i_{\text{trans},n}$$
$$m^i_{w,n+1} = m^i_{w,n+1} + \Delta m^i_{\text{trans},n}$$
$$\Delta m^i_{\text{trans},n+1} = \Delta m^i_{\text{trans},n+1} + \Delta m^i_{\text{trans},n}$$
$$\Delta m^i_{\text{trans},n} = \Delta Q^i_{n,\text{cons}} / L$$
$$m^i_{w,n+1} = m^i_{w,n+1} - \Delta m^i_{\text{trans},n}$$
$$\Delta m^i_{\text{trans},n+1} = \Delta m^i_{\text{trans},n+1} - \Delta m^i_{\text{trans},n}$$
$$\Delta Q^i_{n,\text{cons}} = 0$$
$$\Delta m^i_{\text{evap},n} = \Delta m^i_{\text{trans},n}$$

STOP